DISSERTATION

UNDERSTANDING THE SOLID ELECTROLYTE INTERFACE (SEI) ON ALLOYING ANODES: DEVELOPMENT OF A METHODOLOGY FOR SEI SAMPLE PREPARATION AND X-RAY PHOTOELECTRON SPECTROSCOPY CHARACTERIZATION AND STUDIES OF THE SEI ON ELECTRODEPOSITED THIN FILM INTERMETALLIC ANODES FOR Li-ION BATTERIES

Submitted by

Leslie A. Kraynak

Department of Chemistry

In partial fulfillment of the requirements

For the Degree of Doctor of Philosophy

Colorado State University

Fort Collins, Colorado

Summer 2020

Doctoral committee:

Advisor: Amy L. Prieto

Matthew Shores
Steven Strauss
Todd Bandhauer

ABSTRACT

UNDERSTANDING THE SOLID ELECTROLYTE INTERFACE (SEI) ON ALLOYING ANODES: DEVELOPMENT OF A METHODOLOGY FOR SEI SAMPLE PREPARATION AND X-RAY PHOTOELECTRON SPECTROSCOPY CHARACTERIZATION AND STUDIES OF THE SEI ON ELECTRODEPOSITED THIN FILM INTERMETALLIC ANODES FOR Li-ION BATTERIES

The solid electrolyte interface (SEI) is an important component of Li-ion rechargeable batteries that forms due to the potential stability limits of the organic electrolyte falling within the large operating potential window of the battery. It plays a crucial role in battery performance by passivating the electrode surface; it also affects the safety, Li-ion consumption/inventory, and Li-ion transport rates of the battery. Despite decades of study, there is still much that is unknown about the SEI, especially how to intentionally modify the composition and properties of the SEI in order to obtain better performance as measured by metrics that include reversible capacity and cycle lifetime. The gaps in understanding of the SEI are even more pronounced for alloying anode materials, and the mechanical and chemical instability of electrode surfaces and the SEI formed from conventional secondary battery electrolytes is one of the bottlenecks in the development of next generation battery technologies.

The first chapter of this dissertation is an overview of studies from the past two decades concerning the SEI formed on metallic alloying anodes, examining SEI formation, the evolution of the SEI over long term cycling, and improvements to the SEI through the use of additives and novel electrolytes. Compared to the body of literature on the SEI on other anode materials such as graphite, Li metal, and silicon, there has been relatively little published about the SEI on metallic alloying anodes such as tin, antimony, and intermetallics, especially considering the scope of these types of anode materials. However, a comparison of the existing literature concerning the SEI on alloying anodes reveals interesting

similarities and difference between the SEI formation and evolution on metallic alloying anodes and highlights some critical gaps in knowledge for the field.

The second chapter concerns the development of a methodology to study the SEI formed on alloying anodes, and in particular binder- and additive-free thin film electrodes. The formation, composition, and properties of the SEI are dependent on a number of experimental variables, which makes it difficult understand the factors that affect SEI performance and limits progress towards the goal of more controlled or intentional SEI formation for better battery performance. One of the first steps towards this goal is to be able to make and characterize SEI samples in a reproducible manner. This chapter outlines some of the important considerations for SEI sample preparation that are not widely discussed in the battery community in addition to some of the important considerations for using X-ray photoelectron spectroscopy to characterize the SEI.

The third and fourth chapters are about using the methodology described in Chapter 2 to characterize the SEI formed on intermetallic thin film anodes. The third chapter examines the role that vinylene carbonate, a conventional SEI-improving electrolyte additive, plays in passivating the surface and extending the cycle lifetime of Cu_2Sb electrodes. The fourth chapter is concerned with understanding what role the SEI plays in the cycle performance of pure phase SnSb thin film electrodes. Studying changes in the SEI on SnSb over different stages of cycling can help elucidate whether the SEI plays a role in the capacity retention and long cycle lifetime of SnSb and whether it ultimately contributes to the failure of the electrode.

ACKNOWLEDGMENTS

Working on my research and dissertation in graduate school has been a lot of hard work, but I have been incredibly fortunate to have the support of many people throughout my graduate school career. Finishing graduate school without all of their support, guidance, and advice would have been incredibly challenging, and I would not be the person who I am today without them.

First, I'd like to thank my advisor, Professor Amy Prieto. I feel so lucky to have been able to work with someone who I admire so much. I am so grateful to have had an advisor who pushed me to challenge myself and learn new things but who also gave me space to explore my own interests. I can't thank Amy enough for all of her patience, time, support, and advice, both in and out of the lab over the past seven years.

I would also like to thank all of my committee members. Thank you to Professor Matt Shores for always providing helpful feedback on my writing and for asking so many insightful questions (and for making really good brisket). I'd like to thank Professor Steve Strauss for reminding me of the importance of details and the use of correct grammar (including the conventional way to spell "acknowledgments" in the United States!). Finally, I'd like to thank Professor Todd Bandhauer for always reminding me to take a step back and look at the big picture, which has been extremely helpful advice to recall during my graduate school career.

I have been incredibly lucky to work with so many smart and talented people in the Prieto lab over the years; I appreciate all of you. Thank you to Dr. Everett Jackson for teaching me all about electrodeposition and batteries when I first joined the Prieto lab. Many thanks to Dr. Dan Agocs for being a great Lab Dad who I could always approach with all of my questions, even the ones I should have already known the answer to. Thank you to Dr. Rebecca Miller for being a source of support from day one of graduate school and for answering all of my dissertation related questions over the past few

months! So many thanks to Jacob Schneider for taking the time to design and make an XPS holder for air free sample transfer that was so essential for studying the SEI. Dr. Max Schulze, thank you for sharing your infectious enthusiasm for science and for being the reason that I learned how to use Python. Jennifer Lee, thank you for being such an inspiration and for being so supportive always; it has meant so much to me. Jeffrey Ma, thank you for always being so generous with your time and always being willing to help me, whether it's making me the best SnSb films for my experiments or spending way too long helping me look for my favorite pair of tweezers. Lily Moloney, thank you for letting me bother you about ordering and for always being so supportive and asking good questions. Nathan Gimble, thank you for reading all of the drafts that I send your way and for geeking out about XPS and the SEI with me. Amanda Kale, thank you for helping me finally understand the difference between i.e. and e.g.; it has actually helped a lot while writing this dissertation. Thank you to Chris Rom for always being so positive and for being willing to take over the care of the fish tank. Kelly Nieto, thank you so much for being my go-to person for questions about Python; you always help me figure out my coding problems!

I've had a lot of people outside of the lab at CSU who have also helped me over the years. Thank you to Professor Jamie Neilson for teaching me solid state chemistry. Many thanks to Professor C. Michael Elliott for teaching me electrochemistry and for the grits. Many thanks to Dr. Patrick McCurdy for all of the help with XPS and SEM over the years. I'm also incredibly grateful for Kathy, Desi, Nadya, Karen, Connie, Jan, and Elizabeth for always patiently answering my administrative questions over the years. Finally, many thanks to Dr. Kristina Quynn for CSU writes, especially the writing retreats, and for teaching me the important difference between drafting and editing.

I've also been fortunate to have the support of many others outside of the CSU community. Thank you to Rod and Amy for making me feel like a part of the Fort Collins community and for growing the best collard greens. Many, many thanks to Carrie for all of the support and help over several rough

years; I can't imagine how different my life would be without your help. Thank you to Matt Jones and the rest of the Jones/Sandoski clan for the support during the early years of my graduate school career.

Many thanks to all of my friends. To Amanda, for being good about keeping in touch even when I am the worst at responding to texts. To Becca, for always being willing to chat about two of my favorite things: books and cats. To my stitch and bitch/book exchange/writing group friends- Jen, Annalise, Eve, Lily, Chris, Kim, Hailey, Angela, and Jas- thank you for making grad. school much more enjoyable and productive. To my trivia friends- Dan, Jenna, Josh, Nathan, Amanda, and Carly- I am atomic orange level thankful for you.

I have been incredibly lucky to have such a supportive family that has sent me lots of love and care packages over the years. Mom and Dad, thank you so much for literally everything and for keeping me well fed with boiled peanuts, steak, chex mix, and pound cake over the years. To Sarah, Brian, and Naomi, thank you for always brightening my day with your faces (and sometimes with Jeni's ice cream!). To Annie and Trey, thank you for coming to have adventures with me in Colorado, and to Gabriel and Hutson, thank you for always making me smile. To Grandma and Aunt Kim, thank you for all of the love and care packages that you have sent over the years. To my Glenn Girls, thank you for making me laugh until I cry and for your support.

Finally, last, but definitely not least, many, many thanks to Kane. Thank you for being the best. You have somehow managed to make some of my busiest and most stressful years of grad. school also the most enjoyable. Writing this dissertation would have been so much more difficult without your support; thank you for keeping me well fed with brisket and cheesecake and for picking up all of the slack over the past few months. (Also, you were right).

TABLE OF CONTENTS

LIST OF FIGURES

CHAPTER 1: THE SOLID ELECTROLYTE INTERFACE ON ALLOYING ANODES FOR Li-ION BATTERIES*

Chapter summary

Lithium alloying materials have been studied extensively as anode candidates for next generation Li-ion batteries due to having high volumetric capacities. However, the understanding of the solid electrolyte interface (SEI), an important component of rechargeable batteries, remains limited for this class of anode materials. This chapter provides an overview of the current understanding of the SEI on alloying anode materials, including SEI formation over short term cycling, the evolution of the SEI over extended cycling, and improvements in SEI performance through the use of additives and unconventional electrolyte formulations.

1.1) Introduction

Rechargeable battery technologies, specifically Li-ion batteries, have found utility in a variety of important applications, including personal electronic devices and hybrid-electric/all electric vehicles. These technologies requiring the storage of large amounts of energy make use of anode and cathode materials with large differences in redox potentials in order to increase the average voltage.[1] However, the electrochemical stability window of most liquid electrolytes, in particular the organic liquid electrolytes used for rechargeable batteries, falls within the voltage window of the battery electrodes.[1] In order for the battery to function, the formation of a passivating layer on the electrode surface that blocks electron transport to limit excessive electrolyte degradation while still allowing for the transport of Li ions is necessary.[2] This passivating layer is known as the solid electrolyte interface (or interphase) (SEI).[3]

The SEI is a film composed of electrolyte salt and solvent reduction or decomposition products.[2,4] Conventional Li-ion battery electrolyte solutions contain $LiPF_6$ as the Li salt supporting electrolyte and

* This chapter was written to be submitted for peer review and publication in the *Journal of the Electrochemical Society* with Leslie A. Kraynak and Amy L. Prieto as authors. The paper was written by Leslie A. Kraynak with guidance and editing provided by Amy L. Prieto.

various mixtures of organic carbonates, including ethylene carbonate (EC), propylene carbonate (PC), dimethyl carbonate (DMC), diethyl carbonate (DEC), and EMC, as the cosolvents.[5] Some of the proposed reduction and decomposition pathways for the most common electrolyte components are shown in Scheme 1.1. Many of the proposed reactions result in the formation of radical intermediates, which is one reason the SEI formation is so complex.[5] Much of the current understanding of the SEI for Li-ion batteries comes from XPS, FTIR, and electrochemical characterization of graphite and Li metal anodes.[4–7] Based on these works, the SEI formed on Li-ion battery anodes is generally accepted to be a heterogeneous, layered structure. It consists of an inner layer near the anode surface composed of inorganic species such as LiF, Li_2O, and Li_2CO_3 and an outer organic-rich layer composed of solvent reduction species like Li alkyl carbonates, PEO oligomers, and metal carboxylates.[7]

While it is not typically considered as a component of Li-ion batteries like the anode, cathode, electrolyte, and separators are, the SEI plays a crucial role in the performance of the battery. It is thought to function as a solid electrolyte, and a decade ago Martin Winter referred to it as "the most important and least understood solid electrolyte".[8] It affects the safety, charge/discharge rates, cycle lifetime, calendar lifetime, and reversible capacity of Li-ion batteries. As a crucial battery component, there are several important criteria for a functional and safe SEI, as outlined elsewhere.[5,9] First, the SEI must be stable over the cycle lifetime of the battery, without excessive deposition or dissolution. Second, the SEI must be mechanically stable; specifically, it should be flexible and robust enough to accommodate volume changes during lithiation and delithiation. To allow for fast Li ion transport, it should have a low electrical impedance and/or be relatively thin and uniform in thickness, and it should be a good conductor for unsolvated Li ions. Finally, it should provide a barrier for solvent molecules.[5,9] The SEI formed from conventional electrolyte solutions on graphite satisfies most of these requirements adequately, which has enabled it to be used as the anode in most commercial Li-ion batteries.[5,8] However, for next generation

Scheme 1.1: Common examples of proposed electrolyte reduction pathways and products for conventional organic carbonate solvents in Li-ion battery electrolytes.[10,11]

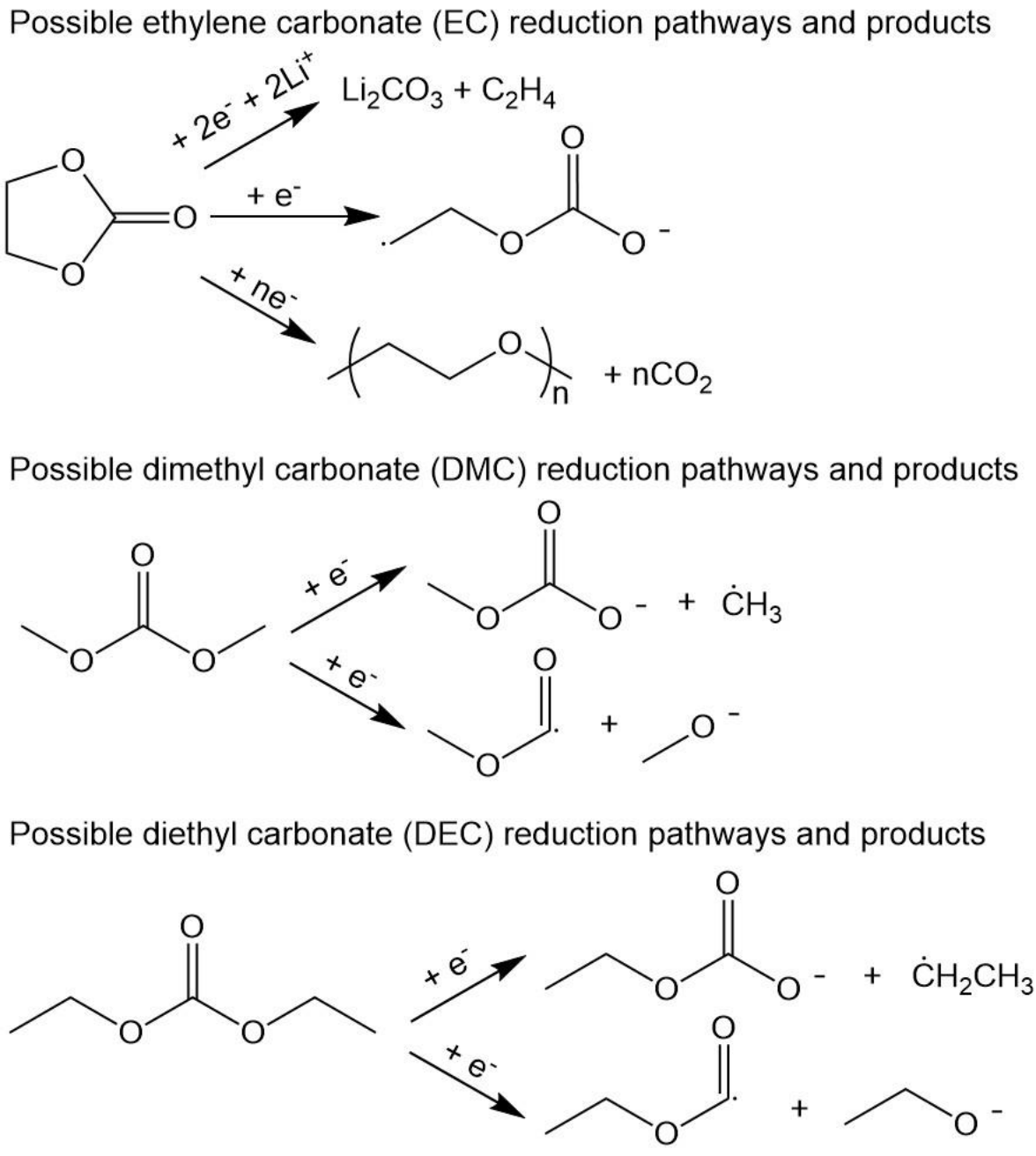

anode materials with higher capacities, most of these criteria are not met when using conventional Li-ion battery electrolytes.

Materials that alloy with lithium, including elements such as Sn, Sb, and Si, and Sb- and Sn-based intermetallics and alloys, are attractive as next generation anode materials due to their high volumetric capacities.[12,13] Unfortunately, this is also a drawback of alloying anodes, as it plays a role in SEI instability. These materials undergo large volume changes during lithiation and delithiation, which leads to cracking of both the electrode active material and the SEI. When new electrode surfaces are exposed due to these volume changes, it leads to additional electrolyte reduction and SEI formation.[12] The chemical and mechanical instability of the SEI ultimately leads to low coulombic efficiency and capacity fade due to either sluggish Li ion transport kinetics or active material loss, respectively. Additionally, the surface reactivity of alloying anodes results in large first cycle irreversible capacity loss due to excessive SEI formation and Li ion consumption.[12] One of the most common approaches to alleviating the mechanical stress of the electrode associated with lithium alloying and dealloying is the use of micro- or nano-sized active material particles, which can also exacerbate issues associated with the SEI due to increased surface area, so SEI formation is an issue for alloying anodes even when problems associated with volume expansion have been moderated.[12]

Research on the SEI is a continuously growing field, and there have been numerous excellent reviews chronicling the progress and limitations of the field. Kang Xu has published two exhaustive reviews on electrolytes and interfaces in rechargeable batteries, describing decades worth of research on both conventional and novel electrolytes and additives as well as interphases on various electrode materials for rechargeable batteries.[5,14] Verma and coworkers published a review focusing on compositional characterization of the SEI formed on graphite from carbonate-based electrolytes, highlighting the importance of many variables in SEI formation and characterization and how those play a role in the species commonly reported to make up the SEI as well as species that continue to be a topic of debate in

the field.[4] Others such as Gauthier and coworkers and Peled and Menkin have written reviews that provide a survey of field of SEI research for Li-based battery systems, describing current knowledge of SEI formation, composition, and characterization for cathodes and the most common anode materials such as graphite, silicon, and tin as well as the gaps in knowledge for the field.[2,7] Most of the existing SEI reviews are quite broad in scope, covering SEI literature for the most commonly studied electrodes, although some have written an in depth review of the SEI on Si alloying anodes.[15] To the best of our knowledge, there are no reviews yet that provide an in depth look at SEI formation and composition for metallic alloying anode materials, which are considerably different than graphite, Li metal, and Si alloying anodes in terms of surface reactivity and/or lithiation/delithiation mechanisms.

While the SEI formed on graphite and other carbon-based anode materials has been studied extensively and covered in several of the reviews mentioned previously, there have been fewer studies of the SEI formed on alloying anode materials, which are attractive as next-generation anode materials due to considerably higher volumetric capacities compared to graphite.[12] However, the different lithiation pathways and reactivities of graphite and alloying anodes affect SEI formation and growth, so conclusions drawn from SEI studies on graphite electrodes may not be translatable to alloying anodes. Using on-line mass spectrometry, Wagner and coworkers observed differences in gas evolution when cycling graphite and tin/tin antimonide based anodes, suggesting differences in electrolyte reduction reactions and SEI formation for the intercalation and alloying anodes. The authors observed the evolution of ethylene and propylene when using EC- and PC-based electrolytes, respectively, for graphite but not the Sn-based anode; these gases are proposed to form due to the two electron reduction of EC and PC, which suggests that solvent reduction on alloying anode may follow different pathways than those proposed for graphite.[16] Bryngelsson and coworkers have also observed some differences between the SEI layers formed on graphite anodes compared to AlSb anodes; based on X-ray photoelectron spectroscopy (XPS) characterization, there are differences in the predominant carbonaceous species at the SEI surface for the

graphite and AlSb anodes after 50 cycles, and the SEI formed on AlSb seems to be much thinner than the one formed on graphite.[17] Furthermore, Wachtler and coworkers have pointed out that the requirements of alloying and intercalation anodes are different because alloying anodes undergo such large volume changes during cycling, as depicted in Figure 1.1; while the SEI on graphite needs to passivate the surface, allow for Li ion transport, and hinder solvent co-intercalation, the SEI formed on alloying anodes needs to be flexible enough to withstand volume changes during cycling in addition to passivating the surface and allowing for fast Li ion transport.[18] Additionally, alloying anodes tend to exhibit large initial irreversible capacity loss and short cycle lifetimes due to capacity fade, likely due to interfacial instability associated with the SEI.[12] As such, it is important to study the SEI formed on alloying anodes in order to gain a better understanding of the formation processes, composition, and properties of the SEI on alloying anodes in order to ultimately be able to control SEI formation and impart the desired properties for a SEI on alloying anodes.

While it is important to study the SEI formed on alloying anodes because it seems to be different than the SEI formed on graphite, it is also important because the varying reactivities and lithium alloying pathways of different types of alloying anodes also seem to play a role in SEI formation and evolution. Therefore, it is important to study the SEI on alloying anodes to understand SEI formation on different lithium alloying materials, but the diversity among alloying anode materials also makes them interesting for fundamental SEI studies. For example, some alloying electrodes form a passivation layer upon exposure to electrolyte without any applied current or voltage,[19–21] while others do not.[22–24] Bridel and coworkers have observed considerable EC reactivity at the surface of thin film alloying anodes like Sn, Bi, and Pb at high potentials, but not Sb and Si thin films.[25] Additionally, others have observed differences in the SEI speciation on Sn and Au electrodes using FTIR and MALDI-MS.[26,27]

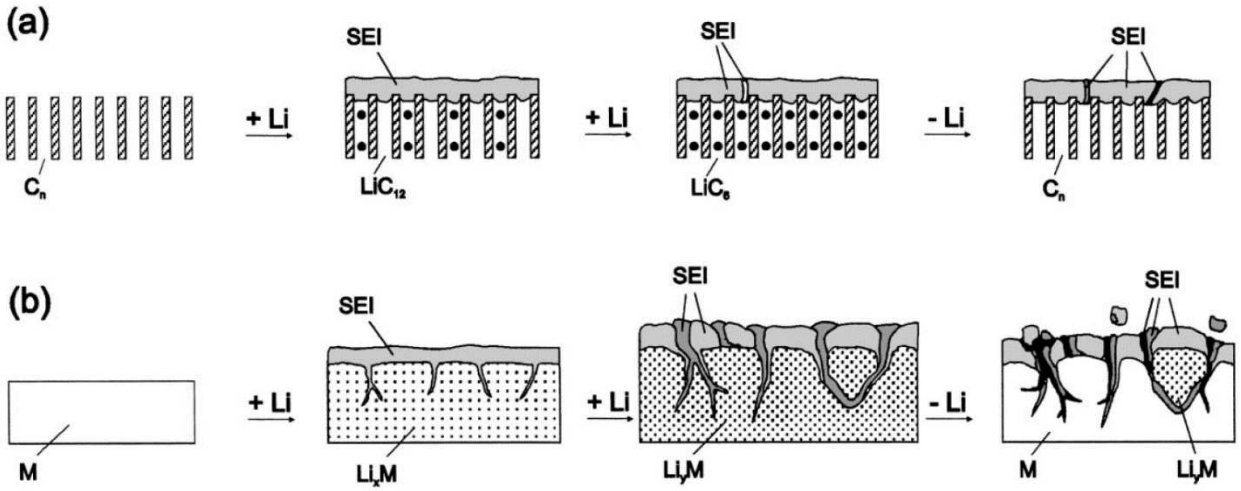

Figure 1.1: Illustrations depicting SEI formation and the changes to the electrode and SEI during cycling for (a) graphite anodes and (b) alloying anode materials. Reprinted from Reference 18 with permission from Elsevier.

As described above, the reactivity of the electrode material can affect SEI formation and composition, but there are many other variables that can also affect the SEI. Some researchers have found that the electrode fabrication methods and conditions can also influence the SEI.[11,28–33] The cycling conditions such as temperature, applied current, and potential limits have also been found to influence the SEI.[4,11,34–36] Finally, it should come as no surprise that the electrolyte components, including the lithium supporting electrolyte, solvents, additives, and impurities, also affect the SEI formation, composition, and properties.[37–45] As such, it is incredibly difficult to compare results from SEI studies across the literature, especially for alloying anodes. In this review, we have gathered and summarized the results of existing alloying anode SEI studies in one place with the hope of better understanding the formation, composition, and properties of the SEI on alloying anodes. In many ways, the study of the SEI on alloying anodes is still in its infancy despite decades of study. Comparison of studies of the SEIs on alloying anodes can help clarify what has been discovered about the similarities and differences among alloying anode SEIs while also helping to see the directions that should be pursued in future research.

1.1.1) Scope of review

In this review we will focus on the SEI formed on lithium alloying anodes in non-aqueous electrolytes but will not include any artificial SEI or anode coating studies. This review is limited to metallic lithium alloying anode materials, which we are defining as any metal, semimetal, or metallic alloy that is a good electronic conductor in its delithiated form without the use of dopants. As such, Si is beyond the scope of this review, but the reader will be referred to SEI studies on Si anodes where relevant. A discussion of SEI studies on metallic current collectors will also be included here because many of those studies have helped provide insight into studies of alloying materials, and along with studies on lithium metal and graphite (both of which are outside the scope of this work) have helped form the basis of the community's understanding of the SEI.

1.1.2) Definitions

The field of battery research is remarkably multidisciplinary and as such often uses of language that can lead to confusion. This is particularly true for terms used to describe battery and half-cell electrochemistry. Most studies of the SEI formed on alloying anode materials make use of half cells, so we will use those terms in this review. In two electrode half cells, the anode material is the working electrode and lithium metal acts as the counter and pseudo reference electrode, so all potentials in this work are referenced to Li/Li^+ unless noted otherwise. Discharging a half cell refers to applying a reducing current and lithiating the working electrode active material, and charging refers to applying an oxidizing current and delithiating the working electrode active material. In cases where cyclic voltammetry is used instead of galvanostatic cycling, or when the electrolyte decomposition and SEI formation processes are being discussed, we may refer to the processes as reduction/oxidation instead of discharge/charge. Finally, our definition of alloying anodes encompasses the elemental lithium alloying materials, including Sn and Sb; lithium alloying intermetallic compounds that are often referred to as conversion anodes; and

binary metal alloys. A list defining all of the acronyms used in this review can be found at the end of this work on page 210.

1.2) Electrode Reactivity

1.2.1) Metallic current collectors and noble metal model systems

Studying electrolyte reduction and passivation layer formation on metallic current collectors is useful for fundamental studies on electrolyte reactivity even if they do not alloy with lithium or are not practical electrode materials. These metals are useful as model electrodes to help improve our understanding of the SEI formed on metallic surfaces, especially since some intermetallic and binary metal alloy anode materials incorporate elements such as Cu or Ni which do not alloy with lithium but may still react with electrolyte components.

Studies of lithium salt and organic solvent decomposition on noble metal electrodes like Au have helped form the basis of the understanding of electrolyte decomposition and SEI formation, providing details about electrolyte cathodic and anodic stability limits, reduction and oxidation species, and the effects of solution contaminants or additives.[46–49] Additionally, inactive/non-alloying metal electrodes have proven extremely useful for studies of the SEI where lithiation and delithiation of the electrode could complicate the interpretation of the results. Studies of SEI formation on Cu electrodes have been useful for understanding Li ion transport in the SEI and studying changes in the SEI structure and morphology with potential.[50–53] For example, based on Li isotopic ratios, ToF-SIMS characterization of the SEI formed on Cu electrodes suggests that the outer organic-rich layer of the SEI forms before the inner, inorganic rich layer of the SEI.[52] Soft XAS studies of the SEI formed on Cu reveal oscillating or dynamic behavior of the SEI, suggesting that SEI is thicker during discharging and becomes thinner during charging but slowly increases in thickness with cycling.[53] Model electrodes have also been useful in demonstrating the utility of certain characterization techniques without convolution from Li alloying electrodes; for example, valence band XPS was demonstrated to be a useful technique for identifying carbonate species in the SEI

that cannot be differentiated using C 1s or O 1s core spectra.[54] Others have found utility in using model electrodes like Ni and Cu to study surface passivation in unconventional electrolytes like $LiBH_4$ in THF, which does not seem react to form a thick SEI to the same extent as conventional battery electrolytes.[55,56] In other experiments, model electrodes have been useful for fundamental studies of molecular level interactions between solvents and the electrode surface and for evaluating proposed electrolyte reduction pathways.[57,58]

While the utility of model electrodes has been demonstrated for many different applications, they do have limitations. Some of these limitations have been revealed in studies comparing SEI formation on Au model electrodes and Sn alloying anodes. In-situ FTIR studies of the electrolyte reduction and SEI formation revealed that some species for the Au and Sn SEIs were different.[26] Likewise, EQCM characterization showed higher mass gain for the Au electrodes compared to Sn, and MALDI-ToF MS results suggested the formation of high molecular weight oligomeric species with regularly repeating units for Au electrodes while high molecular weight species formed on the Sn electrodes during the first cycle decomposed or reacted to form lower molecular weight species over subsequent cycles.[27] These studies suggest that there is a difference in the reactivity of Au and Sn electrodes, and that model electrodes have limitations. SEI studies on model electrodes are a useful complement to but not a replacement for studies of SEI formation, composition, and properties on alloying anodes.

1.2.2) Spontaneous passivation layer formation

As mentioned above, one reason alloying anodes are interesting is due to the variation in surface reactivities for different materials. Some alloying anode materials have been found to spontaneously form a passivation layer upon contact with an electrolyte solution while others do not. Song and Baek observed some evidence of electrolyte decomposition on Sn thin films after 30 hours of soaking in electrolyte. Using FTIR, they saw bands corresponding to inorganic PF-containing species as well as some organic species containing alkyl and carboxyl groups on the surface of the soaked electrode.[19] However, Martín and

coworkers did not see any evidence of a passivation layer on Sb pellets soaked in electrolyte for several hours based on XPS characterization. The authors did not observe any attenuation of the Sb 4d peaks after soaking, and there were only very weak C 1s and F 1s signals, suggesting little to no spontaneous passivation of the Sb electrode.[22]

Intermetallic alloying anode materials show similar variations in surface reactivity. Chamas and coworkers observed the formation of a passivation layer on $FeSn_2$ composite electrodes upon contact with the electrolyte based on the EIS results at OCP.[21] Tesfaye and coworkers also observed the formation of a thin passivation layer on SnSb composite electrodes at OCP based on EIS and TEM characterization.[59] Using XPS to characterize their samples, Naille and coworkers observed the formation of a passivation layer on Cu_6Sn_5 composite electrodes after soaking in electrolyte for 24 hours. Most of the peaks corresponding to the underlying Cu_6Sn_5 electrode either disappeared or were attenuated. The appearance of C 1s peaks corresponding to carbonate, C–O, and aliphatic carbon binding environments and F 1s peaks corresponding to LiF and $LiPF_6$ species suggests the formation of a passivation layer composed of both organic and inorganic electrolyte decomposition species.[20] The results for other Sn-based intermetallic anodes were mixed. After soaking TiSnSb composite electrodes in electrolyte for 24 hours there was no evidence of passivation layer formation,[24] although others found that storing TiSnSb electrodes in assembled half cells for three weeks did result in a passivating layer at the electrode surface.[34] Finally, Ni_3Sn_4 composite electrodes did not show any evidence of passivation layer formation after soaking in electrolyte for an unspecified amount of time, respectively.[23]

It is not readily apparent why some alloying anode materials spontaneously form a passivation layer while others do not, especially considering the variation in reactivity for the Sn-based electrodes described above. Washing the electrodes does not seem to play a role, since for the examples mentioned above where ex-situ characterization techniques were used, the electrodes were washed with either DMC or acetonitrile prior to characterization. Soaking time does not seem to consistently play a role since some

electrodes soaked for 24 hours had a passivation layer and others did not. Similarly, the electrolyte formulation does not seem to be a factor; in most of the cases described above, all electrolytes contained 1 M $LiPF_6$ and EC as well as either DMC, DEC, PC, or some combination. When a Cu_6Sn_5 electrode was soaked in 1 M $LiPF_6$ in EC/PC/DMC (1:1:3 by volume) a passivation layer was formed, whereas no passivation layer was observed to form at OCP on a Ni_3Sn_4 electrode soaked in the same electrolyte formulation. One interesting observation for the electrodes characterized by XPS is the correlation between surface oxidation and surface reactivity. The surface of the pristine Sb and Ni_3Sn_4 electrodes both contained more metallic Sb/Sn compared to oxidized Sb/Sn binding environments based on XPS characterization and did not form a passivation layer upon contact with the electrolyte, while the pristine Cu_6Sn_5 electrode surface, which was passivated in electrolyte, was richer in oxidized Sn binding environments compared to metallic Sn. It is not clear whether these observations are related, although there is mention in the literature of surface oxides affecting surface reactivity and spontaneous film formation on surface oxides as well.[60,61]

1.2.3) Native oxides

Many of the materials used for alloying anodes, including Sn, Sb, and intermetallics all readily form surface oxides in air, and typically active materials and electrodes for alloying anodes are synthesized or fabricated in air, respectively, so the native oxide layer needs to be considered when studying SEI formation on these anodes. Characterization of pristine electrodes prior to cycling and SEI formation is important for understanding the composition of the electrode surface before the SEI is formed because there have been several studies suggesting that the surface oxide layer may affect electrolyte reactivity and SEI formation. Many alloying anode materials react spontaneously upon exposure to carbonate-based liquid electrolytes to form a passivation layer before any external current or voltage is applied as described above. XPS characterization of the surfaces of pristine SnO_2 films and SnO_2 films from assembled half cells rested at OCP for 48 hours suggested a small amount of spontaneous surface passivation occurring upon

exposure to the electrolyte, although the passivation layer seemed to be quite thin because Sn 3d photoemission peaks from the SnO_2 were still detected.[60] In another study, Sn film anodes that were fabricated to include an intentional SnO_2 layer exhibited better capacity retention than the unmodified Sn films, which authors attributed to the SnO_2 passivating the electrode surface.[62] Others have hypothesized that the native oxide on Sn may affect electrolyte reduction and SEI formation in other ways. Based on differences in electrolyte decomposition products for Au and Sn electrodes, Shi and coauthors hypothesized that there is a strong interaction between the surface oxide on Sn DEC, which leads to the formation of intermediates that react with EC to form DEDOHC, which was observed for Sn but not Au with FTIR.[26] Finally, the studies of Webb et al. concerning the surface passivation of In thin film electrodes also highlights the importance of surface oxides. The authors observed that surface oxidation seemed to affect the degree of electrolyte reduction, with more electrolyte reduction observed at 1.4 V on samples exposed to more oxygen and with a thicker surface oxide layer even when 5% FEC was used as an additive to suppress excessive electrolyte reduction.[61]

1.3) Initial SEI formation over short term cycling

1.3.1) Initial SEI formation on Sn anodes

Much of what is known about the SEI formed on metallic alloying anodes comes from studies on Sn anodes. In addition to being attractive anodes due to high volumetric capacity and the ability to fabricate electrodes without binders or additives through physical deposition methods and electrodeposition,[19,63–70] Sn anodes are particularly appealing for interfacial studies due to interesting surface reactivity. Beattie and coworkers observed a large voltage plateau around 1.5 V (vs. Li/Li^+) corresponding to an irreversible electrochemical process for Sn thin films prepared by sputtering and electrodeposition in electrolyte containing 1 M $LiPF_6$ in EC/DEC, as shown in the top of Figure 1.2.[63] The authors observed a correlation between this feature and subsequent reduced capacity and poor cycling behavior, which was mitigated by lowering the upper cutoff voltage, although others have found that

increasing the applied current density also eliminates this behavior.[25,63,67] This behavior was observed for pure Sn anodes but not Cu-Sn anodes, leading the authors to hypothesize that Sn surfaces catalyze electrolyte decomposition at high potentials.[63] Others have also observed irreversible electrochemistry at high potentials on Sn anodes. Beaulieu and coworkers observed the formation of a thick film on Sn electrodes around 1.6 V on the first discharge/reduction via AFM and optical microscopy. Like Beattie and others, Beaulieu and coworkers observed excessive electrolyte decomposition in 1 M $LiPF_6$ in EC/PC electrolyte; electrolyte decomposition at 1.6 V lasted about 17 hours before Sn lithiation began when Sn thin films were cycled with an applied current density of 38 $\mu A/cm^2$, as shown in the bottom of Figure 1.2.[64]

This excessive electrolyte decomposition on Sn has prompted many other researchers to study this phenomenon. Like Beattie et al., Bridel and coworkers hypothesized that Sn surfaces catalyze electrolyte decomposition; however, their results suggested that Sn catalyzed EC decomposition in particular. The authors observed excessive electrolyte decomposition at 1.5 V in 1 M $LiPF_6$ in EC/DMC electrolyte but did not observe the same electrochemistry in $LiPF_6$-based electrolyte solutions containing only DMC, THF, or PC as the solvent.[25] This is somewhat contradictory to the observations of Beattie and coworkers though, as they reported observing the voltage plateau at 1.5 V corresponding to electrolyte reduction in $LiPF_6$- and $LiClO_4$-based electrolyte solutions with PC as the solvent.[63] Discrepancies like this and others such as the reported electrolyte reduction potentials on Sn[63,65,66] and the current density threshold for avoiding excessive electrolyte reduction[25,64,67] could be due in part to differences in the composition of the Sn electrode surface, such as the presence of native oxides. When studying the SEI formation processes on Sn in 1 M $LiClO_4$ in PC electrolyte, Inaba and coworkers did not observe any cathodic features corresponding to electrolyte reduction via cyclic voltammetry or

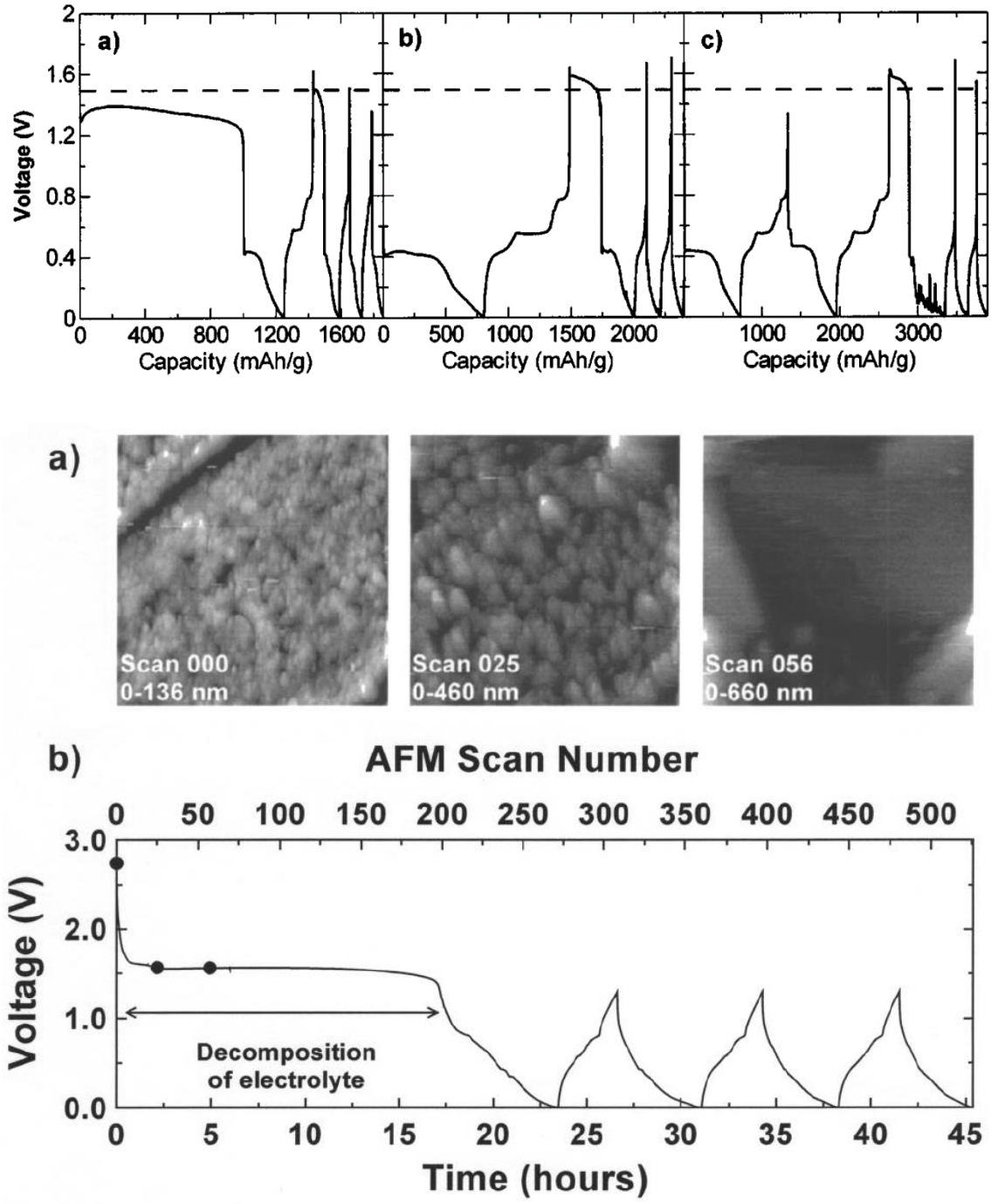

Figure 1.2: Top: voltage profiles of Sn electrodes cycled in Li half cells with conventional electrolytes demonstrating the effects of (a) cycling from OCP above 1.2 V, (b) restricting the upper voltage limit for the first cycle but not subsequent cycles, and (c) restricting the upper voltage limit for the first two cycles but not subsequent cycles. Reprinted from Reference 63 with permission from IOP Publishing. Bottom: (a) images from in situ AFM showing changes in Sn electrode surface morphology and (b) corresponding voltage response during the in situ AFM measurements. Reprinted from Reference 64 with permission from IOP Publishing.

galvanostatic cycling, but they did see evidence of electrolyte reduction between 1.4 V and 1.0 V on the second through fifth cycles. They speculated that electrolyte reduction was not observed on the first cycle due to the presence of a surface oxide layer and that electrolyte reduction was only observed after the surface oxide layer had been reduced and/or after underlying Sn surfaces had been exposed due to electrode volume expansion.[65] Bridel and coworkers reported that they did not observe excessive electrolyte decomposition at 1.5 V when Sn composite electrodes were cycled in electrolyte solutions containing EC, although they were still exploring the reason for this observation.[25] It is possible that surface of the micro- or nanoparticulate Sn active material in the composite electrode was more oxidized than the Sn thin film electrode, resulting in the differences in reactivity. However, as described in the previous section, other researchers have hypothesized that surface oxides on alloying anodes like Sn enhance rather than suppress electrolyte reactivity.[26]

Another possibility for observed differences in the electrochemical behavior of Sn electrodes is differences in the reactivity of the Sn active material itself. Researchers have found distinct differences in the reactivities of different β-Sn crystal faces as demonstrated in Figure 1.3. Cyclic voltammetry of different Sn crystal faces in 1 M $LiPF_6$ in EC/DEC (1:2 wt%) has revealed that the Sn (100) surface does not passivate well while the Sn (001) surface passivates after one cycle.[71,72] SEM characterization revealed that the SEI surface morphologies for the two crystal planes were quite different; the SEI formed in Sn (100) was thick, porous, and nonuniform, while the SEI formed on Sn (001) was smooth, uniform, and more compact than the film on the (100) surface.[71,72] In situ AFM and ellipsometry also revealed differences in the formation and properties of the SEI on the two surfaces. The SEI on the Sn (100) surface seemed to grow continually with cycling and was quite soft and did not adhere well to the Sn surface in many regions. In contrast, the SEI on the Sn (001) surface initially formed thin, dense film that grew slowly over time.[71] The compositions of the SEIs formed on the two different Sn surfaces also seemed to be different based on soft X-ray absorption spectroscopy characterization. The Sn (100) SEI,

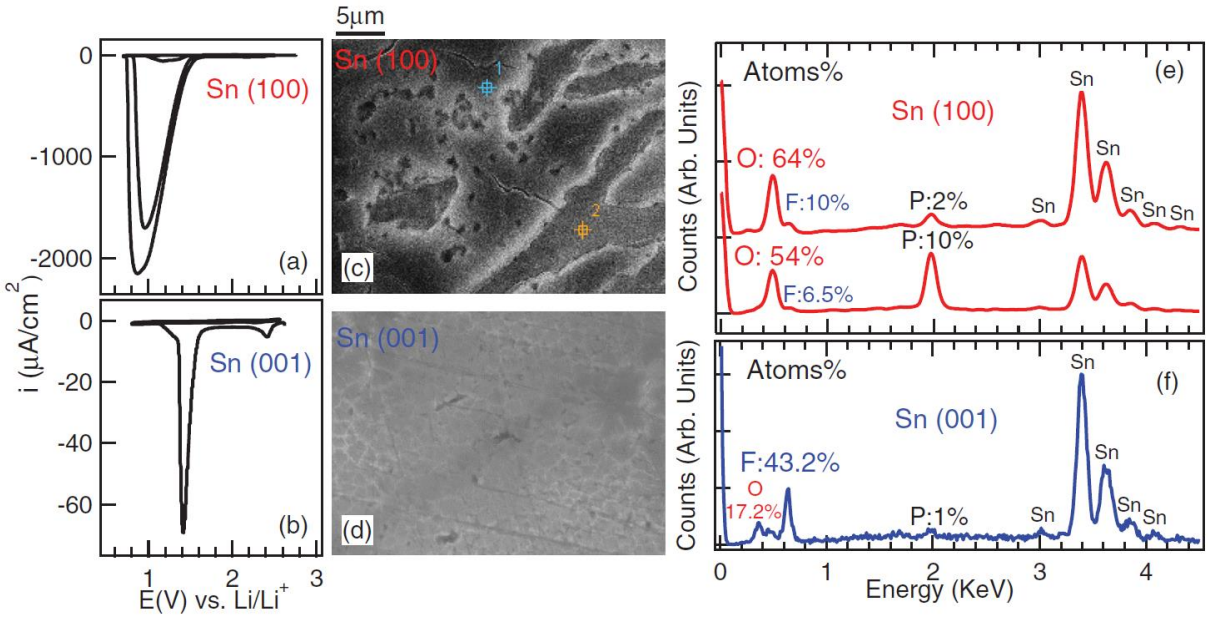

Figure 1.3: Results from cyclic voltammetry, scanning electron microscopy, and energy dispersive X-ray spectroscopy characterization of different Sn crystalline faces, demonstrating the differences in the surface passivation, morphology, and composition of the SEI on Sn (100) and Sn (001). Reprinted from Reference 72 with permission from John Wiley and Sons.

which was nonuniform based on SEM characterization also seemed to be nonuniform in terms of the lateral composition; the Sn (100) SEI was predominantly Li_2CO_3, with some $LiPF_6$ possibly present as well. The Sn (001) SEI was predominantly LiF, with some organic species as well; there was also evidence for some Li_2CO_3 and $LiPF_6$ in the bulk SEI.[72]

The studies on single crystal surfaces reveal interesting trends in terms of Sn surface reactivity and passivation that can be extended to more commonly studied polycrystalline samples since polycrystalline electrodes likely contain some combination Sn (100) and Sn (001) faces. Like Sn (100), the SEI formed on polycrystalline Sn does not seem to passivate the electrode surface well in conventional electrolytes. Lucas and coworkers observed poor passivation of polycrystalline Sn foil electrodes in $LiPF_6$-based organic carbonate electrolyte; with cyclic voltammetry, the authors saw features associated with electrolyte reduction even after the first cycle, which was supported by in-situ AFM.[73] Work from others on other Sn electrodes also suggests poor SEI passivation. Park and coworkers also saw evidence of

$LiPF_6$/carbonate electrolyte reduction on Sn films via CV even after five and ten cycles, and data from electrode bending experiments suggested that the SEI formed on Sn was brittle and poorly passivating.[68] Poor surface passivation, leading to continuous electrolyte reduction and SEI growth even seems to be a problem for composite Sn anodes based on electrochemical impedance spectroscopy results showing an increase in impedance with cycling in $LiPF_6$-based electrolyte.[69] Given the poor surface passivation and continual SEI formation on Sn anodes, it is not surprising that the SEI on Sn can be as thick as 1 μm after just ten cycles based on cross sectional SEM.[68] The poor passivation of Sn surfaces does not seem to be limited to $LiPF_6$-based electrolytes either; Tavassol and coworkers saw evidence of poor Sn surface passivation and continued SEI decomposition on Sn thin films in $LiClO_4$/carbonate electrolytes using ToF-SIMS and EQCM. With ToF-SIMS, the authors observed the formation of high molecular weight oligomeric species initially, but by the fifth cycle much of the SEI was composed of smaller MW species with $m/z < 500$, suggesting SEI instability.[27]

While many studies of the cycling behavior and electrolyte reactivity of Sn anodes suggest that much of the electrolyte reduction on Sn occurs at potentials above 1.0 V vs. Li/Li^+, a study of SEI formation on Sn using EQCM from Li and coworkers suggested that electrolyte reduction and SEI formation occurs at several stages during the cathodic polarization/reduction of Sn. Using calculations of the mass accumulation per mole of electrons (MPE) from EQCM data, the authors concluded that between 1.9 V and 1.6 V mass changes were due to solvent adsorption at the electrode surface. Between 1.6 V and 0.7 V, electrolyte reduction and SEI formation takes place, although the MPE values over this potential region were lower than expected, which the authors believed could be due to either the formation of soluble species upon electrolyte reduction or the adsorption of solvent molecules onto the electrode surface prior to reduction. Between 0.7 V and 0.07 V, where Sn lithiation occurs, the actual MPE was higher than the theoretical value based solely on the mass change associated with Sn lithiation, suggesting that electrolyte reduction/SEI formation is also occurring over this potential range.[66] Results from the

characterization of changes in the SEI morphology over cycling seem to reflect these different stages of SEI growth, although in some cases the potential regions differ. Using in-situ AFM, Lucas and coworkers saw the initial formation of a 100-150 nm thick SEI between 2.5 V and 2.0 V that seemed to be composed primarily of inorganic species based on unsuccessful attempts to scrape away the film with the AFM tip. Below 2.0 V (but still above the Sn lithiation potential), perturbation of the AFM reflection signal suggested the formation of a soft and/or viscous material on the sample surface, most likely due to the formation of organic SEI species.[73] Results from studies of SEI formation on Sn from Yang and coworkers using EQCM-D suggest a thinner, more compact SEI forms initially at potentials above lithiation, but as lithiation begins, the SEI increases in thickness and becomes softer and more porous, although the experiment could not clarify whether the softer, porous layer formed on top of the initial compact layer or if the initial layer became softer and more porous at lower potentials.[70]

The composition of the SEI formed on Sn anodes has been studied using various methods, although FTIR is the most commonly used technique because it allows for the identification of carbonate reduction species such as Li_2CO_3 and Li alkyl carbonates that make up much of the SEI in. Based on FTIR characterization of the SEI formed on Sn thin film and composite anodes in $LiPF_6$-based carbonate electrolytes cycled to various potentials, Li_2CO_3 seems to be a major species, although Li alkyl carbonate species are also detected.[25,67,68] Using in-situ FTIR, Shi and coworkers detected Li propionate and also observed the formation of the alkyl carbonate species diethyl 2,5-diaohexane dicarboxylate at 1.4 V on Sn.[26] Similarly, Song and Baek also observed bands corresponding to alkyl carbonate and alkyl carboxylate species via ex-situ FTIR characterization of the SEI formed on Sn after one cycle, although they found that the SEI was predominantly composed of PF-containing species with small amounts of P–O and P=O containing species as well as small amounts of alkyl carbonate and alkyl carboxylate species. After three cycles, the SEI on Sn was similar based on FTIR, although the intensity of features corresponding to the PF-containing species became more intense and the authors saw new features corresponding to Li_2CO_3

that were not observed after the first cycle.[19] Based on FTIR characterization, the SEI formation on polycrystalline Sn seems to agree well with the composition of the Sn (100) and Sn (001) model systems determined using soft X-ray absorption spectroscopy.[72]

Although limited to characterization of the top 5–10 nm of the SEI surface, XPS is also useful for studying SEI composition, especially for detecting species like LiF that are not IR active.[19,74] XPS characterization of the SEI on Sn suggests that in addition to being rich in Li_2CO_3, the SEI on Sn is also rich in inorganic species like LiF, particularly after the first cycle.[68,75] After the first cycle, Park and coworkers found that the SEI surface on Sn thin films was composed of roughly 30% F, most of which was due to LiF and a small amount of LiP_xF_y species,[68] while Seo and coworkers found that the SEI surface for their Sn composite electrode system was roughly 10% F in the form of LiF after the first cycle, which dropped to about 4% after the third and tenth cycles.[75] While the F 1s spectra helped provide information about the SEI that IR could not, the C 1s spectra corresponding to carbonaceous SEI components supported the conclusions drawn from IR. Based on XPS quantification, the SEI surface on Sn is carbon rich, with C making up roughly 40% and 60% of the SEI surface after the first cycle on Sn composite and thin film electrodes, respectively.[68,75] The C 1s HRES spectra showed features corresponding to aliphatic, C–O, O=C–O, and carbonate binding environments, likely corresponding to the Li alkyl carbonate species, Li alkyl carboxylate species, and Li_2CO_3 detected by FTIR.[19,26,68,75] Seo and coworkers also saw a small amount of Li_2O in the O 1s HRES spectrum for the SEI on Sn composite anodes after the first cycle, which differs from the studies on the single crystal model systems in which no Li_2O_2, Li_2O, or LiOH were detected.[72,75]

1.3.2) Initial SEI formation on Sb anodes

Unlike the SEI on Sn anodes, the SEI on Sb anodes has not been characterized nearly as extensively. This could be due in part to differences in reactivity; while Sn electrode surfaces are thought to react catalytically with organic carbonate-based electrolytes,[25,63] as described above, Sb does not seem to exhibit the same reactivity. While Bridel and coworkers observed a large voltage plateau around 1.5 V

corresponding to electrolyte reduction when Sn anodes were cycled in electrolyte containing EC, this behavior was not observed for Sb thin film anodes, suggesting differences in surface reactivity.[25] However, despite these reactivity differences, SEI studies of Sb are still just as important and interesting as those on Sn. Like other alloying anode materials, Sb electrodes typically exhibit large first cycle irreversible capacity losses; some researchers have reported irreversible capacity losses as high as 30% for Sb composite electrodes.[29,76] Additionally, Sb anodes cycled in standard electrolytes without the addition of SEI-improving additives often exhibit rapid capacity fade after only tens of cycles and can become pulverized from large volume changes due to lithiation/delithiation after only a few cycles.[76]

Like the SEI on Sn, results from studies of the SEI on Sb anodes suggest that the SEI increases in thickness rapidly during reduction/discharge on the first cycle. When Sb electrodes were reduced/discharged galvanostatically to 0.5 V on the first cycle, the Sb peaks in the Sb 3d photoelectron spectrum were almost completely attenuated, even after Ar^+ etching.[22] Similarly, others found that the Sb peaks in the Sb 3d photoelectron spectra were completely attenuated halfway through the first reduction/discharge for conventional Sb composite electrodes.[29] Also like the SEI on Sn, the SEI formed on Sb seems to exhibit dynamic behavior, at least over the initial stages of SEI formation; Bodenes and coworkers observed that during charging, the SEI on Sb composite anodes partially dissolved to allow for the detection of underlying electrode components with XPS.[29] Bian and coworkers may have also observed this phenomenon, as there may have been some contribution from the conductive carbon additive Super P in the C 1s photoelectron spectrum of an Sb composite electrode after 5 cycles.[76]

Most of the knowledge about the composition of the SEI on Sb anodes comes from XPS characterization. After sputtering away residual electrolyte and possibly some of the SEI surface, XPS characterization of Sb electrodes reduced/discharged to 0.5 V by Martín and coworkers suggested that the SEI contained LiF, aliphatic carbon binding environments, C–O binding environments attributed to PEO oligomers, Li_2CO_3, Li alkyl carbonate species, and carbide species.[22] Most of the species detected for the

SEI on Sb are similar to those reported for other anode materials, including Sn, except for carbide. The presence of carbide species in the SEI seems curious; although there has been a report of carbide formation due to Li_2CO_3 reduction,[77] it seems more likely that the C 1s peak at 283.9 eV assigned to carbide is either an artifact of sputtering[78] or actually sp^2 carbon from a species such as Li vinylene carbonate or Li vinylene alkoxide[68,79] based on the SEI formation conditions and low potential cutoff of 0.5 V.[80] Percent atomic composition values from XPS characterization of the SEI surface on Sb composite electrodes after 5 cycles revealed that the SEI surface was rich in Li and O, with the surface composition being roughly 30% Li, 1% P, 20% C, 50% O, 4% F.[76] Some of the oxygen content was likely due to the presence of carbonaceous SEI components, because aliphatic, C–O, O=C–O, Li alkyl carbonate, and Li_2CO_3 binding environments were all thought to be present in the C 1s HRES photoelectron spectrum. Peaks in the F 1s HRES photoelectron spectrum were assigned to LiF, P–F, and C–F binding environments, although PF_xO_y species could also account for the peak at ca. 686 eV assigned to fluorocarbon species.[29,76]

Another study of the SEI composition on Sb composite anodes using XPS from Bodenes and coworkers revealed interesting differences in SEI formation and speciation depending on the binder and solvent used for the fabrication of composite electrodes.[29] In general, they found that the SEI surface over the first cycle contained LiF, aliphatic, C–O, O=C–O, and carbonate binding environments regardless of preparation method, which is in agreement with the findings described above.[22,29,76] When PVdF was used as the binder, the SEI seemed to grow preferentially on the active material and conductive carbon additive. The predominant species at the SEI surface were $LiPF_6$ and $LiPF_6$ degradation products like LiF and PF_xO_y species in addition to C–O containing species such as Li alkyl carbonates, alkoxides, and PEO oligomers. When CMC was used as the binder, most of the peaks corresponding to CMC were attenuated during the first cycle, suggesting that the SEI forms on the active material, conductive additive, and binder. The predominant SEI surface species based on XPS characterization included Li_2O, LiOH, and some LiF.[29]

Finally, another study of the SEI composition was conducted in order to better understand the thermal stability of Sb anodes. XPS characterization of lithiated Sb composite electrodes showed that the SEI surface consisted of mostly LiF, aliphatic carbon containing species, and C–O containing species, as well as a small amount of O=C–O containing species based on the relative intensities of features in the C 1s HRES spectrum. After heating the lithiated electrode to 350 °C under Ar, LiF, aliphatic carbon, and C–O binding environments were still observed; however, the O=C–O binding environment was no longer seen, and a new feature corresponding to a carbonate binding environment appeared in the C 1s spectrum. Interestingly, these changes in the SEI surface composition after heating were different than those observed for the SEI formed on graphite electrodes. Comparison of the quantitative DSC results for thermal runaway onset temperatures for Sb and graphite anodes revealed that they were different, with the heat generation per mole of Li being 37% lower for the Sb-based electrode than the graphite electrode. The authors hypothesize that this is due to the capacity of Sb versus graphite (i.e. less SEI formation per capacity), but there could be some difference in SEI layer decomposition based on differences in the SEI composition, which could be due to electrode reactivity differences or possibly potential differences since graphite is lithiated at a lower potential than Sb electrodes.[81]

1.3.3) Initial SEI formation on other elemental alloying anodes

The SEI on other elemental metal alloying anodes have been studied very little, unlike elemental Sn and Sb alloying anodes, but the few examples of studies we were able to find suggest that this is an important area of study for understanding the role the SEI plays in electrode instability and poor cycle performance. Kuwata and colleagues observed poor performance for Bi composite electrodes cycled in conventional electrolytes; the capacity faded rapidly, dropping below 80% of the initial capacity within 5 cycles, and the coulombic efficiency never exceeded 95%. In situ FTIR characterization of model Ni electrodes in the same electrolyte solution showed evidence of typical SEI species like $LiPF_6$ and carbonate decomposition products.[55] Bridel and coworkers observed that like Sn, Bi films cycled in electrolyte

solutions containing EC also exhibited a large voltage plateau around 1.7 V due to irreversible processes such as electrolyte reduction and SEI formation, which could explain the poor cycling behavior observed by Kuwata et al.[25] Similarly, Webb and coworkers observed excessive electrolyte decomposition around 1.4 V for In thin film anodes during the first discharge and limited storage capacity of the active material when using conventional electrolytes.[61] Finally, Qin and coworkers found that Al composite electrodes also exhibited severe capacity fade within the first 10 cycles and had low CEs. Characterization of the SEI surface with XPS revealed low intensity peaks in the C 1s HRES spectrum corresponding to carbonate and O=C–O binding environments as well as peaks in the F 1s HRES spectrum assigned to $LiPF_6$, $Li_xPF_yO_z$, and LiF.[82] The surface species and binding environments observed by the authors with XPS are typical solvent and salt reduction and decomposition species commonly reported in the SEI literature, so the reason for the poor performance of the Al anode is not clear from the compositional characterization of the SEI surface alone. These studies suggest that excessive electrolyte decomposition and/or SEI instability on elemental alloying anodes like Bi, In, and Al prevents them from being functional anodes in conventional carbonate-based electrolytes. Studies understanding why additives or alternative electrolyte formulations are necessary for these types of anodes, which will be discussed later, are crucial for understanding the role the SEI plays in alloying anode capacity retention and cycle lifetime.

1.3.4) Initial SEI formation on intermetallics and binary metal alloys

Other alloying anode materials like intermetallics and binary metal alloys typically exhibit longer lifetimes than their elemental alloying anode counterparts like Sn and Sb in part due to more modest volume changes due to often containing one inactive component to help buffer volume changes.[12,13] However, this subset of alloying anode materials also has issues associated with SEI formation and instability, including large first cycle irreversible capacity losses and rapid capacity fade after extended cycling.[12] Studies of the SEI formed on intermetallics and binary metal alloys have covered a wide range of different materials and SEI formation conditions, so it can be difficult to compare all of them and draw

conclusions from the myriad studies. The studies do reveal some common themes and interesting differences regarding SEI formation on these types of anodes, as well as some similarities and notable differences compared to the elemental alloying anodes.

Some aspects of the initial SEI formation process and initial SEI characteristics are similar to those observed for other alloying anodes. Based on ToF-SIMS characterization, Li and coworkers saw evidence of the formation of a multilayered SEI on Ni-Sn electrodes during the first cycle, with an organic rich outer layer and an inorganic rich inner layer near the electrode surface,[83] which is in agreement with observations made for the SEI on Sn electrodes. The SEI formation process seems to occur in different stages on intermetallic anodes as well as for elemental lithium alloying anodes. Based on MPE values and EQCM characterization, Yang et al. found that for Cu_6Sn_5 electrodes, solvent adsorption occurs between 2.8 V (OCP) and 1.7 V. Electrolyte reduction occurred between 1.7 V and 0.8 V, with Li_2CO_3 and $LiOCH_3$ being some of the proposed major electrolyte reduction species, and between 0.8 V and 0.1 V there may be some Li_2O formation occurring in addition to the lithiation of Sn.[84] Similarly, Stjerndahl et al. observed that the DOD/lower cutoff voltage affected the relative SEI speciation of AlSb anodes; based on XPS characterization, the SEI surface of the electrode cycled to 0.01 V was richer in organic/carbonaceous species than the electrode discharged to 0.5 V.[85] During the first discharge of F-doped Ni-Sn films, Hong et al. did not observe any SEI formation until reduction to 0.45 V; based on XPS and FTIR characterization, both solvent and salt species were reduced starting at 0.45 V, resulting in the formation of both carbonaceous and inorganic SEI species. As the sample was reduced to lower potentials, the major species detected with FTIR suggested either continued solvent reduction or further reduction of the carbonaceous SEI species.[86]

Much of the SEI growth on intermetallic and binary metal alloys seems to take place over the first cycle. FTIR characterization of F-doped Ni-Sn electrodes suggested continual SEI formation and increasing SEI thickness over the first cycle based on increasing intensity of IR bands corresponding to solvent

reduction species in the SEI.[86] Similarly, EQCM characterization of Cu_6Sn_5 electrodes indicated that most of the SEI formation occurred during the first discharge, although it continued to grow over 10 cycles.[84] EIS characterization of $FeSn_2$ and SnSb electrodes also suggested considerable SEI growth during the first discharge based on increasing impedance.[21,59] However, rate studies on $FeSn_2$ electrodes suggest that cycling rate also plays a role in the initial formation and growth of the SEI; the impedance of the SEI formed at faster rates (C/5) was much smaller than that of the SEI formed at slower rates (C/50) after the first cycle.[21]

While XPS characterization of Sn[68] and Sb[22,29] electrodes after the first discharge suggest the formation of a relatively thick SEI layer, one commonality for most intermetallic and binary metal alloying anodes seems to be that the SEI layer formed during the first cycle is quite thin despite much of the SEI formation process taking place during the first cycle. XPS studies of the SEI surface on different anode materials have suggested that the SEI layer formed during the first cycle is less than about 10 nm because the core photoemission peaks from the underlying electrode materials can still be detected. This behavior has been observed for Cu_6Sn_5 composite and thin film electrodes,[20,87] Ni_3Sn_4 composite electrodes,[23] $MnSn_2$ composite electrodes,[88] TiSnSb composite electrodes,[24,45] and AlSb composite electrodes.[85] In fact, the SEI formed on AlSb was thin enough that after 3 cycles, carbon black and PVDF peaks from the composite electrode were still observed in the C 1s spectra,[85] although this may also be related to differences in reactivity for the electrode active material compared to the conductive additive and binder, similar to what has been reported for Sb electrodes.[29]

Although the SEI formed on many intermetallic anodes seems to be quite thin initially, there are some examples of studies where this was not found to be the case. For example, when Li and coworkers characterized Ni-Sn and Co-Sn thin films with XPS after the first discharge, the peaks corresponding to the electrodes had been completely attenuated, suggesting the formation of a thicker SEI during the first discharge.[83,89] In this case the thickness of the SEI during the initial cycling could be related to the

electrolytes used; Li et al. used 1 M $LiClO_4$ in PC as the electrolyte in their SEI studies, whereas for the examples where the SEI was still thin enough to detect photoemission peaks from the underlying electrode, the electrolytes were either 1 M $LiPF_6$ in EC/DMC (1:1),[87,88] 1 M $LiPF_6$ in EC/PC/DMC (1:1:3),[20,23,24,45] or 1 M $LiPF_6$ in EC/DEC (2:1).[85] It is not clear whether the reported differences in initial SEI thickness are due to the use of $LiClO_4$ instead of $LiPF_6$ as the salt, the use of PC as the solvent, or some combination of both. However, for a study comparing the SEI formed on Ag-Sn thin film electrodes in EC- and PC-based electrolytes, XPS and EIS results suggested that the SEI formed in the PC-based electrolyte was thicker.[90] Hong and colleagues also observed the formation of a thicker SEI over the first cycle via XPS for fluorine-doped Ni-Sn thin film electrodes in 1 M $LiPF_6$ in EC/EMC (3:7).[86] In this case, however, the difference in SEI thickness may be due to a difference in electrode surface reactivity rather than electrolyte reactivity because Choo and others observed the formation of a thicker SEI on fluorine-doped Ni-Sn compared to undoped Ni-Sn films in an earlier study.[91]

While the initial thickness of the SEI on Sn- and Sb-based intermetallics may differ from pure Sn and Sb anodes, the SEIs formed on different types of alloying anodes seem to be similar in the sense that SEI formation on alloying anodes seems to be a dynamic process. Just as SEI mass increases and decreases were seen with EQCM during discharging and charging of Sn electrodes, respectively,[70] researchers have reported similar behavior for the SEI on intermetallic and alloying anodes. Much of the evidence for this behavior has come from studies involving XPS characterization of the SEI surface at different points during the first cycle. This behavior has been reported for Cu_6Sn_5,[20] Ni_3Sn_4,[23] $MnSn_2$,[88] TiSnSb,[45] and AlSb[85] composite electrodes based on XPS characterization, where core photoemission peaks from the electrode active material and conductive carbon additive either reappear or increase in intensity during charging/oxidation. The detection of these peaks could also be explained by electrode and SEI fracturing due to volume changes, but others have observed a decrease in impedance for $MnSn_2$ composite electrodes during charging on the first cycle that may be indicative of SEI dissolution, resulting in a thinner

SEI layer.[92] Overall, the results from the studies are consistent in that the SEI seems to undergo dissolution during charging/oxidation of the electrode/SEI. However, EIS and EM characterization of the SEI formed on SnSb suggests that the dynamic behavior of the SEI could be a little more complicated, with fluctuations in properties and thickness occurring during both discharging and charging, as demonstrated by the trends in resistance values determined from EIS and TEM characterization shown in Figure 1.4.[59]

There are also some conflicting results as to which species in the SEI are changing during cycling and specifically during charging/oxidation. The results of some studies have suggested that inorganic components such as LiF are changing. Based on F ssNMR characterization of TiSnSb eletrodes, LiF was present in the SEI at the end of discharging but the peak corresponding to LiF mostly disappeared at the end of charging, which authors attributed to partial SEI dissolution.[24] Changes in the LiF content over the first cycle were also observed for Ni_3Sn_4 electrodes, although the amount of LiF at the surface was higher at the end of charging based on XPS.[23] TEM characterization of SnSb electrodes also suggests changes in inorganic SEI components because samples were sonicated for several minutes in ethanol prior to characterization, which likely only left the inner, inorganic rich layer of the SEI intact. Authors observed that this portion of the SEI layer fluctuated in thickness over the first cycle, as seen in Figure 1.4; it was ca. 6 nm partway through discharge (0.68 V) and 3.5–3.8 nm at the end of discharge and during charging.[59] In contrast, others have observed evidence of the dissolution of carbonaceous SEI components during cycling. Based on XPS characterization of the SEI formed on AlSb during the first cycle, the carbonaceous species seemed fluctuate during cycling while the salt degradation species seemed to remain consistent.[85] In addition to seeing fluctuations in LiF content for the SEI on TiSnSb with cycling, Marino et al. also observed some fluctuations in carbonaceous species based on XPS characterization. At the end of the first discharge, the highest intensity peaks in the C 1s spectra were the peaks attributed to carbonate species, whereas at the end of the first charge, there was an increase in the intensities of the aliphatic, C-O, and O=C-O peaks.[24] Even during the initial SEI formation process, the dynamic behavior of the SEI seems to be

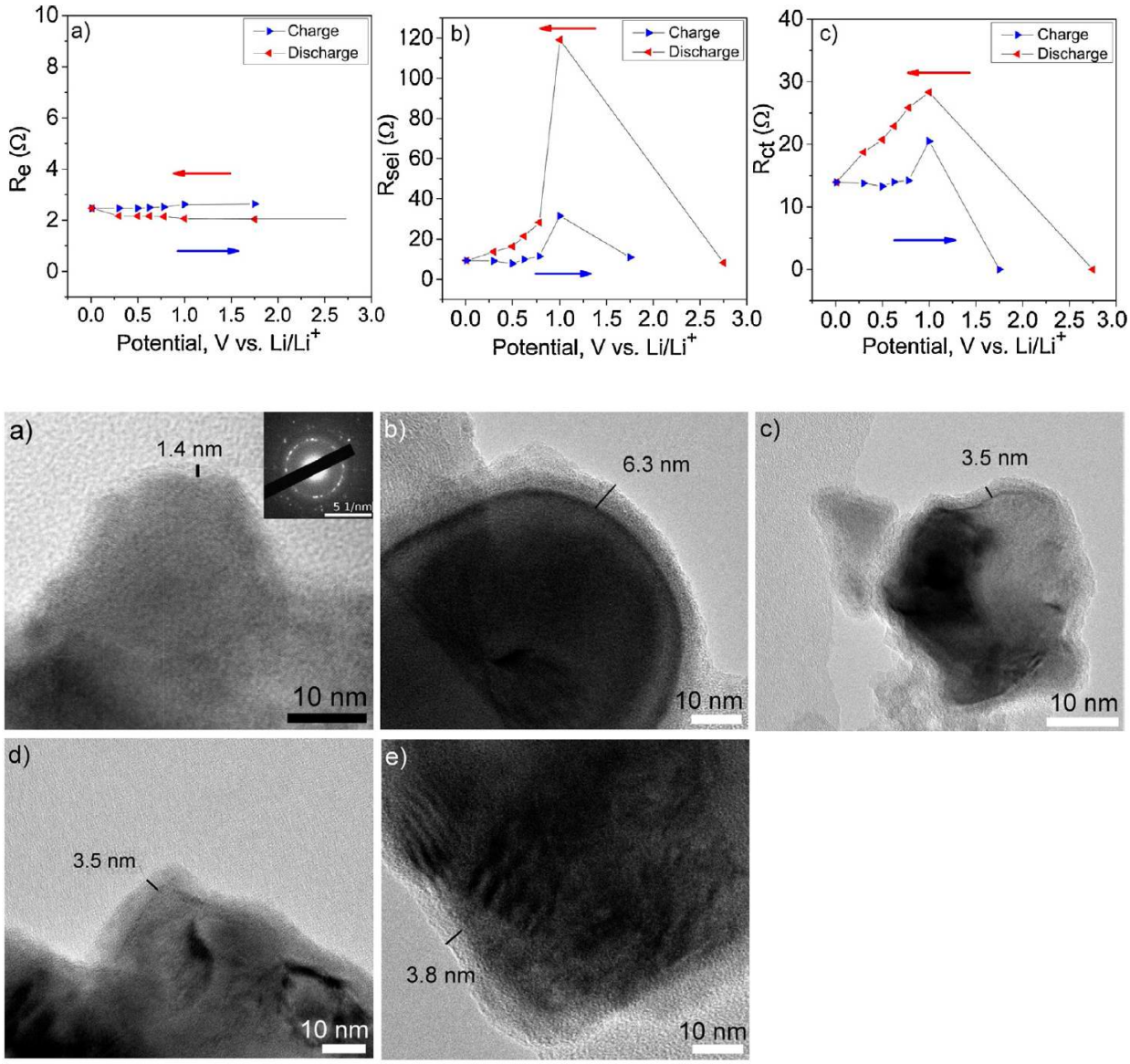

Figure 1.4: Top: changes in (a) electrolyte, (b) SEI, and (c) charge transfer resistance values, obtained from modeling and fitting electrochemical impedance spectroscopy data, during the first cycle for SnSb electrodes. Bottom: Transmission electron micrographs of SnSb electrode particles over different stages of the first cycle: (a) at OCP, (b) discharged to 0.68 V, (c) discharged to 0.01 V, (d) charged to 0.75 V, and (e) charged to 1.75 V. Reprinted from Reference 59 with permission from Elsevier.

quite complex. Further studies of SEI dissolution and evolution during short term cycling of alloying anodes could help improve understanding of SEI instability.

Comparing the formation process and morphology of the SEIs on different intermetallic and binary metal alloying anodes prepared under various conditions is challenging, but comparing the compositions is even more difficult due to the limitations of different characterization techniques used for studying the SEI composition. Like the SEI formed on Sn anodes, the SEIs on many intermetallic and binary metal alloying anodes, including Cu_6Sn_5,[20,84,87] Ni_3Sn_4,[23] F-doped Ni-Sn,[86] $FeSn_2$,[93] Ag-Sn,[90] Co-Sn,[89] SnSb,[94] TiSnSb,[24,45] AlSb,[17,85] and $CoSb_3$ electrodes[95] are rich in carbonate species. It is difficult to distinguish between Li_2CO_3 and Li alkyl carbonate species with XPS,[96] so in some cases it is not clear whether the SEI contains Li_2CO_3, Li alkyl carbonates, or a combination of both.[17,24,45,85,87–90,93] Valence band XPS characterization, which can help differentiate between carbonate species,[54,96] has suggested that the main carbonate species in the SEI on Cu_6Sn_5 and Ni_3Sn_4 anodes is Li_2CO_3.[20,23] Additionally, calculations of MPE values from EQCM experiments with a Cu_6Sn_5 electrode also suggest that Li_2CO_3 is one of the major SEI species.[84] Results from FTIR characterization have suggested that the SEIs on F-doped Ni-Sn, SnSb, and $CoSb_3$ anodes have both Li_2CO_3 and Li alkyl carbonate species.[86,94,95]

Other possible carbon-containing species in the SEIs on intermetallic and binary metal alloying anodes include PEO oligomers, Li alkoxide species, Li carboxylate salts, Li oxalate species, and ester species. These species cannot be distinguished by XPS, but the SEIs on Ni_3Sn_4,[23] Ni-Sn,[83] $FeSn_2$,[93] $MnSn_2$,[88] Co-Sn,[89] TiSnSb,[24,45] Cu_2Sb,[81] and AlSb[17,85] electrodes may contain some of these species in addition to Li_2CO_3 and/or Li alkyl carbonates based on the binding environments seen in C 1s HRES spectra. Interestingly, a SEI study for Cu_2Sb thin film anodes from Song et al. using FTIR revealed that the primary carbonaceous SEI species included metal carboxylates and esters, while minor species included alkoxides and Li_2CO_3.[97] Hong et al. also saw evidence of carboxylate species on F-doped Ni-Sn anodes using FTIR,[86]

and Yang et al. found evidence for alkoxide species, specifically $LiOCH_3$, on Cu_6Sn_5 anodes using EQCM and MPE values.[84]

Inorganic species primarily from $LiPF_6$ since most SEI studies for these types of anode materials done using $LiPF_6$ as the salt. Like the SEI on Sn and Sb electrodes, the SEIs initially formed on many intermetallic and binary metal alloying anodes contain LiF. Valence band XPS characterization revealed that LiF was a major component of the SEI surface for Cu_6Sn_5 and Ni_3Sn_4 electrodes, while the combination of ^{19}F ssNMR and XPS suggested that LiF was a minor component of the SEI on TiSnSb electrodes.[20,23,24] Based on F 1s HRES photoelectron spectra LiF has also been detected at the SEI surface on a variety of other electrodes, including Ni-Sn, F-doped Ni-Sn, $MnSn_2$, Ag-Sn, Cu_2Sb, and AlSb electrodes.[17,81,85–88,90,91] Using ^{19}F ssNMR, some have found that $LiPF_6$ gets incorporated into the SEI formed on TiSnSb,[24] while ^{7}Li ssNMR studies on $MnSn_2$ electrodes have suggested that it gets removed with washing.[98] The surfaces of the SEIs formed on Cu_6Sn_5, Ni_3Sn_4, $MnSn_2$, and AlSb electrodes also contain $LiPF_6$ or $LiPF_6$ degradation products ($Li_xP_yF_z$) based on XPS characterization.[17,20,23,85,87,88] While LiF and $LiPF_6$/$Li_xP_yF_z$ are the most commonly reported fluorinated SEI species, others have been reported as well. Hong and coworkers reported the formation of organic phosphorus fluoride species ($OPF_{3-x}(OR)_y$) in the SEI of F-doped Ni-Sn based on IR characterization.[86] Marino and coauthors saw $Li_xPF_yO_z$/PF_xO_y species with ^{19}F ssNMR for unwashed TiSnSb samples but not for washed samples, suggesting that these species are either not incorporated into the SEI on TiSnSb or that they are soluble in DMC.[24] Finally, F 1s binding environments assigned to C–F containing species were reported for the SEIs formed on Cu_6Sn_5 thin film electrodes;[87] these species are often reported for XPS characterization of composite electrodes containing PVDF binder,[20] but they are not often reported as SEI species.

The two other inorganic species that are often reported as components of the SEI formed on alloying anodes are Li_2O and LiOH. Li_2O forms from the reduction of oxides on the electrode surface,[99,100] although it may also be an artifact introduced during characterization.[33,101] LiOH is believed to form from

reactions between electrolyte reduction products like LiF and Li_2CO_3 and trace water.[11] The surfaces of metallic films and particles are typically covered by native oxide layers,[20,23,83,84,87,88] so it is reasonable that Li_2O has been detected or hypothesized as a component of the SEI during short term cycling in studies of many intermetallic and binary metal alloy anodes, including Cu_6Sn_5,[84] Ni-Sn,[83] $FeSn_2$,[98] $MnSn_2$,[88] Ag-Sn.[90] However, in some instances, the detection of Li_2O in the SEI of alloying anodes could be an artifact introduced during characterization. Li et al. detected LiO^- during ToF-SIMS characterization of the SEI on Ni-Sn electrodes, which could be due to Li_2O, but the authors cautioned that it could also be due to the degradation of other SEI components.[83] Similarly, Marino et al. saw evidence of Li_2O in O 1s HRES spectra from XPS characterization of the SEI surface on TiSnSb electrodes but hypothesized that it was an artifact from degradation of LiOH in the SEI.[24] Water was used as a solvent in the preparation of the TiSnSb composite electrodes with CMC as a binder, so authors hypothesized that trace water from electrode fabrication could lead to the formation of LiOH in the SEI.[24,45] Based on their findings from multinuclear ssNMR studies of $FeSn_2$ electrodes, Huo and colleagues hypothesized that at faster cycling rates, LiOH is formed and incorporated into the SEI, while at slower rates, the LiOH gets converted to Li_2O and possibly $Li_xPF_yO_z$ species.[98]

Most studies of the SEI formed on intermetallic and binary metal anodes over short term cycling focus on the formation process and composition of the SEI, although there are a couple that examine changes in the SEI upon heating or aging. Like the SEI on Sb anodes, the SEI on Cu_2Sb electrodes also changes upon heating, although the SEI on Cu_2Sb undergoes different changes than the one on Sb. When lithiated Cu_2Sb electrodes were heated to 350 °C under Ar, there was an increase in the amount of LiF detected at the SEI surface with XPS, in contrast to what was observed for Sb electrodes. There was also a decrease in carbonaceous with the exception of carbonates. While the SEI on Cu_2Sb underwent different changes upon heating than Sb electrodes, it generated roughly the same amount of heat per unit of energy storage as the Sb electrode, which was roughly 37% less than that of the graphite anode.[81] As

mentioned above, rate studies with $FeSn_2$ electrodes suggested that cycling rate also plays a role in SEI formation; electrodes cycled at faster rates like C/3 had higher capacities and longer cycle lifetimes than those cycled at slower rates like C/50, which the authors attributed to the formation of a more stable SEI at faster rates.[21] While the SEI formed on $FeSn_2$ at faster rates seems to be more stable during cycling compared to the SEI formed at slower cycling rates, the SEI formed at faster rates does exhibit some evidence of instability during resting or aging. When lithiated $FeSn_2$ electrodes were aged in a half-cell at OCP, EIS characterization showed an increase in impedance for both SEI and charge transfer components. The authors hypothesized that as the lithiated $FeSn_2$ self-charges, the diffusing Li ion reacts with electrolyte or SEI components to either increase the SEI thickness and/or decrease the SEI porosity during aging.[102]

1.4) SEI evolution on alloying anodes over extended cycling

As described in previous sections, the cycle lifetime of alloying anodes is often short due to electrode mechanical instability and SEI chemical and mechanical instability. Extending the lifetime of some alloying anodes beyond 10 cycles requires the use of electrolyte additives or unconventional electrolyte formulations. As such, there are relatively few reports of SEI studies on alloying anodes cycled for extended periods of time, which we are defining here as greater than 10 cycles, in conventional electrolyte solutions without the use additives. However, the studies that do exist for alloying anodes have helped provide some insights into the role the SEI plays in cycle lifetime for alloying anodes and also helps highlight some areas of research where our understanding is lacking.

1.4.1) SEI and electrode morphology

For most alloying anodes, the thickness of the SEI seems to increase dramatically based on various characterization techniques. After 20 cycles, Park and coworkers saw the formation of a thick SEI layer (>1 μm) on Sn thin film anodes with cross sectional SEM, and based on EDS mapping some Sn seemed to be incorporated in the SEI with extended cycling.[68] XPS characterization of TiSnSb composite electrodes after

20 cycles also suggested the formation of a thicker SEI; after 20 cycles, the SEI was thick enough that no Sn from the electrode was detected even at the end of charging when some SEI dissolution occurs.[45] Others have also used compositional analysis techniques as rough indicators for SEI thickness; Hong et al. hypothesized that the SEI on F-doped Sn-Ni thin film electrodes increased in thickness after 50 cycles based on FTIR peak intensities,[86] and others reported similar results for Sn film electrodes after 50 cycles.[19] Interestingly, Bryngelsson et al. reported that the SEI formed on AlSb composite electrodes seems to be thin even after 50 cycles based on peaks from the PVDF binder and carbon black conductive additive still being detected in the C 1s photoelectron spectra.[17] However, this observed behavior could be related to the findings of Bodenes et al. that different binder formulations affect SEI formation.[29] Madec and coworkers observed that the binder and solvent used in electrode fabrication could play a role in the SEI composition and morphology even after extended cycling; in particular, they still observed peaks corresponding to PVDF binder via XPS even after cycling TiSnSb electrodes for 100 cycles.[28]

While the overall thickness of the SEI layer seems to increase with cycle number, TEM characterization of the SEI formed on SnSb over many cycles suggests than the inner portion of the SEI composed mainly of inorganic species might not grow considerably. Tesfaye et al. sonicated SnSb electrodes stopped at different stages of cycling in ethanol for several minutes prior to TEM sample preparation and characterization, so most of the SEI remaining on the surface of the electrode particles is most likely the inner, inorganic rich layer. This layer of the SEI seemed to grow very slowly over extended cycling based on TEM characterization. After the 10^{th} cycle, the layer was 4.7 nm thick, while it only increased in thickness to 5.5 nm and 5.7 nm after the 30^{th} and 50^{th} cycles, respectively.[59]

Another interesting observation from some long-term cycling studies has been the increase in electrode thickness in addition to the increase in SEI thickness. SEM of electrode cross sections revealed that Sb composite electrodes increased from 10 μm for the pristine electrode to 30 μm after 20 cycles.[76] Similarly, Madec and coworkers observed that the thickness NbSnSb composite electrodes cycled for 400

cycles increased by 3 times when cells were cycled at 25 °C and by 1.5 times when cells were cycled at 60 °C.[103] Schulze and coworkers saw similar behavior for Sb/carbon nanotube composite electrodes, which increased from 5 μm to 30 μm in thickness over extended cycling.[104] The authors attributed this increase in electrode thickness to SEI formation at new electrode surfaces exposed by volume expansion during lithiation; for electrodes that maintain good electrical connectivity throughout the active material and with the current collector, this can lead to increased electrode thickness with increased cycling as the SEI continues to form on newly exposed electrode surfaces.[104] This behavior could also explain the observations of Park and coworkers, who saw increased carbon content in the Sn electrode with cross sectional SEM-EDS after 20 cycles.[68]

In addition to increasing in overall thickness with extended cycling, the SEIs formed on many alloying anodes over longer periods of cycling show evidence of either mechanical or chemical instability. For example, after 20 cycles, Li and coauthors saw the reappearance of Sn peaks in the XPS Sn 3d spectrum for Sn-Co thin film electrodes, which they suggested was indicative of SEI cracking and possible delamination.[89] Similarly, after 30 cycles Sb composite electrodes appeared to be composed of smaller particles due to pulverization based on SEM characterization, and excessive delamination from current collector was apparent.[76] SEM was also used to characterize the surface of a Bi composite electrode cycled in conventional electrolyte after 50 cycles; it revealed that the micron-sized Bi particles were severely pulverized and the SEI on the surface of electrode appeared porous and loose rather than compact.[55] While alloying thin film and composite electrodes showed signs of pulverization and poor SEI mechanical stability over extended cycling, Jackson and Prieto saw signs chemical instability for the SEI formed on Cu_2Sb nanowire arrays. SEM characterization revealed that the Cu_2Sb nanowires were intact and still in contact with the current collector after 50 cycles, but all of the space between wires had been filled in by SEI and there was evidence of a thick surface film, suggesting poor surface passivation and continual electrolyte reduction.[43]

1.4.2) SEI properties

The SEI layers formed on many alloying anodes over the initial phases of cycling seem to exhibit some instability either in terms of electrode passivation or in dynamic behavior suggested by fluctuations in the SEI composition at different states of discharge or charge. As described in a previous section of this review, electrolyte reduction and SEI formation seems to be catalyzed on Sn anodes, and over short term cycling the SEI does not seem to passivate Sn electrodes sufficiently. However, the SEI formed on Sn does seem to passivate the electrode eventually; Park and coworkers observed that the peak around 1.4 V associated with electrolyte reduction and SEI formation on Sn was no longer present after the 20th cycle during characterization with CV.[68] Unlike for Sn, our studies of the SEI evolution over longer cycling for Cu_2Sb thin film anodes suggests that without electrolyte additives, the SEI formed on Cu_2Sb in 1 M $LiClO_4$ in EC/DMC/DEC (1:1:1 vol) electrolyte does not passivate the surface well based on evidence of Cu diffusion and Cu_2Sb/Cu oxidation around 3.0 V and may contribute to the rapid capacity fade observed after about 10 cycles.[105] XPS characterization of AlSb anodes after 50 cycles at the end of discharging and charging suggested that the behavior of the SEI formed on some alloying anodes is still dynamic even after many cycles based on differences in the C 1s spectra that suggest fluctuations in the SEI surface composition at different stages of cycling.[17]

Changes in other properties, such as SEI resistance, observed for alloying anodes after extended periods of cycling make sense based on the changes observed for the morphology of the SEI. There have been many reports of increasing SEI resistance with extended cycling based on EIS characterization. Increases in impedance have been reported for Sb, $MnSn_2$, and SnSb electrodes after 15–20 cycles, suggesting that the SEI either increases in thickness or decreases in porosity after extended cycling.[59,76,92] These results suggest that the thickness and resistance of the SEI plays an important role in long term cycling behavior, and some have attributed the capacity fade observed for alloying anodes like $MnSn_2$ and SnSb to continual SEI growth.[59,92] Similarly, previous work in our group studying SEI formation on Cu_2Sb

nanowire arrays suggested that surface instability and the related SEI formation were main cause of failure due to hindering Li ion transport, which was supported by SEM characterization.[43]

1.4.3) SEI composition

It is more difficult to understand how changes in the composition of the SEI formed on alloying anodes may play a role in capacity retention and cycle lifetime as reports on the evolution of the SEI composition during extended cycling have been varied. Some have reported seeing the same species after cycling that were observed after initial SEI formation over the first cycle. Based on FTIR characterization, Hong et al. saw the same SEI species for F-doped Ni-Sn electrodes cycled 50 times that were seen during the first cycle, including organic fluorophosphates, alkyl carboxylates, alkyl carbonates, and Li_2CO_3.[86] In contrast, Song and Baek reported seeing new SEI species after extended cycling of Sn electrodes; after 50 cycles, new features in the FTIR spectra were seen corresponding to ester, oxalate, and either alkyl carbonate or carboxylate species in addition to the peaks for P–F containing species detected after initial SEI formation. Interestingly, the authors saw Li_2CO_3 in the SEI initially but did not observe any after 50 cycles.[19] Members of our group found that the SEI surface on Cu_2Sb NW arrays was carbonate rich after 50 cycles based on XPS characterization, which was hypothesized to be due to uncontrolled polycarbonate formation, and they also saw evidence of alkyl carbonates, alkoxides, LiF and $LiPF_6/P_xF_y$ species.[43] After 20 cycles, Marino and Zhang still detected Li_2O/LiOH at the surface of the SEI on TiSnSb electrodes based on O 1s photoemission spectra, and they saw a decrease in carbonate binding environments based on XPS as well. After 20 cycles, the authors also saw the appearance of a low binding energy C 1s photoemission peak that could be due to sp^2 carbon and a high binding energy O 1s photoemission peak that could be due to polycarbonate species.[45] In contrast to the SEI formed on TiSnSb, others have reported an increase in carbonates for other alloying anodes. After 50 cycles, Seo et al. saw an increase in Li_2CO_3 and Li alkyl carbonate species for the SEI on Sn based on XPS and FTIR characterization,[75] and Li et al. saw an increase in carbonate species for the SEI on Sn-Co electrodes after 20 cycles with XPS and ToF SIMS, which the

authors attributed to Li_2CO_3.[89] In addition to an increase in carbonate species, Seo and coworkers also saw an increase in LiF content at the SEI surface on Sn after 50 cycles.[75] Increases in the amount of LiF at the SEI surface on Sn-Sb-Cu and AlSb electrodes after 30 and 50 cycles, respectively, were also reported.[17,106] Ulus and coauthors hypothesized that more LiF may make the SEI more brittle and play a role in the ability of the SEI to accommodate the volume expansion of Sn-Sb-Cu electrodes.[106]

1.5) Electrolyte additives and novel electrolytes

1.5.1) Vinylene carbonate and fluoroethylene carbonate

Additives like VC and FEC, which have been found to help improve the performance and stability of the SEI formed on both intercalation and alloying anodes, tend to dramatically increase the cycle lifetime of alloying anodes.[22,43,69,76,103] They are believed to behave as sacrificial additives that prevent excessive SEI formation, although other studies have suggested that these additives play other roles as well.[44,107] These additives also seem to help limit excessive electrolyte reduction and SEI formation on alloying anodes, based in part on the electrochemical behavior and SEI morphology for alloying anodes cycled with these additives. Webb et al. found that the addition of 5% FEC eliminated the excessive electrolyte consumption at 1.4 V on the first cycle for In electrodes, while increasing the additive amount to 13% FEC eliminated the excessive electrolyte consumption for both the first and the second cycles.[61] Yang et al. hypothesized that the addition of 2% FEC in 1.2 M $LiPF_6$ in EC/EMC (3:7 wt) electrolyte helped suppress EMC decomposition on Cu_6Sn_5 electrodes based on results from differential capacity analysis.[84] Some of our XPS studies have suggested that the addition of 5% VC to $LiClO_4$-based carbonate electrolytes help passivate the surface of Cu_2Sb thin film electrodes better and prevent Cu_2Sb/Cu oxidation and Cu diffusion.[105] Results of studies from Madec and coworkers on TiSnSb and NbSnSb electrodes have revealed that the addition of VC and FEC can even help minimize excessive electrolyte reduction and SEI formation at elevated temperatures of 60 °C and that the additives may even perform better at 60 °C than at 25 °C.[34,103]

Results from studies of FEC and VC as additives for alloying anodes suggest that the SEIs formed with additives help passivate the electrode surface more effectively and prevent excessive solvent reduction, which is supported by studies comparing the initial thicknesses of SEI layers formed with and without additives. EQCM-D results for Cu_6Sn_5 and Sn electrodes suggested that the SEI formed in the additive-free electrolyte was initially thicker compared to the electrolyte containing FEC.[70,84] Similarly, The SEI formed in VC-based electrolytes also seems to be thinner than the additive-free SEI initially based on XPS characterization of the SEI formed on Sb electrodes with and without VC.[22]

While results for the characterization of the SEI thickness during the initial stages of SEI formation are consistent, the results for the evolution of the thickness and morphology of SEIs formed in electrolytes containing additives vary based on the additive used. Comparisons between FEC-based and VC-based SEI layers revealed some differences. For example, the SEI formed on Sn anodes with VC as an additive had very high impedance after 50 cycles, whereas the SEI formed with FEC as an additive was much lower in impedance.[75] After cycling Cu_2Sb nanowire arrays for 100 cycles, the SEIs formed with the addition of either 5% FEC or 5% VC were both quite thin, as there was still void space visible between the nanowires with SEM, as shown in Figure 1.5.[43] However, after 250 cycles that there was a notable difference in the surface morphologies of the SEIs formed on the Cu_2Sb NWs; the FEC-based SEI was thick and porous with no NWs visible, whereas the VC-based SEI appeared nonporous and relatively thick in places, but also had wires visible.[43]

There also seems to be some variation in the evolution of SEI thickness for a given additive, which could be due to a number of factors, including the electrode material, choice of solvent, or cycling conditions. While initially thinner than the additive-free SEI, the SEI formed with FEC on Cu_6Sn_5 became thicker than the SEI formed without FEC during extended cycling.[84] The SEI formed on TiSnSb electrodes in electrolyte containing FEC also gets thicker with increasing cycling number.[45] In contrast, results from EIS characterization of Sb electrodes after the 5^{th} and 20^{th} cycles suggested that the thickness of the SEI

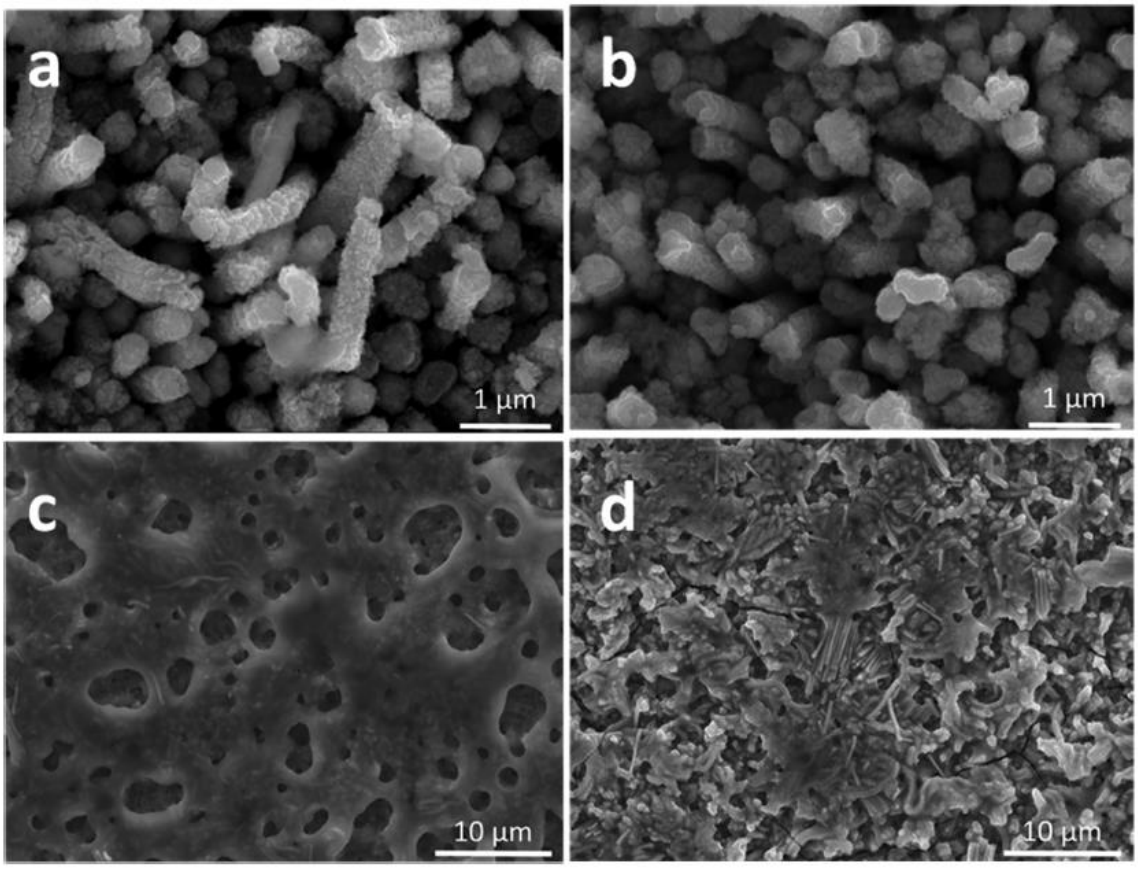

Figure 1.5: Scanning electron micrographs of Cu_2Sb nanowire arrays cycled in conventional electrolyte after 100 cycles with (a) 5% FEC additive and (b) 5% VC additive and after 250 cycles with (c) 5% FEC and (d) 5% VC. Reprinted with permission from Reference 43 copyright 2016 American Chemical Society.

formed in PC-based electrolyte with 10% FEC remains relatively consistent compared to the SEI formed without FEC, which shows an increase in impedance with continued cycling.[76] In contrast, an increase in impedance between the 1st and 15th cycles was observed for the SEI formed on a Sb-based electrode cycled with 2% VC but not for the SEI formed from the additive-free electrolyte.[22] EIS characterization of the SEIs formed on Sn-based electrodes with and without 10% VC showed a decrease in impedance with continued cycling for the VC-based SEI and an increase in impedance with continued cycling for the additive-free SEI.[69] Comparisons of the electrode cross sections with SEM after 10 and 20 cycles showed that the SEI formed on Sn with 1 M $LiPF_6$ in EC/DMC (1:1) with 5% VC was thinner compared to the SEI formed in the electrolyte without VC.[68]

Some researchers have observed electrode volume expansion with extended cycling for alloying anodes in conventional electrolyte without additives, and some have also observed similar behavior for alloying anodes cycled with FEC or VC. After 20 cycles, Park et al. observed that the Sn electrode cycled in electrolyte containing 5% VC was thicker than the electrode cycled without additives based on SEM characterization of electrode cross sections. EDS of the electrode cross section for the VC-based sample showed Sn signal in the SEI and carbon signal in the electrode, so the thickness increase is likely from SEI formation between Sn particles, leading to increased electrode thickness, similar to what others have observed.[68,103,104] Similarly, Madec and coworkers also saw larger electrode thickness increases after cycling NbSnSb electrodes with a combination of 1% VC and 5% FEC compared to the electrodes without additives; after 400 cycles, electrodes cycled at 25 °C with VC and FEC were 5 times thicker and electrodes cycled at 60 °C with VC and FEC were 4 times thicker than the pristine electrodes.[103] Interestingly, while Bian et al. observed a thickness increase for Sb-based electrodes cycled without additives, the electrodes cycled with 10% FEC experienced negligible increases in thickness after 20 cycles; the pristine electrode was 10 μm thick, while the electrode cycled with FEC was 13 μm thick.[76] Again, it is unclear at this point whether these contrasting results are due to differences in the additives, the electrodes, or the cycling conditions.

Despite some differences in morphology and thickness for the SEIs formed on various alloying anodes with either VC or FEC as additives, studies of the SEI composition reveal some striking similarities for SEI layers formed on different electrodes with a given additive. In general, the SEI formed with FEC as an additive tends to be more rich in fluorinated species, especially LiF, than either additive-free or VC-modified SEIs based on XPS characterization of In,[61] Sn,[75] Sb,[76] Cu_2Sb,[43] TiSnSb,[45] and NbSnSb electrodes;[103] Bian and coworkers reported that the SEI surface of Sb electrodes cycled with 10% FEC consisted of 20% F, while the SEI formed without additives had only 4% F at the surface.[76] MPE values and EQCM-D characterization of Cu_6Sn_5 electrodes during the SEI formation process suggested the formation of LiF

and/or LiOH species when the electrolyte contained FEC, compared to carbonaceous species for the electrolyte without FEC.[84] In many systems, the addition of FEC also seems to result in a carbonate rich SEI formed on alloying anodes. This was observed for In,[61] Sn,[68] Sb,[76] Cu_2Sb,[43] and TiSnSb[45] electrodes using XPS and/or FTIR characterization. Comparison of FEC-modified SEIs to additive-free SEIs for some alloying anodes revealed some differences in carbonate speciation between the two types of SEIs. Based on FTIR characterization of the SEI on Sn electrodes, the SEI formed with 5% or 10% FEC as an additive contained fewer Li alkyl carbonate species and slightly more Li_2CO_3 than the SEI formed without additives, as well as polycarbonate species that were not observed for the sample without additives.[75] Based on XPS characterization, Zhang and coworkers concluded that during the initial stages of SEI formation on TiSnSb, the SEI formed with 5% FEC was richer in Li alkyl carbonate species while the FEC-free SEI was richer in Li_2CO_3; after 20 cycles, the FEC-free SEI was still thought to be rich in Li_2CO_3 while the carbonate speciation for the FEC-based SEI was thought to be dependent on the state of charge or discharge, with the SEI at the end of discharge being Li_2CO_3 rich and the SEI surface at the end of charge containing Li alkyl carbonates.[45] Similarly, Madec and coworkers reported Li_2CO_3 in the SEIs formed on NbSnSb electrodes with and without additives, but the SEIs formed from the electrolyte without additives tended to contain more Li_2CO_3 based on XPS characterization.[103]

Compared to the SEIs formed with FEC as an additive, the SEIs formed when VC is used as an additive tend to be less fluorine rich,[43,75] although fluorinated species like LiF are still present from the $LiPF_6$ Li salt.[22,43,68,69] In some cases the VC-modified additives are also less F rich than the SEIs formed without additives; for example, based on XPS characterization of the SEI surface on Sn electrodes, Park and coworkers found that SEI formed with VC was only ca. 5% F, while the SEI formed without VC was ca. 30% F,[68] and XPS characterization of Sb-based electrodes also suggested that less LiF was present at the SEI surface when VC was used compared to when it was absent.[22] Like the SEIs formed with FEC as an additive, the SEIs formed with VC as an additive tend to be rich in carbonates, as seen for Sn,[68,75] Sb,[22] and

Cu_2Sb electrodes,[43,105] although comparisons of the SEIs formed on Sn electrodes suggest that the SEI formed with VC is less rich in Li_2CO_3 and Li alkyl carbonate species than SEIs formed without additives or with FEC as an additive based on FTIR characterization.[68,75] The most notable difference in the composition of the SEI layer formed in electrolyte with VC as an additive compared to either FEC or without additives is the presence of polycarbonate species, such as poly VC. These types of species have been reported in FTIR and XPS studies of the SEI on Sn electrodes[68,69,75] as well as XPS studies of the SEI on Cu_2Sb electrodes.[105] While polycarbonates have also been reported to form on Sn electrodes when FEC was used as an additive, the VC-based SEI was richer in poly carbonate species than the FEC-based SEI.[75] Based on these results, it seems that for without additives, solvent reduction and reduction of organic SEI components to form Li_2CO_3 is favored for the SEI on alloying anodes. When FEC is used as an additive, salt reduction seems to be favored when fluorine-containing salts like $LiPF_6$ are used as the supporting electrolyte, resulting in more LiF in the SEI. The use of VC as an additive seems to also favor solvent reduction but results in formation of poly carbonate species like poly VC rather than smaller molecular species like Li_2CO_3 or short chain Li alkyl carbonates.

Characterization of the SEI formed with and without additives on alloying anodes has also suggested that the properties of the SEIs formed with the additives are quite different than those of the SEI formed without additives. Sb electrodes cycled in PC-based electrolyte without any additives showed poor performance at faster cycling rates, while the electrodes cycled with 10% FEC demonstrated good rate capabilities.[76] Based on TEM characterization of microsized Sb from composite electrodes, the Sb particles remained intact after 5 cycles when 10 % FEC was added to the electrolyte, unlike the Sb particles cycled without FEC, which were already beginning to show signs of fracturing, as seen in the top of Figure 1.6.[76] There were also notable differences in the electrode morphology and apparent SEI properties after longer cycling. After 30 cycles without FEC, the Sb electrode was severely delaminated and SEM showed signs of pulverization; however, the Sb electrode cycled with FEC showed no signs of delamination even

after 50 cycles and seemed to still have larger micron-sized particles, as seen in Figure 1.6 (bottom).[76] This suggests that the SEI formed on Sb with FEC as an additive may help improve the mechanical stability of the SEI and prevent severe electrode pulverization and delamination.

FEC and VC additives have also improved the properties of Sn and Sn-based electrodes. EQCM-D characterization of SEI formation on Sn anodes with and without FEC suggested that the SEI formed from the additive-free electrolyte was softer and more heterogeneous than the FEC-based SEI and that the FEC-based SEI was more elastic than the one formed without additives.[70] Similarly, the SEI formed on Sn electrodes with VC as an additive also seems to be more flexible than the SEI formed without VC based on electrode bending experiments, which the authors attributed to the presence of more organic species in the VC-based SEI.[68]

While the addition of FEC or VC to the electrolyte seems to result in the formation of SEIs with better mechanical properties for alloying anodes, the additive modified SEIs still might not meet all of the criteria of an ideal solid electrolyte as outlined in the introduction. MPE values derived from EQCM-D characterization of Cu_6Sn_5 electrodes cycled with FEC additive were lower than expected over the potential region where the material alloys with lithium, suggesting an incomplete alloying reaction. This behavior was not observed for electrodes cycled without additives, suggesting that the SEI formed with the additive may impede lithium transport more than the SEI formed without the additive, resulting in incomplete lithiation during the first discharge.[84] The SEI dissolution behavior observed during charging/oxidation for many alloying anodes cycled in conventional electrolyte has also been observed for TiSnSb electrodes cycled with a combination of 1% VC and 5% FEC after short term (end of first cycle charge) and long term cycling (end of 20^{th} cycle charge).[45] Madec and coworkers also observed this behavior for TiSnSb electrodes cycled for 400 cycles with 1% VC and 5% FEC; at the end of charge on the 400^{th} cycle, low intensity Sn 3d and Na KLL features corresponding to electrode components could still be

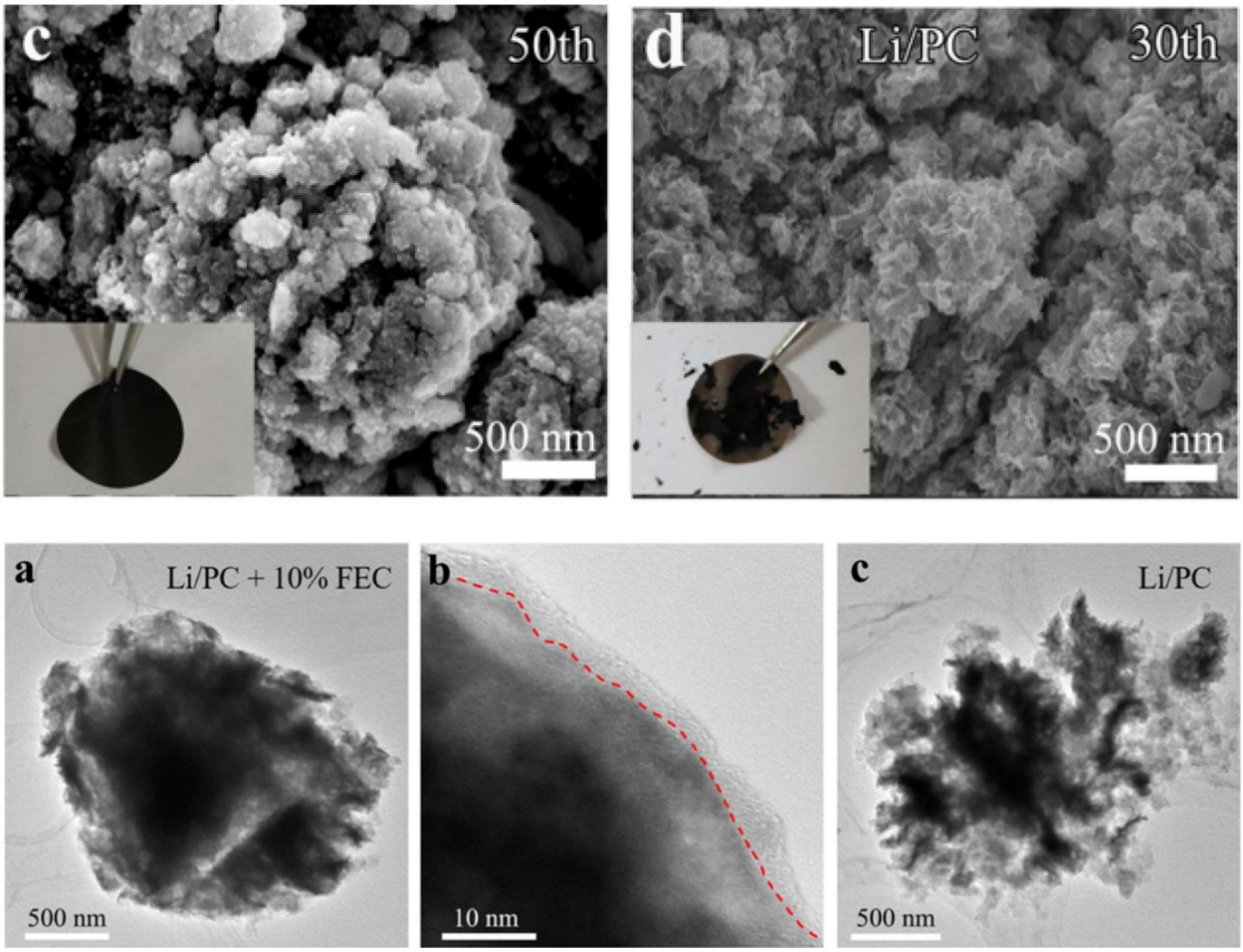

Figure 1.6: Top: scanning electron micrographs and digital photographs (insets) of Sb electrodes (c) after 50 cycles when FEC was used as an additive and (d) after 30 cycles without additives. Bottom: transmission electron micrographs of Sb electrode particles after (a, b) 1 cycle with FEC additive and (c) without FEC additive. Reprinted with permission from Reference 76 copyright 2020 American Chemical Society.

detected with XPS when the sample was cycled at 25 °C.[34] This could imply that while FEC and VC improve SEI mechanical stability, they may not improve the chemical stability.

1.5.2) Acid scavenging additives

While the roles of FEC and VC as performance improving additives for alloying anodes are still being clarified after numerous studies, others have started studying the effects of electrolyte additives that serve a specific purpose. In conventional $LiPF_6$-based electrolytes, the formation of HF due to the presence of trace water in the electrolyte has been found to affect SEI stability and lead to SEI

dissolution.[37] Some researchers have started study the effects of acid scavenging additives, specifically trimethyl phosphite (TMP), on SEI formation and stability for Ni-Sn alloying anodes.[91]

Choo and coworkers observed improved electrochemical reversibility and modest improvements in CE and capacity retention for Ni-Sn thin film electrodes when 3% TMP was added to 1 M $LiPF_6$ in EC/EMC (3:7 by vol) electrolyte. Based on characterization of the SEIs with FTIR and XPS, the compositions and thicknesses of the SEIs formed with and without TMP were different. The signal for the FTIR spectrum for the SEI formed on Ni-Sn without TMP was not very intense and primarily consisted of bands corresponding to P=O and P–O–C stretching modes, which the authors attributed to organic phosphorus fluoride species ($OPF_{3-x}(OR)_y$). For the electrodes cycled with the additive, the peaks in the FTIR spectrum were more intense, suggesting a thicker SEI. The features corresponded mostly to Li_2CO_3, but there were also minor peaks corresponding to Li alkyl carbonates as well as peaks corresponding to methyl and methylene groups. XPS characterization of the SEI surface on the sample cycled without TMP suggested that the SEI was quite thin because Sn 3d peaks were still detected. The C 1s HRES spectrum contained carbonate and aliphatic carbon binding environments, but the peaks were not very intense, suggesting that Li alkyl carbonates and Li_2CO_3 were minor surface species; based on the F 1s HRES spectrum, LiF was predominant on the SEI surface when no additive was used. The addition of 3% TMP seemed to result in the formation of a thicker SEI based on the Sn 3d peaks from the underlying electrode being completely attenuated. The additive-modified SEI surface was more carbon-rich based on intense peaks in the C 1s spectrum corresponding to carbonate and aliphatic binding environments, as well as lower intensity features corresponding to C–O and O=C–O binding environments. Based on the F 1s spectrum, the SEI surface formed from electrolyte containing TMP also had small amounts of LiF and $Li_xPF_yO_z$ species. The formation of a thicker SEI on Ni-Sn electrodes may help passivate the electrode surface more effectively. The TMP additive also seems to be helping to change the $LiPF_6$ reactivity in some way to help create a passivation layer that consists of solvent reduction products like Li_2CO_3 and Li alkyl carbonates rather than salt

degradation products like LiF and $OPF_{3-x}(OR)_y$, although it is not clear how this difference in SEI composition helps improve cycling performance.[91]

1.5.3) Unconventional electrolyte formulations

In addition to the use of small amounts of additives, many researchers are looking to different electrolyte formulations in order to improve the SEI formed on metallic alloying anodes. Hong and coworkers took a combined approach to improving the SEI formed on F-doped Ni-Sn thin film electrodes; they used 3% TMP as an acid-scavenging additive, but they also replaced EC with FEC as one of the solvents in their electrolyte. Cycling F-doped Ni-Sn electrodes in 1 M $LiPF_6$ in FEC/DEC (1:1 by vol) with 3% TMP resulted in notable morphological and compositional changes in the SEI compared to conventional electrolyte. Even after one cycle, the active particles at the surface of the thin film electrode appear to be better-connected by the formation of a surface film based on SEM characterization of the electrode cycled in the FEC-based electrolyte, while the surface of the electrode cycled in EC-based electrolyte appears rougher, and the electrode particles appear smaller, suggesting more pulverization. Based on FTIR characterization, the FEC-based SEI contains primarily Li_2CO_3 and metal carboxylate species; the EC-based SEI also contained these species as well as more alkyl carbonate species. Additionally, FTIR characterization of the two SEIs over different stages of the first cycle suggest the formation of a more stable SEI from the FEC-based electrolyte; the spectra for the FEC-based sample remained relatively consistent, while the spectra for the EC-based sample showed an increase in carbonate species towards the end of the first cycle. XPS characterization of the SEI surfaces also revealed some notable differences between the FEC- and EC-based electrolytes. Based on the C 1s HRES spectra, the EC-based SEI surface was richer in carbonate and carboxylate species, while the FEC-based SEI was richer in aliphatic carbon, which the authors hypothesized to be due to the formation of polyethylene based on proposed electrolyte reduction pathways. Additionally, the F 1s HRES spectra revealed that the FEC-based SEI surface was richer in fluorinated species, including LiF.[86]

Zhang et al. also studied changes in the SEI formed when conventional SEI improving additives like VC and FEC were used in conjunction with an alternative electrolyte formulation composed of a carbonate and ionic liquid mixture. They found that the cycle lifetime of TiSnSb composite electrodes cycled at a 4C rate could be extended to nearly 500 cycles in LiTFSI in Pyr_{14}/DMC (1:1) with 1% VC and 5% VC electrolyte, although the reversible capacity was slightly lower than in more conventional electrolytes. Like many SEIs formed from conventional electrolytes, the SEI formed from the IL/DMC mixture with VC and FEC showed some instability in terms of SEI dissolution during charging. Based on XPS characterization, the SEI surface formed in this electrolyte contained similar species as the SEI formed in conventional electrolytes. The addition of FEC and VC decreased the interfacial resistance, increased the LiF content, and decreased the carbonate species at the SEI surface for the IL/DMC electrolyte, which are trends often observed for conventional electrolytes as well.[108]

Qin and coworkers also studied SEI formation in ILs. They found that cycling Al composite electrodes in 0.2 m LiTFSI in N-butyl-N-methylpyrrolidinium bis(fluorosulfonyl)imide (Pyr_{14}FSI) resulted in good capacity retention over 10 cycles and relatively high CE, although the capacity began fading around 15 cycles, so the improvement over conventional electrolytes was still modest in the ionic liquid. The authors hypothesized that the improvement in cycling performance may be related to the incorporation of TFSI and FSI salts and their reduction products into the SEI. Based on XPS characterization, some of these reduction products include $LiSO_2F$, LiF, and LiNSO.[82]

While immediate capacity fading was observed for Bi composite electrodes cycled in conventional electrolyte, Kuwata and colleagues found that replacing the conventional electrolyte with 1 M $LiBH_4$ in THF extended the cycle lifetime, with no notable capacity fade after 50 cycles. Based on SEM characterization, particles were pulverized after 50 cycles, but the electrode surface appeared to be covered by a dense, rough film, which could have helped maintain good electrical connectivity despite fracturing. In situ IR on model Ni electrodes cycled in the $LiBH_4$/THF electrolyte showed peaks

corresponding to $LiBH_4$, THF, and $LiBH_4$-THF complexes but no electrolyte reduction or degradation products, suggesting that the $LiBH_4$/THF electrolyte solution does not passivate the electrode surface in the same way that carbonate-based electrolytes with fluorinated supporting electrolytes passivate the electrode surface.[55]

Others, like Chan and coworkers, have found promise in using conventional electrolytes with unconventional formulations. Instead of using more conventional 1 M Li salt concentrations, the authors used a roughly 1:1 mol:mol ratio of LiFSI to DMC. Over short term cycling (ca. 30 cycles), concentrated electrolyte showed better capacity retention than the conventional electrolyte, which may be due to better electrode passivation in the concentrated electrolyte. Based on Li ion solvation studies using Raman and DFT, the authors hypothesized that poor surface passivation of Al electrodes in less concentrated electrolytes was due to insufficient FSI^- reduction. This hypothesis was supported by XPS characterization of the SEI surface after one discharge, which showed that the speciation of the SEIs formed in both electrolytes were similar, but the surface on the SEI formed from the concentrated electrolyte was richer in salt and salt reduction products like LiFSI and LiF, while the surface of the SEI formed from conventional electrolyte was richer in solvent reduction products like carbonates. SEM and EIS characterization also suggested that excessive electrolyte reduction and SEI growth was suppressed in the concentrated electrolyte. SEM also showed that although the Al electrode seems to be passivated better in the concentrated electrolyte, it does not prevent fracturing of the active material, which was observed after 5 cycles for both the standard and super concentrated electrolyte solutions.[109]

1.6) Conclusions and future directions

Overall, the SEIs formed on alloying anodes share many similarities. Much of the SEI formation occurs during the first cycle over different potential-dependent stages. The SEI initial thickness on Sn and Sb anodes tends to be thicker than for other alloying anodes like intermetallics, which could be related to differences in volume expansion and/or surface reactivity. Despite differences in initial thickness, the SEIs

most alloying anodes seem to exhibit dynamic behavior in terms of changes in thickness and speciation during different stages of cycling, with SEI thickness decreasing during charging/oxidation. However, with extended cycling, the SEI increases in thickness on alloying anodes. As with other types of electrode materials, the SEI formed on alloying anodes seems to be primarily composed of electrolyte solvent reduction species like Li_2CO_3 and Li alkyl carbonate species and $LiPF_6$ reduction species like LiF. Other SEI components have also been reported, although the reports are varied due to the use of different characterization techniques and SEI sample preparation methods (different electrode compositions, electrolyte compositions, and cycling conditions).

Studies of the influence of electrolyte additives and unconventional electrolytes on SEI formation, composition, and properties have helped provide some insights into how SEI composition and structure affect capacity retention and cycle lifetime of alloying anodes. However, there are still many gaps in our understanding of how SEI composition affects the properties, and what role that plays in cycle performance. For example, it is still not clear whether LiF is a beneficial SEI species for alloying anodes; it appears to contribute to good electrode passivation during the initial stages of SEI formation[72,109] but may not be beneficial over long term cycling.[106,109] Similarly, the role that carbonate species play in surface passivation and SEI stability for alloying anodes remains unclear. Additionally, there are still large gaps in the understanding of how the SEI changes over extended cycling and how those changes affect the cycling performance. If the ultimate goal of SEI studies is the more intentional design of electrolytes, additives, and even artificial SEIs, a fundamental understanding of SEI formation and evolution and the relationship between SEI composition, structure, and properties is required.

Overall there is a need for more SEI studies of alloying anodes using binder- and additive-free electrodes. Multiple studies of the SEI formed on alloying anode materials have revealed that the conductive carbon additives, binders, and solvent used for fabricating slurry cast composite electrodes can affect SEI formation.[28,29] Another drawback to using composite electrodes for SEI studies is that the

amount of active material used is often quite low; many of the studies described here make use of electrodes with only 60–70% by weight active material, so many of the findings concerning SEI formation on alloying anode materials are likely convoluted or diminished by the low amounts of active material.[24,28,29,34,59,75,76,82,103] Fortunately, electrodes of many alloying anode materials can be fabricated without binders or additives using physical or electrochemical deposition techniques, allowing for more direct analysis of SEI formation on these materials.[19,25,43,61,63,83,87,89–91,97,110–112] However, since most of these fabrication techniques usually involve exposure to air prior to cell assembly and SEI formation, it is also important to know the composition of the pristine electrode surface since native oxides may affect SEI formation.[26,61,62]

Another area of research that is lacking in SEI studies of metallic alloying anodes is SEI studies of anodes in full cell configurations, which are important for several reasons. The limited Li inventory in full cells could affect SEI formation and speciation as well as electrode failure mechanisms.[113] Additionally, SEI formation on alloying electrodes seems to be potential dependent, and the potentials anodes are polarized to in full cells is typically different compared to half cells.[113,114] The use of a Li-ion cathode instead of a Li metal electrode could also affect the SEI formed on alloying anodes in several ways. It has been observed that the reactivity of the counter electrode and electrode "cross talk" can affect electrolyte reduction species and SEI formation and composition.[115,116] Additionally, metal dissolution from cathodes to graphite anodes has been found to exacerbate electrolyte reduction, leading to excessive Li consumption and decreases in both anode reversibility and capacity, which may affect the SEI on alloying anodes as well.[114,117–121] Finally, although anodes in full cells are not cycled over the same potential ranges as cathodes,[113,114] it is not clear if metal oxidation and dissolution from alloying anodes could also affect the SEI on cathodes, especially when intermetallics or alloys containing Cu, which may diffuse to other parts of the cell, are used as anodes.

CHAPTER 1 REFERENCES

(1) Goodenough, J. B.; Kim, Y. Challenges for Rechargeable Li Batteries. *Chem. Mater.* **2010**, *22* (3), 587–603. https://doi.org/10.1021/cm901452z.

(2) Peled, E.; Menkin, S. Review—SEI: Past, Present and Future. *J. Electrochem. Soc.* **2017**, *164* (7), A1703–A1719. https://doi.org/10.1149/2.1441707jes.

(3) Peled, E. THE ELECTROCHEMICAL-BEHAVIOR OF ALKALI AND ALKALINE-EARTH METALS IN NON-AQUEOUS BATTERY SYSTEMS - THE SOLID ELECTROLYTE INTERPHASE MODEL. *J. Electrochem. Soc.* **1979**, *126* (12), 2047–2051. https://doi.org/10.1149/1.2128859.

(4) Verma, P.; Maire, P.; Novák, P. A Review of the Features and Analyses of the Solid Electrolyte Interphase in Li-Ion Batteries. *Electrochim. Acta* **2010**, *55* (22), 6332–6341. https://doi.org/10.1016/J.ELECTACTA.2010.05.072.

(5) Xu, K. Nonaqueous Liquid Electrolytes for Lithium-Based Rechargeable Batteries. *Chem. Rev.* **2004**, *104* (10), 4303–4417. https://doi.org/10.1021/cr030203g.

(6) Aurbach, D. Review of Selected Electrode-Solution Interactions Which Determine the Performance of Li and Li Ion Batteries. *J. Power Sources* **2000**, *89* (2), 206–218. https://doi.org/10.1016/S0378-7753(00)00431-6.

(7) Gauthier, M.; Carney, T. J.; Grimaud, A.; Giordano, L.; Pour, N.; Chang, H. H.; Fenning, D. P.; Lux, S. F.; Paschos, O.; Bauer, C.; Maglia, F.; Lupart, S.; Lamp, P.; Shao-Horn, Y. Electrode-Electrolyte Interface in Li-Ion Batteries: Current Understanding and New Insights. *Journal of Physical Chemistry Letters*. American Chemical Society November 19, 2015, pp 4653–4672. https://doi.org/10.1021/acs.jpclett.5b01727.

(8) Winter, M. The Solid Electrolyte Interphase- The Most Important and the Least Understood Solid Electrolyte in Rechargeable Li Batteries. *Z. Phys. Chem.* **2009**, *223* (10–11), 1395–1406. https://doi.org/10.1524/zpch.2009.6086.

(9) Lemordant, D.; Zhang, W.; Ghamouss, F.; Farhat, D.; Darwiche, A.; Monconduit, L.; Dedryvère, R.; Martinez, H.; Cadra, S.; Lestriez, B. Artificial SEI for Lithium-Ion Battery Anodes: Impact of Fluorinated and Nonfluorinated Additives. In *Advanced Fluoride-Based Materials for Energy Conversion*; Nakajima, T., Groult, H., Eds.; Elsevier, 2015; pp 173–202.

(10) Michan, A. L.; Leskes, M.; Grey, C. P. Voltage Dependent Solid Electrolyte Interphase Formation in Silicon Electrodes: Monitoring the Formation of Organic Decomposition Products. *Chem. Mater.* **2016**, *28* (1), 385–398. https://doi.org/10.1021/acs.chemmater.5b04408.

(11) Schroder, K. W.; Celio, H.; Webb, L. J.; Stevenson, K. J. Examining Solid Electrolyte Interphase Formation on Crystalline Silicon Electrodes: Influence of Electrochemical Preparation and Ambient Exposure Conditions. *J. Phys. Chem. C* **2012**, *116* (37), 19737–19747. https://doi.org/10.1021/jp307372m.

(12) Zhang, W. J. A Review of the Electrochemical Performance of Alloy Anodes for Lithium-Ion Batteries. *J. Power Sources* **2011**, *196* (1), 13–24. https://doi.org/10.1016/j.jpowsour.2010.07.020.

(13) Thackeray, M. M.; Vaughey, J. T.; Johnson, C. S.; Kropf, A. J.; Benedek, R.; Fransson, L. M. L.; Edström, K. Structural Considerations of Intermetallic Electrodes for Lithium Batteries. *J. Power Sources* **2003**, *113* (1), 124–130. https://doi.org/10.1016/S0378-7753(02)00538-4.

(14) Xu, K. Electrolytes and Interphases in Li-Ion Batteries and Beyond. *Chem. Rev.* **2014**, *114* (23), 11503–11618. https://doi.org/10.1021/cr500003w.

(15) Zhang, Y.; Du, N.; Yang, D. Designing Superior Solid Electrolyte Interfaces on Silicon Anodes for High-Performance Lithium-Ion Batteries. *Nanoscale* **2019**, *11* (41), 19086–19104. https://doi.org/10.1039/c9nr05748j.

(16) Wagner, M. R.; Raimann, P. R.; Trifonova, A.; Moeller, K. C.; Besenhard, J. O.; Winter, M. Electrolyte Decomposition Reactions on Tin- and Graphite-Based Anodes Are Different. *Electrochem. Solid-State Lett.* **2004**, *7* (7), A201–A205. https://doi.org/10.1149/1.1739312.

(17) Bryngelsson, H.; Stjerndahl, M.; Gustafsson, T.; Edström, K. How Dynamic Is the SEI? *J. Power Sources* **2007**, *174* (2), 970–975. https://doi.org/10.1016/j.jpowsour.2007.06.050.

(18) Wachtler, M.; Besenhard, J. O.; Winter, M. Tin and Tin-Based Intermetallics as New Anode Materials for Lithium-Ion Cells. *J. Power Sources* **2001**, *94* (2), 189–193. https://doi.org/10.1016/S0378-7753(00)00585-1.

(19) Song, S.-W. W.; Baek, S.-W. W. Surface Layer Formation on Sn Anode: ATR FTIR Spectroscopic Characterization. *Electrochim. Acta* **2009**, *54* (4), 1312–1318. https://doi.org/10.1016/j.electacta.2008.09.021.

(20) Naille, S.; Dedryvère, R.; Martinez, H.; Leroy, S.; Lippens, P.-E.; Jumas, J.-C.; Gonbeau, D. XPS Study of Electrode/Electrolyte Interfaces of η-Cu6Sn5 Electrodes in Li-Ion Batteries. *J. Power Sources* **2007**, *174* (2), 1086–1090. https://doi.org/10.1016/j.jpowsour.2007.06.043.

(21) Chamas, M.; Lippens, P.-E.; Jumas, J.-C.; Hassoun, J.; Panero, S.; Scrosati, B. Electrochemical Impedance Characterization of FeSn2 Electrodes for Li-Ion Batteries. *Electrochim. Acta* **2011**, *56* (19), 6732–6736. https://doi.org/10.1016/j.electacta.2011.05.069.

(22) Martin, F.; Morales, J.; Sanchez, L. Elucidating the Beneficial Effect of Vinylene Carbonate on the Electrochemistry of Antimony Electrodes in Lithium Batteries. *CHEMPHYSCHEM* **2008**, *9* (17), 2610–2617. https://doi.org/10.1002/cphc.200800567.

(23) Ehinon, K. K. D.; Naille, S.; Dedryvère, R.; Lippens, P.-E.; Jumas, J.-C.; Gonbeau, D. Ni3Sn4 Electrodes for Li-Ion Batteries: Li-Sn Alloying Process and Electrode/Electrolyte Interface Phenomena. *Chem. Mater.* **2008**, *20* (16), 5388–5398. https://doi.org/10.1021/cm8006099.

(24) Marino, C.; Darwiche, A.; Dupre, N.; Wilhelm, H. A.; Lestriez, B.; Martinez, H.; Dedryvere, R.; Zhang, W.; Ghamouss, F.; Lemordant, D.; Monconduit, L. Study of the Electrode/Electrolyte Interface on Cycling of a Conversion Type Electrode Material in Li Batteries. *J. Phys. Chem. C* **2013**, *117* (38), 19302–19313. https://doi.org/10.1021/jp402973h.

(25) Bridel, J.-S. S.; Grugeon, S.; Laruelle, S.; Hassoun, J.; Reale, P.; Scrosati, B.; Tarascon, J.-M. M. Decomposition of Ethylene Carbonate on Electrodeposited Metal Thin Film Anode. *J. Power Sources* **2010**, *195* (7, SI), 2036–2043. https://doi.org/10.1016/j.jpowsour.2009.10.038.

(26) Shi, F.; Ross, P. N.; Zhao, H.; Liu, G.; Somorjai, G. A.; Komvopoulos, K. A Catalytic Path for Electrolyte Reduction in Lithium-Ion Cells Revealed by in Situ Attenuated Total Reflection-Fourier Transform Infrared Spectroscopy. *J. Am. Chem. Soc.* **2015**, *137* (9), 3181–3184. https://doi.org/10.1021/ja5128456.

(27) Tavassol, H.; Buthker, J. W.; Ferguson, G. A.; Curtiss, L. A.; Gewirth, A. A. Solvent Oligomerization during SEI Formation on Model Systems for Li-Ion Battery Anodes. *J. Electrochem. Soc.* **2012**, *159* (6), A730–A738. https://doi.org/10.1149/2.067206jes.

(28) Madec, L.; Coquil, G.; Ledeuil, J.-B.; Gachot, G.; Monconduit, L.; Martinez, H. How the Binder/Solvent Formulation Impacts the Electrolyte Reactivity/Solid Electrolyte Interphase Formation and Cycling Stability of Conversion Type Electrodes. *J. Electrochem. Soc.* **2020**, *167* (6), 060533. https://doi.org/10.1149/1945-7111/ab861f.

(29) Bodenes, L.; Darwiche, A.; Monconduit, L.; Martinez, H. The Solid Electrolyte Interphase a Key Parameter of the High Performance of Sb in Sodium-Ion Batteries: Comparative X-Ray Photoelectron Spectroscopy Study of Sb/Na-Ion and Sb/Li-Ion Batteries. *J. Power Sources* **2015**, *273*, 14–24. https://doi.org/10.1016/j.jpowsour.2014.09.037.

(30) Chan, C. K.; Ruffo, R.; Hong, S. S.; Cui, Y. Surface Chemistry and Morphology of the Solid Electrolyte Interphase on Silicon Nanowire Lithium-Ion Battery Anodes. *J. Power Sources* **2009**, *189* (2), 1132–1140. https://doi.org/10.1016/j.jpowsour.2009.01.007.

(31) Fransson, L.; Eriksson, T.; Edström, K.; Gustafsson, T.; Thomas, J. O. Influence of Carbon Black and Binder on Li-Ion Batteries. *J. Power Sources* **2001**, *101* (1), 1–9. https://doi.org/10.1016/S0378-7753(01)00481-5.

(32) Jaumann, T.; Balach, J.; Klose, M.; Oswald, S.; Langklotz, U.; Michaelis, A.; Eckert, J.; Giebeler, L. SEI-Component Formation on Sub 5 Nm Sized Silicon Nanoparticles in Li-Ion Batteries: The Role of Electrode Preparation, FEC Addition and Binders. *Phys. Chem. Chem. Phys.* **2015**, *17* (38), 24956–24967. https://doi.org/10.1039/c5cp03672k.

(33) Edström, K.; Herstedt, M.; Abraham, D. P. A New Look at the Solid Electrolyte Interphase on Graphite Anodes in Li-Ion Batteries. *J. Power Sources* **2006**, *153* (2), 380–384. https://doi.org/10.1016/j.jpowsour.2005.05.062.

(34) Madec, L.; Gachot, G.; Coquil, G.; Martinez, H.; Monconduit, L. Toward Efficient Li-Ion Cells at High Temperatures: Example of TiSnSb Material. *J. Power Sources* **2018**, *391*, 51–58. https://doi.org/10.1016/j.jpowsour.2018.04.068.

(35) Aurbach, D.; Weissman, I.; Yamin, H.; Elster, E. The Correlation between Charge/Discharge Rates and Morphology, Surface Chemistry, and Performance of Li Electrodes and the Connection to Cycle Life of Practical Batteries. *J. Electrochem. Soc.* **1998**, *145* (5), 1421–1426. https://doi.org/10.1149/1.1838498.

(36) Tokranov, A.; Kumar, R.; Li, C.; Minne, S.; Xiao, X.; Sheldon, B. W. Control and Optimization of the Electrochemical and Mechanical Properties of the Solid Electrolyte Interphase on Silicon Electrodes in Lithium Ion Batteries. *Adv. Energy Mater.* **2016**, *6* (8), 1–12. https://doi.org/10.1002/aenm.201502302.

(37) Aurbach, D.; Markovsky, B.; Shechter, A.; EinEli, Y.; Cohen, H. A Comparative Study of Synthetic Graphite and Li Electrodes in Electrolyte Solutions Based on Ethylene Carbonate Dimethyl Carbonate Mixtures. *J. Electrochem. Soc.* **1996**, *143* (12), 3809–3820. https://doi.org/10.1149/1.1837300.

(38) Nie, M.; Lucht, B. L. Role of Lithium Salt on Solid Electrolyte Interface (SEI) Formation and Structure in Lithium Ion Batteries. *J. Electrochem. Soc.* **2014**, *161* (6), A1001–A1006. https://doi.org/10.1149/2.054406jes.

(39) Jurng, S.; Brown, Z. L.; Kim, J.; Lucht, B. L. Effect of Electrolyte on the Nanostructure of the Solid Electrolyte Interphase (SEI) and Performance of Lithium Metal Anodes. *Energy Environ. Sci.* **2018**, *11* (9), 2600–2608. https://doi.org/10.1039/c8ee00364e.

(40) Leroy, S.; Martinez, H.; Dedryvère, R.; Lemordant, D.; Gonbeau, D. Influence of the Lithium Salt Nature over the Surface Film Formation on a Graphite Electrode in Li-Ion Batteries: An XPS Study. *Appl. Surf. Sci.* **2007**, *253* (11), 4895–4905. https://doi.org/10.1016/j.apsusc.2006.10.071.

(41) Nguyen, C. C.; Lucht, B. L. Comparative Study of Fluoroethylene Carbonate and Vinylene Carbonate for Silicon Anodes in Lithium Ion Batteries. *J. Electrochem. Soc.* **2014**, *161* (12), A1933–A1938. https://doi.org/10.1149/2.0731412jes.

(42) Yoon, T.; Chapman, N.; Seo, D. M.; Lucht, B. L. Lithium Salt Effects on Silicon Electrode Performance and Solid Electrolyte Interphase (SEI) Structure, Role of Solution Structure on SEI Formation. *J. Electrochem. Soc.* **2017**, *164* (9), A2082–A2088. https://doi.org/10.1149/2.1421709jes.

(43) Jackson, E. D.; Prieto, A. L. Copper Antimonide Nanowire Array Lithium Ion Anodes Stabilized by Electrolyte Additives. *ACS Appl. Mater. Interfaces* **2016**, *8* (44), 30379–30386. https://doi.org/10.1021/acsami.6b08033.

(44) Jin, Y.; Kneusels, N. J. H.; Marbella, L. E.; Castillo-Martínez, E.; Magusin, P. C. M. M.; Weatherup, R. S.; Jónsson, E.; Liu, T.; Paul, S.; Grey, C. P. Understanding Fluoroethylene Carbonate and Vinylene Carbonate Based Electrolytes for Si Anodes in Lithium Ion Batteries with NMR Spectroscopy. *J. Am. Chem. Soc.* **2018**, *140* (31), 9854–9867. https://doi.org/10.1021/jacs.8b03408.

(45) Zhang, W.; Ghamouss, F.; Darwiche, A.; Monconduit, L.; Lemordant, D.; Dedryvère, R.; Martinez, H. Surface Film Formation on TiSnSb Electrodes: Impact of Electrolyte Additives. *J. Power Sources* **2014**, *268*, 645–657. https://doi.org/10.1016/j.jpowsour.2014.06.041.

(46) Aurbach, D.; Daroux, M.; Faguy, P.; Yeager, E. The Electrochemistry of Noble Metal Electrodes in Aprotic Organic Solvents Containing Lithium Salts. *J. Electroanal. Chem.* **1991**, *297* (1), 225–244. https://doi.org/10.1016/0022-0728(91)85370-5.

(47) Moshkovich, M.; Cojocaru, M.; Gottlieb, H. E.; Aurbach, D. The Study of the Anodic Stability of Alkyl Carbonate Solutions by in Situ FTIR Spectroscopy, EQCM, NMR and MS. *J. Electroanal. Chem.* **2001**, *497* (1–2), 84–96. https://doi.org/10.1016/S0022-0728(00)00457-5.

(48) Aurbach, D.; Moshkovich, M.; Cohen, Y.; Schechter, A. The Study of Surface Film Formation on Noble-Metal Electrodes in Alkyl Carbonates/Li Salt Solutions, Using Simultaneous in Situ AFM, EQCM, FTIR, and EIS. *LANGMUIR* **1999**, *15* (8), 2947–2960. https://doi.org/10.1021/la981275j.

(49) Aurbach, D.; Chusid, O. IN-SITU FTIR SPECTROELECTROCHEMICAL STUDIES OF SURFACE-FILMS FORMED ON LI AND NONACTIVE ELECTRODES AT LOW POTENTIALS IN LI SALT-SOLUTIONS CONTAINING CO2. *J. Electrochem. Soc.* **1993**, *140* (11), L155–L157. https://doi.org/10.1149/1.2221034.

(50) Lu, P.; Harris, S. J. Lithium Transport within the Solid Electrolyte Interphase. *Electrochem. Commun.* **2011**, *13* (10), 1035–1037. https://doi.org/10.1016/j.elecom.2011.06.026.

(51) Lu, P.; Li, C.; Schneider, E. W.; Harris, S. J. Chemistry, Impedance, and Morphology Evolution in Solid Electrolyte Interphase Films during Formation in Lithium Ion Batteries. *J. Phys. Chem. C* **2014**, *118* (2), 896–903. https://doi.org/10.1021/jp4111019.

(52) Liu, Z.; Lu, P.; Zhang, Q.; Xiao, X.; Qi, Y.; Chen, L. Q. A Bottom-Up Formation Mechanism of Solid Electrolyte Interphase Revealed by Isotope-Assisted Time-of-Flight Secondary Ion Mass Spectrometry. *J. Phys. Chem. Lett.* **2018**, *9* (18), 5508–5514. https://doi.org/10.1021/acs.jpclett.8b02350.

(53) Zhuo, Z.; Lu, P.; Delacourt, C.; Qiao, R.; Xu, K.; Pan, F.; Harris, S. J.; Yang, W. Breathing and Oscillating Growth of Solid-Electrolyte-Interphase upon Electrochemical Cycling. *Chem. Commun.* **2018**, *54* (7), 814–817. https://doi.org/10.1039/c7cc07082a.

(54) Dedryvère, R.; Laruelle, S.; Grugeon, S.; Gireaud, L.; Tarascon, J.-M. M.; Gonbeau, D. XPS Identification of the Organic and Inorganic Components of the Electrode/Electrolyte Interface Formed on a Metallic Cathode. *J. Electrochem. Soc.* **2005**, *152* (4), A689–A696. https://doi.org/10.1149/1.1861994.

(55) Kuwata, H.; Matsui, M.; Sonoki, H.; Manabe, Y.; Imanishi, N.; Mizuhata, M. Improved Cycling Performance of Intermetallic Anode by Minimized SEI Layer Formation. *J. Electrochem. Soc.* **2018**, *165* (7), A1486–A1491. https://doi.org/10.1149/2.0951807jes.

(56) Sonoki, H.; Matsui, M.; Imanishi, N. Effect of Anion Species in Early Stage of SEI Formation Process. *J. Electrochem. Soc.* **2019**, *166* (15), A3593–A3598. https://doi.org/10.1149/2.0191915jes.

(57) Bozorgchenani, M.; Naderian, M.; Farkhondeh, H.; Schnaid, J.; Uhl, B.; Bansmann, J.; Gross, A.; Behm, R. J.; Buchner, F. Structure Formation and Thermal Stability of Mono- and Multilayers of Ethylene Carbonate on Cu(111): A Model Study of the ElectrodelElectrolyte Interface. *J. Phys. Chem. C* **2016**, *120* (30), 16791–16803. https://doi.org/10.1021/acs.jpcc.6b05012.

(58) Zhang, X. R.; Kostecki, R.; Richardson, T. J.; Pugh, J. K.; Ross, P. N. Electrochemical and Infrared Studies of the Reduction of Organic Carbonates. *J. Electrochem. Soc.* **2001**, *148* (12), A1341–A1345. https://doi.org/10.1149/1.1415547.

(59) Tesfaye, A. T.; Yucel, Y. D.; Barr, M. K. S.; Santinacci, L.; Vacandio, F.; Dumur, F.; Maria, S.; Monconduit, L.; Djenizian, T. The Electrochemical Behavior of SnSb as an Anode for Li-Ion Batteries Studied by Electrochemical Impedance Spectroscopy and Electron Microscopy. *Electrochim. Acta* **2017**, *256*, 155–161. https://doi.org/10.1016/j.electacta.2017.10.031.

(60) Ferraresi, G.; Villevieille, C.; Czekaj, I.; Horisberger, M.; Novak, P.; El Kazzi, M. SnO2 Model Electrode Cycled in Li-Ion Battery Reveals the Formation of Li2SnO3 and Li8SnO6 Phases through Conversion Reactions. *ACS Appl. Mater. Interfaces* **2018**, *10* (10), 8712–8720. https://doi.org/10.1021/acsami.7b19481.

(61) Webb, S. A.; Baggetto, L.; Bridges, C. A.; Veith, G. M. The Electrochemical Reactions of Pure Indium with Li and Na: Anomalous Electrolyte Decomposition, Benefits of FEC Additive, Phase Transitions and Electrode Performance. *J. Power Sources* **2014**, *248*, 1105–1117. https://doi.org/10.1016/j.jpowsour.2013.10.033.

(62) Chiu, K. F.; Lin, H. C.; Lin, K. M.; Lin, T. Y.; Shieh, D. T. The Significant Role of Solid Oxide Interphase in Enhancement of Cycling Performance of Sn Thin-Film Anodes. *J. Electrochem. Soc.* **2006**, *153* (6), A1038–A1042. https://doi.org/10.1149/1.2189246.

(63) Beattie, S. D.; Hatchard, T.; Bonakdarpour, A.; Hewitt, K. C.; Dahn, J. R. Anomalous, High-Voltage Irreversible Capacity in Tin Electrodes for Lithium Batteries. *J. Electrochem. Soc.* **2003**, *150* (6), A701–A705. https://doi.org/10.1149/1.1569477.

(64) Beaulieu, L. Y.; Beattie, S. D.; Hatchard, T. D.; Dahn, J. R. The Electrochemical Reaction of Lithium with Tin Studied by in Situ AFM. *J. Electrochem. Soc.* **2003**, *150* (4), A419–A424. https://doi.org/10.1149/1.1556595.

(65) Inaba, M.; Uno, T.; Tasaka, A. Irreversible Capacity of Electrodeposited Sn Thin Film Anode. *J. Power Sources* **2005**, *146* (1–2, SI), 473–477. https://doi.org/10.1016/j.jpowsour.2005.03.052.

(66) Li, J.-T.; Chen, S.-R.; Fan, X.-Y.; Huang, L.; Sun, S.-G. Studies of the Interfacial Properties of an Electroplated Sn Thin Film Electrode/Electrolyte Using in Situ MFTIRS and EQCM. *LANGMUIR* **2007**, *23* (26), 13174–13180. https://doi.org/10.1021/la701168x.

(67) Hassoun, J.; Reale, P.; Panero, S. The Role of the Interface of Tin Electrodes in Lithium Cells: An Impedance Study. *J. Power Sources* **2007**, *174* (1), 321–327. https://doi.org/10.1016/j.jpowsour.2007.09.046.

(68) Park, S.; Heon Ryu, J.; Oh, S. M. Passivating Ability of Surface Film Derived from Vinylene Carbonate on Tin Negative Electrode. *J. Electrochem. Soc.* **2011**, *158* (5), A498–A503. https://doi.org/10.1149/1.3561424.

(69) Kilibarda, G.; Schlabach, S.; Winkler, V.; Bruns, M.; Hanemann, T.; Szabo, D. V. Electrochemical Performance of Tin-Based Nano-Composite Electrodes Using a Vinylene Carbonate-Containing Electrolyte for Li-Ion Cells. *J. Power Sources* **2014**, *263*, 145–153. https://doi.org/10.1016/j.jpowsour.2014.04.030.

(70) Yang, Z.; Dixon, M. C.; Erck, R. A.; Trahey, L. Quantification of the Mass and Viscoelasticity of Interfacial Films on Tin Anodes Using EQCM-D. *ACS Appl. Mater. Interfaces* **2015**, *7* (48), 26585–26594. https://doi.org/10.1021/acsami.5b07966.

(71) Lucas, I. T.; Syzdek, J.; Kostecki, R. Interfacial Processes at Single-Crystal Beta-Sn Electrodes in Organic Carbonate Electrolytes. *Electrochem. Commun.* **2011**, *13* (11), 1271–1275. https://doi.org/10.1016/j.elecom.2011.08.026.

(72) Qiao, R.; Lucas, I. T.; Karim, A.; Syzdek, J.; Liu, X.; Chen, W.; Persson, K.; Kostecki, R.; Yang, W. Distinct Solid-Electrolyte-Interphases on Sn (100) and (001) Electrodes Studied by Soft X-Ray Spectroscopy. *Adv. Mater. Interfaces* **2014**, *1* (3), 1–6. https://doi.org/10.1002/admi.201300115.

(73) Lucas, I. T.; Pollak, E.; Kostecki, R. In Situ AFM Studies of SEI Formation at a Sn Electrode. *Electrochem. Commun.* **2009**, *11* (11), 2157–2160. https://doi.org/10.1016/j.elecom.2009.09.019.

(74) Ayache, M.; Lux, S. F.; Kostecki, R. IR Near-Field Study of the Solid Electrolyte Interphase on a Tin Electrode. *J. Phys. Chem. Lett.* **2015**, *6* (7), 1126–1129. https://doi.org/10.1021/acs.jpclett.5b00263.

(75) Seo, D. M.; Nguyen, C. C.; Young, B. T.; Heskett, D. R.; Woicik, J. C.; Lucht, B. L. Characterizing Solid Electrolyte Interphase on Sn Anode in Lithium Ion Battery. *J. Electrochem. Soc.* **2015**, *162* (13), A7091–A7095. https://doi.org/10.1149/2.0121513jes.

(76) Bian, X.; Dong, Y.; Zhao, D.; Ma, X.; Qiu, M.; Xu, J.; Jiao, L.; Cheng, F.; Zhang, N. Microsized Antimony as a Stable Anode in Fluoroethylene Carbonate Containing Electrolytes for Rechargeable Lithium-/Sodium-Ion Batteries. *ACS Appl. Mater. Interfaces* **2020**, *12* (3), 3554–3562. https://doi.org/10.1021/acsami.9b18006.

(77) Tian, N.; Hua, C.; Wang, Z.; Chen, L. Reversible Reduction of Li2CO3. *J. Mater. Chem. A* **2015**, *3* (27), 14173–14177. https://doi.org/10.1039/c5ta02499d.

(78) Greczynski, G.; Hultman, L. X-Ray Photoelectron Spectroscopy: Towards Reliable Binding Energy Referencing. *Prog. Mater. Sci.* **2020**, *107*, 100591. https://doi.org/10.1016/j.pmatsci.2019.100591.

(79) Ota, H.; Sakata, Y.; Inoue, A.; Yamaguchi, S. Analysis of Vinylene Carbonate Derived SEI Layers on Graphite Anode. *J. Electrochem. Soc.* **2004**, *151* (10), A1659–A1669. https://doi.org/10.1149/1.1785795.

(80) Schmitz, R.; Mueller, R. A.; Schmitz, R. W.; Schreiner, C.; Kunze, M.; Lex-Balducci, A.; Passerini, S.; Winter, M. SEI Investigations on Copper Electrodes after Lithium Plating with Raman Spectroscopy and Mass Spectrometry. *J. Power Sources* **2013**, *233*, 110–114. https://doi.org/10.1016/j.jpowsour.2013.01.105.

(81) Allcorn, E.; Manthiram, A. Thermal Stability of Sb and Cu2Sb Anodes in Lithium-Ion Batteries. *J. Electrochem. Soc.* **2015**, *162* (9), A1778–A1786. https://doi.org/10.1149/2.0331509jes.

(82) Qin, B.; Jeong, S.; Zhang, H.; Ulissi, U.; Carvalho, D. V.; Varzi, A.; Passerini, S. Enabling Reversible (De)Lithiation of Aluminum by Using Bis(Fluorosulfonyl)Imide-Based Electrolytes. *ChemSusChem* **2019**, *12* (1), 208–212. https://doi.org/10.1002/cssc.201801806.

(83) Li, J.-T. T.; Światowska, J.; Maurice, V.; Seyeux, A.; Huang, L.; Sun, S.-G. G.; Marcus, P. XPS and ToF-SIMS Study of Electrode Processes on Sn-Ni Alloy Anodes for Li-Ion Batteries. *J. Phys. Chem. C* **2011**, *115* (14), 7012–7018. https://doi.org/10.1021/jp201232n.

(84) Yang, Z.; Gewirth, A. A.; Trahey, L. Investigation of Fluoroethylene Carbonate Effects on Tin-Based Lithium-Ion Battery Electrodes. *ACS Appl. Mater. Interfaces* **2015**, *7* (12), 6557–6566. https://doi.org/10.1021/am508593s.

(85) Stjerndahl, M.; Bryngelsson, H.; Gustafsson, T.; Vaughey, J. T.; Thackeray, M. M.; Edström, K. Surface Chemistry of Intermetallic AlSb-Anodes for Li-Ion Batteries. *Electrochim. Acta* **2007**, *52* (15), 4947–4955. https://doi.org/10.1016/j.electacta.2007.01.064.

(86) Hong, S.; Choo, M.-H.; Kwon, Y. H.; Kim, J. Y.; Song, S.-W. Mechanisms for Stable Solid Electrolyte Interphase Formation and Improved Cycling Stability of Tin-Based Battery Anode in Fluoroethylene Carbonate-Containing Electrolyte. *Adv. Mater. INTERFACES* **2016**, *3* (22), 1–9. https://doi.org/10.1002/admi.201600172.

(87) Polat, D. B.; Lu, J.; Abouimrane, A.; Keles, O.; Amine, K. Nanocolumnar Structured Porous Cu-Sn Thin Film as Anode Material for Lithium-Ion Batteries. *ACS Appl. Mater. Interfaces* **2014**, *6* (14), 10877–10885. https://doi.org/10.1021/am405994b.

(88) Philippe, B.; Mahmoud, A.; Ledeuil, J. B.; Sougrati, M. T.; Edström, K.; Dedryvère, R.; Gonbeau, D.; Lippens, P. E. MnSn2 Electrodes for Li-Ion Batteries: Mechanisms at the Nano Scale and Electrode/Electrolyte Interface. *Electrochim. Acta* **2014**, *123*, 72–83. https://doi.org/10.1016/j.electacta.2014.01.010.

(89) Li, J.-T. T.; Swiatowska, J.; Seyeux, A.; Huang, L.; Maurice, V.; Sun, S.-G. G.; Marcus, P. XPS and ToF-SIMS Study of Sn – Co Alloy Thin Films as Anode for Lithium Ion Battery. *J. Power Sources* **2010**, *195* (24, SI), 8251–8257. https://doi.org/10.1016/j.jpowsour.2010.07.043.

(90) Shieh, D. T.; Yin, J. T.; Yamamoto, K.; Wada, M.; Tanase, S.; Sakai, T. Surface Characterization on Lithium Insertion/Deinsertion Process for Sputter-Deposited AgSn Thin-Film Electrodes by XPS. *J. Electrochem. Soc.* **2006**, *153* (1), A106–A112. https://doi.org/10.1149/1.2133711.

(91) Choo, M.-H.; Nguyen, C. C.; Hong, S.; Kwon, Y. H.; Woo, S.-W.; Kim, J. Y.; Song, S.-W. Combination of Acid-Resistor and -Scavenger Improves the SEI Stability and Cycling Ability of Tin-Nickel Battery Anodes in LiPF6-Containing Electrolyte. *Electrochim. Acta* **2013**, *112*, 252–257. https://doi.org/10.1016/j.electacta.2013.08.121.

(92) Mahmoud, A.; Chamas, M.; Lippens, P.-E. Electrochemical Impedance Study of the Solid Electrolyte Interphase in MnSn2 Based Anode for Li-Ion Batteries. *Electrochim. Acta* **2015**, *184*, 387–391. https://doi.org/10.1016/j.electacta.2015.10.078.

(93) Chamas, M.; Lippens, P.-E.; Jumas, J.-C.; Boukerma, K.; Dedryvere, R.; Gonbeau, D.; Hassoun, J.; Panero, S.; Scrosati, B. Comparison between Microparticles and Nanostructured Particles of FeSn2 as Anode Materials for Li-Ion Batteries. *J. Power Sources* **2011**, *196* (16, SI), 7011–7015. https://doi.org/10.1016/j.jpowsour.2010.09.113.

(94) Li, H.; Shi, L. H.; Lu, W.; Huang, X. J.; Chen, L. Q. Studies on Capacity Loss and Capacity Fading of Nanosized SnSb Alloy Anode for Li-Ion Batteries. *J. Electrochem. Soc.* **2001**, *148* (8), A915–A922. https://doi.org/10.1149/1.1383070.

(95) Alcantara, R.; Fernandez-Madrigal, F. J.; Lavela, P.; Tirado, J. L.; Jumas, J. C.; Olivier-Fourcade, J. Electrochemical Reaction of Lithium with the CoSb3 Skutterudite. *J. Mater. Chem.* **1999**, *9* (10), 2517–2521. https://doi.org/10.1039/a902060h.

(96) Dedryvère, R.; Gireaud, L.; Grugeon, S.; Laruelle, S.; Tarascon, J. M.; Gonbeau, D. Characterization of Lithium Alkyl Carbonates by X-Ray Photoelectron Spectroscopy: Experimental and Theoretical Study. *J. Phys. Chem. B* **2005**, *109* (33), 15868–15875. https://doi.org/10.1021/jp051626k.

(97) Song, S. W.; Reade, R. P.; Cairns, E. J.; Vaughey, J. T.; Thackeray, M. M.; Striebel, K. A. Cu2Sb Thin-Film Electrodes Prepared by Pulsed Laser Deposition for Lithium Batteries. *J. Electrochem. Soc.* **2004**, *151* (7), A1012–A1019. https://doi.org/10.1149/1.1758719.

(98) Huo, H.; Chamas, M.; Lippens, P.-E.; Menetrier, M. Multinuclear NMR Study of the Solid Electrolyte Interface on the Li-FeSn2 Negative Electrodes for Li-Ion Batteries. *J. Phys. Chem. C* **2012**, *116* (3, SI), 2390–2398. https://doi.org/10.1021/jp210017b.

(99) Courtney, I. A.; Dahn, J. R. Key Factors Controlling the Reversibility of the Reaction of Lithium with SnO2 and Sn2BPO6 Glass. *J. Electrochem. Soc.* **1997**, *144* (9), 2943–2948. https://doi.org/10.1149/1.1837941.

(100) Wang, Y.; Sakamoto, J.; Huang, C.; Surampudi, S.; Greenbaum, S. G. Lithium-7 NMR Investigation of Electrochemical Reaction of Lithium with SnO. *SOLID STATE IONICS* **1998**, *110* (3–4), 167–172. https://doi.org/10.1016/S0167-2738(98)00147-7.

(101) Dedryvère, R.; Laruelle, S.; Grugeon, S.; Poizot, P.; Gonbeau, D.; Tarascon, J. M. Contribution of X-Ray Photoelectron Spectroscopy to the Study of the Electrochemical Reactivity of CoO toward Lithium. *Chem. Mater.* **2004**, *16* (6), 1056–1061. https://doi.org/10.1021/cm0311269.

(102) Chamas, M.; Mahmoud, A.; Tang, J.; Sougrati, M. T.; Panero, S.; Lippens, P.-E. E. Aging Processes in Lithiated FeSn2 Based Negative Electrode for Li-Ion Batteries: A New Challenge for Tin Based Intermetallic Materials. *J. Phys. Chem. C* **2017**, *121* (1), 217–224. https://doi.org/10.1021/acs.jpcc.6b11302.

(103) Madec, L.; Ledeuil, J.-B.; Coquil, G.; Gachot, G.; Monconduit, L.; Martinez, H. Cross-Section Auger Imaging: A Suitable Tool to Study Aging Mechanism of Conversion Type Electrodes. *J. Power Sources* **2019**, *441*, 227213. https://doi.org/10.1016/j.jpowsour.2019.227213.

(104) Schulze, M. C.; Belson, R. M.; Kraynak, L. A.; Prieto, A. L. Electrodeposition of Sb/CNT Composite Films as Anodes for Li- and Na-Ion Batteries. *ENERGY STORAGE Mater.* **2020**, *25*, 572–584. https://doi.org/10.1016/j.ensm.2019.09.025.

(105) Kraynak, L. A.; Schneider, J. D.; Prieto, A. L. Exploring the Role of Vinylene Carbonate in the Passivation and Capacity Retention of Cu_2Sb Thin Film Anodes. *Submitt. to J. Phys. Chem. C* **2020**.

(106) Ulus, A.; Rosenberg, Y.; Burstein, L.; Peled, E. Tin Alloy-Graphite Composite Anode for Lithium-Ion Batteries. *J. Electrochem. Soc.* **2002**, *149* (5), A635–A643. https://doi.org/10.1149/1.1469029.

(107) Shkrob, I. A.; Wishart, J. F.; Abraham, D. P. What Makes Fluoroethylene Carbonate Different? *J. Phys. Chem. C* **2015**, *119* (27), 14954–14964. https://doi.org/10.1021/acs.jpcc.5b03591.

(108) Zhang, W.; Ghamouss, F.; Mery, A.; Lemordant, D.; Dedryvere, R.; Monconduit, L.; Martinez, H. Improvement of the Stability of TiSnSb Anode under Lithiation Using SEI Forming Additives and Room Temperature Ionic Liquid/DMC Mixed Electrolyte. *Electrochim. Acta* **2015**, *170*, 72–84. https://doi.org/10.1016/j.electacta.2015.04.009.

(109) Chan, A. K.; Tatara, R.; Feng, S.; Karayaylali, P.; Lopez, J.; Stephens, I. E. L.; Shao-Horn, Y. Concentrated Electrolytes for Enhanced Stability of Al-Alloy Negative Electrodes in Li-Ion Batteries. *J. Electrochem. Soc.* **2019**, *166* (10), A1867–A1874. https://doi.org/10.1149/2.0581910jes.

(110) Mosby, J. M.; Prieto, A. L. Direct Electrodeposition of Cu_2Sb for Lithium-Ion Battery Anodes. *J. Am. Chem. Soc.* **2008**, *130* (32), 10656–10661. https://doi.org/10.1021/ja801745n.

(111) Lahiri, A.; Endres, F. Review — Electrodeposition of Nanostructured Materials from Aqueous , Organic and Ionic Liquid Electrolytes for Li-Ion and Na-Ion Batteries : A Comparative Review. *J. Electrochem. Soc.* **2017**, *164* (9), D597–D612. https://doi.org/10.1149/2.1011709jes.

(112) Ma, J.; Prieto, A. L. Understanding the Electrodeposition of Pure Phase SnSb from Deep Eutectic Ethaline Solution and Its Application as a Lithium-Ion Anode. *unpublished* **2020**.

(113) Dupré, N.; Moreau, P.; De Vito, E.; Quazuguel, L.; Boniface, M.; Bordes, A.; Rudisch, C.; Bayle-Guillemaud, P.; Guyomard, D. Multiprobe Study of the Solid Electrolyte Interphase on Silicon-Based Electrodes in Full-Cell Configuration. *Chem. Mater.* **2016**, *28* (8), 2557–2572. https://doi.org/10.1021/acs.chemmater.5b04461.

(114) Gilbert, J. A.; Shkrob, I. A.; Abraham, D. P. Transition Metal Dissolution, Ion Migration, Electrocatalytic Reduction and Capacity Loss in Lithium-Ion Full Cells. *J. Electrochem. Soc.* **2017**, *164* (2), A389–A399. https://doi.org/10.1149/2.1111702jes.

(115) Bjorklund, E.; Brandell, D.; Hahlin, M.; Edstrom, K.; Younesi, R. How the Negative Electrode Influences Interfacial and Electrochemical Properties of LiNi1/3Co1/3Mn1/3O2 Cathodes in Li-Ion Batteries. *J. Electrochem. Soc.* **2017**, *164* (13), A3054–A3059. https://doi.org/10.1149/2.0711713jes.

(116) Sahore, R.; Dogan, F.; Bloom, I. D. Identification of Electrolyte-Soluble Organic Cross-Talk Species in a Lithium-Ion Battery via a Two-Compartment Cell. *Chem. Mater.* **2019**, *31* (8), 2884–2891. https://doi.org/10.1021/acs.chemmater.9b00063.

(117) Joshi, T.; Eom, K.; Yushin, G.; Fuller, T. F. Effects of Dissolved Transition Metals on the Electrochemical Performance and SEI Growth in Lithium-Ion Batteries. *J. Electrochem. Soc.* **2014**, *161* (12), A1915–A1921. https://doi.org/10.1149/2.0861412jes.

(118) Solchenbach, S.; Hong, G.; Freiberg, A. T. S.; Jung, R.; Gasteiger, H. A. Electrolyte and SEI Decomposition Reactions of Transition Metal Ions Investigated by On-Line Electrochemical Mass Spectrometry. *J. Electrochem. Soc.* **2018**, *165* (14), A3304–A3312. https://doi.org/10.1149/2.0511814jes.

(119) Vissers, D. R.; Chen, Z.; Shao, Y.; Enselhard, M.; Das, U.; Redfern, P.; Curtiss, L. A.; Pang, B.; Liu, J.; Amine, K. Role of Manganese Deposition on Graphite in the Capacity Fading of Lithium Ion Batteries. *ACS Appl. Mater. Interfaces* **2016**, *8* (22), 14244–14251. https://doi.org/10.1021/acsami.6b02061.

(120) Komaba, S.; Kumagai, N.; Kataoka, Y. Influence of Manganese(II), Cobalt(II), and Nickel(II) Additives in Electrolyte on Performance of Graphite Anode for Lithium-Ion Batteries. *Electrochim. Acta* **2002**, *47* (8), 1229–1239. https://doi.org/10.1016/S0013-4686(01)00847-7.

(121) Delacourt, C.; Kwong, A.; Liu, X.; Qiao, R.; Yang, W. L.; Lu, P.; Harris, S. J.; Srinivasan, V. Effect of Manganese Contamination on the Solid-Electrolyte-Interphase Properties in Li-Ion Batteries. *J. Electrochem. Soc.* **2013**, *160* (8), A1099–A1107. https://doi.org/10.1149/2.035308jes.

CHAPTER 2: CONSIDERATIONS FOR SOLID ELECTROLYTE INTERFACE SAMPLE PREPARATION AND X-RAY PHOTOELECTRON SPECTROSCOPY CHARACTERIZATION[♣]

Chapter Summary

Solid electrolyte interface (SEI) formation is sensitive to many variables that can be observed through characterization techniques such as differential capacity analysis and X-ray photoelectron spectroscopy (XPS). Here we present some examples of important considerations for SEI sample preparation and XPS characterization based on our results, including replicate samples, contamination, rest time, and representative data. We discuss the importance of small details when it comes to preparing and characterizing SEI samples, especially when using surface-sensitive techniques such as XPS.

2.1) Introduction

The solid electrolyte interface (SEI) forms on electrode surfaces due to the instability of the electrolyte over the large operating potential windows of Li-ion rechargeable batteries.[1,2] It is a necessary battery component in the sense that a stable SEI layer helps passivate the electrode surface and allows the battery to function by limiting excessive electrolyte degradation, preventing electrode corrosion, and allowing for the transport of Li^+.[3,4] An SEI that meets these three criteria and has other desirable properties such as good mechanical stability help extend the battery lifetime. However, it also can play a detrimental role in battery performance, affecting the irreversible capacity and lithium consumption, capacity retention, cycling rate, and safety.[3,4] Decades of research have been devoted to studying the SEI in hopes of better understanding the role that SEI components and structure play in the

[♣] This chapter was prepared as a manuscript to be submitted to the American Chemical Society *Journal of Applied Energy Materials* for peer review and publication with Leslie A. Kraynak and Amy L. Prieto as the authors. Leslie A. Kraynak wrote the manuscript and Amy L. Prieto provided guidance and helped with editing.

SEI properties and cell performance, with the aim of being better able to control the formation and improve the properties of the SEI.[3] However, studying the SEI is difficult for a number of reasons, which has prevented major breakthroughs towards the aims described above.

One reason studying the SEI is so challenging is that SEI formation and composition are affected by a variety of factors. Since the SEI is composed of electrolyte reduction species, electrolyte components such as the solvent, supporting electrolyte salt, additives, and contaminants play a major role in the formation, composition, and morphology of the SEI.[5–13] The electrodes also play a role, as the reactivity of the active material, the use of binders and additives, and the electrode preparation method have also been demonstrated to affect the SEI.[14–23] Finally, the cycling conditions used, such as temperature, cycling rate, and potential limits also play a role.[4,24–27] Due to all of these factors, there are many differing, and sometimes conflicting, reports on the composition of the SEI depending on the systems and conditions used for SEI formation.[4] As a result, it is difficult to determine which variable results in the observed battery performance, and it is difficult to develop synthetic design rules for improving the SEI.

In addition to the multitude of variables, another reason studying the SEI is so challenging is because it is complex and heterogenous structure and typically requires the use of multiple complementary characterization techniques in order to gain a complete representation of the SEI. While many research efforts have been focused on developing in-situ techniques for studying the SEI,[28] post-mortem and ex-situ techniques are still used for most SEI characterization since they are the most readily accessible. Some of the techniques that have been employed to better understand the SEI composition and structure include X-ray photoelectron spectroscopy (XPS), IR spectroscopy, solid state NMR, mass spectrometry, and electron microscopy, while techniques such as atomic force microscopy, electrochemical impedance spectroscopy, cyclic voltammetry, and differential capacity analysis have been used to study the formation and properties of the SEI.[4,29]

While there is no single technique capable of comprehensively characterizing the SEI, XPS has been and remains one of the most widely used SEI characterization techniques for several reasons.[4,30] It is surface sensitive, which makes it useful for studying interfaces such as the SEI, but it can also be used in conjunction with depth profiling via ion sputtering to gain information about thicker SEI layers.[4] Additionally, XPS provides information on different species present in the SEI through binding energy shifts of high-resolution core spectra as well as quantitative (or semi-quantitative) information about the composition of the SEI.[4,30]

Given the complex nature of the SEI, studying it requires a multidisciplinary approach, and the SEI community consists of researchers from many different backgrounds including materials science, chemistry, and engineering. However, because the field is so multidisciplinary, there can often be a lack of consistency in terms of research protocols and reporting experimental details in the field. Because the SEI is so sensitive to many different variables and because much of the characterization is done ex-situ, the details of sample preparation and characterization are very important. Unfortunately, they do not often get discussed in much detail, which can make it difficult to compare results and draw conclusions from the literature.

In this paper we will discuss some of the factors that are important for preparing samples and studying the SEI composition with XPS, some of which were quite unexpected and warrant discussion. Often factors that don't seem to be that important can notably affect the results and how they are interpreted. While the focus of this paper is on the characterization of the SEI formed on binder- and additive-free thin film anodes, we expect that our findings can be extended to composite electrodes as well. Additionally, while we focus on XPS characterization, for which this level of detail is important due to the surface sensitive nature of the characterization method, some of our observations may be relevant to other characterization techniques as well. This paper is not intended to be a comprehensive list of all of the important considerations for sample preparation and XPS characterization, but we hope

that it can serve as a resource for others in the field, both new and experienced. We hope that it will also encourage the discussion of the importance of attention to detail in sample preparation and characterization and the importance of discussing those details in published works so that others can be made aware in order to help further advance the field.

2.2) Experimental

Some of the experimental conditions for sample preparation and characterization were varied, and the complete relevant experimental details will be provided in Appendix A and in the Results and Discussion section where appropriate. Samples have been given generic names with number and letter designations such that two comparable samples (i.e. prepared using the same variables and often from the same Cu_2Sb film) will be named with different numbers and the same letter (e.g. Sample 1a and Sample 2a). With this sample naming convention, two samples that were prepared using the same conditions such as electrolyte, potential limits, cycling rate and are being compared to each other are named using the same letter and a different number (such as Samples 1a and 2a or Samples 1b and 2b in Table A1 of Appendix A). When two samples cycled using slightly different conditions are being compared, the samples are named using different letters and the same number (such as Samples 1f and 1g in Table A1, which were prepared without and with 5% VC additive, respectively). The experimental details described in this section are an overview of the procedures relevant to all results discussed in this paper.

Electrode preparation

Copper antimonide (Cu_2Sb) thin film electrodes were electrodeposited onto Cu substrates (110 Cu foil, 0.002-in thick, McMaster-Carr, cleaned by electropolishing in a 2:1 by volume H_3PO_4/H_2O solution) following an established procedure.[31] Briefly, Cu_2Sb was electrodeposited at −1.05 V versus a saturated calomel electrode (SCE) from an aqueous (Millipore 18 MΩ) solution of 80 mM copper (II) nitrate hemipentahydrate ($Cu(NO_3)_2 \cdot 2.5\ H_2O$, Aldrich >99.99%+), 25 mM antimony (III) oxide

nanopowder (Sb_2O_3, <250 nm, Aldrich ≥99.99%), and 400 mM citric acid monohydrate (Fischer Scientific, certified ACS grade) adjusted to a pH of 6 with saturated potassium hydroxide (KOH, Fischer Scientific, certified ACS grade). All films were electrodeposited for 600 s at room temperature unless otherwise noted. The average mass loading of the Cu_2Sb films, determined by mass difference, was 0.9 mg/cm^2. Half-inch diameter circular punches were made from the films for use in half-cells (average 1.2 mg Cu_2Sb per punch).

Half-cell preparation and cycling

Swagelok half cells were prepared in an Ar-filled glovebox (O_2<1 ppm) using the Cu_2Sb punches as the working electrode, Li metal foil as the counter/pseudo reference electrode, and a glass fiber filter (Whatman GF/A) layered between two polypropylene films (Celgard, 25 μm) as the separators. The cleaning procedure used for cell parts is described in Appendix A. The electrolyte (200 μL per half-cell) was 1 M lithium perchlorate ($LiClO_4$, Aldrich, 99.999% battery grade) in a mixture of ethylene carbonate (EC, Aldrich, 99% anhydrous, recrystallized from ethanol), dimethyl carbonate (DMC, Aldrich, ≥99% anhydrous), and diethyl carbonate (DEC, Aldrich, ≥99% anhydrous) (1:1:1 by volume) with or without 5% (by volume) vinylene carbonate (VC, Aldrich 99% with 80 ppm butylated hydroxytoluene added as stabilizer) added, unless otherwise noted. Half cells were cycled galvanostatically at a C/20 rate (average 19 μA/cm^2) using an Arbin BT-2143 battery tester. Various potential limits and cycle times were used; please refer to Table A1 in Appendix 1 for complete details. In this work, discharging refers to a negative applied current and reduction/lithiation of the working electrode, and charging refers to a positive applied current and oxidation/delithiation of the working electrode.

X-ray photoelectron spectroscopy characterization

X-ray photoelectron spectroscopy characterization was performed on a Physical Electronics (PHI) 5800 series Multi-technique ESCA system with Al Kα (hν = 1486.6 eV) monochromatized radiation source operating at 350.0 W. Most samples were transferred under vacuum directly from the Ar-filled

glovebox (O_2<1 ppm) to the XPS sample introduction chamber using a custom-built sample holder so that air exposure prior to XPS characterization was minimized.[32] An electron flood gun operating with a 5 μA emission current, 1.5 V bias voltage, and 40.0 V extractor voltage was used for charge neutralization on all SEI samples. Survey spectra were collected with a pass energy of 187.85 eV in intervals of 1.6 eV/step. High resolution (HRES) spectra for the elements of interest were collected with a pass energy of 23.5 eV in intervals of 0.100 eV/step. Spectra were collected from at least 3 areas on each sample (area 126.7 mm^2) using a 0.6 mm by 2 mm analysis area (area 1.2 mm^2) to ensure that any lateral heterogeneity in the SEI was accounted for. Short HRES scans were collected prior to the longer acquisitions so that any sample damage could be identified, although even the longer HRES scans were relatively short (20–30 minutes) to avoid prolonged beam exposure and possible sample damage.[30] When appropriate, HRES spectra were shifted for charge correction so that the Cl $2p_{3/2}$ peak for ClO_4^- species in the SEI was located at 208.6 eV. CasaXPS software (Version 2.3.16) was used for peak fitting and quantification of the HRES spectra. A nonlinear Shirley background and 30% Lorentzian/70% Gaussian line shape were used for peak fitting, and PHI relative sensitivity factors corrected for angular distribution were used for quantification based on the peak fitting. The fitted spectra and tabulated fitting data for the SEI samples discussed in this chapter can be found in Figures A1–A7 and Tables A2–A8, respectively.

2.3) Results and Discussion

2.3.1) Sample preparation

Replicate samples and differential capacity analysis

The SEI is a notoriously complex structure that is difficult to form in a controlled manner and challenging to characterize, as described above. As such, it can be difficult to know that the SEI sample being characterized is a reasonable representative sample. Because SEI formation can be so variable and sensitive to a variety of factors, it is important to make and study multiple replicate samples to get the

fullest and most accurate representation of the SEI possible. Additionally, because of this extreme variability and sensitivity, sometimes two samples prepared the same way can show different results. For example, the surfaces of two SEI samples prepared under the same conditions in terms of electrolyte formulation, cycling rate, and potential limits may show variations in terms of different relative atomic compositions or different species based on XPS characterization. In particular, we have observed this for SEI layers formed on binder- and additive-free electrodes fabricated by electrodeposition, which can sometimes show some variability across a film surface in terms of native oxide content or can show some variability in composition over time, especially when electrodeposited on Cu substrates. However, this is also relevant to composite electrodes where materials are mixed by ball milling or ground in a mortar and pestle for electrode fabrication, as these methods can introduce contaminants or result in uneven or incomplete mixing, respectively, which could affect results of "replicate" electrode/SEI samples.[33] Since the SEI formation process is sensitive to a number of variables, including electrode surface heterogeneity, it is helpful to have a method such as differential capacity analysis to evaluate differences in SEI formation processes prior to ex situ characterization.

Electrochemical techniques such as cyclic voltammetry and differential capacity analysis are useful for understanding SEI formation processes. While cyclic voltammetry is more commonly employed in studying SEI electrochemistry because the information it provides is limited to processes occurring at the electrode surface, differential capacity analysis offers the advantage of information about SEI formation during galvanostatic cell cycling. One of the drawbacks to differential capacity analysis is that features corresponding to SEI formation/dissolution at electrode lithiation/delithiation potentials are usually obscured. However, at higher potentials where initial SEI formation occurs, it is possible to see features associated with processes occurring at the electrode surface by narrowing in on the differential capacity analysis plots to see the low intensity features associated with electrolyte

reduction. This portion of the differential capacity analysis plot can serve as a useful tool for comparing SEI formation between different samples.

Figure 2.1a shows the differential capacity analysis plots of two Cu_2Sb thin film samples cycled between 1.8 and 3.0 V vs. Li/Li^+ where some SEI formation but no Cu_2Sb lithiation/delithiation is occurring. The half-cells were prepared from punches of different Cu_2Sb films, but both were prepared in the same way and had similar active material mass loadings of ca. 0.9 mg/cm^2. Despite being prepared the same way and cycled under the same conditions, the differential capacity plot features of the two samples show some differences. The differential capacity plot of Sample 1a is mostly featureless with the exception of the onset of a reduction feature around 2.1 V vs. Li/Li^+ on the first cycle. In contrast, the differential capacity plot of Sample 2a, prepared the same way as Sample 1a, shows a reduction feature around 1.9 V vs. Li/Li^+ and the onset of an oxidation feature around 2.8 V vs. Li/Li^+ on the first cycle as well as a low intensity reduction feature around 2.6 V vs. Li/Li^+ for multiple cycles.

The SEI formation processes for Samples 1a and 2a seem to be quite different based on the differential capacity analysis despite being prepared the same way, and the SEI surface composition based on XPS characterization also reveals that the SEI composition for the two samples is quite different, as shown in Figure 2.1b. The Sample 1a SEI is quite uniform, with similar compositions for multiple analysis regions, whereas the Sample 2a SEI appears to be more heterogeneous. The Sample 1a SEI is very carbon-rich, consisting of 65–70% C compared to 50–55% for Sample 2a. Unlike the Sample 1a SEI, which only has 2–4% Cl present as ClO_4^- species, the Sample 2a SEI has 6–8% Cl due to ClO_4^-. Additionally, ca. 8% Li was consistently detected across different regions of Sample 1a, but Li was only detected in one of three analysis regions for Sample 2a. Finally, while a small amount of Sb was detected for both samples, Cu was only detected in Sample 2a.

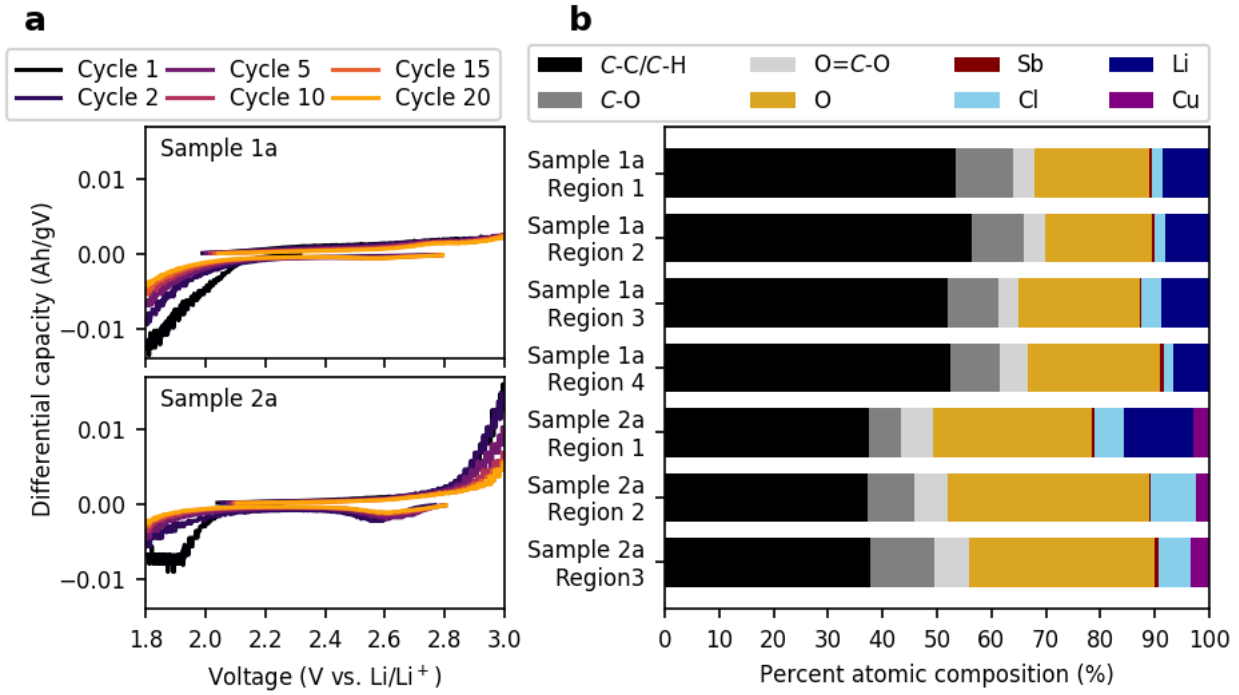

Figure 2.1: Differential capacity analysis plots for two Cu_2Sb thin film samples prepared and cycled under the same conditions (a) and the percent atomic compositions for multiple analysis regions of the two samples based on XPS characterization (b).

Although these two samples were prepared in the same way, qualitatively they are not replicate samples based on the differential capacity analysis and the XPS quantification results. One could draw very different conclusions about the SEI formed on Cu_2Sb over this potential region depending on which sample was used, so it emphasizes the importance of looking at multiple samples to ensure that they are representative of the SEI. It also demonstrates the utility of differential capacity analysis as a tool for comparing SEI samples prior to ex-situ characterization. In this scenario, the SEIs were quite thin due to being formed over a potential region that precluded Cu_2Sb lithiation, allowing for some small amount of correlation between differences observed in the differential capacity analysis and XPS results. Typically, the SEI layers being formed are much thicker, so this is not likely to be the case for many samples, but differential capacity analysis can still be used to determine whether a sample is worth the time and effort of further characterization. Additionally, this example demonstrates just how sensitive the SEI can be to different variables since both samples were prepared keeping almost all variables the same (the

only differences were that the different Cu_2Sb films prepared from different electrodeposition solutions and two different batches of the same electrolyte solution were used). There are a couple of hypotheses as to why the results from these two samples prepared the same way may have been different. The differences observed in the results from differential capacity analysis and XPS characterization may have been due to differences in the amount of surface oxides present on the different Cu_2Sb films used, as there have been other studies suggesting that surface oxides may play a role in SEI formation and composition.[15,17,34] Another hypothesis is that the observed differences were due to changes in some other variable that were not accounted for, such as the atmosphere in the Ar glovebox where samples were prepared or in the XPS analysis chamber where samples were characterized, that could have affected the SEI. It is not clear whether these differences would be notable with less surface sensitive characterization techniques, but it is certainly important to consider for XPS characterization.

The approach we use to determine whether two SEI samples are replicates is a qualitative approach that is based on notable differences in the features of the differential capacity analysis plots and HRES XPS spectra features and quantification, as described above. However, the main criterion we use for whether two samples are qualitatively the same or not is whether the same conclusions about the SEI could be drawn from data from two different SEI samples. Unfortunately it is not clear how often replicate SEI samples are studied in general, as the number of samples analyzed are rarely reported in the literature,[35,36] and when it is reported, there is not much detail provided about the results from the replicate samples and the criteria used to evaluate them.[35] This is one area where members of the SEI community could provide more detail into the procedures used for the preparation and evaluation of samples.

Contamination

Contamination is one of the major factors influencing the formation, composition, and stability of the SEI. In the SEI research community, contamination is most often thought of in terms of water

content in electrolyte solutions, which can affect SEI formation.[37] Additionally, commonly used salts such as $LiPF_6$ and $LiBF_4$ are particularly moisture sensitive, reacting with water to form HF, which can affect SEI composition and stability.[5] Another type of contamination commonly considered in this community is exposure to air prior to characterization, which can alter the SEI composition due to the SEI containing many species that are sensitive to moisture and oxygen, and as such precautions are taken to avoid air exposure prior to SEI characterization.[26,38,39] Additionally, in terms of XPS characterization, contamination from adventitious carbon is usually unavoidable, even with very careful sample handling and even under ultra-high vacuum conditions.[40,41] While these are common sources of sample contamination that are often considered for SEI studies, we have discovered other sources that may not be anticipated, as described below.

The following example illustrates several things: 1) the importance of thoroughly cleaning cell parts (but more generally the importance of being meticulous when preparing SEI samples), 2) the utility of differential capacity for evaluating the early stages of SEI formation, and 3) the sensitivity of both SEI formation and XPS characterization to contaminants in a system. Figure 2.2 shows the differential capacity plots of the first two cycles of replicate Cu_2Sb samples cycled galvanostatically between 1.8 and 3.0 V vs. Li/Li^+ in 1 M $LiClO_4$ in EC/DEC/DMC (1:1:1 vol) with 5% VC electrolyte. The two show considerably different features in the differential capacity analysis plots. On the first cycle discharge of Sample 1b, there is a reduction peak at approximately 2.1 V vs Li/Li^+ and the onset of another reduction peak around 2.0 V vs Li/Li^+; there is also an oxidation peak at 2.7 V vs Li/Li^+ that is seen for both the first and second cycles. In contrast, the differential capacity plots of replicate Sample 2b are relatively featureless in comparison, with only the onset of a reduction peak near 2.0 V vs Li/Li^+ for the first and second cycles. These differences in the differential capacity plots of replicate samples suggest differences in SEI formation.

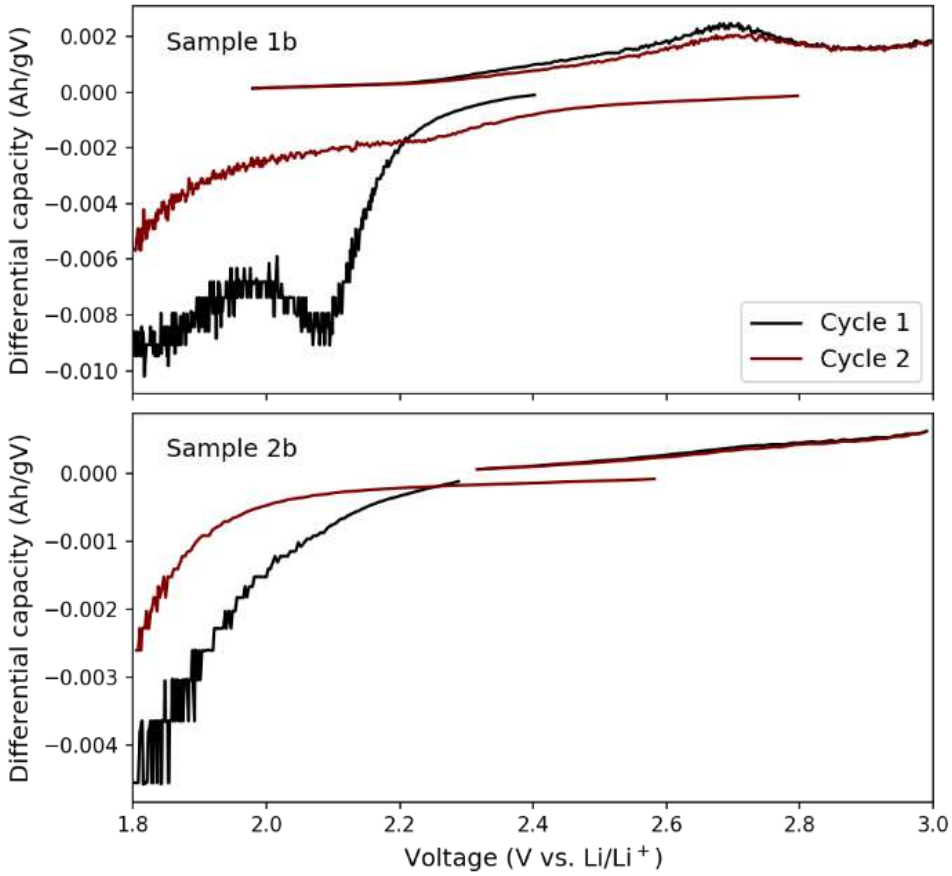

Figure 2.2: Differential capacity analysis plots for two Cu_2Sb samples prepared and cycled the same way showing different features due to contamination of Sample 1b (top).

The XPS survey spectra of the sample surfaces also reveal considerable differences in the composition of the SEIs formed on the two samples (representative survey spectra are shown in Figure 2.3). Based on the survey spectra, carbon, oxygen, and small amounts of chlorine, copper, and antimony were detected for both samples. However, Sample 1b, which showed more reduction and oxidation peaks in the differential capacity plots than Sample 2b over the first two cycles, also has fluorine on the surface, even though the electrolyte used to cycle both Samples 1 and 2 contained no fluorinated species such as $LiPF_6$ or FEC. Fluorine was detected on the surface of all three regions of Sample 1b that were characterized with XPS (although data from only one region is shown in Figure 2.3 for clarity), suggesting that much of the sample surface was contaminated with fluorine.

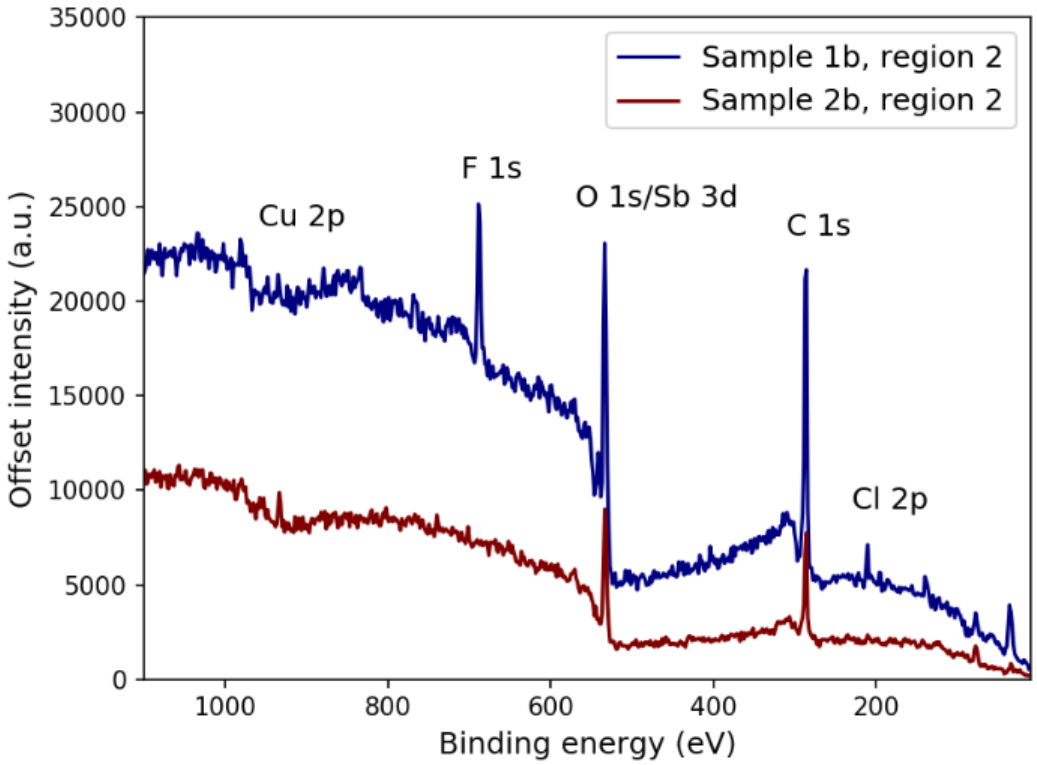

Figure 2.3: Representative XPS survey spectra for the contaminated (Sample 1b) and uncontaminated (Sample 2b) SEI samples.

High resolution (HRES) XPS spectra for different regions of Samples 1b and 2b were collected, and quantitative peak fitting analysis was performed to gain information about the compositions of the SEI surfaces formed on the two samples. The fluorine contamination in Sample 1b is considerable, with fluorine composing about 10% of the surface for all three analysis regions as shown in Figure 2.4. The fluorine contaminant, likely $LiPF_6$ or $LiPF_6$ degradation products,[5,26,39] was most likely introduced prior to cycling and SEI formation rather than after because other samples disassembled and prepared for characterization at the same time as Sample 1b did not contain fluorine based on XPS characterization. The only possible source of contamination prior to cycling, considering samples from other half cells prepared at the same time using the same materials (electrodeposited thin films, separators, lithium foil, and electrolyte) did not show evidence of contamination, is from improperly cleaned polytetrafluoroethylene (PTFE) Swagelok cell parts, which may have contained residual fluorinated

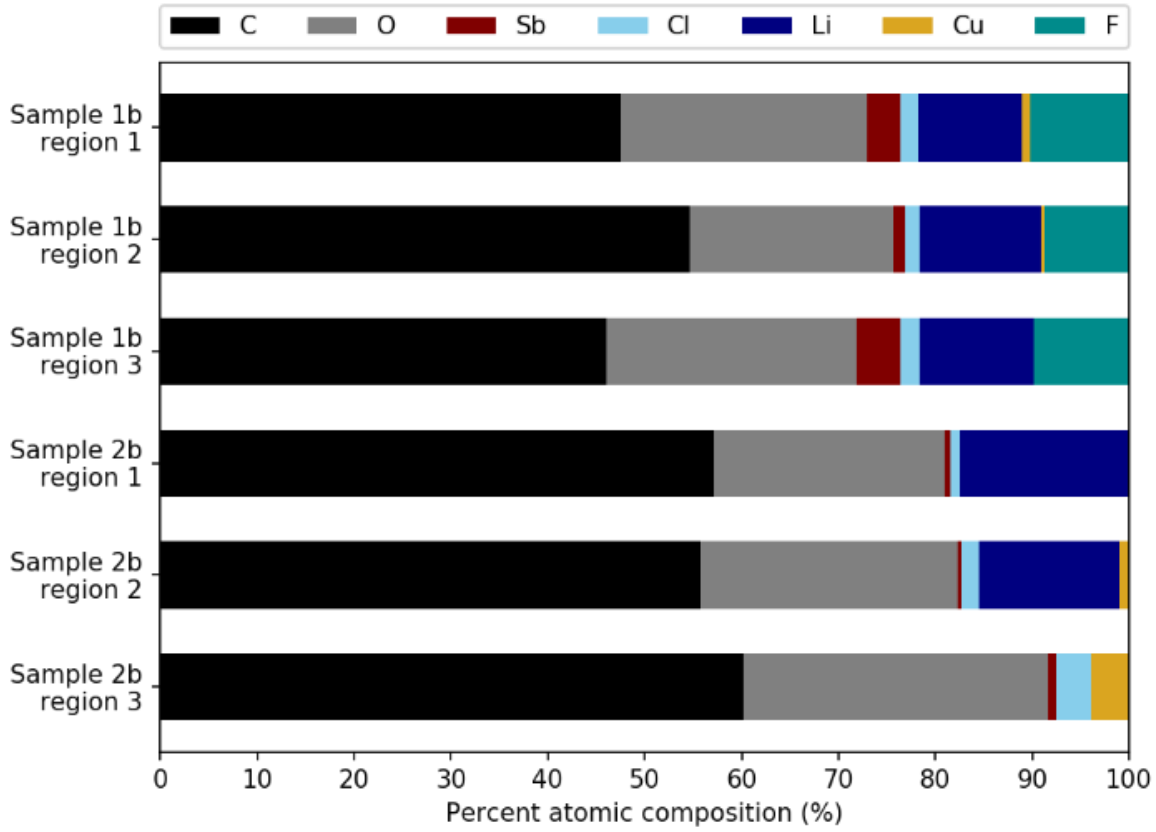

Figure 2.4: Percent atomic compositions based on peak fitting of XPS HRES spectra for multiple analysis regions of the contaminated (1b) and uncontaminated (2b) SEI samples.

species from a $LiPF_6$-based electrolyte. This highlights not only how sensitive the SEI can be to contaminants, but also the importance of careful SEI sample preparation at all stages, from electrode fabrication to cell assembly to cell disassembly, which is applicable when using reusable equipment such as beaker cell setups or Swagelok type cells. The introduction of a contaminant into the system prior to SEI formation could have notable implications for the characterization of the SEI at a later point as demonstrated by Figure 2.4. In addition to having a considerable amount of fluorine at the surface, the surface of Sample 1b (contaminated) also has considerably more Sb from the underlying Cu_2Sb electrode than uncontaminated Sample 2b, suggesting that the presence of contaminants can affect SEI formation as well, possibly further convoluting the results from contaminated samples. Contamination is often unavoidable, especially in the case of water content in electrolyte solutions and adventitious carbon

during the preparation of samples for XPS characterization, but with careful sample preparation and handling, other types of contamination, such as from cell parts or during sample preparation for characterization can be avoided.

Importance of time as an experimental variable

There are many important variables to consider when it comes to SEI formation, one of which includes time, as many of the species in the SEI are hypothesized to be thermodynamically unstable.[42] There are numerous examples in the literature demonstrating the importance of time as a variable. For example, the rate and method (e.g. galvanostatic versus a potential sweep) at which an electrode is cycled has been found to influence the composition, morphology, and properties of the SEI on different anode materials, including Li metal and Si.[24–26] Lithiated anodes can also experience self-discharge♦ over time as a result of SEI instability and dissolution.[5,43] Even before current is passed in a cell, time can be an important factor for the SEI, especially for reactive anode materials. A passivation layer forms on Li metal anodes stored in carbonate electrolytes, with changes in composition and increasing resistance being observed over time.[5] The formation of a passivation layer or changes to the electrode surface prior to cell cycling when an electrode has just been soaked in electrolyte has also been observed for alloying anodes including Si,[27] Sn,[44] Cu_6Sn_5,[45] and Cu_2Sb (see Figures A9–10 in Appendix A). We also have observed the importance of time in regard to changes in the SEI on delithiated/charged anodes after cycling.

We have observed changes in the composition of the SEI surface via XPS characterization for both rested half-cells after cycling and samples stored under inert atmosphere after cell disassembly. In general, we see the biggest change in the composition of the carbon species at the SEI surface, as

♦ Note that the term self-discharge is used in the literature to refer to a lithiated anode in a full cell setup discharging/delithiating. We use the term here to be consistent with the literature even though for our experiments and throughout the rest of this paper we refer to the lithiation process as discharging and the delithiation process as charging due to the use of half-cells.

demonstrated in the C 1s HRES spectra in Figure 2.5a. In the sample rested for longer after cycling (11 days), Sample 1c, we observe an increase in the contribution from carbonate binding environments and a decrease in the contribution from aliphatic and O=C–O binding environments (and little to no change in C–O binding environment contribution), compared to the sample rested for a shorter length of time (1 day) prior to XPS characterization (Sample 2c). We also observe an overall decrease in the carbon contribution to the percent atomic composition of the surface and an increase in the oxygen contribution for the sample rested for longer (Sample 1c in Figure 2.5b), which is expected based on the increase in carbonate species.

These changes are surprising for several reasons. This aging phenomenon has been observed consistently; even when the SEI samples were prepared using different formation conditions than those in the example above, we consistently observed an increase in the relative amount of carbonate species for samples rested for longer than 1–2 days. Additionally, we observe these changes in the distribution of carbon species in the SEI regardless of whether the delithiated/charged electrodes are rested in assembled cells or stored under inert atmosphere (Ar) after they have been disassembled and washed, which is surprising because one might expect to see different changes if the electrode/SEI sample is rested in the half-cell where it is in contact with the electrolyte and soluble SEI species to undergo further reactions.[5,27,46] We observed the same changes in electrodes that have been cycled over the SEI formation region but not the region where the electrode is lithiated and delithiated, so these observations in charged/delithiated samples do not seem to be due to further reactivity or self-discharging as a result of incomplete delithiation.[5,43] Additionally, we have observed these changes in half-cells cycled with $LiClO_4$-based electrolyte, so they are free of reactive $LiPF_6$ decomposition species such as HF that are known to react further with SEI components and lead to SEI dissolution.[5]

These findings are important because one can draw very different conclusions about the SEI composition from samples characterized a short time after cycling compared to samples characterized

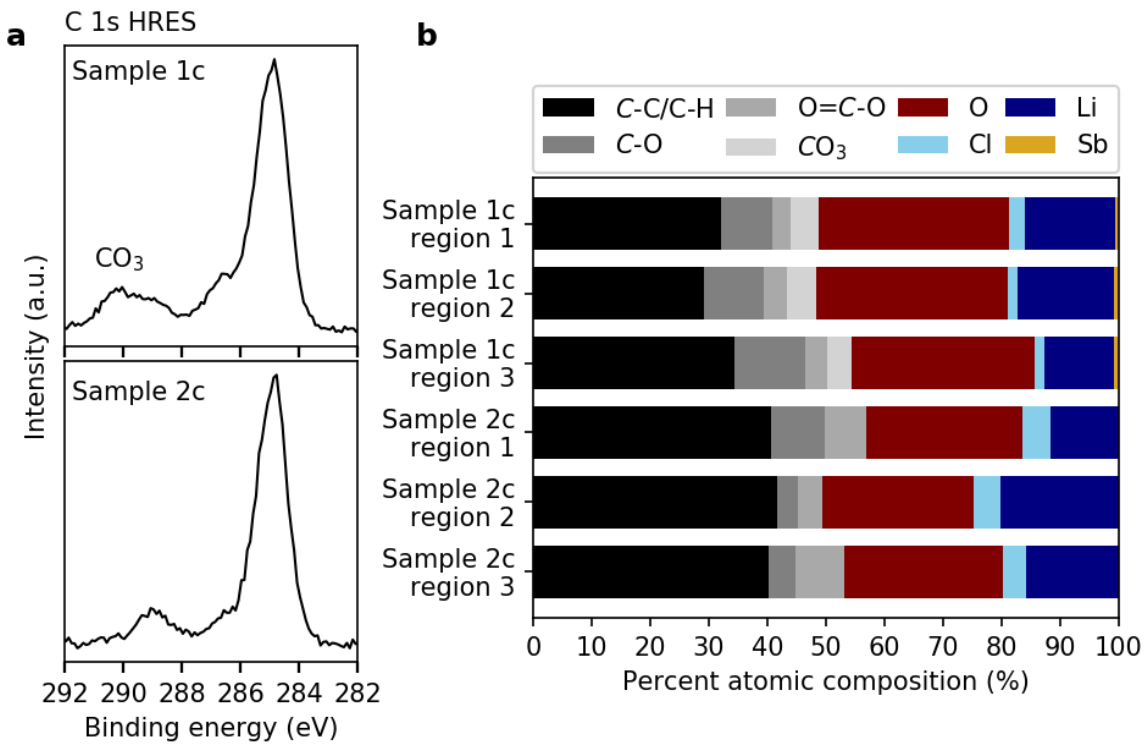

Figure 2.5: Comparison of C 1s HRES spectra for SEI samples rested for longer (1c) and shorter (2c) times prior to characterization (a) and comparison of the compositions of multiple analysis regions of the SEI samples rested for different lengths of time based on fitting of HRES spectra (b).

days or weeks after cycling. Based on the data for Sample 1c (rested for longer) one might conclude that carbonate species are incorporated into the SEI whereas the data from Sample 2c (characterized shortly after cycling) demonstrates that carbonates are not actually incorporated into the SEI under these formation conditions. The observations that the rest time after cycling and the time between cell disassembly and characterization can affect the SEI composition have important implications for SEI studies. These results stress the importance of careful experimental planning and observation to ensure that SEI samples can be characterized in a timely manner or that the amount of time between cycling completion and characterization can be considered when interpreting characterization results. It also has important implications for collaborative experiments, in which the time between sample preparation and characterization, due to factors like shipping samples, could be considerable. The time between cell cycling and characterization is rarely reported in the SEI literature,[47] but since time can

make a difference in the SEI composition, it is another factor that should be considered during data interpretation and an area where more detail should be provided in experimental sections to allow for better comparison of results in the literature when ex-situ characterization techniques are used.

Sample washing

Another consideration for SEI sample preparation prior to characterization is whether or not to wash the samples prior to analysis because many of the commonly used SEI characterization techniques are ex-situ. Typically, washing the SEI sample is done by rinsing or soaking the electrode in one of the solvents that make up the electrolyte solution, such as DMC, or in another organic solvent such as acetonitrile.[29,48–51] This decision tends to be dependent on the characterization method(s) to be used, as it can have an impact on the results obtained. For surface-sensitive characterization methods like XPS, washing the sample is often performed to remove excess salts and other species not incorporated into the SEI that could attenuate signal from the SEI,[30] but it could also rinse away SEI species that are soluble in solvents like DMC.[46] A comparison of washed and unwashed SEI layers formed on graphite revealed some minor differences in the types and relative amounts of species present in the SEI, but in general the unwashed sample contained higher quantities of F and P from salts and salt reduction species while the washed sample contained higher quantities of C and O from carbonaceous SEI species and electrode components.[38] We have also observed that for the SEI formed on Cu_2Sb thin films, unrinsed SEI samples characterized by XPS have more salt species at the surface compared to the washed samples, as shown in Figure A10. However, others have observed via XPS that washing leads to the detection of different salt reduction species in addition to decreased signal from said salt reduction species or to the elimination of some species when washed extensively.[48,52] For other techniques such as SEM and FTIR, washing the sample can change it in ways that may lead to different conclusions about the data. For example, Somerville and coworkers observed differences in the surface morphology for graphite electrodes based on how the electrodes were treated after cycling; there was evidence of a film

covering the unwashed graphite electrodes that was not observed for the washed samples.[48] Additionally, Shi and coworkers were able to detect some electrolyte degradation or SEI species via in-situ ATR-FTIR that were not observed via ex-situ ATR-FTIR measurements of washed samples.[15] Like many aspects of SEI sample preparation and characterization, there is not one correct approach for sample washing; instead, it is highly dependent on the type of sample, characterization method, and desired information since both approaches have associated disadvantages.[38,48,53] Instead, the best approach seems to be to use care during sample preparation, to rigorously report the procedure used so that it can be reproduced by others, and to consider the sample preparation method used when interpreting data and comparing to the literature.[29,53]

2.3.2) XPS characterization

XPS is a useful technique for studying interfaces like the SEI because binding energy shifts of core level spectra can provide information about species present in the SEI while quantification results can provide information about the SEI composition.[4,30] However, XPS is not straightforward even for uniform samples,[54] and for complex, heterogeneous structures like the SEI, XPS characterization and interpretation becomes even more challenging.[4] As such, there are many factors to consider for XPS characterization, and as others have pointed out previously, there is unfortunately no single correct approach when it comes to the treatment and interpretation of XPS data for the SEI.[55] Here we describe some of the challenges associated with XPS data collection and some considerations and possible approaches for SEI characterization.

Air exposure

One important consideration for XPS characterization of the SEI is avoiding air exposure during sample transfer because the SEI is composed of many reactive species that are sensitive to air and moisture.[30] Edström and coworkers observed notable changes in the speciation of the SEI on graphite after 3 hours of air exposure; in particular, notable changes in the C 1s spectra suggested that air

exposure affects organic SEI species.[39] Shorter air exposure times on the order of minutes rather than hours have also been observed to cause changes in the SEI and the types of species detected with XPS. Schroder and coworkers also found that some organic species were susceptible to changes after air exposure; studying the SEI formed on Si anodes before and after air exposure, they observed that CO and OCO bonds were particularly reactive based on changes in the C 1s spectra.[26] Interestingly, the effects of air exposure also seem to be dependent on SEI formation and sample preparation conditions. When different electrochemical procedures were employed to form the SEI on Si, resulting in the formation of different SEI species, some SEI layers underwent more dramatic changes upon air exposure than others. For example, the SEI formed by linear sweep voltammetry that contained more oxygen-poor organic species and LiF was not changed as much by air exposure as the SEI formed by chronoamperometry, which contained more phosphorus oxyfluoride species and oxygen-rich organic species like carbonates.[26] Malmgren and coworkers also observed that sample preparation can affect the degree to which the SEI is affected by air exposure; they observed that unwashed SEI samples underwent more dramatic changes upon air exposure compared to the washed SEI samples.[38]

While sample preparation and SEI formation conditions appear to play a role in the degree to which the SEI may be affected by and change as a result of air exposure, the best practice is to err on the side of caution and avoid air exposure prior to characterization whenever possible. Some researchers are able to utilize XPS instruments connected to inert atmosphere glove boxes to avoid air exposure during sample transfer,[41,48,49] but fortunately there are also options for commercial and homemade air free sample transfer devices when this is not feasible.[30] Air free sample transfer devices can range from glove bags[37,52] or simple holders that keep the sample under vacuum until a lower vacuum pressure in the XPS sample introduction chamber is achieved[32] to more complex designs.[38,56,57]

Charge correction

Much of the focus of methodology papers for SEI studies has been on charge correction procedures for XPS HRES spectra because accounting for sample charging is important for interpretation of the data and comparison to the literature.[40,41,55,58] Typically, charge correction (also commonly referred to as binding energy calibration- see Reference 54) is performed by shifting all of the binding energies for a set of spectra based on a known binding energy for a specific peak of one of the core level transitions. Unfortunately, this is difficult for SEI samples, which are heterogeneous, contain unknown phases, and consist of many electronically insulating species that can result in differential charging; additionally, effects from the underlying electrode can further complicate matters.[40,41,55] Several recent studies on model systems have demonstrated the importance of using peaks from SEI components for charge correction, the utility of using Ar as an internal standard for charge correction when doing depth profiling experiments, and the usefulness of characteristic binding energy separations between core level spectra of a given phase for peak identification.[41,55,58] However, the most ubiquitous method for charge correction for spectra of SEI samples is to use either adventitious or aliphatic carbon since the former is unavoidable during sample preparation and the latter is typically present in the SEI.[54,55] However, using an adventitious or aliphatic carbon peak for charge correction is problematic for several reasons, including that the carbon binding environments may not always be the same due to mixtures of carbon species in the SEI or from the adventitious carbon source.[41,54] Additionally, while the C 1s peak typically attributed to adventitious and aliphatic carbon is usually the most intense C 1s peak for SEI samples, this may not always be the case, as demonstrated in Figure 2.6. We have found that using a peak from an inorganic SEI species such as $LiClO_4$ or LiF is useful for charge correction.[59] While this method does not allow for direct comparison to binding energy values in the literature, it is useful for self-consistency. However, there may be instances when these species are not present, as described in the following scenario.

As demonstrated in this example, there can be some challenges associated with charge correction in cases where there is no obvious peak to shift to the accepted value for the aliphatic (C–C/C–H) binding environment and there are also no inorganic SEI components to use for charge correction. In Figure 2.6, the fitted C 1s, O 1s, and Li 1s spectra of an SEI sample are shown unshifted and with binding energies shifted such that the C 1s peak with the highest intensity is at 285 eV, a common practice especially when electrode additives such as conductive carbon are present and make it inappropriate to shift the binding energies using the C 1s peak with the lowest binding energy.[21,47,60] The tentative binding environment assignments based on the approximate binding energies of the peaks for the unshifted and shifted data are shown in Table 2.1. Based on whether or not the spectra are shifted results in different binding energy assignments based on reported binding energies and could lead to different interpretations of the data. Additionally, neither instance is entirely satisfactory; for example, the unshifted data results in the highest binding energy C 1s peak being at ca. 291.2 eV, which is quite high based on many of the reported binding energies for the species expected in this sample such as Li_2CO_3 and Li alkyl carbonates.[26,38,61–63] Typically, only the CO_3 binding environment of poly VC or peaks associated with C–F bonds are reported at such a high binding energy, neither of which should be present in the sample shown, since the electrolyte lacks both VC and fluorinated salts or additives.[52,62,63] Shifting the binding energies using the C 1s peak is also unsatisfactory; for example, the lower binding energy Li 1s peak, which is at ca. 52.7 eV due to this shifting protocol is too low to be anything other than metallic lithium, the presence of which also seems unlikely for the sample based on the cycling conditions.[64] In this case, using C 1s peaks for charge correction is not practical. For the SEI sample described in this example, and for many other preliminary SEI studies where the SEI composition may not be well understood, as in the case of a studying a new electrolyte formulation or additive, using C 1s peaks for charge correction is not ideal, and using photoelectron peaks from other SEI species for charge

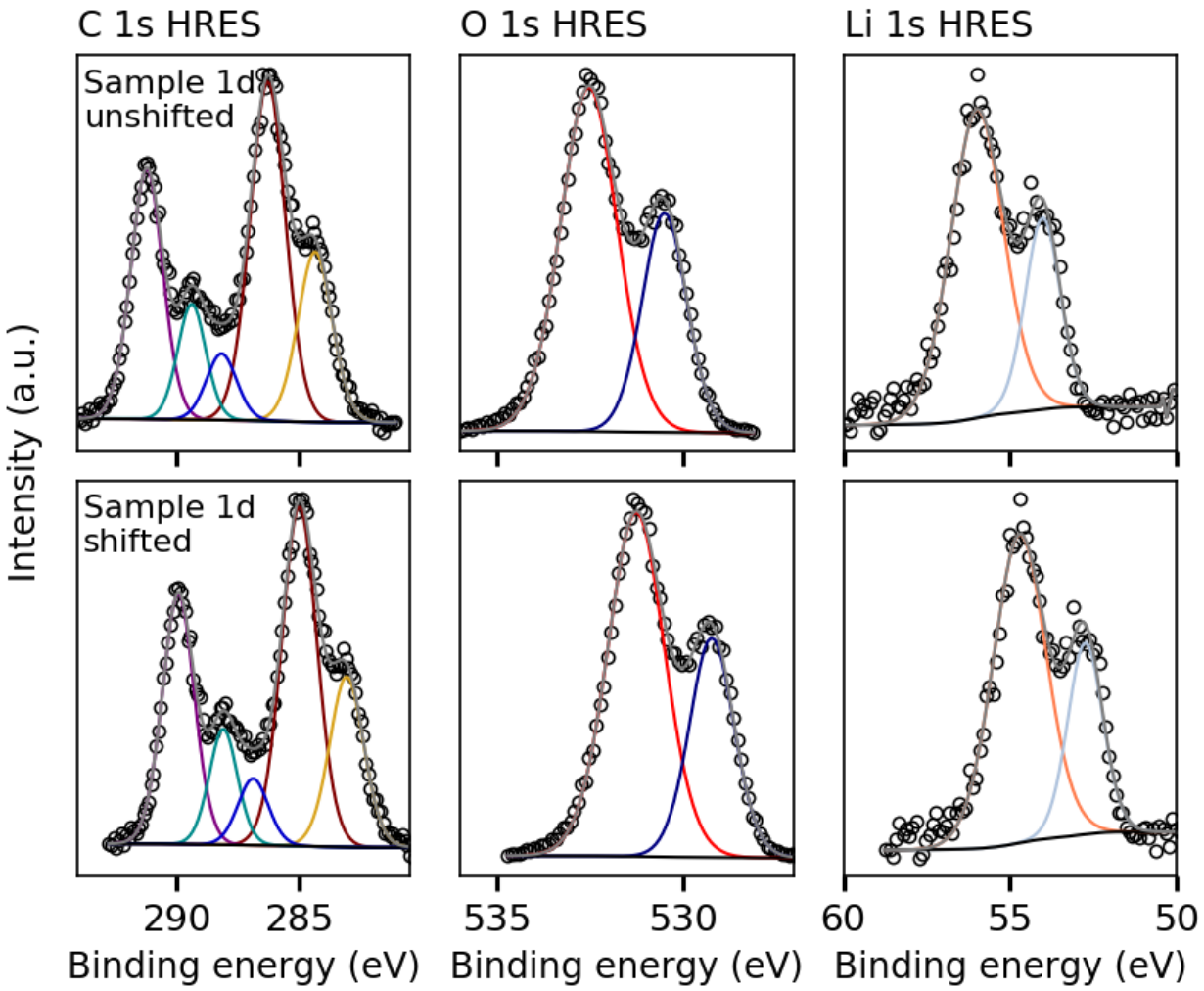

Figure 2.6: Comparison of XPS HRES spectra for an SEI sample showing the differences between unaltered binding energies (top row) and binding energies shifted using the highest intensity C 1s peak (bottom row).

Table 2.1: Binding energies and tentative peak assignments for the fitted spectra in Figure 2.6 based on two different treatments of the data. The text colors correspond to the peak colors in Figure 2.6.

Description	Region	Peak position (eV)	Tentative assignment*
Unshifted (no charge correction)	C 1s	286.3	**C**–O
		291.2	**C**O_3
		284.4	**C**–C/**C**–H
		289.4	O=**C**–O, oxalates/carboxylates
		288.2	O=**C**–O, esters
	O 1s	532.5	C–**O**, C=**O**, Li_2C**O_3**
		530.5	Li**O**H, Li_2**O**
	Li 1s	56.0	**Li_2CO_3**
		54.0	**Li**OH, **Li_2**O
Shifted (most intense C 1s peak set to 285 eV)	C 1s	285.0	**C**–C/**C**–H
		289.9	**C**O_3
		283.1	C sp^2
		288.1	O=**C**–O
		286.9	**C**–O
	O 1s	531.3	C–**O**, C=**O**
		529.2	Li_2**O**
	Li 1s	54.7	**Li_2**O
		52.7	Li^0

* Based on peak position and reported literature values referenced in the text.

correction may not be straightforward either. In these instances, it is useful to have an alternative approach for charge correction.

In instances where instrumentation or time constraints prohibit the collection of good valence band spectra to aid in calibration,[41] there are no inorganic SEI components to use for shifting, and the C 1s spectrum does not make it obvious which peak corresponds to the aliphatic or adventitious carbon binding environment, it would be useful to have another method to aid in charge correction. One such method is the use of an internal reference. Some practices for applying an internal reference include gold sputtering in situ, applying powders to the sample surface, or implanting Ar using the Ar^+ gun, but these methods could lead to the introduction of artifacts due to sample damage or attenuate the signal from the SEI.[30,40,58] We have had success drop casting Ag/Ag_xO_y particles, prepared by sonicating Ag leaf in DMC, onto SEI samples for use as an internal reference. Shown in Figure 2.7 are spectra from the sample SEI sample before and after the Ag internal reference was applied (see Figure A11 for the Ag 3d spectrum), demonstrating that it can be applied to the sample without considerable loss of signal intensity from the SEI components and with only minor artifacts introduced to the data, in this case a small amount of Cl^- from the Ag leaf that could be eliminated by using higher quality starting materials. This method for applying an internal reference is attractive because it does not damage the sample like other application methods such as Au sputtering might and does not attenuate the sample signal as applying a powder to the surface would. The particles are also quite large (µm to mm scale), so size effects associated with nanoscale metal particles is not expected to be a concern.[54,65] This method could be applied to other elements or compounds, including electronic insulators instead of metallic species to have an internal reference with similar properties to the SEI species and avoid issues associated with conductor-insulator interfaces.[40,55] This method would also allow for the application of multiple internal references, so long as they could be suspended in DMC long enough to be drop cast onto the sample, which would allow for multiple points of reference for charge correction.

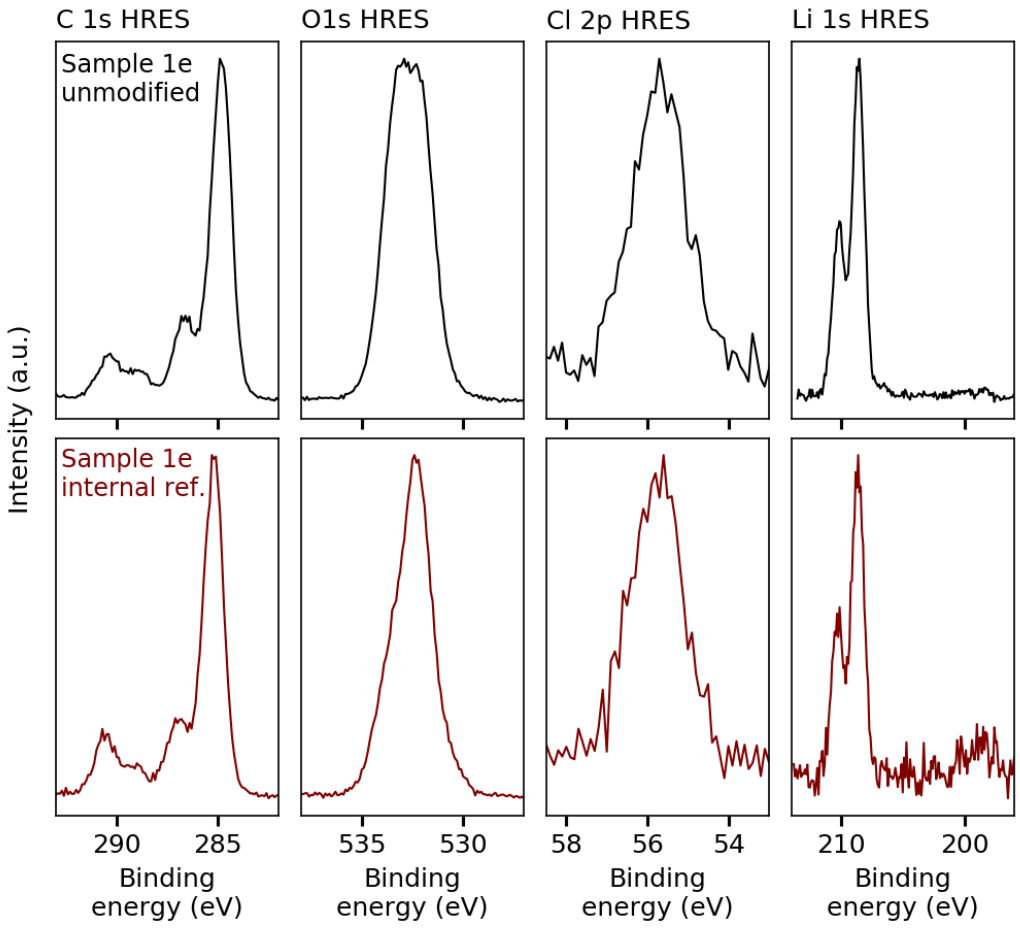

Figure 2.7: Comparison of XPS HRES spectra for an SEI sample before and after an internal reference was drop cast onto the surface, demonstrating that signal from the sample was not severely altered or attenuated.

Analysis regions and representative data

The SEI on many anodes is a heterogeneous, layered structure, and XPS sputtering or synchrotron photoelectron spectroscopy (PES) is often used to characterize this depth-dependent compositional variation.[4,30] Typically, XPS is not used to measure the lateral heterogeneity of the speciation and composition of SEI samples, and in general characterization of the distribution of elements or chemical species across the SEI surface is not especially common in the SEI literature.[27,66–68] The typical XPS analysis areas used to obtain good signal to noise ratios for HRES spectra are quite large (typically on the order of hundreds of square microns to several square millimeters).[49,69] However, compared to the areas of most SEI/electrode samples, which are usually at least hundreds of square

millimeters, the XPS spot size is quite small, and ideally multiple regions of each sample would be characterized.[29] We have found that by looking at multiple regions of an SEI sample formed on electrodeposited thin film electrodes, we can capture some of this compositional heterogeneity even with large XPS analysis areas (ca. 1.2 mm^2 analysis area and ca. 126.7 mm^2 sample area). This may be different for composite electrodes where the active material, conductive additive, and binder are very well mixed before electrode fabrication, but for thin film electrodes where there can be some variation between films and even between regions of the same film, it is useful to be able to characterize this heterogeneity to obtain a more realistic model of the SEI. This has been done by others using a quantitative approach, but unfortunately no details were provided about how the analysis regions were determined to be statistically similar, and no commentary on similarities or differences between analysis regions was provided.[21,70] Below we describe the qualitative approach we have developed for evaluating SEI heterogeneity.

While looking at multiple analysis regions of a SEI sample during XPS characterization can reveal information about the lateral heterogeneity of a SEI sample, it can be challenging to determine which data from different regions of a sample are representative of that sample and what types of differences constitute actual differences between regions. Figure 2.8 shows multiple analysis regions from two different SEI samples, one that did show some variation between analysis regions, suggesting lateral SEI heterogeneity, and one where analysis regions were similar, suggesting a laterally homogenous SEI sample. We determine representative sample regions based on differences in percent atomic composition and spectral features. For example, the different regions of Sample 1f in Figure 2.8b are relatively similar in terms of composition with the exception of some variation in the percent atomic composition of Li. However, looking at the HRES spectra for the three analysis regions of Sample 1f in Figure 2.8a reveals that Region 2 (shown in maroon) shows evidence of Li_2O in the O 1s spectrum and Cl^- in the Cl 2p spectrum, so Region 2 of Sample 1f varies somewhat in terms of the species present

compared to Regions 1 and 3, suggesting that the SEI is heterogeneous and requires looking at multiple spectra as representatives of the sample. In contrast, both the percent atomic compositions and spectral features of Sample 2f are similar in terms of the binding environments present, the relative peak intensities in the HRES spectra, and the percent atomic compositions, suggesting the SEI of this sample is relatively homogenous across the surface. In order to ensure that this lateral heterogeneity is not an artifact of the sample washing procedure or due to differences in current density across the electrode during cycling, we have looked at multiple regions on the center of the sample and on the edges (representative data shown in Figures A12 and Table A9), and we have found that this is generally not the case.

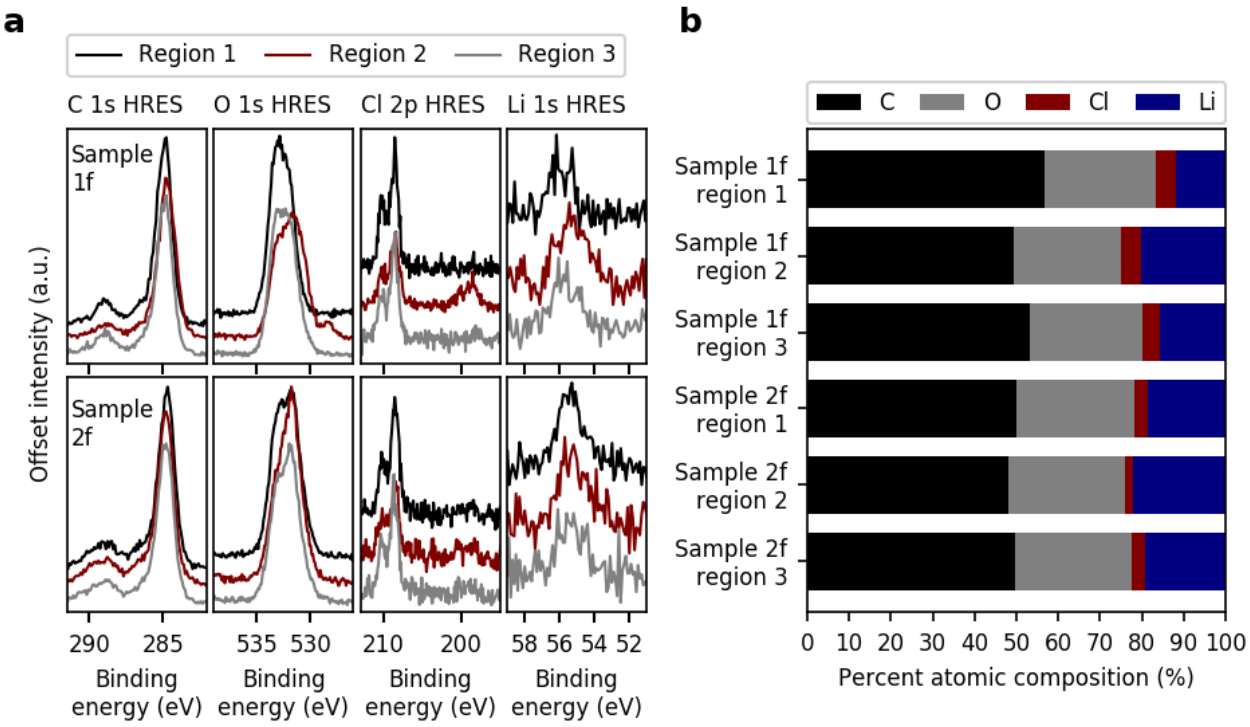

Figure 2.8: Comparison of HRES spectra from multiple analysis regions for two different SEI samples, one heterogeneous (1f) and one homogenous (2f) (a) and comparison of the percent atomic compositions for the two samples based on peak fitting (b).

Sputtering

Given the layered structure of the SEI for many anode materials, it is important to be able to characterize this depth-dependent heterogeneity, and XPS is suited to this due the capabilities to sputter away layers using an ion beam, most commonly Ar^+. Ion sputtering is known to damage samples and introduce artifacts for a variety of samples, including the SEI.[4,30,39,54] Edström and coworkers have found that Ar^+ sputtering of the SEI formed on graphite from $LiPF_6$-based carbonate electrolyte resulted in the decomposition of Li_2CO_3 into Li_2O.[39] Based on these findings, researchers have advocated for the use of synchrotron PES for obtaining depth-sensitive information without sample damage and have demonstrated that it is a useful characterization technique for achieving these ends.[30,47,71] The use of synchrotron PES for non-destructive SEI depth characterization is an attractive technique, but it does come with some drawbacks. First, it is not readily accessible to all researchers, whereas most XPS instruments are equipped with ion-sputtering capabilities. Second, when synchrotron PES sources are available, timing can be problematic, as we have demonstrated that the time between SEI formation and characterization is an important variable.

Despite the disadvantages associated with ion beam sputtering, it is still a valuable and widely accessible tool for gaining information about changes with depth in SEI samples. We have found that when sputtering is done carefully and for short periods of time, it can reveal useful information with minimal sample damage even when using a higher energy Ar^+ beam. Additionally, the use of controls can help with anticipating sample damage and artifact introduction, so that changes in the SEI sample seen as a result of sputtering can be assigned to either sample damage or actual changes in the sample with more confidence. We have observed possible sample damage induced by sputtering when doing Ar^+ depth profiling of SEI samples formed on Cu_2Sb thin films in $LiClO_4$-based carbonate electrolyte in the form of ClO_4^- decomposition. Indeed, when a $LiClO_4$ control sample was sputtered for just 12 s with a 2

kV 3 x 3 mm Ar^+ beam, there was evidence of ClO_4^- degradation and the formation of ClO_3^- and Cl^-, as shown in Figure 2.9.

When sputtering SEI samples containing ClO_4^-, such as the one shown in Figure 2.10, there is no evidence of ClO_4^- degradation over shorter periods of sputtering (up to 30 s total using a 2 kV 3 x 3 mm Ar^+ beam). However, after longer sputtering times (60 to 120 s total sputtering), there is some evidence of ClO_4^- degradation based on the appearance of Cl 2p peaks around 198 eV and 200 eV indicative of a Cl^- binding environment and some broadening on the low binding energy side of the ClO_4^- Cl 2p3/2 peak at ca. 207 eV that could be due to a ClO_3^- binding environment.[72–74] The appearance of the Cl^- and ClO_3^- environments were seen after sputtering the $LiClO_4$ control, suggesting that the $LiClO_4$ present in the SEI is also decomposing into these species as a result of Ar^+ beam exposure. However, Cl^- has been detected in the SEI formed in perchlorate-based electrolytes for samples that have not been sputtered, suggesting that some of the Cl^- detected could actually be present in the SEI and not just an artifact of sputtering.[21,47,59] In particular, this may be the case when the SEI sample was sputtered for a total of 180 s. As seen in Figure 2.10, only one Cl 2p binding environment, corresponding to Cl^-, was detected after 180 s of total sputtering. Some of this Cl^- could be coming from decomposed ClO_4^-, but since there was no ClO_3^- detected, which also seems to be an indicator for ClO_4^- degradation, the layer of the SEI revealed after 180 s of total sputter time seems to contain Cl^- rather than ClO_4^-. This also seems to be supported by notable changes in the features of the C 1s, O 1s/Sb 3d, and Li 1s HRES spectra after 180 s of sputtering compared to samples sputtered for 120 s or less, which suggests the species present in the inner part of the SEI are quite different than those in the outer layer. Therefore, it seems reasonable that Cl^- could actually be more than just an artifact for this deeper layer of the SEI.

The use of ion sputtering for XPS depth profiling studies can be extremely useful when performed carefully, but it does seem to be highly dependent on which types of species are present in the SEI and the sample preparation conditions. For example, we have seen that it takes up to 60 s of

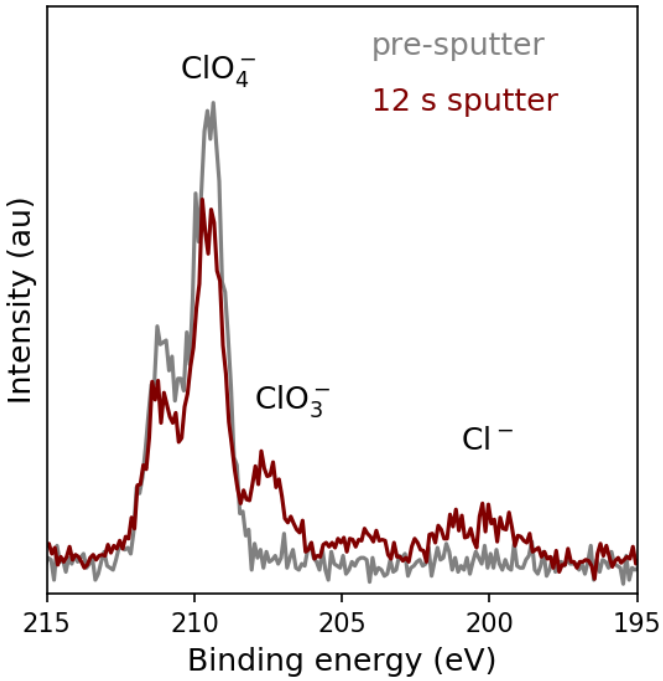

Figure 2.9: Comparison of Cl 2p HRES spectra from a $LiClO_4$ powder control sample before and after 12 s of sputtering with a 2 kV 3 x 3 mm Ar^+ beam.

sputtering to see ClO_4^- degradation in SEI samples that were not exposed to air while ClO_4^- degradation was seen after only 12 s of sputtering $LiClO_4$ that was exposed to ambient conditions prior to XPS characterization, suggesting that air or moisture exposure could exacerbate beam-induced sample damage. Additionally, SEI species present in a hexafluorophosphate-based SEI may behave quite differently than those in a perchlorate-based SEI when exposed to an ion beam; for example, we have not observed the formation of Li_2O as a result of sputtering a $LiClO_4$-based SEI, whereas there have been reports of Li_2O artifacts as a result of sputtering a $LiPF_6$-based SEI. This makes a "one size fits all" approach to SEI depth profiling difficult, similar to other aspects of XPS analysis of the SEI.[55] However, it does not make sputtering less useful, it just requires careful consideration and experimental planning.

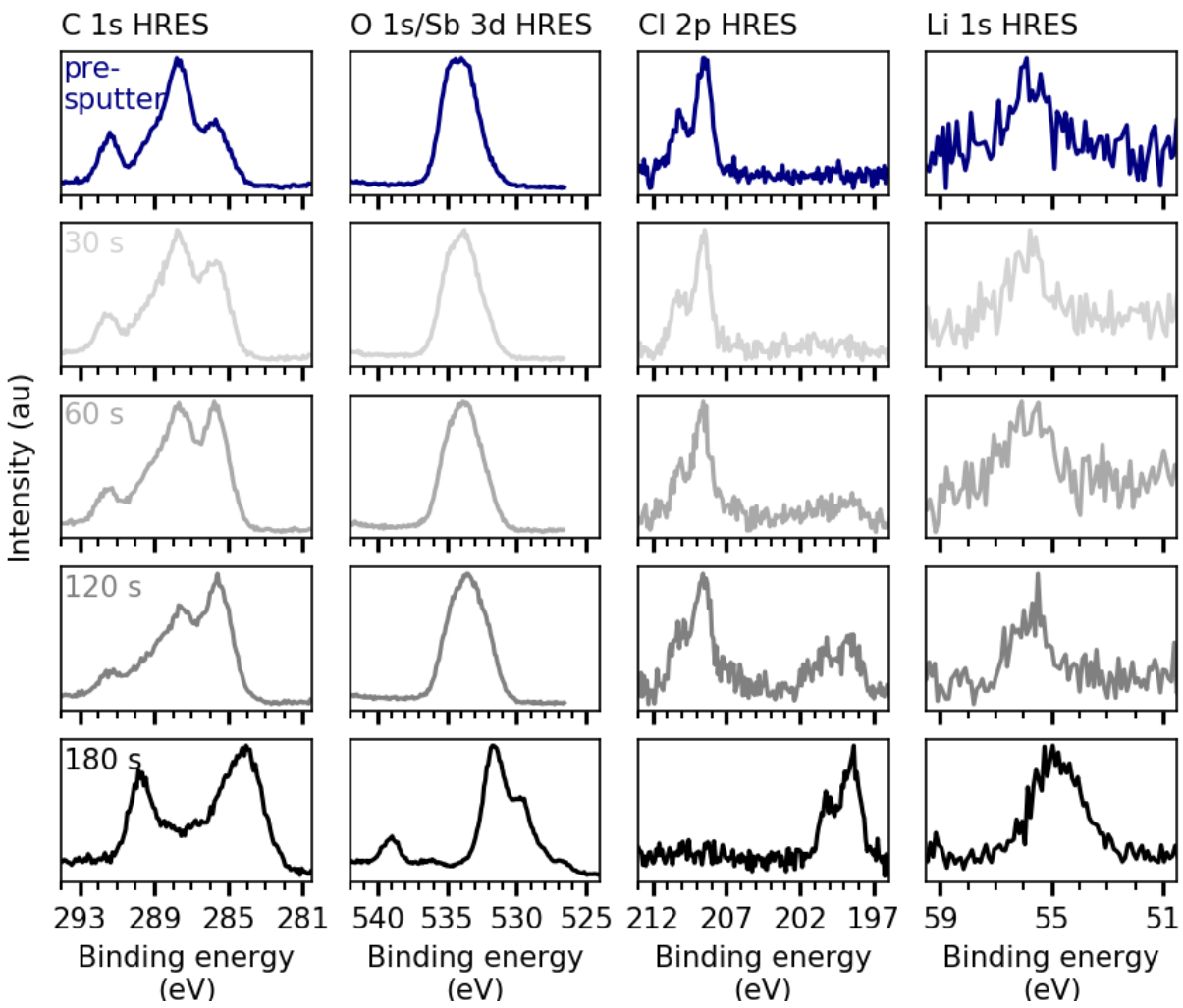

Figure 2.10: Comparison of XPS C 1s, O 1s/Sb 3d, Cl 2p, and Li 1s HRES spectra for a SEI sample sputtered for different total amounts of time with an Ar^+ beam.

2.4) Conclusions

We have found that there are many important factors to consider during the sample preparation and XPS characterization of the SEI layer. There are several considerations during sample preparation, such as preparation and evaluation of replicate samples, sample rest time, and sample contamination, and XPS characterization, such as representative samples, that either do not get discussed in SEI literature or are mentioned only briefly with little detail in experimental sections. In this paper we have discussed our findings concerning these aspects of SEI sample preparation and characterization that suggest they are important considerations for SEI studies. We have also discussed

our findings for other aspects of SEI sample preparation and XPS characterization that are discussed more often in the literature, such as sample washing, air exposure, charge correction, and sputtering, with references to other useful sources on these topics. While the SEI is a very complex system that requires many considerations for preparation and characterization and there is no “one size fits all” approach to characterizing the SEI, we hope that this paper and the references herein can serve as a resource in helping researchers determine the best approach for studying their system of interest as well as generate more discussion in the SEI community about the intricacies of SEI study and the level of detail required when reporting results.

CHAPTER 2 REFERENCES

(1) Goodenough, J. B.; Kim, Y. Challenges for Rechargeable Li Batteries. *Chem. Mater.* **2010**, *22* (3), 587–603. https://doi.org/10.1021/cm901452z.

(2) Xu, K. Nonaqueous Liquid Electrolytes for Lithium-Based Rechargeable Batteries. *Chem. Rev.* **2004**, *104* (10), 4303–4417. https://doi.org/10.1021/cr030203g.

(3) Peled, E.; Menkin, S. Review—SEI: Past, Present and Future. *J. Electrochem. Soc.* **2017**, *164* (7), A1703–A1719. https://doi.org/10.1149/2.1441707jes.

(4) Verma, P.; Maire, P.; Novák, P. A Review of the Features and Analyses of the Solid Electrolyte Interphase in Li-Ion Batteries. *Electrochim. Acta* **2010**, *55* (22), 6332–6341. https://doi.org/10.1016/J.ELECTACTA.2010.05.072.

(5) Aurbach, D.; Markovsky, B.; Shechter, A.; EinEli, Y.; Cohen, H. A Comparative Study of Synthetic Graphite and Li Electrodes in Electrolyte Solutions Based on Ethylene Carbonate Dimethyl Carbonate Mixtures. *J. Electrochem. Soc.* **1996**, *143* (12), 3809–3820. https://doi.org/10.1149/1.1837300.

(6) Nie, M.; Lucht, B. L. Role of Lithium Salt on Solid Electrolyte Interface (SEI) Formation and Structure in Lithium Ion Batteries. *J. Electrochem. Soc.* **2014**, *161* (6), A1001–A1006. https://doi.org/10.1149/2.054406jes.

(7) Jurng, S.; Brown, Z. L.; Kim, J.; Lucht, B. L. Effect of Electrolyte on the Nanostructure of the Solid Electrolyte Interphase (SEI) and Performance of Lithium Metal Anodes. *Energy Environ. Sci.* **2018**, *11* (9), 2600–2608. https://doi.org/10.1039/c8ee00364e.

(8) Leroy, S.; Martinez, H.; Dedryvère, R.; Lemordant, D.; Gonbeau, D. Influence of the Lithium Salt Nature over the Surface Film Formation on a Graphite Electrode in Li-Ion Batteries: An XPS Study. *Appl. Surf. Sci.* **2007**, *253* (11), 4895–4905. https://doi.org/10.1016/j.apsusc.2006.10.071.

(9) Yoon, T.; Chapman, N.; Seo, D. M.; Lucht, B. L. Lithium Salt Effects on Silicon Electrode Performance and Solid Electrolyte Interphase (SEI) Structure, Role of Solution Structure on SEI Formation. *J. Electrochem. Soc.* **2017**, *164* (9), A2082–A2088. https://doi.org/10.1149/2.1421709jes.

(10) Nguyen, C. C.; Lucht, B. L. Comparative Study of Fluoroethylene Carbonate and Vinylene Carbonate for Silicon Anodes in Lithium Ion Batteries. *J. Electrochem. Soc.* **2014**, *161* (12), A1933–A1938. https://doi.org/10.1149/2.0731412jes.

(11) Jackson, E. D.; Prieto, A. L. Copper Antimonide Nanowire Array Lithium Ion Anodes Stabilized by Electrolyte Additives. *ACS Appl. Mater. Interfaces* **2016**, *8* (44), 30379–30386. https://doi.org/10.1021/acsami.6b08033.

(12) Jin, Y.; Kneusels, N. J. H.; Marbella, L. E.; Castillo-Martínez, E.; Magusin, P. C. M. M.; Weatherup, R. S.; Jónsson, E.; Liu, T.; Paul, S.; Grey, C. P. Understanding Fluoroethylene Carbonate and Vinylene Carbonate Based Electrolytes for Si Anodes in Lithium Ion Batteries with NMR Spectroscopy. *J. Am. Chem. Soc.* **2018**, *140* (31), 9854–9867. https://doi.org/10.1021/jacs.8b03408.

(13) Zhang, W.; Ghamouss, F.; Darwiche, A.; Monconduit, L.; Lemordant, D.; Dedryvère, R.; Martinez, H. Surface Film Formation on TiSnSb Electrodes: Impact of Electrolyte Additives. *J. Power Sources* **2014**, *268*, 645–657. https://doi.org/10.1016/j.jpowsour.2014.06.041.

(14) Wagner, M. R.; Raimann, P. R.; Trifonova, A.; Moeller, K. C.; Besenhard, J. O.; Winter, M. Electrolyte Decomposition Reactions on Tin- and Graphite-Based Anodes Are Different. *Electrochem. Solid-State Lett.* **2004**, *7* (7), A201–A205. https://doi.org/10.1149/1.1739312.

(15) Shi, F.; Ross, P. N.; Zhao, H.; Liu, G.; Somorjai, G. A.; Komvopoulos, K. A Catalytic Path for Electrolyte Reduction in Lithium-Ion Cells Revealed by in Situ Attenuated Total Reflection-Fourier Transform Infrared Spectroscopy. *J. Am. Chem. Soc.* **2015**, *137* (9), 3181–3184. https://doi.org/10.1021/ja5128456.

(16) Tavassol, H.; Buthker, J. W.; Ferguson, G. A.; Curtiss, L. A.; Gewirth, A. A. Solvent Oligomerization during SEI Formation on Model Systems for Li-Ion Battery Anodes. *J. Electrochem. Soc.* **2012**, *159* (6), A730–A738. https://doi.org/10.1149/2.067206jes.

(17) Chan, C. K.; Ruffo, R.; Hong, S. S.; Cui, Y. Surface Chemistry and Morphology of the Solid Electrolyte Interphase on Silicon Nanowire Lithium-Ion Battery Anodes. *J. Power Sources* **2009**, *189* (2), 1132–1140. https://doi.org/10.1016/j.jpowsour.2009.01.007.

(18) Vogl, U. S.; Lux, S. F.; Das, P.; Weber, A.; Placke, T.; Kostecki, R.; Winter, M. The Mechanism of SEI Formation on Single Crystal Si(100), Si(110) and Si(111) Electrodes. *J. Electrochem. Soc.* **2015**, *162* (12), A2281–A2288. https://doi.org/10.1149/2.0361512jes.

(19) Fransson, L.; Eriksson, T.; Edström, K.; Gustafsson, T.; Thomas, J. O. Influence of Carbon Black and Binder on Li-Ion Batteries. *J. Power Sources* **2001**, *101* (1), 1–9. https://doi.org/10.1016/S0378-7753(01)00481-5.

(20) Jaumann, T.; Balach, J.; Klose, M.; Oswald, S.; Langklotz, U.; Michaelis, A.; Eckert, J.; Giebeler, L. SEI-Component Formation on Sub 5 Nm Sized Silicon Nanoparticles in Li-Ion Batteries: The Role of Electrode Preparation, FEC Addition and Binders. *Phys. Chem. Chem. Phys.* **2015**, *17* (38), 24956–24967. https://doi.org/10.1039/c5cp03672k.

(21) Bodenes, L.; Darwiche, A.; Monconduit, L.; Martinez, H. The Solid Electrolyte Interphase a Key Parameter of the High Performance of Sb in Sodium-Ion Batteries: Comparative X-Ray Photoelectron Spectroscopy Study of Sb/Na-Ion and Sb/Li-Ion Batteries. *J. Power Sources* **2015**, *273*, 14–24. https://doi.org/10.1016/j.jpowsour.2014.09.037.

(22) Bryngelsson, H.; Stjerndahl, M.; Gustafsson, T.; Edström, K. How Dynamic Is the SEI? *J. Power Sources* **2007**, *174* (2), 970–975. https://doi.org/10.1016/j.jpowsour.2007.06.050.

(23) Bridel, J.-S. S.; Grugeon, S.; Laruelle, S.; Hassoun, J.; Reale, P.; Scrosati, B.; Tarascon, J.-M. M. Decomposition of Ethylene Carbonate on Electrodeposited Metal Thin Film Anode. *J. Power Sources* **2010**, *195* (7, SI), 2036–2043. https://doi.org/10.1016/j.jpowsour.2009.10.038.

(24) Aurbach, D.; Weissman, I.; Yamin, H.; Elster, E. The Correlation between Charge/Discharge Rates and Morphology, Surface Chemistry, and Performance of Li Electrodes and the Connection to Cycle Life of Practical Batteries. *J. Electrochem. Soc.* **1998**, *145* (5), 1421–1426. https://doi.org/10.1149/1.1838498.

(25) Tokranov, A.; Kumar, R.; Li, C.; Minne, S.; Xiao, X.; Sheldon, B. W. Control and Optimization of the Electrochemical and Mechanical Properties of the Solid Electrolyte Interphase on Silicon Electrodes in Lithium Ion Batteries. *Adv. Energy Mater.* **2016**, *6* (8), 1–12. https://doi.org/10.1002/aenm.201502302.

(26) Schroder, K. W.; Celio, H.; Webb, L. J.; Stevenson, K. J. Examining Solid Electrolyte Interphase Formation on Crystalline Silicon Electrodes: Influence of Electrochemical Preparation and Ambient Exposure Conditions. *J. Phys. Chem. C* **2012**, *116* (37), 19737–19747. https://doi.org/10.1021/jp307372m.

(27) Dupré, N.; Moreau, P.; De Vito, E.; Quazuguel, L.; Boniface, M.; Bordes, A.; Rudisch, C.; Bayle-Guillemaud, P.; Guyomard, D. Multiprobe Study of the Solid Electrolyte Interphase on Silicon-Based Electrodes in Full-Cell Configuration. *Chem. Mater.* **2016**, *28* (8), 2557–2572. https://doi.org/10.1021/acs.chemmater.5b04461.

(28) Tripathi, A. M.; Su, W. N.; Hwang, B. J. In Situ Analytical Techniques for Battery Interface Analysis. *Chemical Society Reviews*. Royal Society of Chemistry February 7, 2018, pp 736–751. https://doi.org/10.1039/c7cs00180k.

(29) Waldmann, T.; Iturrondobeitia, A.; Kasper, M.; Ghanbari, N.; Aguesse, F. F.; Bekaert, E.; Daniel, L.; Genies, S.; Gordon, I. J.; Löble, M. W.; De Vito, E.; Wohlfahrt-Mehrens, M. Review-Post-Mortem Analysis of Aged Lithium-Ion Batteries: Disassembly Methodology and Physico-Chemical Analysis Techniques. *J. Electrochem. Soc.* **2016**, *163* (10), A2149–A2164. https://doi.org/10.1149/2.1211609jes.

(30) Philippe, B.; Hahlin, M.; Edström, K.; Gustafsson, T.; Siegbahn, H.; Rensmo, H. Photoelectron Spectroscopy for Lithium Battery Interface Studies. *J. Electrochem. Soc.* **2016**, *163* (2), A178–A191. https://doi.org/10.1149/2.0051602jes.

(31) Mosby, J. M.; Prieto, A. L. Direct Electrodeposition of Cu_2Sb for Lithium-Ion Battery Anodes. *J. Am. Chem. Soc.* **2008**, *130* (32), 10656–10661. https://doi.org/10.1021/ja801745n.

(32) Schneider, J. B.; Agocs, D. B.; Prieto, A. L. Design of a Sample Transfer Holder to Enable Air-Free X-Ray Photoelectron Spectroscopy. **2020**.

(33) Tarascon, J. M.; Morcrette, M.; Saint, J.; Aymard, L.; Janot, R. On the Benefits of Ball Milling within the Field of Rechargeable Li-Based Batteries. *COMPTES RENDUS Chim.* **2005**, *8* (1), 17–26. https://doi.org/10.1016/j.crci.2004.12.006.

(34) Webb, S. A.; Baggetto, L.; Bridges, C. A.; Veith, G. M. The Electrochemical Reactions of Pure Indium with Li and Na: Anomalous Electrolyte Decomposition, Benefits of FEC Additive, Phase Transitions and Electrode Performance. *J. Power Sources* **2014**, *248*, 1105–1117. https://doi.org/10.1016/j.jpowsour.2013.10.033.

(35) Seo, D. M.; Nguyen, C. C.; Young, B. T.; Heskett, D. R.; Woicik, J. C.; Lucht, B. L. Characterizing Solid Electrolyte Interphase on Sn Anode in Lithium Ion Battery. *J. Electrochem. Soc.* **2015**, *162* (13), A7091–A7095. https://doi.org/10.1149/2.0121513jes.

(36) Gimble, N. J.; Kraynak, L. A.; Schneider, J. B.; Schulze, M. C.; Prieto, A. L. X-Ray Photoelectron Spectroscopy as a Probe for Understanding the Potential-Dependent Impact of Fluoroethylene Carbonate on the Solid Electrolyte Interface Formation in Na/Cu2Sb Batteries. **2020**.

(37) Aurbach, D.; Daroux, M.; Faguy, P.; Yeager, E. The Electrochemistry of Noble Metal Electrodes in Aprotic Organic Solvents Containing Lithium Salts. *J. Electroanal. Chem.* **1991**, *297* (1), 225–244. https://doi.org/10.1016/0022-0728(91)85370-5.

(38) Malmgren, S.; Ciosek, K.; Lindblad, R.; Plogmaker, S.; Kühn, J.; Rensmo, H.; Edström, K.; Hahlin, M. Consequences of Air Exposure on the Lithiated Graphite SEI. *Electrochim. Acta* **2013**, *105*, 83–91. https://doi.org/10.1016/j.electacta.2013.04.118.

(39) Edström, K.; Herstedt, M.; Abraham, D. P. A New Look at the Solid Electrolyte Interphase on Graphite Anodes in Li-Ion Batteries. *J. Power Sources* **2006**, *153* (2), 380–384. https://doi.org/10.1016/j.jpowsour.2005.05.062.

(40) Oswald, S. Binding Energy Referencing for XPS in Alkali Metal-Based Battery Materials Research (I): Basic Model Investigations. *Appl. Surf. Sci.* **2015**, *351*, 492–503. https://doi.org/10.1016/j.apsusc.2015.05.029.

(41) Wood, K. N.; Teeter, G. XPS on Li-Battery-Related Compounds: Analysis of Inorganic SEI Phases and a Methodology for Charge Correction. *ACS Appl. ENERGY Mater.* **2018**, *1* (9), 4493–4504. https://doi.org/10.1021/acsaem.8b00406.

(42) Leung, K.; Soto, F.; Hankins, K.; Balbuena, P. B.; Harrison, K. L. Stability of Solid Electrolyte Interphase Components on Lithium Metal and Reactive Anode Material Surfaces. *J. Phys. Chem. C* **2016**, *120* (12), 6302–6313. https://doi.org/10.1021/acs.jpcc.5b11719.

(43) Chamas, M.; Mahmoud, A.; Tang, J.; Sougrati, M. T.; Panero, S.; Lippens, P.-E. E. Aging Processes in Lithiated FeSn2 Based Negative Electrode for Li-Ion Batteries: A New Challenge for Tin Based Intermetallic Materials. *J. Phys. Chem. C* **2017**, *121* (1), 217–224. https://doi.org/10.1021/acs.jpcc.6b11302.

(44) Song, S.-W. W.; Baek, S.-W. W. Surface Layer Formation on Sn Anode: ATR FTIR Spectroscopic Characterization. *Electrochim. Acta* **2009**, *54* (4), 1312–1318. https://doi.org/10.1016/j.electacta.2008.09.021.

(45) Naille, S.; Dedryvere, R.; Martinez, H.; Leroy, S.; Lippens, P.-E. E.; Jumas, J. C.-C.; Gonbeau, D.; Dedryvère, R.; Martinez, H.; Leroy, S.; Lippens, P.-E. E.; Jumas, J. C.-C.; Gonbeau, D. XPS Study of Electrode/Electrolyte Interfaces of η-Cu6Sn5 Electrodes in Li-Ion Batteries. *J. Power Sources* **2007**, *174* (2), 1086–1090. https://doi.org/10.1016/j.jpowsour.2007.06.043.

(46) Tasaki, K.; Goldberg, A.; Lian, J.-J.; Walker, M.; Timmons, A.; Harris, S. J. Solubility of Lithium Salts Formed on the Lithium-Ion Battery Negative Electrode Surface in Organic Solvents. *J. Electrochem. Soc.* **2009**, *156* (12), A1019–A1027. https://doi.org/10.1149/1.3239850.

(47) Philippe, B.; Valvo, M.; Lindgren, F.; Rensmo, H.; Edström, K. Investigation of the Electrode/Electrolyte Interface of Fe2O3 Composite Electrodes: Li vs Na Batteries. *Chem. Mater.* **2014**, *26* (17), 5028–5041. https://doi.org/10.1021/cm5021367.

(48) Somerville, L.; Bareño, J.; Jennings, P.; McGordon, A.; Lyness, C.; Bloom, I. The Effect of Pre-Analysis Washing on the Surface Film of Graphite Electrodes. *Electrochim. Acta* **2016**, *206*, 70–76. https://doi.org/10.1016/j.electacta.2016.04.133.

(49) Dedryvère, R.; Laruelle, S.; Grugeon, S.; Gireaud, L.; Tarascon, J.-M. M.; Gonbeau, D. XPS Identification of the Organic and Inorganic Components of the Electrode/Electrolyte Interface Formed on a Metallic Cathode. *J. Electrochem. Soc.* **2005**, *152* (4), A689–A696. https://doi.org/10.1149/1.1861994.

(50) Li, J.-T. T.; Światowska, J.; Maurice, V.; Seyeux, A.; Huang, L.; Sun, S.-G. G.; Marcus, P. XPS and ToF-SIMS Study of Electrode Processes on Sn-Ni Alloy Anodes for Li-Ion Batteries. *J. Phys. Chem. C* **2011**, *115* (14), 7012–7018. https://doi.org/10.1021/jp201232n.

(51) Li, J.-T. T.; Swiatowska, J.; Seyeux, A.; Huang, L.; Maurice, V.; Sun, S.-G. G.; Marcus, P. XPS and ToF-SIMS Study of Sn – Co Alloy Thin Films as Anode for Lithium Ion Battery. *J. Power Sources* **2010**, *195* (24, SI), 8251–8257. https://doi.org/10.1016/j.jpowsour.2010.07.043.

(52) v. Cresce, A.; Russell, S. M.; Baker, D. R.; Gaskell, K. J.; Xu, K. In Situ and Quantitative Characterization of Solid Electrolyte Interphases. *NANO Lett.* **2014**, *14* (3), 1405–1412. https://doi.org/10.1021/nl404471v.

(53) Williard, N.; Sood, B.; Osterman, M.; Pecht, M. Disassembly Methodology for Conducting Failure Analysis on Lithium-Ion Batteries. *J. Mater. Sci. Electron.* **2011**, *22* (10), 1616–1630. https://doi.org/10.1007/s10854-011-0452-4.

(54) Greczynski, G.; Hultman, L. X-Ray Photoelectron Spectroscopy: Towards Reliable Binding Energy Referencing. *Prog. Mater. Sci.* **2020**, *107*, 100591. https://doi.org/10.1016/j.pmatsci.2019.100591.

(55) Lindgren, F.; Rehnlund, D.; Källquist, I.; Nyholm, L.; Edström, K.; Hahlin, M.; Maibach, J. Breaking Down a Complex System: Interpreting PES Peak Positions for Cycled Li-Ion Battery Electrodes. *J. Phys. Chem. C* **2017**, *121* (49), 27303–27312. https://doi.org/10.1021/acs.jpcc.7b08923.

(56) El-Jawad, M.; Chemin, J.-L. L.; Gilles, B.; Maillard, F. A Portable Transfer Chamber for Electrochemical Measurements on Electrodes Prepared in Ultra-High Vacuum. *Rev. Sci. Instrum.* **2013**, *84* (6), 1–6. https://doi.org/10.1063/1.4809936.

(57) Celio, H. Interface Designed with Differential Pumping and Built-In Figure of Merit Method to Monitor Chambers Where Environmentally Sensitive Samples Are Prepared and Transferred for Analysis. US 9,945,761 B2, 2018.

(58) Oswald, S.; Hoffmann, M.; Zier, M. Peak Position Differences Observed during XPS Sputter Depth Profiling of the SEI on Lithiated and Delithiated Carbon-Based Anode Material for Li-Ion Batteries. *Appl. Surf. Sci.* **2017**, *401*, 408–413. https://doi.org/10.1016/j.apsusc.2016.12.223.

(59) Kraynak, L. A.; Schneider, J. D.; Prieto, A. L. Exploring the Role of Vinylene Carbonate in the Passivation and Capacity Retention of Cu_2Sb Thin Film Anodes. *Submitt. to J. Phys. Chem. C* **2020**.

(60) Ehinon, K. K. D.; Naille, S.; Dedryvère, R.; Lippens, P.-E.; Jumas, J.-C.; Gonbeau, D. Ni3Sn4 Electrodes for Li-Ion Batteries: Li-Sn Alloying Process and Electrode/Electrolyte Interface Phenomena. *Chem. Mater.* **2008**, *20* (16), 5388–5398. https://doi.org/10.1021/cm8006099.

(61) Dedryvère, R.; Gireaud, L.; Grugeon, S.; Laruelle, S.; Tarascon, J. M.; Gonbeau, D. Characterization of Lithium Alkyl Carbonates by X-Ray Photoelectron Spectroscopy: Experimental and Theoretical Study. *J. Phys. Chem. B* **2005**, *109* (33), 15868–15875. https://doi.org/10.1021/jp051626k.

(62) Stjerndahl, M.; Bryngelsson, H.; Gustafsson, T.; Vaughey, J. T.; Thackeray, M. M.; Edström, K. Surface Chemistry of Intermetallic AlSb-Anodes for Li-Ion Batteries. *Electrochim. Acta* **2007**, *52* (15), 4947–4955. https://doi.org/10.1016/j.electacta.2007.01.064.

(63) El Ouatani, L.; Dedryvre, R.; Siret, C.; Biensan, P.; Reynaud, S.; Iraţabal, P.; Gonbeau, D. The Effect of Vinylene Carbonate Additive on Surface Film Formation on Both Electrodes in Li-Ion Batteries. *J. Electrochem. Soc.* **2009**, *156* (2), A103–A113. https://doi.org/10.1149/1.3029674.

(64) Shiraishi, S.; Kanamura, K.; Takehara, Z. I. Influence of Initial Surface Condition of Lithium Metal Anodes on Surface Modification with HF. *J. Appl. Electrochem.* **1999**, *29* (7), 869–881.

(65) Zhang, P.; Sham, T. K. X-Ray Studies of the Structure and Electronic Behavior of Alkanethiolate-Capped Gold Nanoparticles: The Interplay of Size and Surface Effects. *Phys. Rev. Lett.* **2003**, *90* (24), 1–4. https://doi.org/10.1103/PhysRevLett.90.245502.

(66) Zhao, D.; Wang, J.; Wang, P.; Liu, H.; Li, S. Regulating the Composition Distribution of Layered SEI Film on Li-Ion Battery Anode by LiDFBOP. *Electrochim. Acta* **2020**, *337*, 135745. https://doi.org/10.1016/j.electacta.2020.135745.

(67) Boniface, M.; Quazuguel, L.; Danet, J.; Guyomard, D.; Moreau, P.; Bayle-Guillemaud, P. Nanoscale Chemical Evolution of Silicon Negative Electrodes Characterized by Low-Loss STEM-EELS. *NANO Lett.* **2016**, *16* (12), 7381–7388. https://doi.org/10.1021/acs.nanolett.6b02883.

(68) Ayache, M.; Lux, S. F.; Kostecki, R. IR Near-Field Study of the Solid Electrolyte Interphase on a Tin Electrode. *J. Phys. Chem. Lett.* **2015**, *6* (7), 1126–1129. https://doi.org/10.1021/acs.jpclett.5b00263.

(69) Lu, P.; Li, C.; Schneider, E. W.; Harris, S. J. Chemistry, Impedance, and Morphology Evolution in Solid Electrolyte Interphase Films during Formation in Lithium Ion Batteries. *J. Phys. Chem. C* **2014**, *118* (2), 896–903. https://doi.org/10.1021/jp4111019.

(70) Ferraresi, G.; Villevieille, C.; Czekaj, I.; Horisberger, M.; Novak, P.; El Kazzi, M. SnO2 Model Electrode Cycled in Li-Ion Battery Reveals the Formation of Li2SnO3 and Li8SnO6 Phases through Conversion Reactions. *ACS Appl. Mater. Interfaces* **2018**, *10* (10), 8712–8720. https://doi.org/10.1021/acsami.7b19481.

(71) Philippe, B.; Mahmoud, A.; Ledeuil, J. B.; Sougrati, M. T.; Edström, K.; Dedryvère, R.; Gonbeau, D.; Lippens, P. E. MnSn2 Electrodes for Li-Ion Batteries: Mechanisms at the Nano Scale and Electrode/Electrolyte Interface. *Electrochim. Acta* **2014**, *123*, 72–83. https://doi.org/10.1016/j.electacta.2014.01.010.

(72) Beard, B. C. Sodium Salts of Chlorine Oxyacid Anions, Cl(+7), Perchlorate, XPS Comparison Spectra. *Surf. Sci. Spectra* **1993**, *2* (2), 97–103. https://doi.org/10.1116/1.1247738.

(73) Beard, B. C. Sodium Salts of Chlorine Oxyacid Anions, Cl(+5), Chlorate, XPS Comparison Spectra. *Surf. Sci. Spectra* **1993**, *2* (1), 26–30. https://doi.org/10.1116/1.1247721.

(74) Beard, B. C. Sodium Salts of Chlorine Oxyacid Anions, Cl(+3), Chlorite, XPS Comparison Spectra. *Surf. Sci. Spectra* **1993**, *2* (1), 20–25. https://doi.org/10.1116/1.1247720.

CHAPTER 3: EXPLORING THE ROLE OF VINYLENE CARBONATE IN THE PASSIVATION AND CAPACITY RETENTION OF Cu_2Sb THIN FILM ANODES[♠]

Chapter Summary

Electrolyte additives such as vinylene carbonate (VC) have been demonstrated to improve the capacity retention for many types of Li-ion battery electrodes, including intermetallic alloying anodes, but it is still unclear why VC extends the cycle lifetime of copper antimonide (Cu_2Sb) anodes so dramatically. Here we have studied how VC affects the solid electrolyte interface (SEI) formed on Cu_2Sb thin film anodes in fluorine-free electrolyte solutions in order to better understand which non-fluorinated species may play an important role in effective Cu_2Sb passivation. Using differential capacity analysis and X-ray photoelectron spectroscopy (XPS), we have found that VC effectively passivates Cu_2Sb and prevents Cu/Cu_2Sb oxidation at high potentials. Carbonate species from the reduction of VC seem to play an important role in passivation, while inorganic species like $LiClO_4$ from the F-free supporting electrolyte do not seem to be beneficial.

3.1) Introduction

Many research efforts in the energy storage field have been focused on increasing the energy density of the anode materials used in secondary battery technologies such as lithium-ion batteries.[1,2] Lithium alloying materials like silicon, tin, antimony, and intermetallics have garnered interest as alternative anode materials to replace graphite, a lithium intercalation anode, due to their large theoretical gravimetric and volumetric capacities.[2,3] However, these materials suffer from problems such

---

[♠] This manuscript was submitted for publication in the American Chemical Society *Journal of Physical Chemistry C* with Leslie A. Kraynak, Jacob D. Schneider, and Amy L. Prieto as authors and is currently under revision. Leslie A. Kraynak wrote this manuscript, and Jacob D. Schneider designed and fabricated the air free XPS sample holder that was essential for acquiring the data presented in this chapter. The potential regions used for studying the regions of SEI formation and growth were based on previous work from Timothy S. Arthur and Matthew T. Rawls. Amy L. Prieto provided guidance and edited the manuscript.

as large irreversible capacities and short cycle lifetimes.[3] One contributing factor is the large volume change associated with lithiation and delithiation of these materials, which leads to cracking, pulverization, and loss of electrical contact of the anode.[3] Interfacial problems associated with the solid electrolyte interface (SEI) also contribute to the issues associated with these anode materials.[3,4]

The SEI plays an important role in battery performance, affecting the anode irreversible capacity, cycle lifetime, self-discharge, rate capability, and safety, making it a crucial component in lithium-ion batteries.[5,6] It forms on Li-ion battery anodes due to the instability of the liquid electrolyte over the potential window where rechargeable batteries operate.[6–8] The heterogeneous, amorphous film, composed of the decomposition products of organic carbonate solvents and the lithium supporting electrolyte, is difficult to characterize due to its heterogeneity, reactivity to air and moisture, and sensitivity to many variables.[6] Variables that can influence the SEI formation, composition, and properties include cycling conditions,[9,10] electrolyte composition,[11–15] and the anode composition and fabrication.[16–22]

Much of the battery community's understanding of the SEI comes from studies of the SEI on graphite anodes.[6] However, it is crucial to study the SEI on next generation alloying and conversion anode materials because while the SEI formed on graphite is relatively stable, the large volume changes associated with cycling alloying anodes means that the SEI is forming throughout the cycling process as new electrode surfaces are exposed due to cracking.[3,23] As such, the requirements of the SEIs formed on these anode materials are different than those of graphite.[5,23] In addition to passivating the electrode surface and allowing for good Li^+ conduction, a stable SEI on high capacity anodes would also be robust enough to accommodate large volume changes.[5,16] Studies of the SEI formed on Si have contributed to the understanding of SEI formation on alloying anodes, but there is still much to be learned about the SEI on metallic and intermetallic alloying electrode materials.[10,14,15,17,24–26]

Intermetallic electrodes, such as SnSb, AlSb, and Cu_2Sb, are particularly attractive materials for SEI studies not only because of the dearth of knowledge of intermetallic SEI formation and composition but also because these materials have interesting chemistries that could enrich fundamental knowledge of the SEI. The variety of metallic elements, both active and inactive towards lithium alloying, that make up intermetallic anode materials result in varying surface reactivities and different lithiation/delithiation reactions and potentials.[4,27–30] Additionally, intermetallic electrodes can be prepared without additives or binders via electrodeposition and physical vapor deposition methods.[31–34] This makes these anodes ideal candidates for fundamental SEI studies because binders and conductive additives can affect SEI formation, complicating studies of SEI formation and composition.[19–21,35,36] Another advantage of electrodeposition in particular as a fabrication method for intermetallic anodes is that it enables both 2D and 3D anode morphologies, which is a useful synthetic control to have for interfacial studies where increased surface area may be desired.[31,37,38]

One route to stabilizing the SEI is to use small amounts of electrolyte additives such as fluoroethylene carbonate (FEC) and vinylene carbonate (VC).[39] Surprisingly, even though these additives were initially found to improve the SEI on graphite anodes, they also result in dramatically improved cycle lifetimes for alloying anodes.[15,38–40] There are many hypotheses about why these additives work so well for all types of anode materials. The prevailing hypothesis is that they behave as a sacrificial component that is reduced before the other electrolyte components to help passivate the electrode surface and prevent excessive SEI formation,[39,40] although computational work suggests that additives like VC may help by altering the reduction pathways of the carbonate solvents.[41] Studies on Si anodes suggest that FEC and VC also improve the cycling performance of alloying anodes by forming cross linking moieties in the SEI to improve the mechanical stability.[24–26] Other work has suggested that these additives favor the formation of components like LiF, Li_2CO_3, and/or polycarbonates to help passivate the electrode surface more effectively.[15,42–44]

Previous work from our group has revealed that FEC and VC effectively stabilize the interface of Cu_2Sb nanowire electrodes cycled in $LiPF_6$-based carbonate electrolyte, although it still not entirely clear why these additives extend the cycle lifetime of Cu_2Sb so dramatically, especially VC, which resulted in the longest lifetime.[38] In the current work, the SEI formed on Cu_2Sb over different potential regions in electrolyte with and without VC was characterized using differential capacity analysis and X-ray photoelectron spectroscopy (XPS) to better understand what types of species or functional groups in the SEI formed with VC may be beneficial for Cu_2Sb electrodes. In this study, the SEIs formed on Cu_2Sb thin film anodes in $LiClO_4$-based carbonate electrolyte solutions were examined to eliminate some variables associated with the use of $LiPF_6$-based electrolytes that could complicate the study. $LiPF_6$-based electrolytes often contain small amounts of very reactive HF, which can react with electrolyte and SEI components and affect the SEI composition, convoluting the results.[45] Additionally, while inorganic species such as LiF are thought to passivate the electrode surface, eliminating fluorinated components from the electrolyte may help reveal what other types of organic and inorganic species are beneficial for effectively passivating the surface of intermetallic electrodes.[14,15,46]

3.2) Experimental

Materials

Citric acid monohydrate (Fisher Scientific, certified ACS), antimony (III) oxide nanopowder (Sb_2O_3, <250 nm, Aldrich ≥99.99%), and copper (II) nitrate hemipentahydrate ($Cu(NO_3)_2{\cdot}2.5H_2O$, Aldrich ≥99.99%+) were used as received. Saturated potassium hydroxide was prepared from pellets (KOH, Fisher Scientific, Certified ACS). Phosphoric acid (H_3PO_4, 85% EMD Chemicals, ACS grade) was used to make a 2:1 (vol) H_3PO_4:H_2O solution. Ultrapure water (18 MΩ, Millipore) was used for all experiments. Dimethyl carbonate (DMC, anhydrous, ≥99%), diethyl carbonate (DEC, anhydrous, ≥99%), vinylene carbonate (VC, 99% with 80 ppm butylated hydroxytoluene added as stabilizer), and lithium perchlorate ($LiClO_4$, battery grade, 99.999%) were purchased from Aldrich and kept in an Ar-filled glovebox without

further purification. Ethylene carbonate (EC, anhydrous, Aldrich 99%) was recrystallized from ethanol, dried, and stored in an Ar-filled glovebox. Lithium metal was stored in an Ar-filled glovebox and cleaned prior to use by manually scraping away any surface oxide layer present to reveal the metallic Li underneath. Glass fiber separators (Whatman GF/A) were dried in an oven prior to being pumped into an Ar-filled glovebox for storage and use.

Anode preparation

Copper antimonide (Cu_2Sb) was electrodeposited at room temperature following a previously established procedure.[32] Briefly, Cu_2Sb was electrodeposited onto copper substrates (110 Cu foil, 0.002" thick, McMaster-Carr) from a solution containing 400 mM citric acid monohydrate, 25 mM Sb_2O_3 nanopowder, and 40 mM $Cu(NO_3)_2 \cdot 2.5H_2O$ and adjusted to pH 6 with saturated KOH. The Cu_2Sb films were electrodeposited at −1.05 V vs. a saturated calomel electrode (SCE) onto copper substrates for 10 minutes at room temperature using a Gamry Reference 3000 potentiostat. The ca. 1" x 1.5" copper foil substrates were cleaned prior to electrodeposition by sonicating in isopropanol for 3 minutes to remove organic residue, followed by electropolishing in a H_3PO_4 solution for 30 seconds to remove copper oxide; the substrates were then covered on one side with Kapton tape. After electrodeposition, the Cu_2Sb films were rinsed thoroughly with water, followed by isopropanol, and then dried before transferring to an Ar-filled glovebox to minimize native oxide growth. The Cu_2Sb mass loading for the 10-minute electrodepositions was ca. 1.0 mg/cm^2, determined by mass difference. The X-ray diffraction (XRD) pattern from a representative Cu_2Sb film can be found in Appendix B, Figure 1B.

Electrochemical half-cell preparation and cycling

Swagelok half-cells were assembled in an Ar-filled glovebox (O_2 < 1.0 ppm, H_2O < 0.5 ppm). Circular punches (1.27 cm diameter) of the electrodeposited Cu_2Sb films were sealed in the Swagelok cell body. Two polypropylene separators (Celgard, 25 µm) and a glass fiber separator, soaked in either 200 µL of 1 M $LiClO_4$ in EC/DMC/DEC (1:1:1 vol) electrolyte or 200 µL of 1 M $LiClO_4$ in EC/DMC/DEC (1:1:1

vol) with 5% (vol) VC added, were placed between the Cu_2Sb working electrode and lithium metal counter/pseudo reference electrode. All potentials in this work are referenced to the Li/Li^+ couple unless noted otherwise.

All half cells were cycled using an Arbin BT-2143 battery tester with an 18-hour rest step before cycling. Half-cells for the cycle lifetime studies were cycled galvanostatically between 0.05 V and 3.0 V at a C/20 rate (ca. 15 $\mu A/cm^2$). For the SEI preparation, the Cu_2Sb half-cells were galvanostatically reduced from the open circuit potential (ca. 2.3 V) at a C/20 rate (ca. 15 $\mu A/cm^2$) until a particular voltage limit was reached. Then the current polarity was switched so that the Cu_2Sb was oxidized to a higher, predetermined potential. At that point, the cells were cycled galvanostatically over that potential range for a total of 20 cycles. Three different potential regions were chosen to study SEI formation at different stages of half-cell cycling: the high potential region (HPR) between 1.8 V and 3.0 V, the middle potential region (MPR) between 0.9 V and 1.8 V, and the low potential region (LPR) between 0.05 V and 0.9 V. For a given potential region, half-cells were made using the $LiClO_4$-based electrolytes with and without VC using Cu_2Sb punches from the same film to minimize variability due to differences between films. After galvanostatic cycling was complete, the half cells had a 24 hour rest step and were then dismantled in an Ar-filled glovebox within 1 to 2 days of cycling completion. All electrodes were washed with ca. 1 mL of DMC so that only the components incorporated into the SEI layer adhered to the electrode surface remained for characterization.

Characterization

X-ray photoelectron spectroscopy (XPS) measurements were performed in order to analyze the chemical bonding and composition of the SEI samples using a Physical Electronics (PHI) 5800 series Multi-Technique ESCA system with a monochromatic Al Kα (hv = 1486.6 eV) source operating at 350.0 W. Samples were transferred under vacuum directly from the Ar-filled glovebox to the XPS sample introduction chamber using a custom-built sample holder so that the SEI samples were never exposed to

air prior to XPS characterization.[47] Samples were pumped down for 30 minutes prior to characterization. An electron flood gun operating with a 5 μA emission current, 1.5 V bias voltage, and 40.0 V extractor voltage was used for charge neutralization on all SEI samples. High resolution (HRES) spectra for the regions of interest (C 1s, Cl 2p, O 1s/Sb 3d, Li 1s, and Cu 2p) were collected sequentially with a pass energy of 23.5 eV in intervals of 0.100 eV/step. The instrument base pressure was 5 x 10^{-8} Torr or lower during data acquisition. Spectra were collected from at least 3 areas on each sample (area 126.7 mm^2) using a 0.6 mm by 2 mm spot size (area 1.2 mm^2) to ensure that any lateral heterogeneity in the SEI was accounted for. Short HRES scans were collected prior to the longer acquisitions so that any sample damage could be identified, although even the longer HRES scans were relatively short (20–30 minutes) to avoid prolonged beam exposure and sample damage.[48] In these studies, we were interested in studying relative changes in binding energies and speciation between samples rather than obtaining absolute binding energies; therefore, all HRES spectra were shifted so that either the Cl $2p_{3/2}$ peak for ClO_4^- was located at 208.6 eV or the Cl $2p_{3/2}$ peak for Cl^- was at 198.6 eV (if no ClO_4^- was detected) based on research suggesting that it is preferable to use SEI species for calibrating binding energies.[49] CasaXPS software (Version 2.3.16) was used for peak fitting and quantification of the HRES spectra. A nonlinear Shirley background and 30% Lorentzian/70% Gaussian line shape were used for peak fitting,[50] and PHI relative sensitivity factors corrected for angular distribution were used for quantification based on the peak fitting. More details about the peak fitting rationale and constraints used can be found in Appendix B.

3.3) Results and Discussion

Previous studies of the effects of additives on the cycling performance of Cu_2Sb in $LiPF_6$-based electrolyte have demonstrated that VC dramatically improves the cycle lifetime of Cu_2Sb nanowires,[38] and we have observed that it also improves the cycle lifetime of Cu_2Sb cycled in $LiClO_4$-based electrolyte. Binder- and additive-free Cu_2Sb films ca. 1 μm thick cycle for about 15 cycles at a C/20 rate in 1 M $LiClO_4$

in EC/DEC/DMC (1:1:1 vol) electrolyte before dropping to 80% of the initial capacity. However, despite the poor performance of Cu_2Sb films in $LiClO_4$-based electrolyte, the addition of 5% VC improves the cycle lifetime considerably. As shown in Figure 3.1, a ca. 1 µm thick Cu_2Sb film cycled over an extreme potential range (0.05 V to 3.0 V) at a C/20 rate shows no capacity fade after 20 cycles when VC is used as an additive; in fact, it cycles for about 70 cycles before exhibiting gradual capacity fade (see Figure B2 in the Appendix B). The Cu_2Sb film cycled with VC actually shows a slight increase in capacity after 10 cycles that is associated with electrochemical roughening or pulverization of the binder- and additive-free film that allows more of the active material to be accessed due to increased surface area.[51,52] The good capacity retention of the film cycled with VC despite electrode roughening or pulverization suggests that the SEI formed with VC has desirable mechanical properties that enable it to accommodate the large volume changes of the Cu_2Sb during cycling and keep the electrode material in good contact with the current collector as it is pulverized rather than delaminating from the substrate.

More insight into the failure of Cu_2Sb cycled in $LiClO_4$-based electrolyte and the increased capacity retention associated with VC can be gained from the differential capacity plots shown in Figure 3.2. The intense features of the differential capacity plots corresponding to Cu_2Sb lithiation and delithiation are similar for the Cu_2Sb cycled with and without VC and are in agreement with the previously reported lithium alloying and dealloying reactions of Cu_2Sb.[53,54] Looking at the much lower intensity peaks between 2.75 V and 1.0 V corresponding to electrolyte reduction and SEI formation processes in Figure B3 also reveals similarities between the samples cycled with and without VC. However, comparison of the differential capacity plots for the first 20 cycles of the Cu_2Sb half cells cycled with and without VC suggests that the failure of the film cycled without VC may be due in part to loss of electrical contact of the active material due to volume changes during lithiation/delithiation

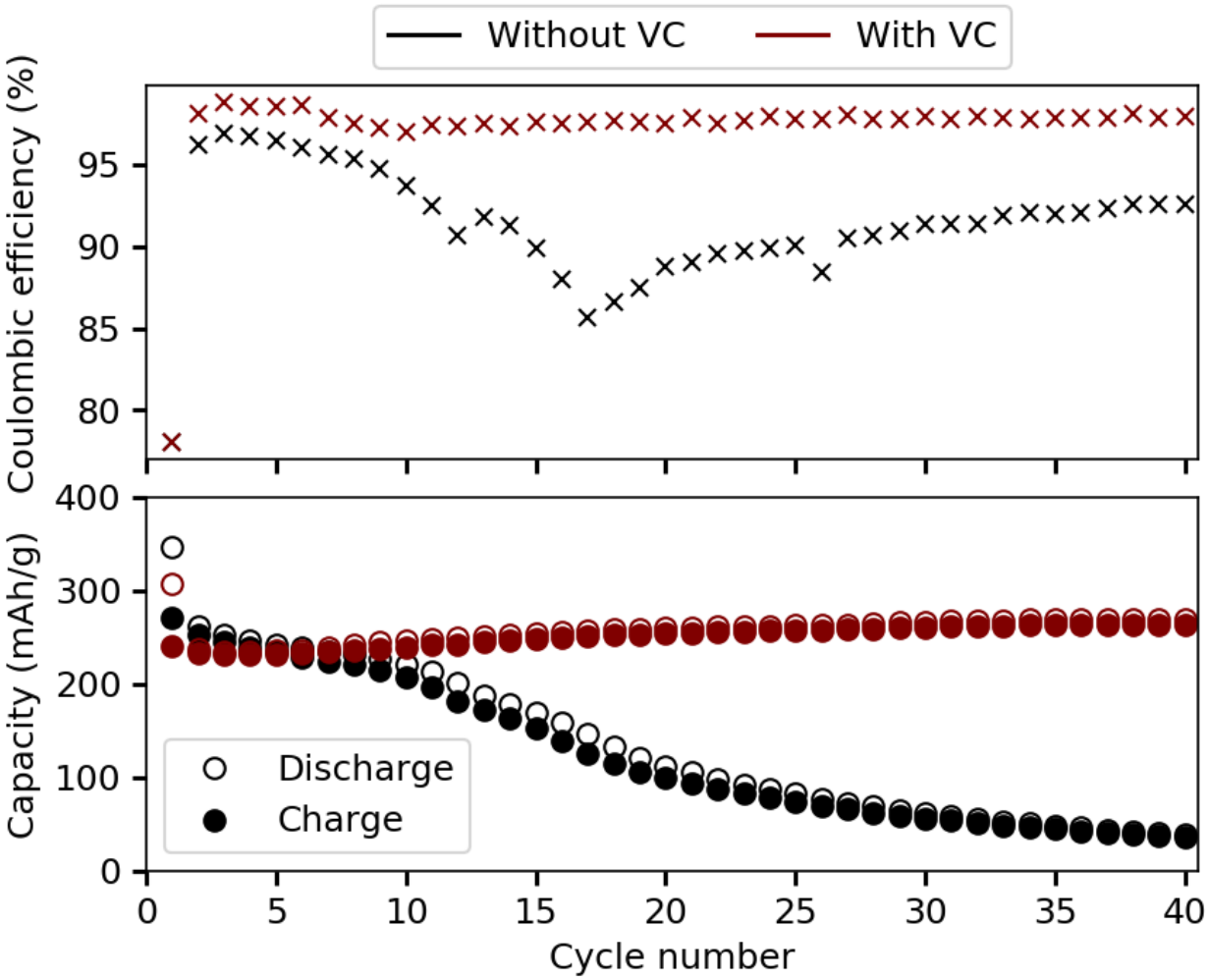

Figure 3.1: Coulombic efficiency and capacity data for 1 µm-thick Cu_2Sb films cycled at a C/20 rate between 0.05 V and 3.0 V vs. Li/Li^+ in $LiClO_4$-based electrolyte with and without 5% VC added for the first 40 cycles.

because the peaks for Cu_2Sb cycled without VC decrease in intensity with cycle number, unlike those for the Cu_2Sb cycled with VC, suggesting that for the film cycled without VC less active material is being lithiated and delithiated with continued cycling.[55] Again, this suggests that VC may help improve the physical properties of the SEI formed on Cu_2Sb, perhaps forming a more robust SEI that is better able to withstand the large volume changes during cycling and prevent cracking and delamination of the film that result in loss of electrical contact. Additionally, there seems to be a difference in the degree of passivation of the Cu_2Sb electrodes cycled with and without VC. The first cycle lithiation peaks shown in black in Figure 3.2 for Cu_2Sb cycled with VC are at slightly more negative overpotentials than those for the Cu_2Sb cycled without VC, especially for the phase transition at ca. 0.7 V, as demonstrated by the dotted grey lines on the right side of Figure 3.2. This suggests that even on the first cycle, the SEI formed on Cu_2Sb with VC is thick enough or passivating enough to slightly impede Li^+ transport compared to the SEI formed without VC.[55] Another striking difference between the differential capacity plots for the Cu_2Sb samples cycled with and without VC are the reduction and oxidation features at potentials above 2.5 V that are seen only for the Cu_2Sb cycled without VC. The differences in the electrochemistry for Cu_2Sb cycled without VC suggest some sort of compositional difference between the SEIs formed with and without VC that affect the electrochemistry of the electrode material and will be discussed in further detail below.

In order to learn about the compositional differences in the SEI formed from $LiClO_4$-based electrolyte with and without VC, Cu_2Sb was electrochemically cycled over three different potential regions to target different stages of SEI formation and growth. The three different regions were chosen based on the characteristics of the voltage profile for Cu_2Sb, shown in Figure 3.3. The high potential region (HPR), cycled between 1.8 V and 3.0 V, was chosen because it is well above the lithiation potential for Cu_2Sb and there is expected to be little to no SEI formation in this region, so any SEI formed by cycling over this potential region may provide insights into the types of species present during the

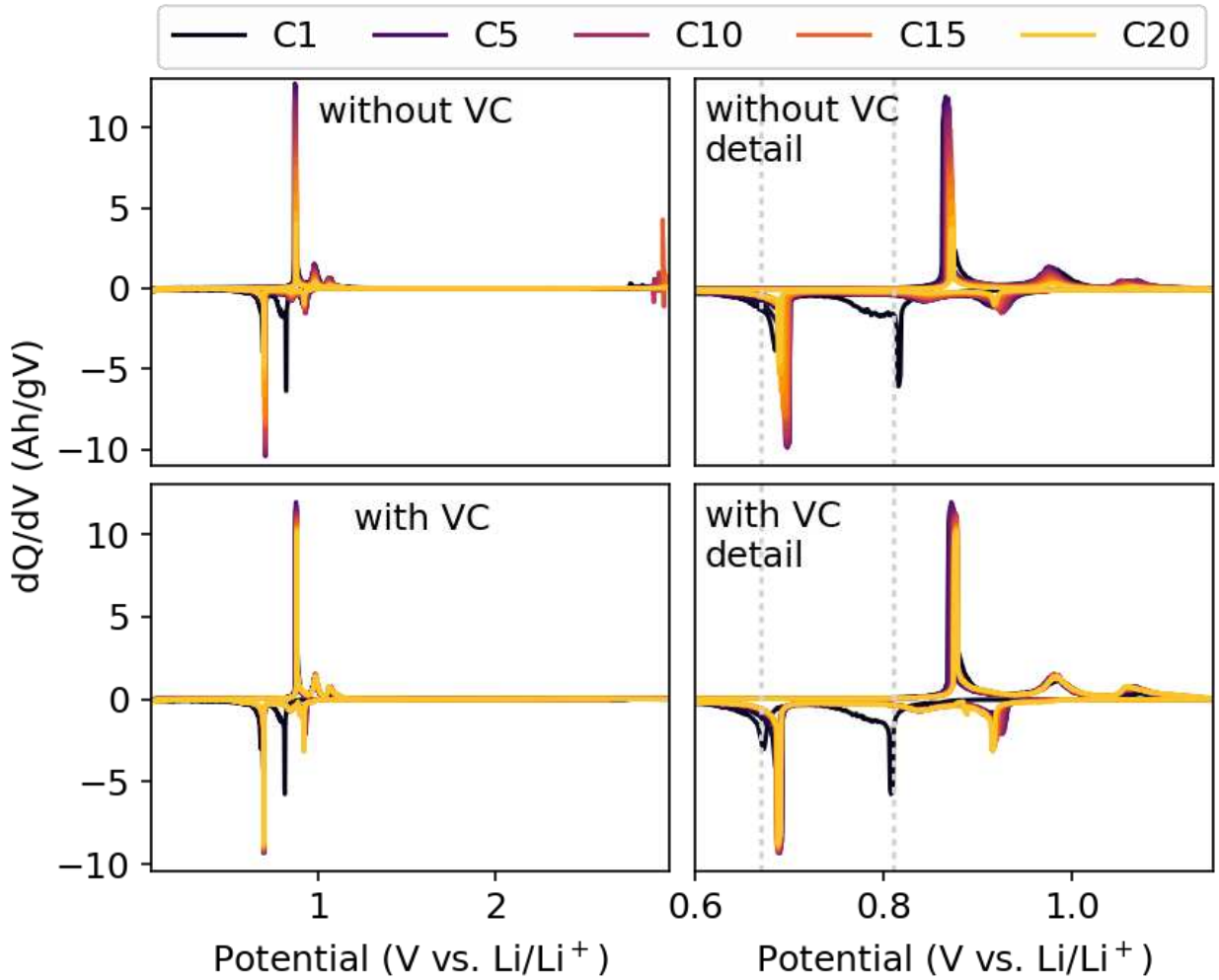

Figure 3.2: (Left) Full differential capacity plots for the first 20 cycles of 1 µm-thick Cu_2Sb films cycled at a C/20 rate between 0.05 V and 3.0 V vs. Li/Li^+ in $LiClO_4$-based electrolyte with (bottom) and without (top) 5% VC added. (Right) Zoomed in differential capacity plots showing the Cu_2Sb lithiation/delithiation features from the left plots in more detail.

initial stages of SEI formation. The middle potential region (MPR), cycled between 0.9 V and 1.8 V, is still higher than the Cu_2Sb lithiation potential, but based on the voltage profile, some capacity is going towards SEI formation and lithiation of surface oxides. The reported reduction potential for EC, DMC, and DEC on metallic electrodes is ca. 1.3 V, while VC reduction has been observed around 1.4 V,[56,57] and the reduction of surface oxides on Sb-based electrodes has been reported around 1.6 V.[58,59] Studying the SEI formed from cycling over the MPR is expected to provide insights into the electrolyte reactions that occur and the SEI species that are formed at higher reduction potentials. Finally, the low potential region (LPR), cycled between 0.9 V and 0.05 V, encompasses Cu_2Sb lithiation and is expected to provide insights into the electrolyte degradation and the types of SEI species that are formed at lower reduction potentials.

X-ray photoelectron spectroscopy (XPS) was used to determine the composition and speciation of the SEIs formed over different potential regions with and without VC as an additive. Due to the heterogeneous nature of the SEI, high resolution (HRES) XPS spectra from at least 3 different regions (1.2 mm^2 analysis area) were collected for each sample (total area 126.7 mm^2) to ensure that an accurate representation of the SEI was obtained. Representative regions for each type of SEI sample were chosen based on a combination of the spectral features and the percent atomic compositions determined from HRES peak fitting and quantification. The analysis regions for most of the SEI samples showed some differences in spectral features and quantification results, suggesting some lateral heterogeneity of the SEI, and two representative regions are reported for each sample to either reflect the sample heterogeneity or demonstrate the consistency between sample regions. In this set of experiments, most of the SEI samples were quite heterogeneous with the exception of the MPR VC SEI sample, which was relatively consistent in terms of spectral features and the percent atomic composition of the sample surface.

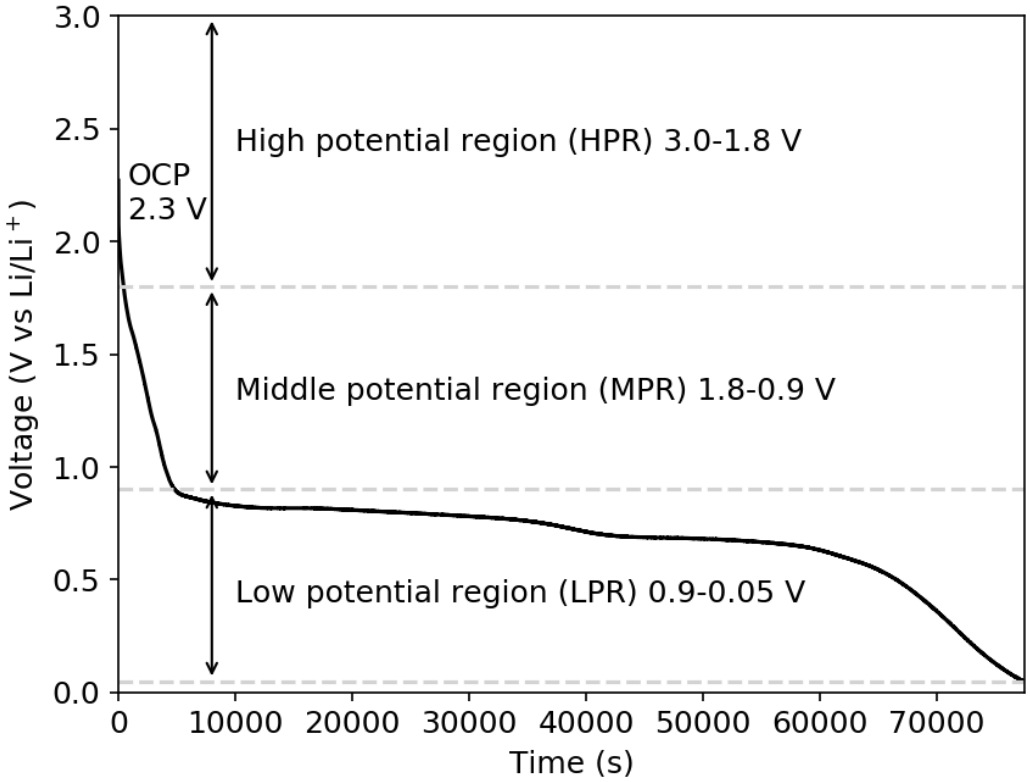

Figure 3.3: First cycle discharge (lithiation) of Cu_2Sb cycled with an applied current of 15 μA/cm^2. The features of the voltage profile were used to determine the potential limits for the three different regions of SEI formation chosen for this study: the high potential region (HPR), middle potential region (MPR), and low potential region (LPR).

The quantification results from the HRES peak fitting of the different SEI samples are shown in Figure 3.4 (See Tables B1–B3 for tabulated quantification results and Figures B4–B9 for all fitted spectra). Both the HPR and HPR VC SEIs are composed primarily of C (ca. 50–60%) and O (ca. 27–34%), with only small differences in composition for the samples with and without VC, which suggests that there is SEI formation at higher potentials even though it is not readily apparent from looking at the voltage profile in Figure 3.3. Additionally, a small amount of Sb (ca. 0.3–0.8%) and a slightly higher amount of Cu (ca. 1–4%) were detected in these samples. In Region 1 for both the HPR and HPR VC samples a small amount of Li (ca. 13–15%) was detected, while for Region 2 of both samples no Li was detected. Finally, the HPR SEI formed without VC tended to be more Cl rich (ca. 6%) than the HPR VC SEI

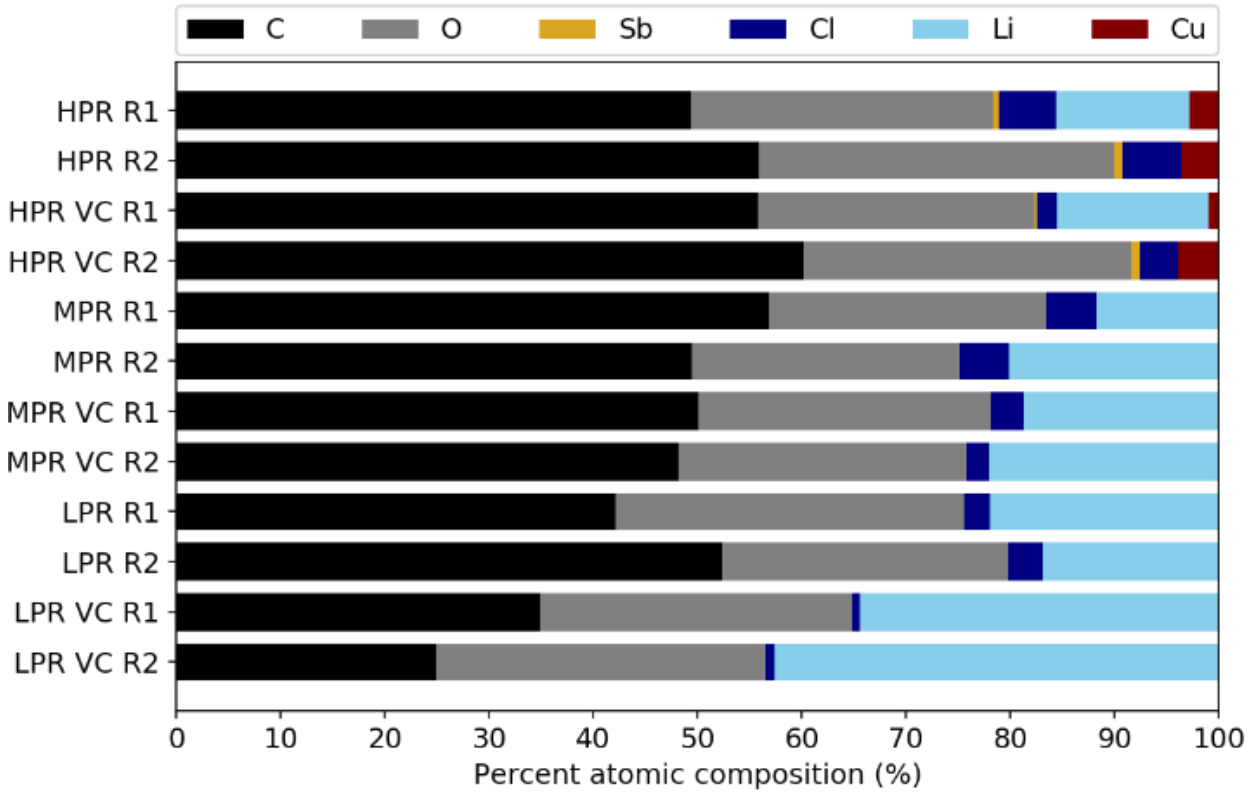

Figure 3.4: Percent atomic compositions for the representative regions (R1 and R2) of the SEI samples formed over different potential regions (HPR, MPR, and LPR) with and without VC, determined from XPS HRES peak fitting.

(ca. 2–4%). Looking at the features of the HRES spectra show more differences between the HPR SEIs formed with and without VC.

The Cl 2p HRES spectra are shown in Figure 3.5 (without fitted data for simplicity). As can be seen for the Cl 2p spectra of the HPR and HPR VC samples on the left of Figure 3.5, the Cl $2p_{3/2}$ and $2p_{1/2}$ peaks are around 208.6 eV and 209.7 eV, respectively, which is indicative of a perchlorate binding environment.[60] The ClO_4^- detected at the SEI surface for both samples cycled over the HPR is from the $LiClO_4$ supporting electrolyte; since the samples were rinsed with DMC prior to XPS characterization to remove residual salt species, this suggests that the ClO_4^- is being incorporated into the SEI.

Interpretation of the O 1s/Sb 3d HRES spectra shown in Figure 3.6 (also presented without fitted data for clarity) is more complicated than that of the Cl 2p spectra. The reported O 1s binding energies

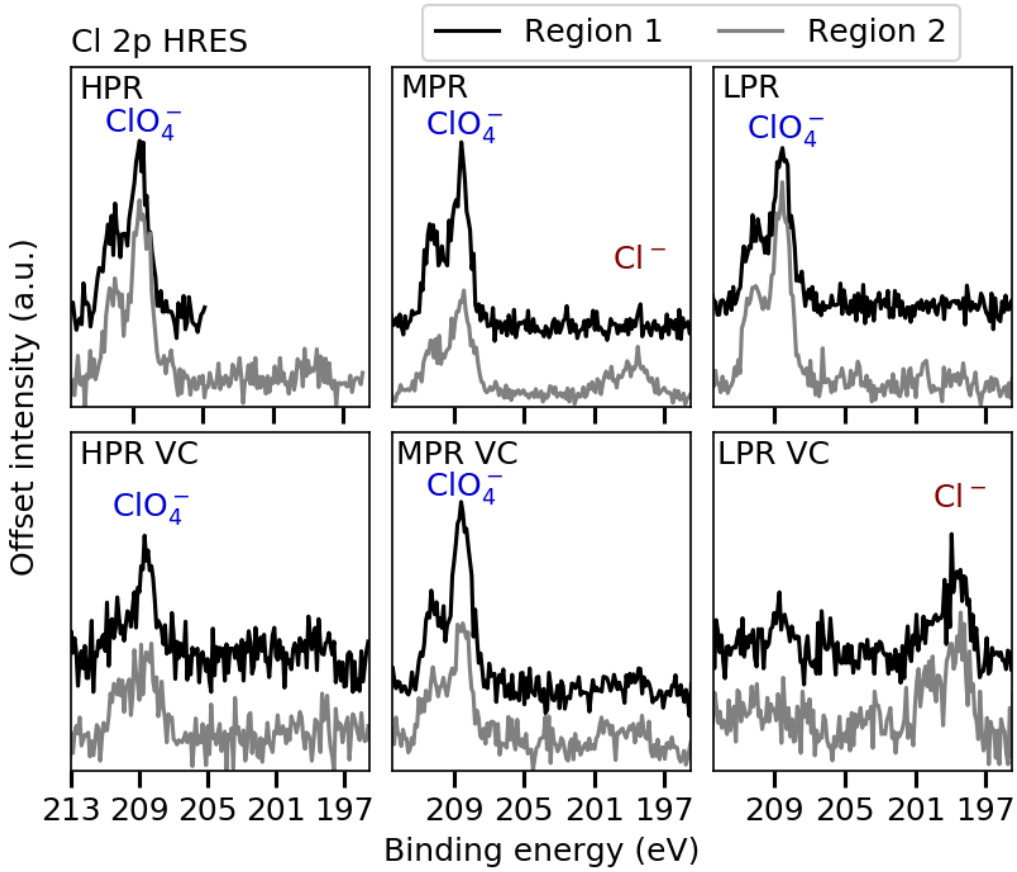

Figure 3.5: Cl 2p HRES spectra from the representative regions (Region 1 and Region 2) of the SEI samples formed over different potential regions (HPR, MPR, and LPR) with and without VC.

for proposed SEI species such as lithium alkyl carbonates and lithium carbonate (Li_2CO_3) range from 531.7 eV to 533.8 eV,[10,17,30,61–63] and the distinguishing O 1s peak for poly VC is located around 534.5 eV to 534.7 eV.[64,65] The reported O 1s binding energies for perchlorates range from 533.0 eV to 533.6 eV.[21,60,66] This makes it difficult to distinguish different binding environments for the SEI samples even when curve fitting is used to deconvolute the O 1s peaks. Additionally, the binding energies of Sb $3d_{5/2}$ peaks range from ca. 528 eV for Sb^0 to 531 eV for Sb oxides, further convoluting the O 1s spectra if Sb is present.[21,58,67] However, the overlapping binding energy ranges of the O 1s and Sb 3d spectra also provide a useful way to obtain rough SEI thickness estimates. The O 1s/Sb 3d HRES spectra for pristine Cu_2Sb (see Figure B10) shows intense Sb $3d_{5/2}$ and $3d_{3/2}$ peaks around 531.0 eV and 540.6 eV, respectively, for antimony oxide species from the surface oxide layer and less intense $3d_{5/2}$ and $3d_{3/2}$

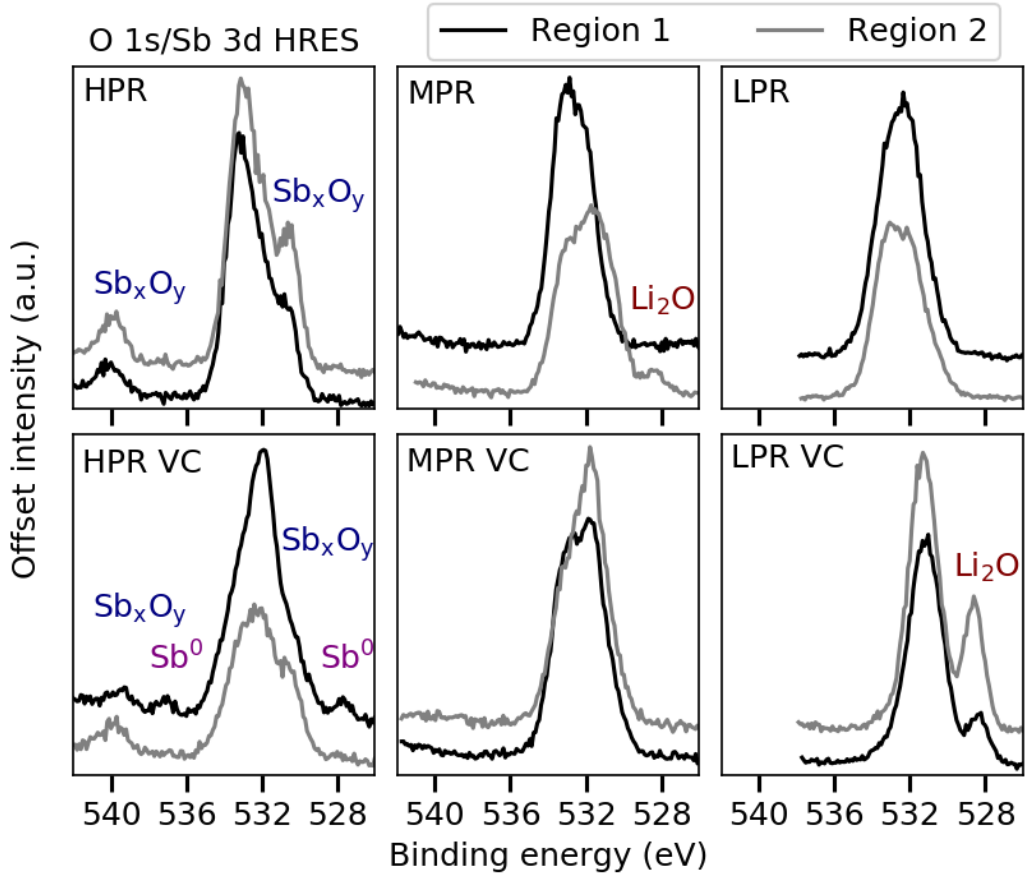

Figure 3.6: O 1s/Sb 3d HRES spectra from the representative regions (Region 1 and Region 2) of the SEI samples formed over different potential regions (HPR, MPR, and LPR) with and without VC.

peaks around 528.3 eV and 537.6 eV, respectively, corresponding to metallic antimony from the Cu_2Sb beneath the surface oxide layer. Both the HPR and HPR VC SEI samples are quite thin (<10 nm based on the information depth of XPS), as there are peaks corresponding to Sb oxide species from the surface oxide layer of the underlying Cu_2Sb film for both types of samples.[68] The HPR VC SEI may be thinner in some regions because metallic Sb peaks are also seen for Region 1 of the HPR VC SEI sample, suggesting that the HPR VC SEI is thin enough in some regions that the metallic Sb from Cu_2Sb can be detected in addition to the Sb oxide species from the Cu_2Sb surface oxide layer.

The presence of Cu in the HPR sample set may hold one of the keys to understanding the differences between the SEIs formed with and without VC. Given the small amount of Sb detected (<1%), the comparatively large amount of Cu (ca. 1–4%) detected for the HPR and HPR VC samples is

curious, as one would expect the Cu amount to be roughly twice that of Sb detected if it were due to signal from the underlying Cu_2Sb film rather 3–5 times the amount as is the case here. Based on the data discussed below, it seems that the considerable amount of Cu detected is due to Cu diffusion as a result of Cu/Cu_2Sb oxidation. Even though the HPR sample set was not discharged to low enough potentials to lithiate the Sb and extrude Cu out of Cu_2Sb (refer to Figure 3.3), it was charged to high enough potentials to result in Cu/Cu_2Sb oxidation (in aqueous solutions, Cu_2Sb oxidation was observed around −0.3 V to 0.0 V vs. a saturated sodium calomel electrode (SSCE) reference depending on solution conditions, which corresponds to ca. 2.5 V to 2.8 V vs. Li/Li^+).[32] This could result in more Cu present at the surface as it is oxidized and reduced when cycling over the HPR. This is more pronounced in the HPR sample without VC, for which about 3–4% Cu was detected for all regions of the sample; differential capacity analysis for the HPR SEI sample Figure 3.7 (top) shows the onset of an oxidation peak around 2.8 V and a reduction peak around 2.6 V that is not seen for the first discharge; these peaks are most likely due to the oxidation and reduction of Cu, respectively. There is also visual evidence to support this hypothesis; when disassembling half cells cycled up to 3.0 V in $LiClO_4$-based electrolyte without VC, the separators are often discolored as shown in Figure B11 due to the presence of Cu as confirmed by energy dispersive X-ray spectroscopy (EDS) in Figure B12. Differential capacity analysis for the HPR VC SEI sample (Figure 3.7, bottom) did not show these features; this could be because there was less Cu oxidation and reduction for this sample, as not all analysis regions of the HPR VC SEI were Cu rich (ca. 1% Cu was detected for Region 1 and ca. 4% for Region 2). Additionally, the separators from half cells cycled with VC do not show signs of discoloration due to Cu diffusion. These results suggest that the SEI formed in the presence of VC is better at protecting and passivating the Cu_2Sb surface as it seems to decrease the amount of Cu/Cu_2Sb oxidation and subsequent Cu diffusion when cycling to high potentials compared to the SEI formed without VC. Based on the XPS results for the HPR samples with and without VC, both SEIs are quite thin and nonuniform, which suggests that the differences in passivating ability are due to

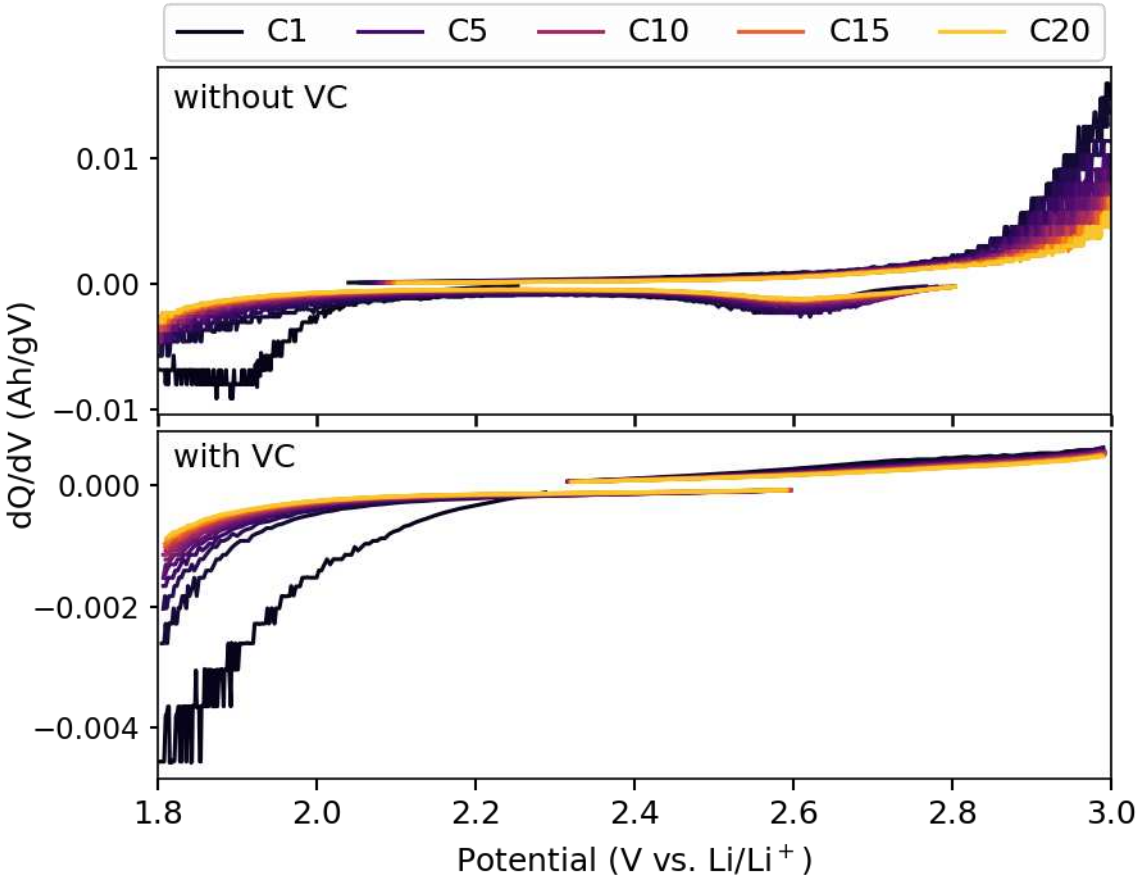

Figure 3.7: Comparison of the differential capacity analysis plots for the samples cycled without VC and with VC for the HPR SEI sample set.

differences in SEI speciation rather than thickness or coverage. The features corresponding to Cu/Cu_2Sb oxidation were also seen in the differential capacity plots of Cu_2Sb cycled over the full 0.05–3 V potential range when no VC was present (Figure 3.2, top left plot), which suggests that even when the electrode is polarized to lower potentials, the SEI that forms does not passivate the surface well enough to prevent Cu/Cu_2Sb oxidation, unlike the SEI formed in the presence of VC, which does not show any signs of Cu/Cu_2Sb oxidation (Figure 3.2, bottom left plot); however, unlike for the HPR SEI case, it is unclear at this point whether differences in passivating ability for the SEIs formed over the full voltage range are due to chemical or physical differences.

The C 1s HRES spectra may be able to provide some insights into why the SEI formed with VC may be better at protecting the Cu_2Sb surface than the SEI formed without VC since much of the SEI

surfaces for both types of samples are composed of carbon. The C 1s spectra are shown in Figure 3.8 with the fitted data included to help illustrate differences between the spectral features for the various SEI samples. The most intense peaks in the C 1s spectra for the HPR samples with and without VC correspond to an aliphatic carbon binding environment around 285.0 eV (red peak), which could be due to some adventitious carbon in addition to organic SEI components.[30,61,62,65] Both the HPR and HPR VC samples also have a peak corresponding to a C–O binding environment around 286.5 eV (blue peak), which could be due to the presence of SEI species such as alkoxides, alkyl carbonates or carboxylates, or PEO oligomers, and a peak around 289.0 eV corresponding to an O=C–O binding environment (gold peak) that could be due to oxalates, alkyl carboxylates, or ester-containing species.[10,17,30,61–63,65] Based on a previous study of the SEI formed on Cu_2Sb thin film anodes in $LiPF_6$-based electrolyte, these three C 1s binding environments may be due primarily to carboxylate and ester species, in addition to small amounts of alkoxides.[33] The most notable difference between the HPR and HPR VC SEIs is the presence of a small carbonate peak around 290.5 eV (teal peak) in Region 1 of the HPR VC SEI, which is the region where the Cu_2Sb seems to be better passivated based on the lower amount of Cu detected. The carbonate peak could be due to the presence of either lithium alkyl carbonates, Li_2CO_3 or poly VC, but it seems that the presence of carbonates could be beneficial for passivation of the Cu_2Sb surface during the initial stages of cycling.[62,65] It seems most likely that the C 1s carbonate binding environment seen in the HPR VC sample is due to a species like poly VC or some other VC reduction product rather than Li alkyl carbonate species or Li_2CO_3 since those species could also be formed from the electrolyte without VC.[43,44,65,69] Because it is difficult to draw any conclusions about the carbonate species based on the XPS results alone, this warrants further exploration in future work using complementary characterization techniques such as FTIR.[14,33,44]

Both the HPR and HPR VC SEIs were quite heterogeneous, but for the MPR samples, the MPR SEI without VC was heterogeneous while the MPR VC SEI was more homogenous in terms of composition

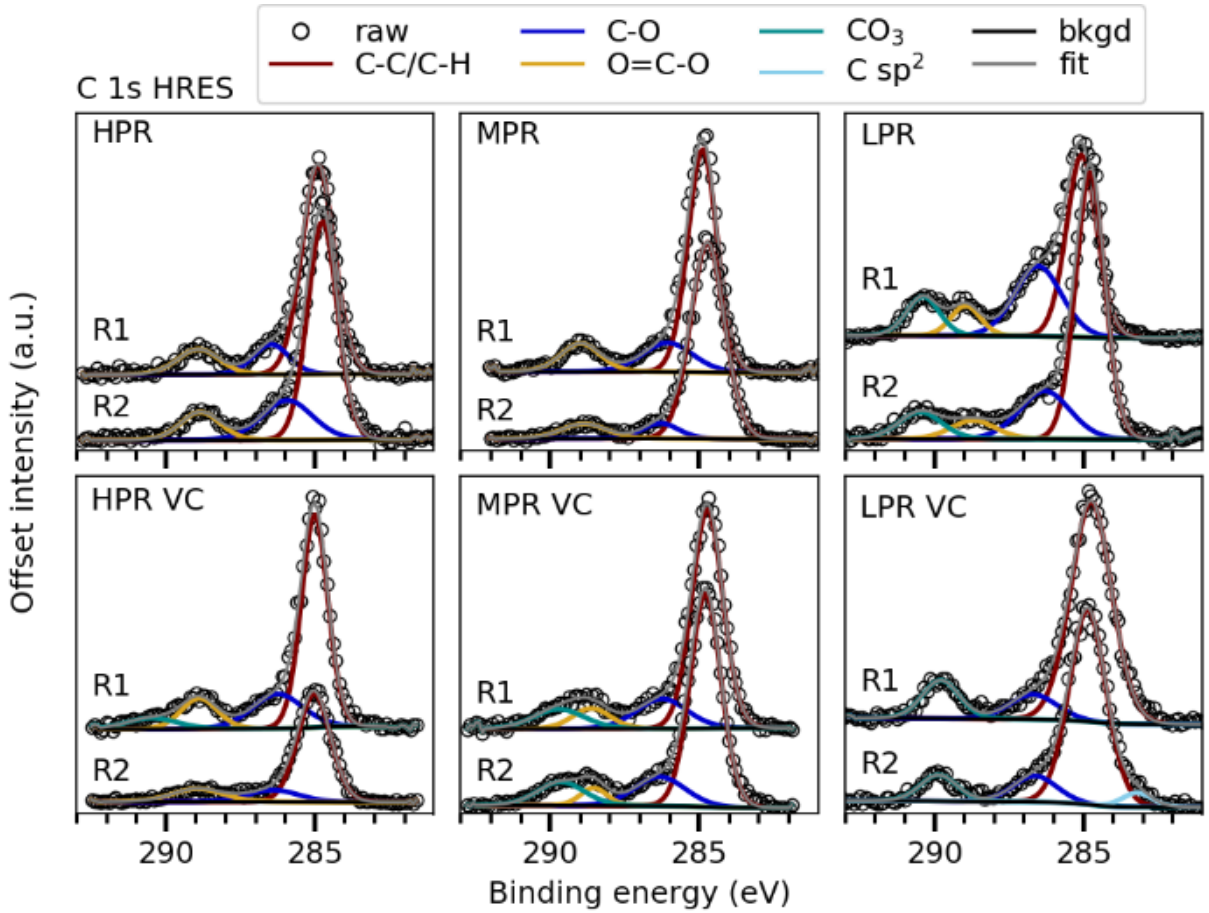

Figure 3.8: Fitted C 1s HRES spectra from the representative regions (R1 and R2) of the SEI samples formed over different potential regions (HPR, MPR, and LPR) with and without VC).

and HRES spectral features. As seen in Figure 3.4 the compositions of the MPR sample set (with and without VC) are quite similar, with C (48–57%) and O (26–28%) making up most of the SEI surface. The MPR VC SEI surface is quite Li rich at 19–22%, while the MPR SEI sample has Li-rich regions (20%) as well as regions with less Li (12%). The MPR VC SEI surface is made up of ca. 2–3% Cl from ClO_4^-, while the MPR SEI surface has about twice the amount of Cl at 5%, with a mixture of ClO_4^- and Cl^- seen for MPR Region 2 as shown in Figure 3.5 (middle column). The SEIs formed over the MPR both with and without VC are thicker than those formed over the HPR based on the absence of Sb peaks in the O 1s/Sb 3d spectra (Figure 3.6, middle column). Again, it is difficult to comment on differences in the O 1s spectra, but one notable feature is the presence of an O 1s peak around 528.3 eV corresponding to Li_2O for

Region 2 of the MPR SEI that is not seen for the other MPR region or for the MPR VC sample.[70] Looking at the C 1s spectra in Figure 3.8, both the MPR and MPR VC samples have aliphatic, C–O, and O=C–O binding environments like the HPR and HPR VC samples. The MPR VC C 1s spectrum has an additional binding environment corresponding to carbonate like Region 1 of the HPR VC sample, while no carbonate binding environment was detected at the surface of the MPR sample without VC. The intensity of the carbonate peak relative to the other C 1s peaks is higher for the MPR VC sample compared to HPR VC Region 1. This seems to reiterate that one important difference between the SEI formed without VC and with VC is the presence of carbonates, possibly in the form of poly VC or other species formed from VC reduction.[65]

Both the LPR and LPR VC SEI are also heterogeneous, and the compositions of the representative sample regions are shown in Figure 3.4. Like the SEIs formed with and without VC over potential regions more positive than Cu_2Sb lithiation (HPR and MPR), the SEIs formed over the LPR are composed primarily of C and O. Both the LPR and LPR VC SEI contain roughly the same amount of oxygen as the SEIs from the HPR and MPR sample sets (27–34%). However, the LPR SEI is more C-rich (42–52% C) than the LPR VC SEI (25–35% C), which contains roughly as much Li as C (34–43%). The LPR SEI is Li-rich compared to the HPR and MPR samples, but it only contains about half the amount of Li as the LPR VC SEI (17–22%).

The Cl 2p and O 1s/Sb 3d spectra, shown in Figures 3.5 and 3.6 (right columns), reveal more differences between the LPR and LPR VC SEI surfaces. The LPR SEI surface is similar to the HPR and MPR SEIs in that it is composed of ca. 3% Cl from ClO_4^-. In contrast, the LPR VC SEI surface is composed of only ca. 1% Cl present as Cl^-/LiCl.[21,66] Like the MPR SEI set, the LPR and LPR VC SEIs are thick, as no Sb 3d peaks are seen. The O 1s spectra reveal that the LPR VC sample surface contains Li_2O, while the LPR SEI surface does not. Compared to Region 2 of the MPR SEI, which also has Li_2O, the LPR VC SEI surface contains more Li_2O based on the intensity of the Li_2O O 1s peak relative to the intensity of the peak

formed by the other O 1s binding environments at higher binding energies. The presence of a considerable amount of Li_2O on the surface of the LPR VC SEI is likely the reason that the LPR VC SEI surface is so rich in Li compared to all of the other SEI samples.

The C 1s HRES spectra in Figure 3.8 (right column) for the LPR sample set also highlight several differences between the SEI formed over the LPR with and without VC. Both regions of the LPR SEI sample have four C 1s binding environments corresponding to aliphatic, C–O, O=C–O, and carbonate binding environments. The C 1s spectra for both regions of the LPR VC SEI sample are notably different in that they do not show a C 1s peak corresponding to an O=C–O binding environment, suggesting that the surface of the LPR VC SEI does not contain any oxalate, alkyl carboxylate, or ester species. The LPR VC SEI surface may also contain some sp^2 C, as the C 1s spectrum for Region 2 of the LPR VC sample seems to have a small lower binding energy peak around 283.0 eV, which could be due to the presence of species such as Li vinylene carbonate or Li vinylene alkoxide.[43] In the case of the LPR VC SEI surface, it seems like poly VC is not contributing to the C 1s carbonate binding environment because there is no corresponding O 1s peak around 534.5 eV to 535 eV that has been reported for poly VC.[64,65]

Carbon species make up a large percentage of the SEI surface for the samples formed over all three potential regions, both with and without VC, and the types of carbon binding environments or species present seem to play an important role in capacity retention for Cu_2Sb cycled in $LiClO_4$-based electrolytes, which has been suggested previously in studies of the SEI formed on Cu_2Sb nanowires in $LiPF_6$-based electrolyte with and without additives and for other alloying anodes such as Sn.[38,43] Based on the differences in the XPS C 1s HRES spectra for the SEI layers formed with and without VC, it seems that carbonate species in particular play an important role in SEI passivation for Cu_2Sb electrodes. The carbonate species formed from VC reduction, such as poly VC, may be necessary for passivating the Cu_2Sb surface during the early stages of cycling (prior to Cu_2Sb lithiation) in $LiClO_4$-based electrolytes and may also improve the mechanical properties of the SEI based on changes observed in the capacity over

cycling. The species that form from the reduction of EC, DEC, and DMC do not seem to be sufficient for surface passivation in the $LiClO_4$-based electrolyte without VC. Based on the peaks at ca. 2.0 V, 1.7 V, and 1.2 V in the differential capacity plots of the different potential region samples (see Figure 3.7 and Figure B13), the carbonate solvents are being reduced for the samples both with and without VC.[56,57] However, no carbonate binding environments were detected for the SEI samples formed at higher potentials (HPR and MPR) in the absence of VC; instead, species such as carboxylate salts, esters, or Li alkoxides are formed from solvent reduction based on the C 1s HRES spectra of the HPR and MPR SEI samples formed without VC. These differences in speciation for the SEIs formed without and with VC over the HPR and MPR could be due to differences in favored solvent reduction pathways or to differences in SEI reactivity based on electrode surface passivation.[41,71] In the latter case, initial solvent reduction species in the SEI formed without VC such as Li alkyl carbonates may have reacted further to form carboxylate salts, esters, or alkoxides due to poor surface passivation when VC was not used as an additive. This preliminary passivation (or lack thereof) may be particularly important for high capacity anode materials such as Cu_2Sb that experience large volume changes during cycling. Even though carbonate species are incorporated into the SEI formed without VC at lower potentials (refer to the LPR C 1s spectra in Figure 3.8), it does not seem to be sufficient for passivating the electrode surface, as there are still signs of Cu/Cu_2Sb oxidation when the film is cycled over the full voltage range from 0.05 V to 3.0 V vs. Li/Li^+ (refer to Figure 3.2). This electrode oxidation could be due in part to new electrode surfaces being exposed due to volume changes during cycling, but it could also be due in part to continued insufficient passivation because the Cu/Cu_2Sb oxidation features in the differential capacity plot for the VC-free sample shift to higher overpotentials with increased cycling, suggesting that continued SEI growth is resulting in a kinetic limitation of the process but not completely preventing it. Therefore, the stage at which the beneficial species are incorporated into the SEI may be important in addition to what types of species are formed, which has also been demonstrated for tin anodes.[44]

However, additional work characterizing the SEI/electrode morphology and passivating ability using techniques such as scanning electron microscopy[15,17,38,72] and redox-probe experiments,[73] respectively, is necessary to determine whether electrode volume changes and the physical properties of the SEI play a role in the differences in electrochemistry observed for the electrodes cycled over the full voltage range with and without VC in addition to the types of species present in the SEI.

Inorganic species make up a smaller percentage of the SEI surface in the samples examined in this study but may also play an important role in SEI performance and surface passivation, although based on the literature it is still unclear whether they are beneficial for alloying anodes.[14,43,44,46,73–75] Based on comparisons of the percent atomic composition of Cl at the SEI surface due to the presence of ClO_4^- and/or Cl^- species, the SEIs formed without VC over the HPR, MPR, and LPR were more rich in Cl-containing inorganic species. While the inorganic SEI species such as LiF that are formed from electrolytes containing fluorinated components such as $LiPF_6$ or FEC are believed to be beneficial SEI components that passivate the electrode surface,[44,46,74] the presence of perchlorate in the SEI on Cu_2Sb films when $LiClO_4$-based electrolytes are used does not seem to be beneficial. Although the SEI layers formed without VC over different potential regions are quite rich in ClO_4^- compared to their VC counterparts, the SEI layers formed without VC do not passivate the Cu_2Sb surface well and Cu_2Sb oxidation has been observed when charging to 3.0 V. This suggests that not all inorganic SEI components are beneficial, and the presence of ClO_4^- in the SEI does not appear to help with surface passivation for Cu_2Sb electrodes. Chloride species and Li_2O were also detected at the surface of SEIs formed on Cu_2Sb with and without VC, but at this point, it is unclear what role Cl^- species and Li_2O play in the properties and performance of the SEI. The formation of both species may be undesirable since the reduction of $LiClO_4$ to form LiCl and Li_2O consumes eight moles of electrons and eight moles of Li^+.[35] The formation of LiCl and Li_2O from $LiClO_4$ reduction results in a more Li rich SEI based on the percent atomic composition of Li for the LPR VC SEI sample, which may be beneficial for Li^+ diffusion, especially in the case of Li_2O

formation.[76] The role of these two species in the passivation and properties of the SEI may warrant further investigation to better understand whether the possible improvements in surface passivation and Li^+ diffusion due to LiCl and Li_2O formation outweigh the unfavorable decrease in Li inventory .

While we have discussed the oxidation of Cu/Cu_2Sb and Cu diffusion in the context of the passivating ability of the SEI and the role of VC, we would be remiss not to also discuss the possible implications of these observations for SEI health and the capacity retention of Cu_2Sb. Without VC, charging the Cu_2Sb to high potentials results in the oxidation of Cu/Cu_2Sb and also some Cu diffusion to other parts of the cell. While metal oxidation and transport are not typically discussed in the context of alloying anodes, it is a very important area of research for cathode materials. VC has previously been found to help prevent Co oxidation in lithium cobalt oxide cathode materials.[77] Additionally, metal transport in systems containing Ni- and Mn-based cathodes has been found to have detrimental effects for the anode SEI layer, affecting the passivating ability of the SEI and exacerbating electrolyte degradation.[73,78,79] It is possible that Cu in the SEI could also play a role in the poor cycling performance observed for Cu_2Sb without VC in a couple of ways. First, the observed Cu diffusion could be playing a role in the short lifetime and rapid capacity fade of the Cu_2Sb thin film cycled without VC. If Cu is diffusing away from electrode, some of the conductive Cu network that allows for good electronic conductivity in the lithiated Sb phases may no longer be present and could result in some loss of active material conductivity and cause the observed capacity fade in addition to the delamination that has been observed for Cu_2Sb cycled without VC.[80] However, this is not consistent with previous observations from our group in which Cu-deficient Cu_2Sb showed good reversibility and cycling stability.[72] Second, it is possible that the Cu species in the SEI formed without VC could be reacting with SEI and electrolyte components, which could be another explanation for why the HPR and MPR SEI samples without VC did not contain carbonate binding environments. This explanation is more consistent with our previous observations in which Cu-rich Cu_2Sb showed large irreversible capacities and short cycle lifetimes.[72]

Research on metal dissolution and transport for cathode materials has revealed that the degree of detrimental effects on the anode SEI depend on the transition metal, with Mn being the most harmful for SEI health, but it is possible that Cu could also prevent effective SEI passivation.[73,78] There is precedence for Cu reactivity in other chemistry fields, as some enzymes known to react with small organic molecules contain Cu active sites.[81] This area is worth exploring further with redox probe experiments to determine the role of Cu in SEI passivation.[73] Metal transport could be an important consideration for other intermetallic anode materials as well, especially when Cu, a fast solid state diffuser, is used as a volume buffering component in alloying anodes.[3,4]

3.4) Conclusions

The SEI formed on Cu_2Sb thin film anodes with and without VC as an electrolyte additive was studied in order to better understand the role that VC plays in stabilizing the SEI and extending the cycle lifetime of Cu_2Sb. The cycling data (capacity vs. cycle number and differential capacity analysis) suggest that some of the improvement in capacity retention observed for Cu_2Sb with VC is due to improved SEI mechanical properties, as the film cycled with VC showed evidence of electrochemical roughening but not delamination from the substrate, unlike the film cycled without VC. The SEI formed with VC also seemed to passivate the Cu_2Sb surface more effectively, as no evidence of Cu/Cu_2Sb oxidation and diffusion was observed for Cu_2Sb films cycled to oxidizing potentials with VC as an additive. The differences in the passivating ability of the SEI formed with and without VC seems to be due in part to differences in the SEI speciation.

The role that inorganic SEI components like LiF play in the passivating ability and stability of the SEI on alloying anode materials is unclear. By studying the SEI formation on Cu_2Sb without fluorinated electrolyte components allowed us to better understand what other types of organic and inorganic species may be beneficial for good SEI performance. During the initial stages of SEI formation at higher reduction potentials, the surface of the SEI formed on Cu_2Sb without VC does not contain any carbonate

species, whereas the SEI surface formed with VC does. VC reduction products such as poly VC or other polycarbonate species seem to play an important role in the passivating ability of the SEI. The surface of the SEI formed without VC tended to contain more inorganic $LiClO_4$-containing species, which do not seem to passivate Cu_2Sb very effectively.

CHAPTER 3 REFERENCES

(1) Choi, J. W.; Aurbach, D. Promise and Reality of Post-Lithium-Ion Batteries with High Energy Densities. *Nat. Rev. Mater.* **2016**, *1*, 1–16. https://doi.org/10.1038/natrevmats.2016.13.

(2) Obrovac, M. N.; Chevrier, V. L. Alloy Negative Electrodes for Li-Ion Batteries. *Chem. Rev.* **2014**, *114* (23), 11444–11502. https://doi.org/10.1021/cr500207g.

(3) Zhang, W. J. A Review of the Electrochemical Performance of Alloy Anodes for Lithium-Ion Batteries. *J. Power Sources* **2011**, *196* (1), 13–24. https://doi.org/10.1016/j.jpowsour.2010.07.020.

(4) Thackeray, M. M.; Vaughey, J. T.; Johnson, C. S.; Kropf, A. J.; Benedek, R.; Fransson, L. M. L.; Edström, K. Structural Considerations of Intermetallic Electrodes for Lithium Batteries. *J. Power Sources* **2003**, *113* (1), 124–130. https://doi.org/10.1016/S0378-7753(02)00538-4.

(5) Winter, M. The Solid Electrolyte Interphase- The Most Important and the Least Understood Solid Electrolyte in Rechargeable Li Batteries. *Z. Phys. Chem.* **2009**, *223* (10–11), 1395–1406. https://doi.org/10.1524/zpch.2009.6086.

(6) Verma, P.; Maire, P.; Novák, P. A Review of the Features and Analyses of the Solid Electrolyte Interphase in Li-Ion Batteries. *Electrochim. Acta* **2010**, *55* (22), 6332–6341. https://doi.org/10.1016/J.ELECTACTA.2010.05.072.

(7) Goodenough, J. B.; Kim, Y. Challenges for Rechargeable Li Batteries. *Chem. Mater.* **2010**, *22* (3), 587–603. https://doi.org/10.1021/cm901452z.

(8) Xu, K. Nonaqueous Liquid Electrolytes for Lithium-Based Rechargeable Batteries. *Chem. Rev.* **2004**, *104* (10), 4303–4417. https://doi.org/10.1021/cr030203g.

(9) Tokranov, A.; Kumar, R.; Li, C.; Minne, S.; Xiao, X.; Sheldon, B. W. Control and Optimization of the Electrochemical and Mechanical Properties of the Solid Electrolyte Interphase on Silicon Electrodes in Lithium Ion Batteries. *Adv. Energy Mater.* **2016**, *6* (8), 1–12. https://doi.org/10.1002/aenm.201502302.

(10) Schroder, K. W.; Celio, H.; Webb, L. J.; Stevenson, K. J. Examining Solid Electrolyte Interphase Formation on Crystalline Silicon Electrodes: Influence of Electrochemical Preparation and Ambient Exposure Conditions. *J. Phys. Chem. C* **2012**, *116* (37), 19737–19747. https://doi.org/10.1021/jp307372m.

(11) Nie, M.; Lucht, B. L. Role of Lithium Salt on Solid Electrolyte Interface (SEI) Formation and Structure in Lithium Ion Batteries. *J. Electrochem. Soc.* **2014**, *161* (6), A1001–A1006. https://doi.org/10.1149/2.054406jes.

(12) Jurng, S.; Brown, Z. L.; Kim, J.; Lucht, B. L. Effect of Electrolyte on the Nanostructure of the Solid Electrolyte Interphase (SEI) and Performance of Lithium Metal Anodes. *Energy Environ. Sci.* **2018**, *11* (9), 2600–2608. https://doi.org/10.1039/c8ee00364e.

(13) Leroy, S.; Martinez, H.; Dedryvère, R.; Lemordant, D.; Gonbeau, D. Influence of the Lithium Salt Nature over the Surface Film Formation on a Graphite Electrode in Li-Ion Batteries: An XPS Study. *Appl. Surf. Sci.* **2007**, *253* (11), 4895–4905. https://doi.org/10.1016/j.apsusc.2006.10.071.

(14) Yoon, T.; Chapman, N.; Seo, D. M.; Lucht, B. L. Lithium Salt Effects on Silicon Electrode Performance and Solid Electrolyte Interphase (SEI) Structure, Role of Solution Structure on SEI Formation. *J. Electrochem. Soc.* **2017**, *164* (9), A2082–A2088. https://doi.org/10.1149/2.1421709jes.

(15) Nguyen, C. C.; Lucht, B. L. Comparative Study of Fluoroethylene Carbonate and Vinylene Carbonate for Silicon Anodes in Lithium Ion Batteries. *J. Electrochem. Soc.* **2014**, *161* (12), A1933–A1938. https://doi.org/10.1149/2.0731412jes.

(16) Wagner, M. R.; Raimann, P. R.; Trifonova, A.; Moeller, K. C.; Besenhard, J. O.; Winter, M. Electrolyte Decomposition Reactions on Tin- and Graphite-Based Anodes Are Different. *Electrochem. Solid-State Lett.* **2004**, *7* (7), A201–A205. https://doi.org/10.1149/1.1739312.

(17) Chan, C. K.; Ruffo, R.; Hong, S. S.; Cui, Y. Surface Chemistry and Morphology of the Solid Electrolyte Interphase on Silicon Nanowire Lithium-Ion Battery Anodes. *J. Power Sources* **2009**, *189* (2), 1132–1140. https://doi.org/10.1016/j.jpowsour.2009.01.007.

(18) Vogl, U. S.; Lux, S. F.; Das, P.; Weber, A.; Placke, T.; Kostecki, R.; Winter, M. The Mechanism of SEI Formation on Single Crystal Si(100), Si(110) and Si(111) Electrodes. *J. Electrochem. Soc.* **2015**, *162* (12), A2281–A2288. https://doi.org/10.1149/2.0361512jes.

(19) Fransson, L.; Eriksson, T.; Edström, K.; Gustafsson, T.; Thomas, J. O. Influence of Carbon Black and Binder on Li-Ion Batteries. *J. Power Sources* **2001**, *101* (1), 1–9. https://doi.org/10.1016/S0378-7753(01)00481-5.

(20) Jaumann, T.; Balach, J.; Klose, M.; Oswald, S.; Langklotz, U.; Michaelis, A.; Eckert, J.; Giebeler, L. SEI-Component Formation on Sub 5 Nm Sized Silicon Nanoparticles in Li-Ion Batteries: The Role of Electrode Preparation, FEC Addition and Binders. *Phys. Chem. Chem. Phys.* **2015**, *17* (38), 24956–24967. https://doi.org/10.1039/c5cp03672k.

(21) Bodenes, L.; Darwiche, A.; Monconduit, L.; Martinez, H. The Solid Electrolyte Interphase a Key Parameter of the High Performance of Sb in Sodium-Ion Batteries: Comparative X-Ray Photoelectron Spectroscopy Study of Sb/Na-Ion and Sb/Li-Ion Batteries. *J. Power Sources* **2015**, *273*, 14–24. https://doi.org/10.1016/j.jpowsour.2014.09.037.

(22) Bryngelsson, H.; Stjerndahl, M.; Gustafsson, T.; Edström, K. How Dynamic Is the SEI? *J. Power Sources* **2007**, *174* (2), 970–975. https://doi.org/10.1016/j.jpowsour.2007.06.050.

(23) Winter, M.; Appel, W. K.; Evers, B.; Hodal, T.; Möller, K. C.; Schneider, I.; Wachtler, M.; Wagner, M. R.; Wrodnigg, G. H.; Besenhard, J. O. Studies on the Anode/Electrolyte Interface in Lithium Ion Batteries. *Monatsh. Chem.* **2001**, *132* (4), 473–486. https://doi.org/10.1007/s007060170110.

(24) Jin, Y.; Kneusels, N. J. H.; Magusin, P. C. M. M.; Kim, G.; Castillo-Martínez, E.; Marbella, L. E.; Kerber, R. N.; Howe, D. J.; Paul, S.; Liu, T.; et al. Identifying the Structural Basis for the Increased Stability of the Solid Electrolyte Interphase Formed on Silicon with the Additive Fluoroethylene Carbonate. *J. Am. Chem. Soc.* **2017**, *139* (42), 14992–15004. https://doi.org/10.1021/jacs.7b06834.

(25) Jin, Y.; Kneusels, N. J. H.; Marbella, L. E.; Castillo-Martínez, E.; Magusin, P. C. M. M.; Weatherup, R. S.; Jónsson, E.; Liu, T.; Paul, S.; Grey, C. P. Understanding Fluoroethylene Carbonate and Vinylene Carbonate Based Electrolytes for Si Anodes in Lithium Ion Batteries with NMR Spectroscopy. *J. Am. Chem. Soc.* **2018**, *140* (31), 9854–9867. https://doi.org/10.1021/jacs.8b03408.

(26) Shkrob, I. A.; Wishart, J. F.; Abraham, D. P. What Makes Fluoroethylene Carbonate Different? *J. Phys. Chem. C* **2015**, *119* (27), 14954–14964. https://doi.org/10.1021/acs.jpcc.5b03591.

(27) Vaughey, J. T.; Johnson, C. S.; Kropf, A. J.; Benedek, R.; Thackeray, M. M.; Tostmann, H.; Sarakonsri, T.; Hackney, S.; Fransson, L.; Edström, K.; et al. Structural and Mechanistic Features of Intermetallic Materials for Lithium Batteries. *J. Power Sources* **2001**, *97–8* (SI), 194–197. https://doi.org/10.1016/S0378-7753(01)00618-8.

(28) Ehinon, K. K. D.; Naille, S.; Dedryvère, R.; Lippens, P.-E.; Jumas, J.-C.; Gonbeau, D. Ni3Sn4 Electrodes for Li-Ion Batteries: Li-Sn Alloying Process and Electrode/Electrolyte Interface Phenomena. *Chem. Mater.* **2008**, *20* (16), 5388–5398. https://doi.org/10.1021/cm8006099.

(29) Naille, S.; Dedryvère, R.; Martinez, H.; Leroy, S.; Lippens, P.-E.; Jumas, J.-C.; Gonbeau, D. XPS Study of Electrode/Electrolyte Interfaces of η-Cu6Sn5 Electrodes in Li-Ion Batteries. *J. Power Sources* **2007**, *174* (2), 1086–1090. https://doi.org/10.1016/j.jpowsour.2007.06.043.

(30) Stjerndahl, M.; Bryngelsson, H.; Gustafsson, T.; Vaughey, J. T.; Thackeray, M. M.; Edström, K. Surface Chemistry of Intermetallic AlSb-Anodes for Li-Ion Batteries. *Electrochim. Acta* **2007**, *52* (15), 4947–4955. https://doi.org/10.1016/j.electacta.2007.01.064.

(31) Lahiri, A.; Endres, F. Review — Electrodeposition of Nanostructured Materials from Aqueous , Organic and Ionic Liquid Electrolytes for Li-Ion and Na-Ion Batteries : A Comparative Review. *J. Electrochem. Soc.* **2017**, *164* (9), D597–D612. https://doi.org/10.1149/2.1011709jes.

(32) Mosby, J. M.; Prieto, A. L. Direct Electrodeposition of Cu2Sb for Lithium-Ion Battery Anodes. *J. Am. Chem. Soc.* **2008**, *130* (32), 10656–10661. https://doi.org/10.1021/ja801745n.

(33) Song, S. W.; Reade, R. P.; Cairns, E. J.; Vaughey, J. T.; Thackeray, M. M.; Striebel, K. A. Cu2Sb Thin-Film Electrodes Prepared by Pulsed Laser Deposition for Lithium Batteries. *J. Electrochem. Soc.* **2004**, *151* (7), A1012–A1019. https://doi.org/10.1149/1.1758719.

(34) Kim, I.; Vaughey, J. T.; Auciello, O. Thin-Film Cu(6)Sn(5) Electrodes: Synthesis, Properties, and Current Collector Interactions. *J. Electrochem. Soc.* **2008**, *155* (6), A448–A451. https://doi.org/10.1149/1.2904525.

(35) Chusid, O.; Ely, Y. E.; Aurbach, D.; Babai, M.; Carmeli, Y. Electrochemical and Spectroscopic Studies of Carbon Electrodes in Lithium Battery Electrolyte Systems. *J. Power Sources* **1993**, *43* (1–3), 47–64.

(36) Michan, A. L.; Leskes, M.; Grey, C. P. Voltage Dependent Solid Electrolyte Interphase Formation in Silicon Electrodes: Monitoring the Formation of Organic Decomposition Products. *Chem. Mater.* **2016**, *28* (1), 385–398. https://doi.org/10.1021/acs.chemmater.5b04408.

(37) Perre, E.; Taberna, P. L.; Mazouzi, D.; Poizot, P.; Gustafsson, T.; Edström, K.; Simon, P. Electrodeposited Cu2Sb as Anode Material for 3-Dimensional Li-Ion Microbatteries. *J. Mater. Res.* **2010**, *25* (8), 1485–1491. https://doi.org/10.1557/JMR.2010.0190.

(38) Jackson, E. D.; Prieto, A. L. Copper Antimonide Nanowire Array Lithium Ion Anodes Stabilized by Electrolyte Additives. *ACS Appl. Mater. Interfaces* **2016**, *8* (44), 30379–30386. https://doi.org/10.1021/acsami.6b08033.

(39) Zhang, S. S. A Review on Electrolyte Additives for Lithium-Ion Batteries. *J. Power Sources* **2006**, *162* (2), 1379–1394. https://doi.org/10.1016/j.jpowsour.2006.07.074.

(40) Haregewoin, A. M.; Wotango, A. S.; Hwang, B.-J. Electrolyte Additives for Lithium Ion Battery Electrodes: Progress and Perspectives. *Energy Environ. Sci.* **2016**, *9* (6), 1955–1988. https://doi.org/10.1039/c6ee00123h.

(41) Ushirogata, K.; Sodeyama, K.; Okuno, Y.; Tateyama, Y. Additive Effect on Reductive Decomposition and Binding of Carbonate-Based Solvent toward Solid Electrolyte Interphase Formation in Lithium-Ion Battery. *J. Am. Chem. Soc.* **2013**, *135* (32), 11967–11974. https://doi.org/10.1021/ja405079s.

(42) Zhang, W.; Ghamouss, F.; Darwiche, A.; Monconduit, L.; Lemordant, D.; Dedryvère, R.; Martinez, H. Surface Film Formation on TiSnSb Electrodes: Impact of Electrolyte Additives. *J. Power Sources* **2014**, *268*, 645–657. https://doi.org/10.1016/j.jpowsour.2014.06.041.

(43) Park, S.; Heon Ryu, J.; Oh, S. M. Passivating Ability of Surface Film Derived from Vinylene Carbonate on Tin Negative Electrode. *J. Electrochem. Soc.* **2011**, *158* (5), A498–A503. https://doi.org/10.1149/1.3561424.

(44) Seo, D. M.; Nguyen, C. C.; Young, B. T.; Heskett, D. R.; Woicik, J. C.; Lucht, B. L. Characterizing Solid Electrolyte Interphase on Sn Anode in Lithium Ion Battery. *J. Electrochem. Soc.* **2015**, *162* (13), A7091–A7095. https://doi.org/10.1149/2.0121513jes.

(45) Aurbach, D.; Markovsky, B.; Shechter, A.; EinEli, Y.; Cohen, H. A Comparative Study of Synthetic Graphite and Li Electrodes in Electrolyte Solutions Based on Ethylene Carbonate Dimethyl Carbonate Mixtures. *J. Electrochem. Soc.* **1996**, *143* (12), 3809–3820. https://doi.org/10.1149/1.1837300.

(46) Chan, A. K.; Tatara, R.; Feng, S.; Karayaylali, P.; Lopez, J.; Stephens, I. E. L.; Shao-Horn, Y. Concentrated Electrolytes for Enhanced Stability of Al-Alloy Negative Electrodes in Li-Ion Batteries. *J. Electrochem. Soc.* **2019**, *166* (10), A1867–A1874. https://doi.org/10.1149/2.0581910jes.

(47) Schneider, J. B.; Agocs, D. B.; Prieto, A. L. Design of a Sample Transfer Holder to Enable Air-Free X-Ray Photoelectron Spectroscopy. **2020**.

(48) Philippe, B.; Hahlin, M.; Edström, K.; Gustafsson, T.; Siegbahn, H.; Rensmo, H. Photoelectron Spectroscopy for Lithium Battery Interface Studies. *J. Electrochem. Soc.* **2016**, *163* (2), A178–A191. https://doi.org/10.1149/2.0051602jes.

(49) Lindgren, F.; Rehnlund, D.; Källquist, I.; Nyholm, L.; Edström, K.; Hahlin, M.; Maibach, J. Breaking Down a Complex System: Interpreting PES Peak Positions for Cycled Li-Ion Battery Electrodes. *J. Phys. Chem. C* **2017**, *121* (49), 27303–27312. https://doi.org/10.1021/acs.jpcc.7b08923.

(50) Sherwood, P. M. A. The Use and Misuse of Curve Fitting in the Analysis of Core X-Ray Photoelectron Spectroscopic Data. *Surf. Interface Anal.* **2019**, *51* (6), 589–610. https://doi.org/10.1002/sia.6629.

(51) Antitomaso, P.; Fraisse, B.; Stievano, L.; Biscaglia, S.; Ayme-Perrot, D.; Girard, P.; Sougrati, M. T.; Monconduit, L. SnSb Electrodes for Li-Ion Batteries: The Electrochemical Mechanism and Capacity Fading Origins Elucidated by Using Operando Techniques. *J. Mater. Chem. A* **2017**, *5* (14), 6546–6555. https://doi.org/10.1039/c6ta10138k.

(52) Schulze, M. C.; Schulze, R. K.; Prieto, A. L. Electrodeposited Thin-Film CuxSb Anodes for Li-Ion Batteries: Enhancement of Cycle Life via Tuning of Film Composition and Engineering of the Film-Substrate Interface. *J. Mater. Chem. A* **2018**, *6* (26), 12708–12717. https://doi.org/10.1039/c8ta01798k.

(53) Matsuno, S.; Noji, M.; Kashiwagi, T.; Nakayama, M.; Wakihara, M. Construction of the Ternary Phase Diagram for the Li-Cu-Sb System as the Anode Material for a Lithium Ion Battery. *J. Phys. Chem. C* **2007**, *111* (20), 7548–7553. https://doi.org/10.1021/jp070397u.

(54) Fransson, L. M. L.; Vaughey, J. T.; Benedek, R.; Edström, K.; Thomas, J. O.; Thackeray, M. M. Phase Transitions in Lithiated Cu2Sb Anodes for Lithium Batteries: An in Situ X-Ray Diffraction Study. *Electrochem. Commun.* **2001**, *3* (7), 317–323. https://doi.org/10.1016/S1388-2481(01)00140-0.

(55) Smith, A. J.; Dahn, J. R. Delta Differential Capacity Analysis. *J. Electrochem. Soc.* **2012**, *159* (3), A290–A293. https://doi.org/10.1149/2.076203jes.

(56) Haregewoin, A. M.; Leggesse, E. G.; Jiang, J.-C.; Wang, F.-M.; Hwang, B.-J.; Lin, S. D. Comparative Study on the Solid Electrolyte Interface Formation by the Reduction of Alkyl Carbonates in Lithium Ion Battery. *Electrochim. Acta* **2014**, *136*, 274–285. https://doi.org/10.1016/j.electacta.2014.05.103.

(57) Zhang, X. R.; Kostecki, R.; Richardson, T. J.; Pugh, J. K.; Ross, P. N. Electrochemical and Infrared Studies of the Reduction of Organic Carbonates. *J. Electrochem. Soc.* **2001**, *148* (12), A1341–A1345. https://doi.org/10.1149/1.1415547.

(58) Bryngelsson, H.; Eskhult, J.; Nyholm, L.; Herranen, M.; Alm, O.; Edström, K. Electrodeposited Sb and Sb/Sb2O3 Nanoparticle Coatings as Anode Materials for Li-Ion Batteries. *Chem. Mater.* **2007**, *19* (5), 1170–1180. https://doi.org/10.1021/cm0624769.

(59) Bryngelsson, H.; Eskhult, J.; Nyholm, L.; Edström, K. Thin Films of Cu2Sb and Cu9Sb2 as Anode Materials in Li-Ion Batteries. *Electrochim. Acta* **2008**, *53* (24), 7226–7234. https://doi.org/10.1016/j.electacta.2008.05.005.

(60) Beard, B. C. Sodium Salts of Chlorine Oxyacid Anions, Cl(+7), Perchlorate, XPS Comparison Spectra. *Surf. Sci. Spectra* **1993**, *2* (2), 97–103. https://doi.org/10.1116/1.1247738.

(61) Dedryvère, R.; Laruelle, S.; Grugeon, S.; Gireaud, L.; Tarascon, J.-M. M.; Gonbeau, D. XPS Identification of the Organic and Inorganic Components of the Electrode/Electrolyte Interface Formed on a Metallic Cathode. *J. Electrochem. Soc.* **2005**, *152* (4), A689–A696. https://doi.org/10.1149/1.1861994.

(62) Dedryvère, R.; Gireaud, L.; Grugeon, S.; Laruelle, S.; Tarascon, J. M.; Gonbeau, D. Characterization of Lithium Alkyl Carbonates by X-Ray Photoelectron Spectroscopy: Experimental and Theoretical Study. *J. Phys. Chem. B* **2005**, *109* (33), 15868–15875. https://doi.org/10.1021/jp051626k.

(63) Li, J.-T. T.; Swiatowska, J.; Seyeux, A.; Huang, L.; Maurice, V.; Sun, S.-G. G.; Marcus, P. XPS and ToF-SIMS Study of Sn – Co Alloy Thin Films as Anode for Lithium Ion Battery. *J. Power Sources* **2010**, *195* (24, SI), 8251–8257. https://doi.org/10.1016/j.jpowsour.2010.07.043.

(64) El Ouatani, L.; Dedryvre, R.; Siret, C.; Biensan, P.; Gonbeau, D. Effect of Vinylene Carbonate Additive in Li-Ion Batteries: Comparison of LiCoO2/C, LiFePO4/C, and LiCoO2/Li4Ti5O12 Systems. *J. Electrochem. Soc.* **2009**, *156* (6), A468–A477. https://doi.org/10.1149/1.3111891.

(65) El Ouatani, L.; Dedryvre, R.; Siret, C.; Biensan, P.; Reynaud, S.; Iraţabal, P.; Gonbeau, D. The Effect of Vinylene Carbonate Additive on Surface Film Formation on Both Electrodes in Li-Ion Batteries. *J. Electrochem. Soc.* **2009**, *156* (2), A103–A113. https://doi.org/10.1149/1.3029674.

(66) Morgan, W. E.; Van Wazer, J. R.; Stec, W. J. Inner-Orbital Photoelectron Spectroscopy of the Alkali Metal Halides, Perchlorates, Phosphates, and Pyrophosphates. *J. Am. Chem. Soc.* **1973**, *95* (3), 751–755. https://doi.org/10.1021/ja00784a018.

(67) Garbassi, F. XPS and AES Study of Antimony Oxides. *Surf. Interface Anal.* **1980**, *2* (5), 165–169. https://doi.org/10.1002/sia.740020502.

(68) James, T. L. Photoelectron Spectroscopy. *J. Chem. Educ.* **1971**, *48* (11), 712–718. https://doi.org/10.1021/ed048p712.

(69) Ota, H.; Sakata, Y.; Inoue, A.; Yamaguchi, S. Analysis of Vinylene Carbonate Derived SEI Layers on Graphite Anode. *J. Electrochem. Soc.* **2004**, *151* (10), A1659–A1669. https://doi.org/10.1149/1.1785795.

(70) Shiraishi, S.; Kanamura, K.; Takehara, Z. I. Influence of Initial Surface Condition of Lithium Metal Anodes on Surface Modification with HF. *J. Appl. Electrochem.* **1999**, *29* (7), 869–881.

(71) Tavassol, H.; Buthker, J. W.; Ferguson, G. A.; Curtiss, L. A.; Gewirth, A. A. Solvent Oligomerization during SEI Formation on Model Systems for Li-Ion Battery Anodes. *J. Electrochem. Soc.* **2012**, *159* (6), A730–A738. https://doi.org/10.1149/2.067206jes.

(72) Jackson, E. D.; Mosby, J. M.; Prieto, A. L. Evaluation of the Electrochemical Properties of Crystalline Copper Antimonide Thin Film Anodes for Lithium Ion Batteries Produced by Single Step Electrodeposition. *Electrochim. Acta* **2016**, *214*, 253–264. https://doi.org/10.1016/j.electacta.2016.07.126.

(73) Harris, O. C.; Tang, M. H. Molecular Probes Reveal Chemical Selectivity of the Solid-Electrolyte Interphase. *J. Phys. Chem. C* **2018**, *122* (36), 20632–20641. https://doi.org/10.1021/acs.jpcc.8b06564.

(74) Qiao, R.; Lucas, I. T.; Karim, A.; Syzdek, J.; Liu, X.; Chen, W.; Persson, K.; Kostecki, R.; Yang, W. Distinct Solid-Electrolyte-Interphases on Sn (100) and (001) Electrodes Studied by Soft X-Ray Spectroscopy. *Adv. Mater. Interfaces* **2014**, *1* (3), 1–6. https://doi.org/10.1002/admi.201300115.

(75) Ulus, A.; Rosenberg, Y.; Burstein, L.; Peled, E. Tin Alloy-Graphite Composite Anode for Lithium-Ion Batteries. *J. Electrochem. Soc.* **2002**, *149* (5), A635–A643. https://doi.org/10.1149/1.1469029.

(76) Chen, Y. C.; Ouyang, C. Y.; Song, L. J.; Sun, Z. L. Electrical and Lithium Ion Dynamics in Three Main Components of Solid Electrolyte Interphase from Density Functional Theory Study. *J. Phys. Chem. C* **2011**, *115* (14), 7044–7049. https://doi.org/10.1021/jp112202s.

(77) Takamatsu, D.; Orikasa, Y.; Mori, S.; Nakatsutsumi, T.; Yamamoto, K.; Koyama, Y.; Minato, T.; Hirano, T.; Tanida, H.; Arai, H.; et al. Effect of an Electrolyte Additive of Vinylene Carbonate on the Electronic Structure at the Surface of a Lithium Cobalt Oxide Electrode under Battery Operating Conditions. *J. Phys. Chem. C* **2015**, *119* (18), 9791–9797. https://doi.org/10.1021/jp511405g.

(78) Solchenbach, S.; Hong, G.; Freiberg, A. T. S.; Jung, R.; Gasteiger, H. A. Electrolyte and SEI Decomposition Reactions of Transition Metal Ions Investigated by On-Line Electrochemical Mass Spectrometry. *J. Electrochem. Soc.* **2018**, *165* (14), A3304–A3312. https://doi.org/10.1149/2.0511814jes.

(79) Joshi, T.; Eom, K.; Yushin, G.; Fuller, T. F. Effects of Dissolved Transition Metals on the Electrochemical Performance and SEI Growth in Lithium-Ion Batteries. *J. Electrochem. Soc.* **2014**, *161* (12), A1915–A1921. https://doi.org/10.1149/2.0861412jes.

(80) Trahey, L.; Kung, H. H.; Thackeray, M. M.; Vaughey, J. T. Effect of Electrode Dimensionality and Morphology on the Performance of Cu2Sb Thin Film Electrodes for Lithium-Ion Batteries. *Eur. J. Inorg. Chem.* **2011**, No. 26, SI, 3984–3988. https://doi.org/10.1002/ejic.201100329.

(81) Doerrer, L. H. Cu in Biology: Unleashed by O-2 and Now Irreplaceable. *Inorganica Chim. Acta* **2018**, *481*, 4–24. https://doi.org/10.1016/j.ica.2017.11.051.

CHAPTER 4: INVESTIGATING THE ROLE OF THE SOLID ELECTROLYTE INTERFACE IN THE CYCLE LIFETIME AND FAILURE OF TIN ANTIMONIDE ELECTRODES FOR Li-ION BATTERIES[†]

Chapter Summary

Tin antimonide (SnSb) anodes are attractive electrodes for Li-ion batteries due to having a high volumetric capacity and exhibiting good reversible capacity. However, there is still a limited understanding of the mode(s) of failure for SnSb electrodes, which is important for designing electrodes with good capacity retention and long cycle lifetimes. In order to understand what roles, if any, the solid electrolyte interface (SEI) plays in the cycling behavior and failure of SnSb thin film electrodes, we studied the formation and evolution of the SEI on SnSb over different stages of cycling using X-ray photoelectron spectroscopy (XPS). The SnSb electrodes were cycled in electrolytes containing different Li salts in order to better understand what roles different species play in the stability of the SEI and cycling performance of SnSb.

4.1) Introduction

Materials that alloy with lithium, including Sn and Sb, are of interest as high capacity anodes for next-generation Li-ion batteries.[1] These materials have high volumetric capacities; compared to the conventional graphite Li intercalation anode, which stores 1 mole of Li for every 6 moles of C, 3 and 4.4 moles of Li can be stored for each mole of Sb and Sn, respectively.[1] Unfortunately, the large Li storage capacity of alloying anodes comes with a cost; during alloying and dealloying, these anode materials

[†] The battery cycling data and XPS data presented in this chapter are preliminary data for work that will be submitted for publication to a peer reviewed journal at a future date with Leslie A. Kraynak, Jeffrey Ma, Nathan J. Gimble, and Amy L. Prieto as the authors. Leslie A. Kraynak designed the experiments, collected data for all short-term cycling experiments, will fit the XPS data for the long-term cycling experiments still in progress, and prepared the manuscript. Jeffrey Ma prepared all of the electrodeposited SnSb thin film anodes used in this work and performed XRD characterization. Nathan J. Gimble will disassemble the cells and perform XPS characterization for the long-term cycling experiments still in progress. Amy L. Prieto provided guidance with experimental planning and helped with editing.

undergo large volume changes that result in electrode pulverization and can ultimately result in electrode failure due to electronic isolation of active material and delamination.[1]

Researchers have devised numerous solutions to remedy the problems associated with the volume changes of alloying anodes, one of which is the use of binary or ternary metal alloys, including intermetallic materials, as electrodes.[1,2] Many intermetallics contain one element such as Cu, Ni, or Ti that does not alloy with Li to decrease the volume expansion of the electrode during lithiation.[1,2] Interestingly, the intermetallic SnSb, which does not contain an inactive component to buffer volume changes, exhibits a much longer cycle lifetime than either Sn or Sb anodes, as demonstrated in Figure 4.1. Some have speculated that one reason for the good cycling performance of SnSb compared to pure Sn and pure Sb is due to the SnSb lithiation pathways. The Sb in SnSb alloys with lithium before the Sn, and the ductile Sn is thought to help buffer the volume expansion associated with the formation of Li_3Sb.[3,4] As demonstrated in Figure 4.1 (top), a mixture of Sn and Sb particles does not exhibit good cycle performance like SnSb does. Antitomaso and colleagues hypothesized that this is due long-range order and shorter diffusion distances between Sn and Sb for SnSb but not for the physical mixture of the two, which must be maintained to some extent during cycling of SnSb.[5]

There are several hypotheses about the mode of electrode failure for SnSb anodes. One hypothesis is that SnSb is not completely reformed upon charging/delithiation, and over time aggregation of Sn or Li_xSn prevents alloying and dealloying of Sb.[5] Another hypothesis is that the large volume changes during cycling lead to cell failure due to loss of active material through delamination or electronic isolation, which is a problem for all alloying anode materials.[6] This mode of failure is linked to the SEI in the sense that with a more mechanically stable SEI, the problems associated with electrode volume expansion might not lead such severe capacity losses because a more robust SEI should help the electrode remain intact even after pulverization due to volume expansion.[7] The results from other studies of SnSb electrodes have suggested that continuous SEI formation during cycling, which can

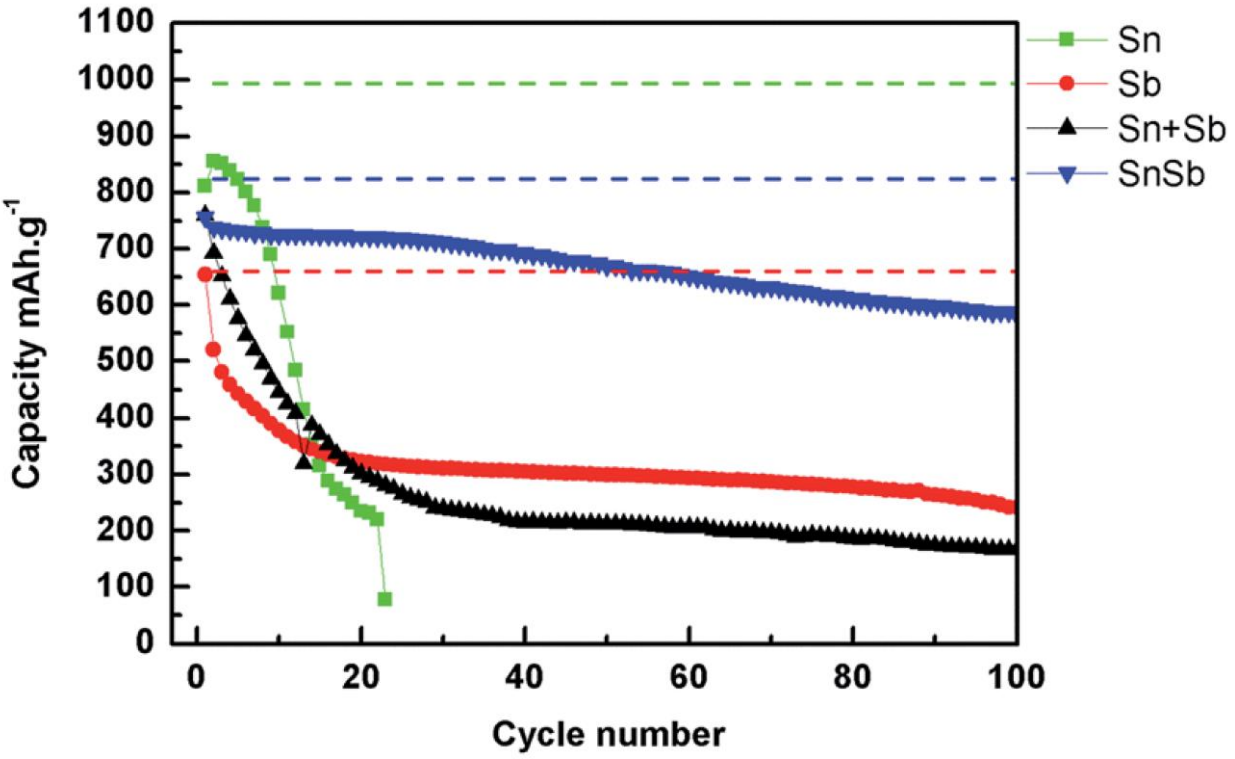

Figure 4.1: Capacity versus cycle number results for Sn, Sb, Sn+Sb, and SnSb composite electrodes showing the dramatic differences in capacity retention and cycle lifetime for different alloying materials. Reprinted from Reference 5 with permission from The Royal Society of Chemistry.

hinder Li^+ transport through the SEI and electron transport in the electrode, is one of the main reasons for the capacity fade of SnSb electrodes.[8] The capacity fade of SnSb is likely due to some combination of all of these factors, although it is difficult to determine the main mode of failure.

The ability to prepare phase pure crystalline SnSb films by electrodeposition provides an ideal system for fundamental studies of the SEI on SnSb for several reasons. First, electrodeposition allows for the fabrication of electrodes without the use of binders or additives, which can affect SEI formation.[9–13] Second, many previously published SnSb electrodeposition syntheses result in the formation of SnSb with crystalline Sn impurities. The presence of these impurities could convolute the interpretation of results from studies of SEI formation on SnSb because Sn is believed to catalytically reduce some electrolyte components.[14–16] We have used this model SnSb thin film electrode system to study SEI formation and

evolution on SnSb in order to understand what role the SEI plays in the capacity retention, cycle lifetime, and failure modes of SnSb electrodes.

4.2) Experimental

SnSb Electrodeposition

The SnSb thin film electrodes were prepared following a previously established procedure.[17] Briefly, the films were electrodeposited onto Ni foil at −0.7 V vs Ag/Ag^+ for 300 s at room temperature from a non-aqueous electrodeposition solution using a Gamry Reference 3000 potentiostat. The electrodeposition solution contained 50 mM $SbCl_3$ (Sigma Aldrich, ACS reagent) and 50 mM $SnCl_2{\cdot}2H_2O$ (Sigma Aldrich, ACS reagent) dissolved in ethaline, which was prepared by combining choline chloride (VWR high purity) and ethylene glycol (Fischer Scientific) in a 1:2 ratio by mass. Phase purity of the electrodeposited films was verified by X-ray diffraction. The approximate SnSb mass loadings of the films were ca. 0.10 mg/cm^2, as determined by the amount of charge passed. Circular punches (1.27 cm diameter) were taken from the films for use in half cells (ca. 0.13 mg SnSb per punch). The films were electrodeposited on substrates that were large enough to obtain 2–3 punches per film for making replicate samples.

Half-Cell Assembly and Cycling

Two electrode half cells were assembled using 1.27 cm diameter Swagelok-type cells in an Ar-filled glovebox (O_2 < 1.0 ppm; H_2O < 0.5 ppm). A complete description of the procedure for cleaning Swagelok cell parts can be found in Appendix A. The cells were assembled with a SnSb punch as the positive electrode, which functions as the working electrode, and a Li metal foil punch as the negative electrode, which functions as the counter and pseudo reference electrode. The Li metal foil was prepared by flattening Li ribbon with a wooden brayer, followed by manually removing the surface oxide layer by scraping the metal on both sides with the rounded end of a double-bladed stainless-steel spatula until the surface was shiny and no dull, grey oxidized Li was apparent. The separators were a 1.27 cm punch of

glass fiber (Whatman, dried overnight in an oven prior to being introduced into the glovebox) layered between two 1.27 cm polypropylene punches (Celgard, 25 μm). 200 μL of electrolyte solution, either 1 M $LiClO_4$ (Aldrich, battery grade 99.999%) in dimethyl carbonate (DMC, Aldrich, anhydrous ≥99%) with 5% by volume vinylene carbonate (VC, Aldrich, 99% with 80 ppm butylated hydroxytoluene added as stabilizer) or 1 M $LiPF_6$ in DMC (Sigma Aldrich, battery grade) with 5% VC by volume, was used in each half cell. Care was taken during half-cell assembly to remove any gas bubbles trapped between the separator layers by gently pressing the cell components down with a pair of plastic tweezers prior to sealing the cell.

The assembled half cells rested at open circuit potential (OCP) for 18 hours before cycling. Half cells were cycled galvanostatically using an Arbin BT-2143 battery tester. Cells were cycled at a C/20 rate (ca. 4 $\mu A/cm^2$) between 0.01 and 1.6 V vs. Li/Li^+ for various periods of time to study different stages of SEI formation and growth, which are described in more detail in the results and discussion section. Each SEI sample was prepared in duplicate to ensure an accurate representation of the SEI formed in SnSb was obtained. Discharging refers to the application of a cathodic current and lithiation of the SnSb active material, and charging refers to the application of an anodic current and delithiation of the active material.

Half Cell Disassembly

With the exception of the first discharge SEI samples, cell cycling was stopped at the end of charging. All cells were rested for 24 hours prior to disassembly, and the cells were disassembled and characterized within 1-2 days of cycling completion. Half cells were disassembled in an Ar-filled glove box. Prior to disassembly, the box was purged for 1 min to minimize exposure to oxygen as much as possible. Plastic tweezers (cleaned with DMC prior to use) were used to remove and separate the cell components to avoid shorting or self-charging in the case of the samples disassembled in the discharged state. Each SEI sample formed on the SnSb working electrode was washed by rinsing with ca. 1 mL DMC. Excess DMC was wicked away from the edge of the sample with a clean Kim Wipe, and the remaining solvent was allowed to evaporate from the surface of the sample before being mounted on the XPS sample holder.

Samples were secured to the custom-built air free sample holder[18] using Cu clips, and care was taken to avoid touching or scratching the sample surface with the clips in order to avoid damaging or contaminating the samples. The sample holder was sealed under vacuum in the glovebox antechamber and remained sealed in either the antechamber or glovebox until XPS characterization.

XPS Characterization

SEI samples were transferred from the Ar glovebox to the XPS sample introduction chamber using a custom-built air free sample holder to minimize air exposure.[18] The air free sample holder was vacuum sealed, and the lid was removed in the XPS sample intro chamber once the chamber pressure was lower than the pressure in the sample holder. The samples were pumped down in the intro chamber for at least 30 min to remove residual solvent and avoid excessive off gassing in the main vacuum chamber.

A Physical Electronics (PHI) 5800 Multi-Technique ESCA system with monochromatic Al Kα radiation source (hν = 1486.6 eV) operating at 350.0 W was used for XPS characterization. An electron flood gun operating with a 5 μA emission current, 1.5 V bias voltage, and 40.0 V extractor voltage was used for charge neutralization during the analysis of all SEI samples. High resolution (HRES) spectra for the regions of interest were collected sequentially with a 23.5 eV pass energy in intervals of 0.100 eV/step. The instrument base pressure was 9×10^{-8} Torr or lower during data acquisition.

The XPS analysis area was 0.6 mm x 2 mm, and data from at least three different regions of each sample were collected to ensure that any lateral heterogeneity was accounted for. Short HRES scans were initially collected over wider binding energy ranges to ensure all features of interest were included in the data collection and to have as a reference in case of sample damage. The HRES scans collected for data analysis were collected over narrower binding energy ranges to only include the features of interest for longer periods of time to obtain better signal to noise ratios. The longer HRES data collection times were still minimized as much as possible (30–45 minutes total depending on the number of regions being collected) in order to minimize sample damage.

Depth profiling studies of pristine SnSb thin films and the long-term cycling SEI samples were also done to characterize any depth dependent heterogeneity. Depth profiling was performed using an Ar^+ gun with a 5 keV 3 mm x 3 mm beam for sputtering of the pristine electrode and a 3 keV 3 mm x 3 mm beam for sputtering of the SEI. Sputtering was performed in short increments, usually 15–30 s, to avoid sample damage. Survey spectra were collected between each sputtering increment to monitor changes in the sample using a pass energy of 187.85 eV and 1.6 eV/step. HRES spectra were collected using the same procedure as described above. Ar^+ sputtering is known to cause sample damage and introduce artifacts, so extreme care must be used when collecting and analyzing data from XPS depth profiling experiments.[19–21]

In this work, we were not concerned with obtaining absolute binding energies; instead we were more interested in studying the relative changes for a given set of samples, so charge correction procedures were based on shifting photoelectron peaks corresponding to certain inorganic SEI species rather than using more conventional charge correction procedures.[19,22] Charge correction for the spectra collected for the pristine SnSb samples was performed by setting the Sb $3d_{5/2}$ peak for metallic Sb to 528 eV, although minimal charging was observed. For charge correction of the HRES spectra for SEI samples prepared in $LiPF_6$-based electrolyte, the F 1s peak for LiF was set to 685 eV, and for the $LiClO_4$-based electrolyte SEI samples, the Cl $2p_{3/2}$ peak for ClO_4^- was shifted to 208.6 eV. CasaXPS software (Version 2.3.16) was used for peak fitting and quantification of the HRES spectra, and the tabulated fitting results can be found in Tables C1–C5 of Appendix C. A nonlinear Shirley background and 30% Lorentzian/70% Gaussian lineshape were used for peak fitting, and PHI relative sensitivity factors corrected for angular distribution were used for quantification based on peak fitting.

4.3) Results and Discussion

Surface Characterization of Pristine SnSb Films

The SnSb films to be used as the electrodes for studying the SEI were prepared under ambient conditions by electrodeposition. The films have a native oxide layer on the surface due to preparation in air, which may affect SEI formation.[23–26] Therefore, the pristine SnSb electrode surface was characterized with XPS in order to better understand the composition of the electrode surface prior to SEI formation.

Based on the quantification from XPS characterization, shown in Figure 4.2, the SnSb surface was composed of ca. 22% C from adventitious carbon (see Figure C1 for the HRES C 1s spectrum) and ca. 42% O, 14% Sb, and 22% Sn, due to the presence of a native oxide layer. Looking at the Sb 3d/O 1s and Sn 3d

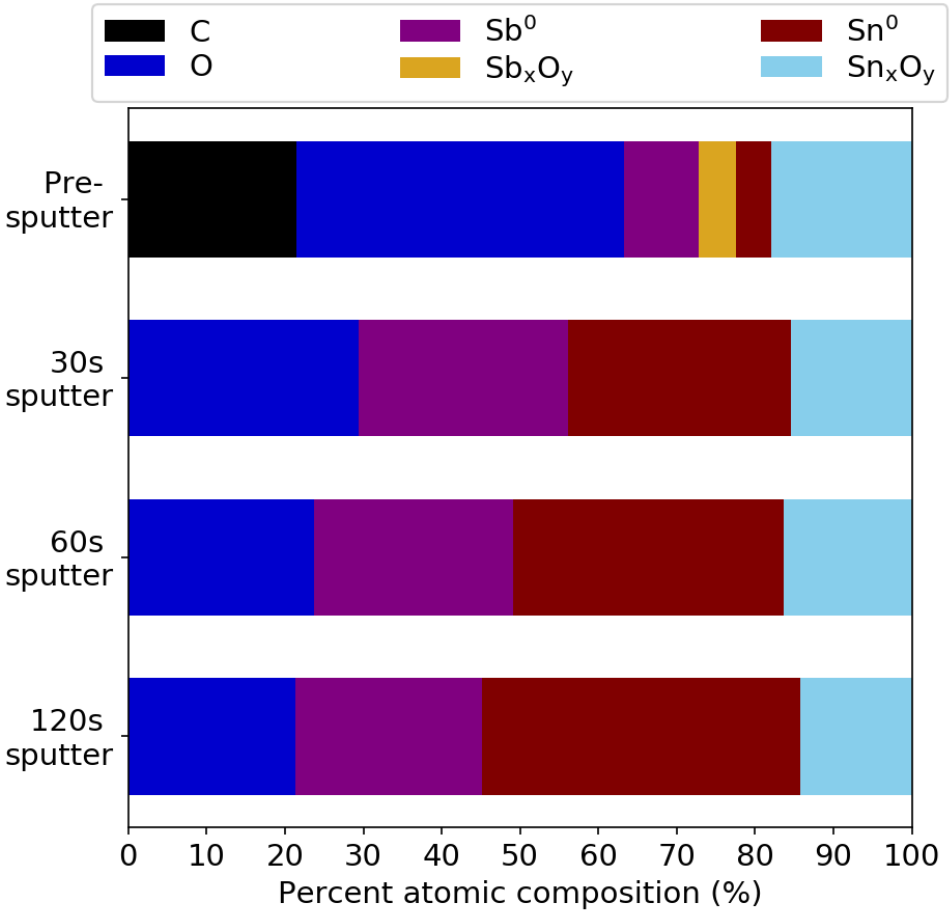

Figure 4.2: Composition data from XPS HRES spectra shown in Figure 4.3 for a pristine SnSb film sputtered for different total lengths of time.

HRES spectra in Figure 4.3, there is evidence of both metallic Sb and Sn as well as oxidized Sb and Sn binding environments.[27–29] Based on relative peak intensities, there is more oxidized Sn on the electrode surface than metallic Sn, while for Sb there is more metallic Sb on the surface than oxidized Sb. Sputtering for 30 s with a 5 keV 3 mm x 3 mm Ar^+ beam removes all of the adventitious carbon, and the surface is composed of ca. 29% O, 27% Sb, and 44% Sn.

Based on the features in the HRES spectra, the oxygen is due to oxidized Sn species. After 30 s of sputtering, the Sb $3d_{3/2}$ peak corresponding to Sb_xO_y species at ca. 540 eV is no longer present (the Sb $3d_{5/2}$ peak overlaps with the O 1s peak at ca. 530 eV), while there are still higher binding energy Sn $3d_{5/3}$ and $3d_{3/2}$ peaks at ca. 486 eV and 495 eV, respectively due to oxidized Sn apparent in the Sn 3d spectrum. Additional sputtering for totals of 60 s and 120 s of sputtering removes small amounts of the oxidized Sn species, but it seems to persist below the film surface. Based on XPS depth profiling of pristine SnSb films, the electrode surface is composed of Sb^0, Sn^0, Sb_xO_y, and Sn_xO_y species due to preparation in ambient conditions; there also seems to be some incorporation of amorphous Sn_xO_y species into the film during electrodeposition based on the presence of Sn_xO_y species after sputtering. Additionally, while XRD and characterization of the films suggests that the films are composed of only crystalline SnSb, and energy dispersive X-ray spectroscopy confirms a 1:1 Sn:Sb ratio in the bulk of the film,[17] comparison of Sn:Sb ratios based on XPS characterization suggests that the surface region of the SnSb films may be Sn rich, although this could also be an artifact of sputtering.

SnSb Cycling Behavior with Different Supporting Electrolytes

The formation, composition, and properties of the SEI are influenced by a number of factors, including the composition of the electrolyte solution. Therefore, the choice of electrolyte is an important consideration for SEI studies. Studies on other anode materials have suggested that for electrolyte solutions containing a combination of ethylene carbonate (EC) and linear organic carbonates like diethyl carbonate (DEC) and/or DMC, the carbonaceous components in the SEI are mainly composed of EC

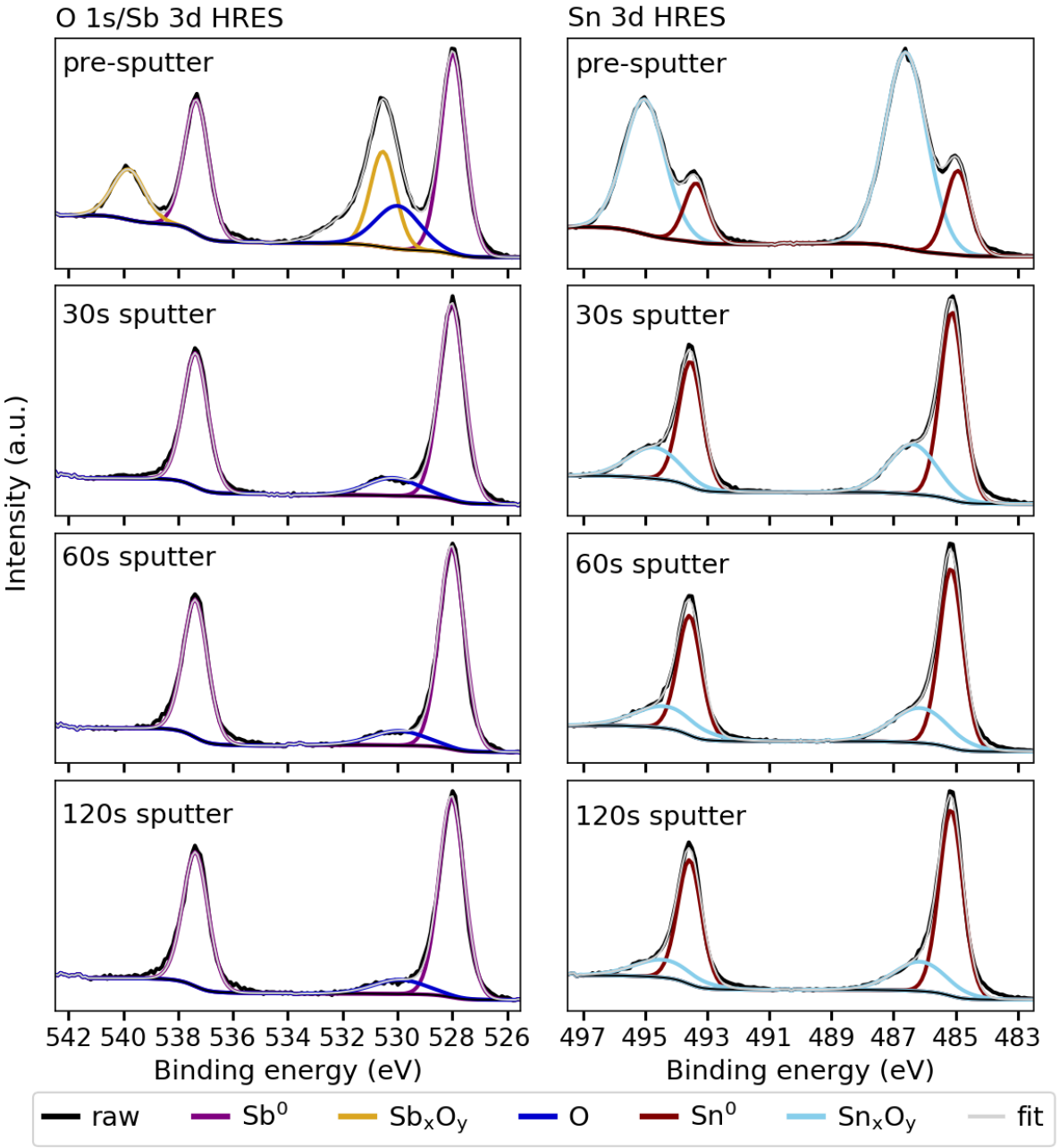

Figure 4.3: XPS HRES O 1s/Sb 3b and Sn 3d spectra for a pristine electrodeposited SnSb film sputtered for different total lengths of time showing the differences in Sb and Sn speciation with film depth.

reduction species.[16,30] Additionally, there is data that suggests EC is catalytically reduced on metallic Sn surfaces.[14–16] Therefore, DMC was used as the solvent to avoid excessive solvent reduction during SEI formation on SnSb. VC was used as an SEI improving additive to help extend the cycle lifetime of SnSb electrodes and allow us to study and understand the evolution of the SEI over extended cycling and understand the role it plays in capacity retention and long cycle lifetimes as well as possibly cell failure. Previous work in our group using this solvent and additive combination to cycle SnSb thin film electrodes has demonstrated good capacity retention and long cycle lifetimes.[17]

In order to better understand the role that the SEI may play in the capacity retention and long cycle lifetime of SnSb anodes, we chose to study SEI formation in electrolytes containing two different supporting electrolytes/Li salts, while the electrolyte solvents and additives were kept consistent. $LiPF_6$ has become the most conventional supporting electrolyte for use in Li-ion studies, and the use of 1 M $LiPF_6$ in DMC with 5% VC results in the formation of a SEI that allows SnSb films to cycle for hundreds of cycles. The use of $LiPF_6$ as a supporting electrolyte results in the incorporation of LiF in the SEI, which is thought to be beneficial for passivating the electrode surface,[31,32] although its role in long term cycling for the SEI on alloying anodes is unclear.[32,33] However, $LiPF_6$-based electrolyte solutions often contain trace amounts of HF due to unavoidable water contamination; HF has been found to contribute to SEI instability, reacting with SEI species and leading to SEI dissolution.[9] Others have found that using trimethyl phosphite (TMP) as an acid-scavenging additive for Sn-based alloying anodes cycled in $LiPF_6$-based electrolyte helps improve cycling performance.[34–36] In order to better understand whether HF and other $LiPF_6$ decomposition species are detrimental to the SEI formed in SnSb, we also chose to study SEI formation in 1 M $LiClO_4$ in DMC with 5% VC, which may help clarify the role of LiF as well.

The differential capacity analysis plots for the first cycle from representative SnSb samples cycled in the $LiPF_6$- and $LiClO_4$-based electrolytes are shown in Figure 4.4. Looking at the plots on the left side of Figure 4.4, it can be seen that changing the supporting electrolyte does not affect the cycling

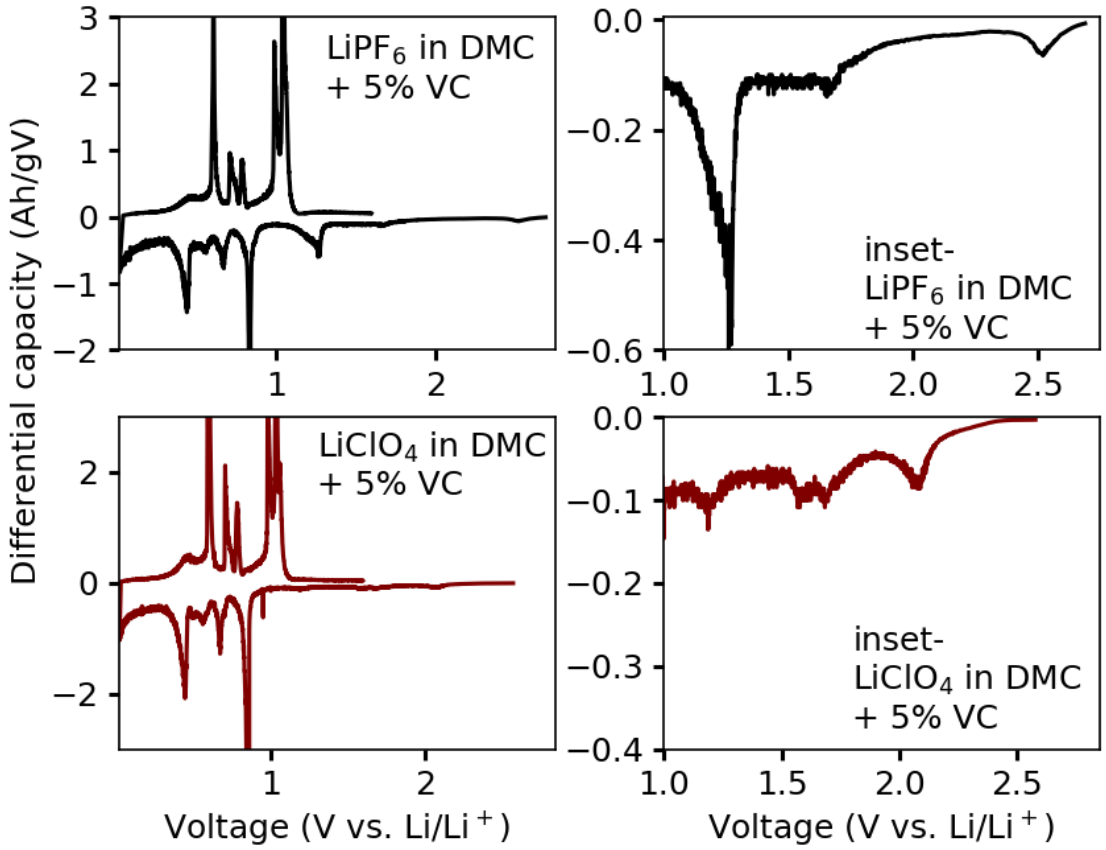

Figure 4.4: First cycle differential capacity analysis plots for SnSb thin films cycled in $LiPF_6$- and $LiClO_4$-based electrolytes, with insets shown on the right side.

behavior on SnSb in the sense that the same phase transitions, represented by sharp peaks in the differential capacity plots, are seen during lithiation (negative differential capacity) and delithiation (positive differential capacity) for both electrolytes. However, there seem to be some differences in the peaks associated with solvent reduction, shown in the insets on the right side of Figure 4.4. Since electrolyte reduction processes only occur at the electrode surface, the peaks associated with these processes in the differential capacity plots are much lower in intensity than those corresponding to phase transitions occurring throughout the bulk of the electrode material. Both the $LiPF_6$- and $LiClO_4$-based electrolytes exhibit electrolyte reduction peaks at ca. 1.7 V and ca. 1.2 V vs Li/Li^+. However, the sample cycled in $LiPF_6$-based electrolyte also has a solvent reduction feature at ca. 2.5 V vs Li/Li^+ that is not observed for the samples cycled in $LiClO_4$-based electrolyte, and the $LiClO_4$-based electrolyte sample has

a peak around ca. 2.2 V vs Li/Li^+ that is absent in the differential capacity analysis plots for the samples cycled in $LiPF_6$-based electrolytes. This suggests that there are some differences in the SEI formation processes on SnSb depending on the type of supporting electrolyte used.

There are also some differences in the cycling data for the SnSb electrodes cycled in $LiPF_6$- and $LiClO_4$-based electrolytes (representative data shown in Figure 4.5). Most notably, the gravimetric capacities of the SnSb electrodes cycled in the $LiClO_4$-based electrolyte are higher than those of electrodes cycled in the $LiPF_6$-based electrolyte, although it is unclear why this is the case. Otherwise, the SnSb electrodes cycled in both electrolytes exhibit low coulombic efficiencies around ca. 97%, as shown in the top right panel of Figure 4.5. This may be due to continual electrolyte reduction and SEI formation; as shown in the bottom right panel of Figure 4.5, the discharge capacity is consistently higher than the charge capacity for both types of samples, which is likely due to SEI formation during discharge.

Stages of SEI Growth and Evolution on SnSb

In order to better understand the role of that the SEI may play in the long cycle lifetime of SnSb thin film electrodes and possibly in the electrode failure, the SEI was characterized at different stages over the cycling of SnSb to isolate different phases of SEI formation and evolution. These stages are illustrated in Figure 4.6, which depicts the typical capacity versus cycle number behavior of thin film alloying anode materials cycled in half cells where there is an unlimited supply of Li.[37] Over short-term cycling, the SEIs formed at the end of the first discharge and the end of the first cycle were characterized with XPS in order to understand what species are initially incorporated into the SEI. The composition of the SEI at this stage has been studied for many different alloying anodes as summarized in Chapter 1 but not for SnSb to the best of our knowledge.

The SEI on SnSb will also be characterized over long-term cycling. In order to have a baseline for comparison to later stages of SEI evolution and growth, the SEI on SnSb will be characterized after the capacity and coulombic efficiency have stabilized, designated as the “established SEI” phase. The SEI on

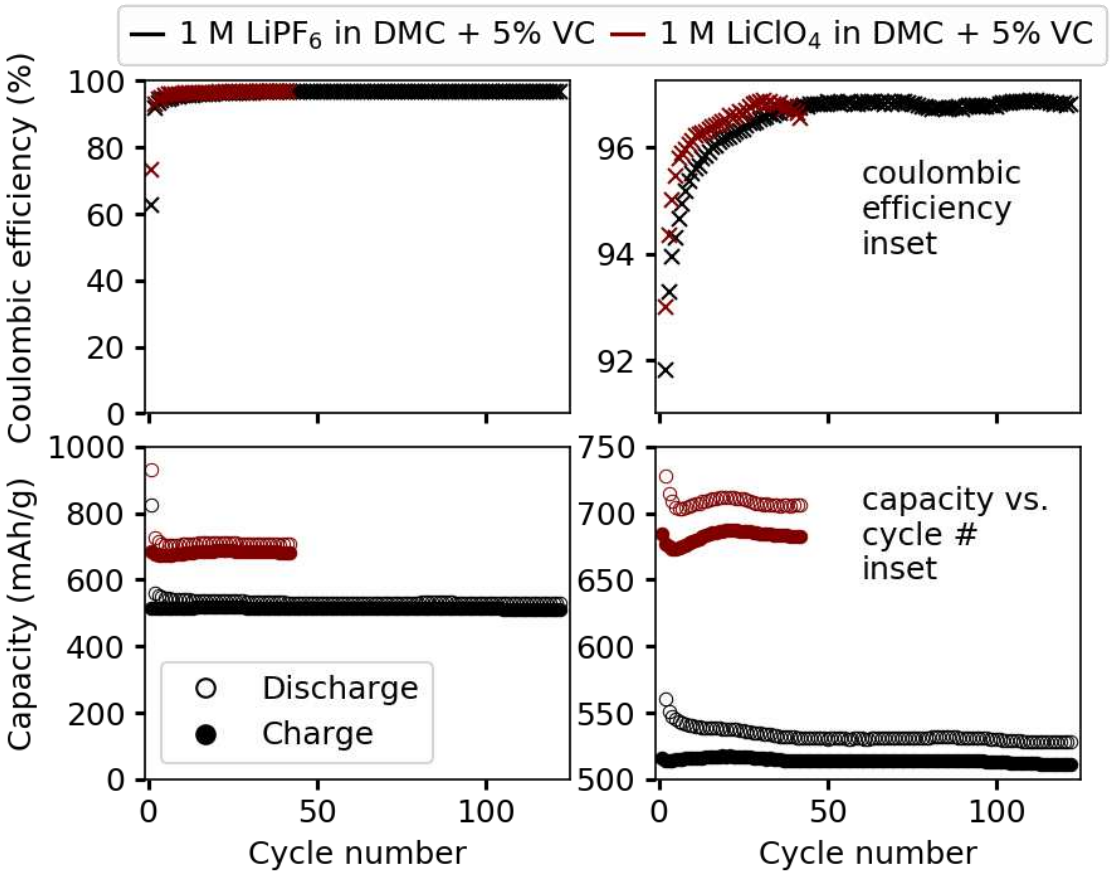

Figure 4.5: Coulombic efficiency versus cycle number and capacity versus cycle number plots (both still in progress) for SnSb films cycled in $LiPF_6$- and $LiClO_4$-based electrolytes, with insets shown on the right.

SnSb will also be characterized at the point where the capacity of the electrode begins to decline, designated as the "pre-failure SEI" in order to determine if there is a difference in speciation between the presumably more stable "established SEI" and the SEI as the electrode begins to fail. Finally, the SEI will also be characterized just after electrode failure, which is defined as the point when the capacity is 80% of its initial value (initial capacity here based on the reversible capacity from the second cycle, not the first cycle, which includes irreversible capacity from SEI formation). By characterizing the SEI on SnSb after failure, we hope to be able to identify which, if any, SEI species may play a role in initiating electrode failure.

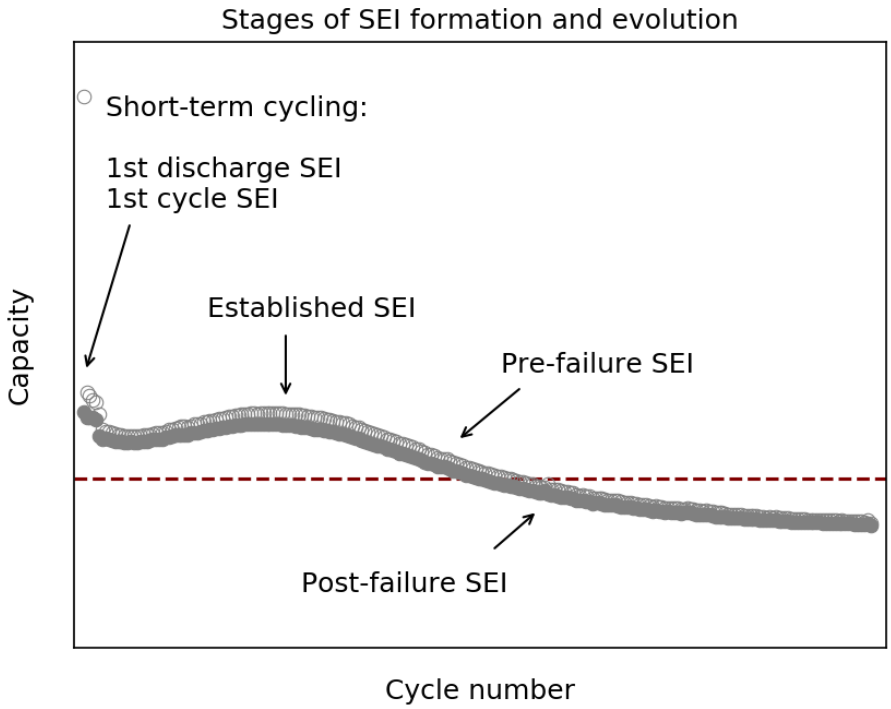

Figure 4.6: Generic capacity versus cycle number plot typically of alloying anodes with labels for the different stages of interest for short-term and long-term SEI studies on SnSb electrodes; the maroon dotted line indicates where the capacity is 80% of the initial capacity value, which is used as the cutoff for failure of the cell.

Short-Term Cycling SEI

The SEI layers formed during the first cycle on SnSb electrodes were characterized with XPS in order to better understand the types of species present on the electrode surface during the initial stages of SEI formation. While this type of characterization has been done for many other Sn- and Sb-based alloying anodes,[27–29,38] it has not yet been reported for SnSb. The SEI formed at the end of the first discharge and at the end of the first cycle (end of 1st charge) were both characterized because the SEI has been found to exhibit dynamic behavior and changes throughout the discharging and charging processes.[10,27–29,38–40] Additionally, in order to assess SEI reproducibility and consistency, each sample was made in duplicate, and to assess lateral heterogeneity, we looked at three different analysis regions per sample. The HRES XPS data for all analysis regions from the duplicate samples for the first discharge and

first cycle SEI samples prepared from SnSb cycled in 1 M $LiPF_6$ in DMC with 5% VC are shown in Figures 4.7–4.9.

The C 1s and Li 1s HRES spectra for the first discharge and first cycle SEI samples are compared in Figure 4.7. From looking at the C 1s spectra for the first discharge replicate SEI samples shown in Figure 4.7a, the SEI formed over this stage of cycling seems to show some minor variability between replicate samples and for different analysis regions of a given sample based on the types of binding environments present. However, overall the results are similar in that the most intense C 1s feature is one corresponding to an aliphatic carbon binding environment at ca. 284.5 eV, which could be due to the presence of adventitious carbon as well as carbonaceous SEI components.[29,41–43] There are also several low intensity features seen in the C 1s spectra. There is one at ca. 286 eV corresponding to a C–O binding environment, which could be due to a number a SEI species, including alkyl carbonates, alkyl carboxylates, esters, alkoxides, or PEO oligomers; there is also a low intensity feature at ca. 288 eV corresponding to an O=C–O binding environment due to species like alkyl carboxylates or esters.[26,29,41–45] Finally, there is also a low intensity feature at ca. 290 eV corresponding to a carbonate binding environment, which could be due to either Li alkyl carbonate species or Li_2CO_3 in the SEI.[27,29,41,42] The only C 1s feature not observed for all regions and samples of the first discharge SEI is one at higher binding energies around 291 eV. It is only observed in analysis regions 1 and 2 for first discharge sample 1 (left side of Figure 4.7a) and is most likely due to poly carbonate species like poly VC.[43,46]

The C 1s HRES spectra for the first cycle SEI samples shown in Figure 4.7c are notably different than those seen for the first discharge SEI samples in the sense that all regions of the SEI samples formed over the first cycle show evidence of at least five carbon binding environments. The feature at ca. 291 eV corresponding to a species like poly VC is seen for all analysis regions of both first cycle SEI samples. Otherwise, the first discharge and first cycle SEI samples have the same types of C 1s binding environments, which could mean similar types of species in both types of SEI sample, but they seem to be

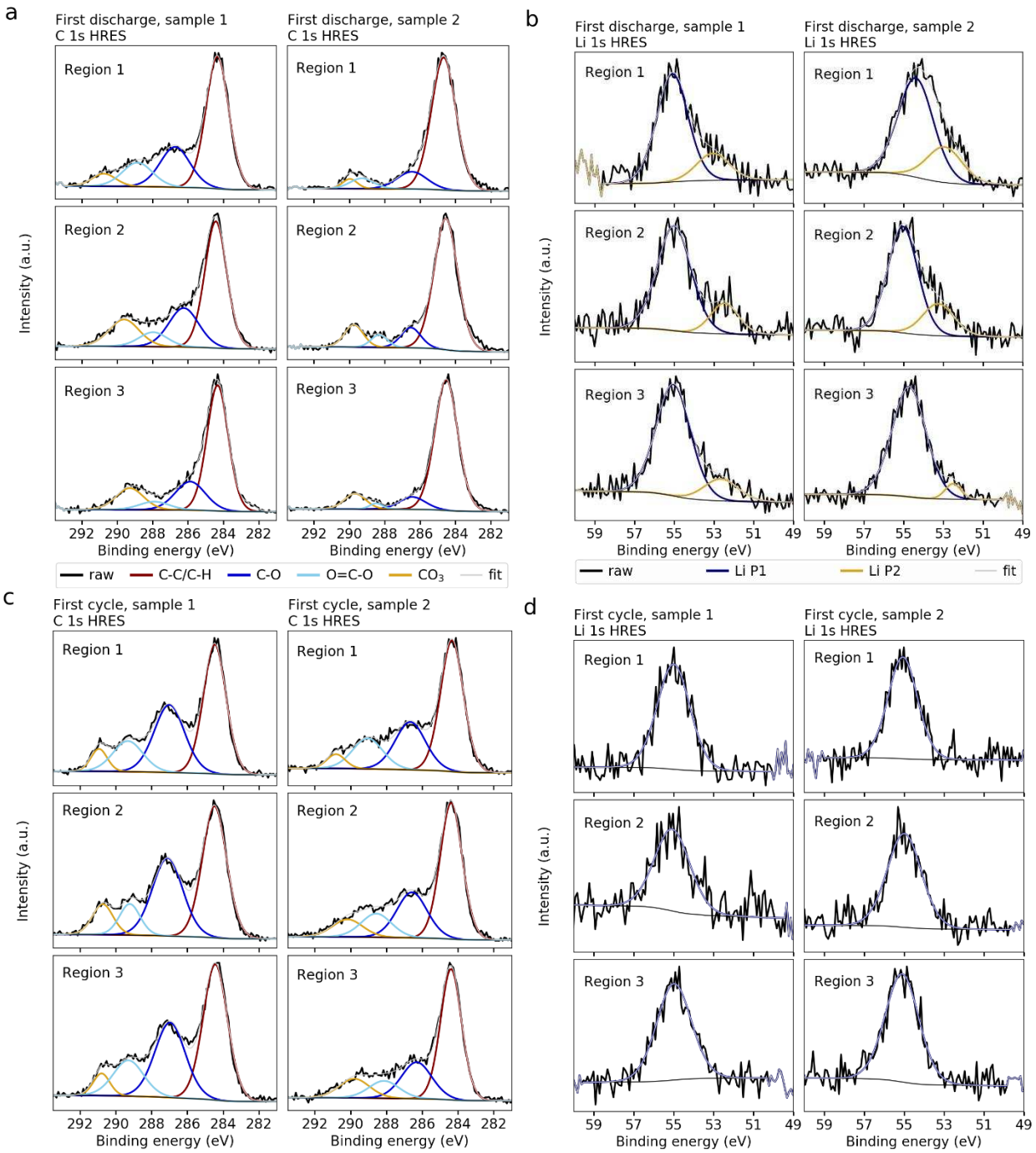

Figure 4.7: HRES XPS spectra for short term cycling SEI samples formed on SnSb cycled in 1 M $LiPF_6$ in DMC with 5% VC as the electrolyte. The C 1s (a) and Li 1s (b) spectra for all three regions of the replicate first discharge SEI samples and the C 1s (c) and Li 1s (d) spectra for all three regions of the replicate first cycle SEI samples are shown.

present in different amounts based on differences in relative peak intensities. For the first cycle SEI samples, the SEI seems heterogeneous for a given sample, but there is some variability between "replicates" based on the relative intensities of features in the C 1s spectra.

The Li 1s spectra for the first discharge and first cycle SEI samples are shown in Figure 4.7b and 4.7d. It is difficult to draw conclusions about the different types of Li-containing species that may be present in the SEI based on the Li 1s spectra due to small binding energy shifts for different Li 1s binding environments. However, the Li 1s spectra for these samples are notable in that the Li 1s peaks are well resolved, which is usually seen only when there are relatively high concentrations of Li present at the sample surface due to the small ionization cross section of Li. This suggests that a large amount of Li is consumed in SEI formation during the first cycle for SnSb electrodes and is consistent with the large first cycle irreversible capacities reported for SnSb electrodes.[6,47]

The F 1s HRES spectra for the first discharge and first cycle SEI samples are shown in Figure 4.8a and 4.8c. All of the spectra show evidence of at least two binding environments. The first, at ca. 685 eV, is assigned to LiF and the second at ca. 687.5 eV could be due to either LiP_xF_y species, including $LiPF_6$, and/or $LiP_xF_yO_z$ species.[26–29,44] Much of the Li detected at the SEI surface likely comes from the $LiPF_6$ salt and $LiPF_6$ degradation or reduction species. There are some small variations in relative F 1s peak intensities for the LiF and LiP_xF_y/$LiP_xF_yO_z$ peaks among the different analysis regions, but overall the spectra appear similar.

The P 2p spectra for the first discharge and first cycle SEI samples are shown in Figure 4.8b and 4.8d. The P 2p spectra for both types of SEI samples also show evidence of at least two different P 2p binding environments. The first, at ca. 133 eV, most likely corresponds to a phosphate binding environment based on the binding energy; P 2p peaks corresponding inorganic and organic phosphates, as well as pyrophosphates are all reported to appear at similar binding energies, so it is difficult to determine what type of phosphorus species is present based on the P 2p spectra alone.[36,42,48] The second

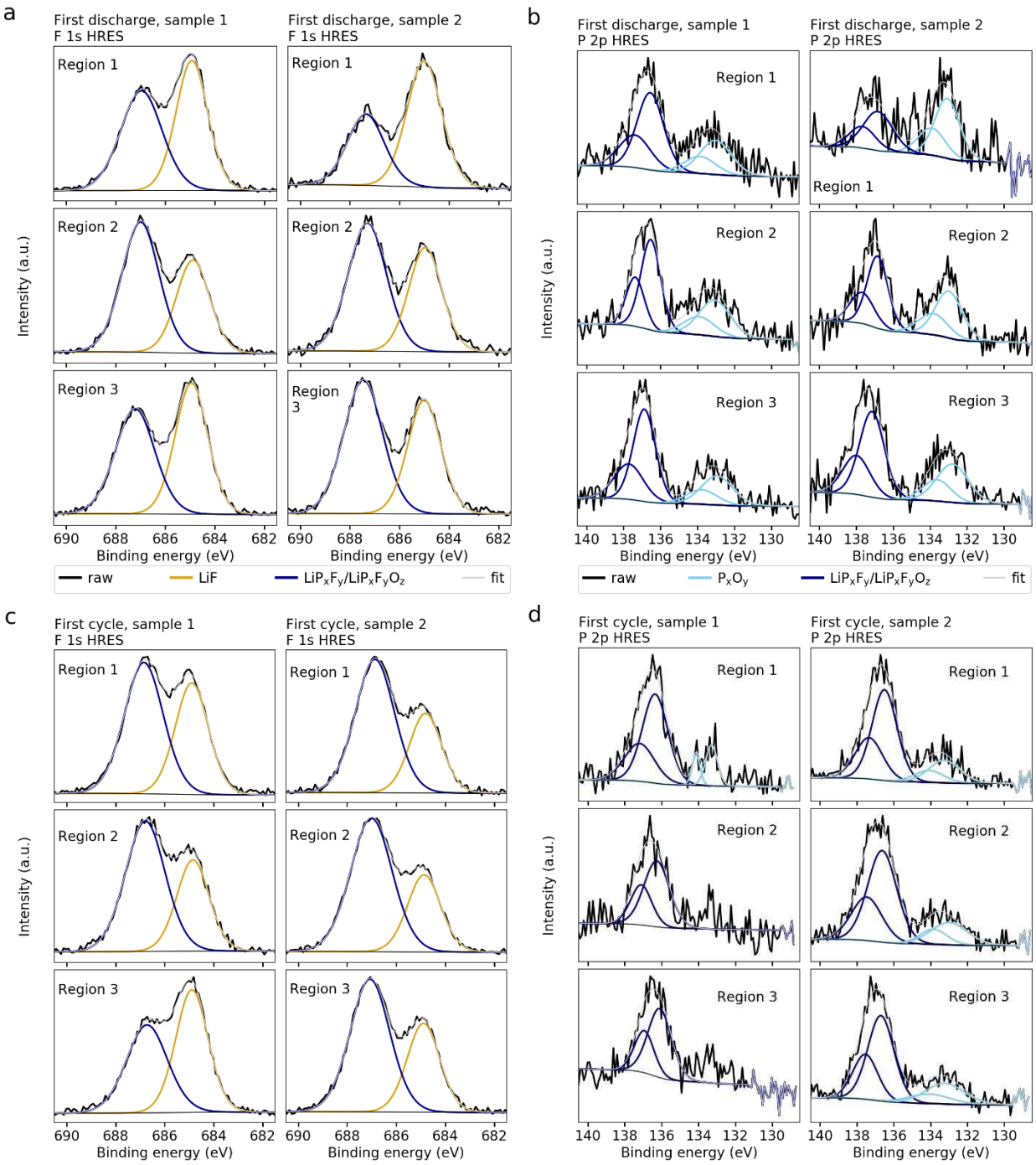

Figure 4.8: HRES XPS spectra for short term cycling SEI samples formed on SnSb cycled in 1 M $LiPF_6$ in DMC with 5% VC as the electrolyte. The F 1s (a) and P 2p (b) spectra for all three regions of the replicate first discharge SEI samples and the F 1s (c) and P 2p (d) spectra for all three regions of the replicate first cycle SEI samples are shown.

P 2p feature at ca. 137 eV is likely due to either LiP_xF_y and/or $LiP_xF_yO_z$ species based on the F 1s spectra. In general, the first discharge SEI samples seem to contain more phosphate species than the first cycle SEI samples based on the intensities of the features at ca. 133 eV.

The O 1s/Sb 3d HRES spectra for the first discharge and first cycle SEI samples are shown in Figure 4.9a and 4.9c. There is some overlap between the Sb $3d_{5/2}$ and O 1s peaks between ca. 528 eV and 530 eV, but the Sb $3d_{3/2}$ peaks are usually high enough in binding energy between ca. 537 eV and 540 eV that there is no overlap with O 1s peaks. No Sb $3d_{3/2}$ peaks corresponding to Sb^0 and Sb_xO_y species were observed around 537 eV and 540 eV, respectively (not shown in Figure 4.9), which suggests that the SEIs formed over the first discharge and over the first cycle are thick enough to attenuate most of the signal from the Sb in the electrode. However, there is a very broad, low intensity feature seen around 525 eV for some regions of the first discharge SEI samples and around 526 eV for the first cycle SEI samples that could be Sb $3d_{5/2}$ peaks due to small amounts of lithiated Sb species being detected at the surface.[29] The features are too low in binding energy to correspond to and O 1s features, and the corresponding Sb $3d_{3/2}$ peaks would be very small and overlap with the high binding energy O 1s features. The O 1s species with binding energies between ca. 530 eV and 535 eV can be difficult to deconvolute even with peak fitting due to small binding energy shifts, but the presence of O 1s features in this binding energy region agree with the features seen in the C 1s, F 1s, and P 2p HRES spectra. The SEI samples formed over the first discharge all contain some amount of Li_2O based on the feature at ca. 528 eV,[49] although for most analysis regions the peak is quite low in intensity.

Finally, the Sn 3d HRES spectra for the first discharge and first cycle SEI samples are shown in Figure 4.9b and 4.9d. Sn 3d peaks were detected for all regions of the replicate first discharge and first cycle SEI samples. It is interesting that little to no Sb was detected at the end of the first discharge and at the end of the first cycle while Sn was detected. It is not clear why this is the case, although it could be related to either differences in lithiation potentials or differences in reactivities of Sn and Sb. The Sn 3d

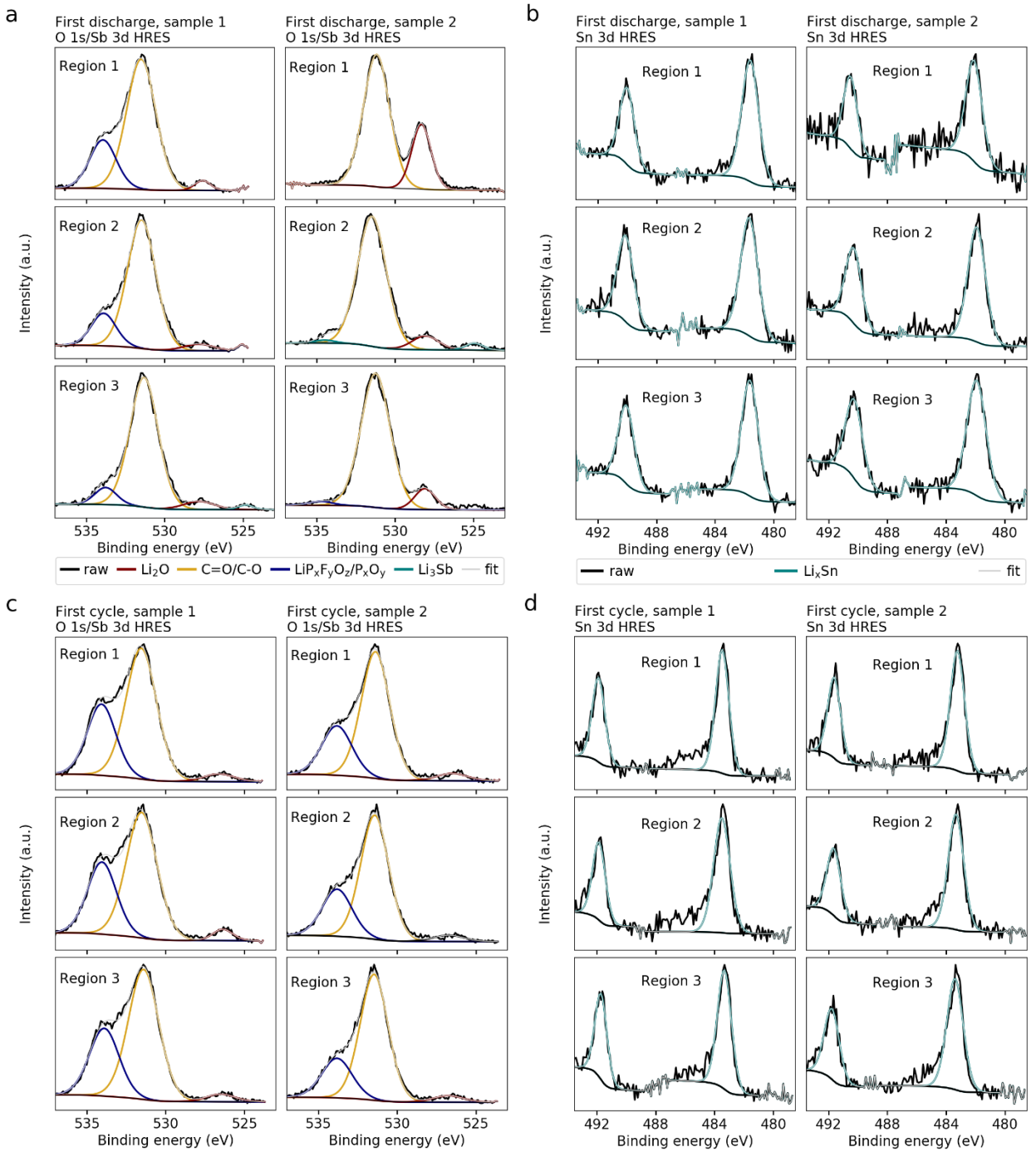

Figure 4.9: HRES XPS spectra for short term cycling SEI samples formed on SnSb cycled in 1 M $LiPF_6$ in DMC with 5% VC as the electrolyte. The O 1s/Sb 3d (a) and Sn 3d (b) spectra for all three regions of the replicate first discharge SEI samples and the O 1s/Sb 3d (c) and Sn 3d (d) spectra for all three regions of the replicate first cycle SEI samples are shown.

peaks for the first discharge SEI samples are located lower binding energies compared to the Sn 3d peaks in the pristine SnSb film, which is likely due to the presence of lithiated Sn in the discharged SEI sample.[27,28] The Sn 3d binding energies for the first cycle SEI sample are higher than those for the first discharge SEI sample, but they are still low compared to the binding energies for the pristine sample, which could be due to either incomplete delithiation or differences in sample charging for the conductive electrode and insulating SEI.[22]

The quantification results from fitting the HRES spectra for the first discharge (labeled as D1 S# R# depending on sample and analysis region) and first cycle SEI samples (labeled as C1 S# R#) are summarized in Figure 4.10. Overall, there was some variation between different analysis regions for a given sample and between the "replicate" samples, which is likely due to slight variations across the surface of the SnSb thin film. Even though Sn 3d peaks from the SnSb electrode were detected, the SEI is still quite thick and seems to cover most of the electrode surface based on the low atomic percent of Sn detected. The SEI surface is Li-rich as predicted based on the good signal to noise ratio and peak resolution of the Li 1s spectra, with Li making up ca. 30% of the surface for the first discharge SEI samples and 20% of the surface for the first cycle SEI samples. The higher percentage of Li detected for the first discharge SEI samples may be due to the Li_2O that was detected for the first discharge SEI samples but not the first charge SEI samples. Compared to the SEIs formed on other Sn-based electrodes cycled in $LiPF_6$-based electrolytes containing VC during the first discharge or during the first cycle, the SEI on SnSb is more F-rich, which may be related to the absence of EC in our electrolyte solution.[30,40,50,51]

Studies of the SEI formed on SnSb over short term cycling in $LiClO_4$-based electrolyte have not been completed yet. However, based on our previous studies of the SEI formed on Cu_2Sb from $LiClO_4$-based electrolyte, we anticipate that the SEI composition will be quite different. The SEI formed from $LiClO_4$-based electrolyte may be more C-rich than the one formed in $LiPF_6$-based electrolyte since there will not be any fluorine source present in the electrolyte to help passivate the electrode surface with

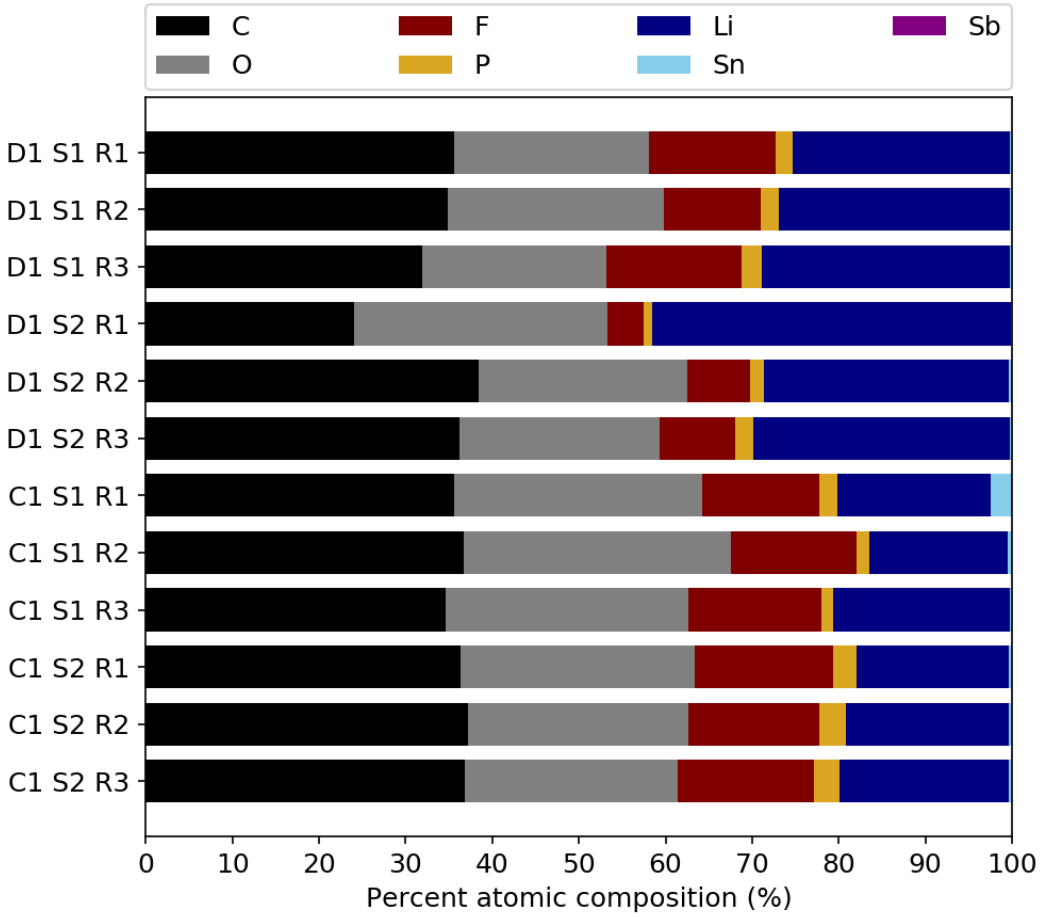

Figure 4.10: Compiled quantification results from the HRES spectra shown in Figures 4.7–4.9 for the short-term cycling SEI studies on SnSb.

LiF.[31,32] Additionally, there may be more Li_2O formed in the $LiClO_4$-based electrolyte samples; results from electrolyte soaking experiments in our group and from others have suggested that trace amounts of HF in $LiPF_6$-based electrolyte solutions can etch surface oxides on Cu_2Sb and Si electrodes.[52]

Long-Term Cycling SEI

The long-term cycling SEI experiments are still in progress. Based on the cycling data discussed in a previous section and previous cycling studies of SnSb thin film electrodes,[17] established SEI samples will likely cycle for about 100 cycles, or until the coulombic efficiency stabilizes, and the pre- and post-failure SEI samples will likely cycle for 200–300 cycles. The low coulombic efficiency values suggest continual SEI formation during cycling for both the $LiPF_6$- and $LiClO_4$-based electrolyte samples, so the SEIs are expected

to be quite thick. Sputtering through the long-term cycling SEI samples to obtain depth profiling information will likely take some time, although short sputter times (ca. 30 s) will be used to try to minimize sample damage and so that changes in the SEI with sputtering can be closely monitored. Based on existing SEI literature and previous work from our group, we expect the outer layer of the SEIs formed in both electrolyte solutions to be rich in organic species such as poly carbonates.[50,53–55] The inner layer of the SEI is expected to be rich in inorganic species, although the predominant species will likely be different for the different supporting electrolytes.[56–58]

During XPS depth profiling characterization, we will also take the time to sputter through some of the SnSb electrode in order to better understand how it is changing during extended cycling as well. This can be informative for several reasons. First, other long term SEI studies on alloying anodes have suggested that some SEI formation occurs within the electrode due to volume changes during cycling, which causes an increase in electrode thickness over time.[50,59–61] Sputtering through some of the electrode will help us determine if this is occurring in our system and what types of electrolyte reduction species may be incorporated into the electrode. Additionally, we may be able determine whether Sn_xO_y species are still present within the electrode and whether the presence of amorphous Sn oxides affects SnSb cycling. Finally, comparing Sn and Sb atomic ratios in the electrode over extended cycling will help us determine if the ratios are changing over time. Sn aggregation has been known to occur in Sn-based anode materials and is thought to play a role in the failure of SnSb anodes.[5,47,62] Increasing Sn:Sb atomic ratios over time coupled with changes in differential capacity plot features may help us determine whether Sn aggregation is occurring.[62] By studying changes in both the SEI and the SnSb electrode over extended cycling, we hope to be able to determine whether changes in the SEI, changes in the electrode, or some combination of both contributes to the failure of SnSb electrodes after hundreds of cycles.

4.4) Conclusions

The surfaces of pristine SnSb thin films and the SEIs formed on SnSb electrodes from two different electrolytes were characterized with XPS in order to better understand the role that interfaces play in the lifetime and failure of SnSb anodes. The surface of electrodeposited SnSb films was composed of Sn^0, Sn_xO_y, Sb^0, and Sb_xO_y species due to preparation in ambient conditions. Additionally, there appeared to be some amorphous Sn_xO_y incorporation in the film based on XPS depth profiling with Ar^+ sputtering. Ultimately, we hope that by studying the evolution of the SEI formed on SnSb over different stages of cycling in addition to studying changes in the electrode with XPS that we will be able to determine whether changes in the SEI or changes in the electrode are the main contribution to the failure of SnSb thin film anodes. Additionally, if our data suggests that changes in the SEI due contribute to electrode failure, we hope to be able to identify what types of species may be responsible.

(1) Zhang, W. J. A Review of the Electrochemical Performance of Alloy Anodes for Lithium-Ion Batteries. *J. Power Sources* **2011**, *196* (1), 13–24. https://doi.org/10.1016/j.jpowsour.2010.07.020.

(2) Thackeray, M. M.; Vaughey, J. T.; Johnson, C. S.; Kropf, A. J.; Benedek, R.; Fransson, L. M. L.; Edström, K. Structural Considerations of Intermetallic Electrodes for Lithium Batteries. *J. Power Sources* **2003**, *113* (1), 124–130. https://doi.org/10.1016/S0378-7753(02)00538-4.

(3) Rom, I.; Wachtler, M.; Papst, I.; Schmied, M.; Besenhard, J. O.; Hofer, F.; Winter, M. Electron Microscopical Characterization of Sn/SnSb Composite Electrodes for Lithium-Ion Batteries. *SOLID STATE IONICS* **2001**, *143* (3–4), 329–336. https://doi.org/10.1016/S0167-2738(01)00886-4.

(4) Winter, M.; Besenhard, J. O. Electrochemical Lithiation of Tin and Tin-Based Intermetallics and Composites. *Electrochim. Acta* **1999**, *45* (1–2), 31–50. https://doi.org/10.1016/S0013-4686(99)00191-7.

(5) Antitomaso, P.; Fraisse, B.; Stievano, L.; Biscaglia, S.; Ayme-Perrot, D.; Girard, P.; Sougrati, M. T.; Monconduit, L. SnSb Electrodes for Li-Ion Batteries: The Electrochemical Mechanism and Capacity Fading Origins Elucidated by Using Operando Techniques. *J. Mater. Chem. A* **2017**, *5* (14), 6546–6555. https://doi.org/10.1039/c6ta10138k.

(6) Wachtler, M.; Besenhard, J. O.; Winter, M. Tin and Tin-Based Intermetallics as New Anode Materials for Lithium-Ion Cells. *J. Power Sources* **2001**, *94* (2), 189–193. https://doi.org/10.1016/S0378-7753(00)00585-1.

(7) Tesfaye, A. T.; Dumur, F.; Gigmes, D.; Maria, S.; Monconduit, L.; Djenizian, T. Superior Electrochemical Performance of Thin-Film Thermoplastic Elastomer-Coated SnSb as an Anode for Li-Ion Batteries. *Sci. Rep.* **2019**, *9*, 1–9. https://doi.org/10.1038/s41598-019-40835-9.

(8) Tesfaye, A. T.; Yucel, Y. D.; Barr, M. K. S.; Santinacci, L.; Vacandio, F.; Dumur, F.; Maria, S.; Monconduit, L.; Djenizian, T. The Electrochemical Behavior of SnSb as an Anode for Li-Ion Batteries Studied by Electrochemical Impedance Spectroscopy and Electron Microscopy. *Electrochim. Acta* **2017**, *256*, 155–161. https://doi.org/10.1016/j.electacta.2017.10.031.

(9) Aurbach, D.; Markovsky, B.; Shechter, A.; EinEli, Y.; Cohen, H. A Comparative Study of Synthetic Graphite and Li Electrodes in Electrolyte Solutions Based on Ethylene Carbonate Dimethyl Carbonate Mixtures. *J. Electrochem. Soc.* **1996**, *143* (12), 3809–3820. https://doi.org/10.1149/1.1837300.

(10) Bodenes, L.; Darwiche, A.; Monconduit, L.; Martinez, H. The Solid Electrolyte Interphase a Key Parameter of the High Performance of Sb in Sodium-Ion Batteries: Comparative X-Ray Photoelectron Spectroscopy Study of Sb/Na-Ion and Sb/Li-Ion Batteries. *J. Power Sources* **2015**, *273*, 14–24. https://doi.org/10.1016/j.jpowsour.2014.09.037.

(11) Madec, L.; Coquil, G.; Ledeuil, J.-B.; Gachot, G.; Monconduit, L.; Martinez, H. How the Binder/Solvent Formulation Impacts the Electrolyte Reactivity/Solid Electrolyte Interphase Formation and Cycling Stability of Conversion Type Electrodes. *J. Electrochem. Soc.* **2020**, *167* (6), 060533. https://doi.org/10.1149/1945-7111/ab861f.

(12) Fransson, L.; Eriksson, T.; Edström, K.; Gustafsson, T.; Thomas, J. O. Influence of Carbon Black and Binder on Li-Ion Batteries. *J. Power Sources* **2001**, *101* (1), 1–9. https://doi.org/10.1016/S0378-7753(01)00481-5.

(13) Jaumann, T.; Balach, J.; Klose, M.; Oswald, S.; Langklotz, U.; Michaelis, A.; Eckert, J.; Giebeler, L. SEI-Component Formation on Sub 5 Nm Sized Silicon Nanoparticles in Li-Ion Batteries: The Role of Electrode Preparation, FEC Addition and Binders. *Phys. Chem. Chem. Phys.* **2015**, *17* (38), 24956–24967. https://doi.org/10.1039/c5cp03672k.

(14) Beattie, S. D.; Hatchard, T.; Bonakdarpour, A.; Hewitt, K. C.; Dahn, J. R. Anomalous, High-Voltage Irreversible Capacity in Tin Electrodes for Lithium Batteries. *J. Electrochem. Soc.* **2003**, *150* (6), A701–A705. https://doi.org/10.1149/1.1569477.

(15) Beaulieu, L. Y.; Beattie, S. D.; Hatchard, T. D.; Dahn, J. R. The Electrochemical Reaction of Lithium with Tin Studied by in Situ AFM. *J. Electrochem. Soc.* **2003**, *150* (4), A419–A424. https://doi.org/10.1149/1.1556595.

(16) Bridel, J.-S. S.; Grugeon, S.; Laruelle, S.; Hassoun, J.; Reale, P.; Scrosati, B.; Tarascon, J.-M. M. Decomposition of Ethylene Carbonate on Electrodeposited Metal Thin Film Anode. *J. Power Sources* **2010**, *195* (7, SI), 2036–2043. https://doi.org/10.1016/j.jpowsour.2009.10.038.

(17) Ma, J.; Prieto, A. L. Understanding the Electrodeposition of Pure Phase SnSb from Deep Eutectic Ethaline Solution and Its Application as a Lithium-Ion Anode. *unpublished* **2020**.

(18) Schneider, J. B.; Agocs, D. B.; Prieto, A. L. Design of a Sample Transfer Holder to Enable Air-Free X-Ray Photoelectron Spectroscopy. **2020**.

(19) Greczynski, G.; Hultman, L. X-Ray Photoelectron Spectroscopy: Towards Reliable Binding Energy Referencing. *Prog. Mater. Sci.* **2020**, *107*, 100591. https://doi.org/10.1016/j.pmatsci.2019.100591.

(20) Edström, K.; Herstedt, M.; Abraham, D. P. A New Look at the Solid Electrolyte Interphase on Graphite Anodes in Li-Ion Batteries. *J. Power Sources* **2006**, *153* (2), 380–384. https://doi.org/10.1016/j.jpowsour.2005.05.062.

(21) Dedryvère, R.; Laruelle, S.; Grugeon, S.; Poizot, P.; Gonbeau, D.; Tarascon, J. M. Contribution of X-Ray Photoelectron Spectroscopy to the Study of the Electrochemical Reactivity of CoO toward Lithium. *Chem. Mater.* **2004**, *16* (6), 1056–1061. https://doi.org/10.1021/cm0311269.

(22) Lindgren, F.; Rehnlund, D.; Källquist, I.; Nyholm, L.; Edström, K.; Hahlin, M.; Maibach, J. Breaking Down a Complex System: Interpreting PES Peak Positions for Cycled Li-Ion Battery Electrodes. *J. Phys. Chem. C* **2017**, *121* (49), 27303–27312. https://doi.org/10.1021/acs.jpcc.7b08923.

(23) Webb, S. A.; Baggetto, L.; Bridges, C. A.; Veith, G. M. The Electrochemical Reactions of Pure Indium with Li and Na: Anomalous Electrolyte Decomposition, Benefits of FEC Additive, Phase Transitions and Electrode Performance. *J. Power Sources* **2014**, *248*, 1105–1117. https://doi.org/10.1016/j.jpowsour.2013.10.033.

(24) Chiu, K. F.; Lin, H. C.; Lin, K. M.; Lin, T. Y.; Shieh, D. T. The Significant Role of Solid Oxide Interphase in Enhancement of Cycling Performance of Sn Thin-Film Anodes. *J. Electrochem. Soc.* **2006**, *153* (6), A1038–A1042. https://doi.org/10.1149/1.2189246.

(25) Shi, F.; Ross, P. N.; Zhao, H.; Liu, G.; Somorjai, G. A.; Komvopoulos, K. A Catalytic Path for Electrolyte Reduction in Lithium-Ion Cells Revealed by in Situ Attenuated Total Reflection-Fourier Transform Infrared Spectroscopy. *J. Am. Chem. Soc.* **2015**, *137* (9), 3181–3184. https://doi.org/10.1021/ja5128456.

(26) Chan, C. K.; Ruffo, R.; Hong, S. S.; Cui, Y. Surface Chemistry and Morphology of the Solid Electrolyte Interphase on Silicon Nanowire Lithium-Ion Battery Anodes. *J. Power Sources* **2009**, *189* (2), 1132–1140. https://doi.org/10.1016/j.jpowsour.2009.01.007.

(27) Naille, S.; Dedryvere, R.; Martinez, H.; Leroy, S.; Lippens, P.-E. E.; Jumas, J. C.-C.; Gonbeau, D.; Dedryvère, R.; Martinez, H.; Leroy, S.; Lippens, P.-E. E.; Jumas, J. C.-C.; Gonbeau, D. XPS Study of Electrode/Electrolyte Interfaces of η-Cu6Sn5 Electrodes in Li-Ion Batteries. *J. Power Sources* **2007**, *174* (2), 1086–1090. https://doi.org/10.1016/j.jpowsour.2007.06.043.

(28) Ehinon, K. K. D.; Naille, S.; Dedryvère, R.; Lippens, P.-E.; Jumas, J.-C.; Gonbeau, D. Ni3Sn4 Electrodes for Li-Ion Batteries: Li-Sn Alloying Process and Electrode/Electrolyte Interface Phenomena. *Chem. Mater.* **2008**, *20* (16), 5388–5398. https://doi.org/10.1021/cm8006099.

(29) Stjerndahl, M.; Bryngelsson, H.; Gustafsson, T.; Vaughey, J. T.; Thackeray, M. M.; Edström, K. Surface Chemistry of Intermetallic AlSb-Anodes for Li-Ion Batteries. *Electrochim. Acta* **2007**, *52* (15), 4947–4955. https://doi.org/10.1016/j.electacta.2007.01.064.

(30) Madec, L.; Gachot, G.; Coquil, G.; Martinez, H.; Monconduit, L. Toward Efficient Li-Ion Cells at High Temperatures: Example of TiSnSb Material. *J. Power Sources* **2018**, *391*, 51–58. https://doi.org/10.1016/j.jpowsour.2018.04.068.

(31) Qiao, R.; Lucas, I. T.; Karim, A.; Syzdek, J.; Liu, X.; Chen, W.; Persson, K.; Kostecki, R.; Yang, W. Distinct Solid-Electrolyte-Interphases on Sn (100) and (001) Electrodes Studied by Soft X-Ray Spectroscopy. *Adv. Mater. Interfaces* **2014**, *1* (3), 1–6. https://doi.org/10.1002/admi.201300115.

(32) Chan, A. K.; Tatara, R.; Feng, S.; Karayaylali, P.; Lopez, J.; Stephens, I. E. L.; Shao-Horn, Y. Concentrated Electrolytes for Enhanced Stability of Al-Alloy Negative Electrodes in Li-Ion Batteries. *J. Electrochem. Soc.* **2019**, *166* (10), A1867–A1874. https://doi.org/10.1149/2.0581910jes.

(33) Ulus, A.; Rosenberg, Y.; Burstein, L.; Peled, E. Tin Alloy-Graphite Composite Anode for Lithium-Ion Batteries. *J. Electrochem. Soc.* **2002**, *149* (5), A635–A643. https://doi.org/10.1149/1.1469029.

(34) Choo, M.-H.; Nguyen, C. C.; Hong, S.; Kwon, Y. H.; Woo, S.-W.; Kim, J. Y.; Song, S.-W. Combination of Acid-Resistor and -Scavenger Improves the SEI Stability and Cycling Ability of Tin-Nickel Battery Anodes in LiPF6-Containing Electrolyte. *Electrochim. Acta* **2013**, *112*, 252–257. https://doi.org/10.1016/j.electacta.2013.08.121.

(35) Hong, S.; Choo, M.-H.; Kwon, Y. H.; Kim, J. Y.; Song, S.-W. Interfacial Chemistry Control for Performance Enhancement of Micron Tin-Nickel/Graphite Battery Anode. *J. Electrochem. Soc.* **2014**, *161* (12), A1851–A1859. https://doi.org/10.1149/2.0661412jes.

(36) Hong, S.; Choo, M.-H.; Kwon, Y. H.; Kim, J. Y.; Song, S.-W. Mechanisms for Stable Solid Electrolyte Interphase Formation and Improved Cycling Stability of Tin-Based Battery Anode in Fluoroethylene Carbonate-Containing Electrolyte. *Adv. Mater. INTERFACES* **2016**, *3* (22), 1–9. https://doi.org/10.1002/admi.201600172.

(37) Schulze, M. C. Using Antimony as a Model Anode to Study the Chemical and Mechanical Stability of Electrodes in Li-Ion and Next Generation Batteries, Colorado State University, 2019.

(38) Philippe, B.; Mahmoud, A.; Ledeuil, J. B.; Sougrati, M. T.; Edström, K.; Dedryvère, R.; Gonbeau, D.; Lippens, P. E. MnSn2 Electrodes for Li-Ion Batteries: Mechanisms at the Nano Scale and Electrode/Electrolyte Interface. *Electrochim. Acta* **2014**, *123*, 72–83. https://doi.org/10.1016/j.electacta.2014.01.010.

(39) Yang, Z.; Dixon, M. C.; Erck, R. A.; Trahey, L. Quantification of the Mass and Viscoelasticity of Interfacial Films on Tin Anodes Using EQCM-D. *ACS Appl. Mater. Interfaces* **2015**, *7* (48), 26585–26594. https://doi.org/10.1021/acsami.5b07966.

(40) Zhang, W.; Ghamouss, F.; Darwiche, A.; Monconduit, L.; Lemordant, D.; Dedryvère, R.; Martinez, H. Surface Film Formation on TiSnSb Electrodes: Impact of Electrolyte Additives. *J. Power Sources* **2014**, *268*, 645–657. https://doi.org/10.1016/j.jpowsour.2014.06.041.

(41) Dedryvère, R.; Gireaud, L.; Grugeon, S.; Laruelle, S.; Tarascon, J. M.; Gonbeau, D. Characterization of Lithium Alkyl Carbonates by X-Ray Photoelectron Spectroscopy: Experimental and Theoretical Study. *J. Phys. Chem. B* **2005**, *109* (33), 15868–15875. https://doi.org/10.1021/jp051626k.

(42) Dedryvère, R.; Laruelle, S.; Grugeon, S.; Gireaud, L.; Tarascon, J.-M. M.; Gonbeau, D. XPS Identification of the Organic and Inorganic Components of the Electrode/Electrolyte Interface Formed on a Metallic Cathode. *J. Electrochem. Soc.* **2005**, *152* (4), A689–A696. https://doi.org/10.1149/1.1861994.

(43) El Ouatani, L.; Dedryvre, R.; Siret, C.; Biensan, P.; Reynaud, S.; Iraţabal, P.; Gonbeau, D. The Effect of Vinylene Carbonate Additive on Surface Film Formation on Both Electrodes in Li-Ion Batteries. *J. Electrochem. Soc.* **2009**, *156* (2), A103–A113. https://doi.org/10.1149/1.3029674.

(44) Schroder, K. W.; Celio, H.; Webb, L. J.; Stevenson, K. J. Examining Solid Electrolyte Interphase Formation on Crystalline Silicon Electrodes: Influence of Electrochemical Preparation and Ambient Exposure Conditions. *J. Phys. Chem. C* **2012**, *116* (37), 19737–19747. https://doi.org/10.1021/jp307372m.

(45) Li, J.-T. T.; Swiatowska, J.; Seyeux, A.; Huang, L.; Maurice, V.; Sun, S.-G. G.; Marcus, P. XPS and ToF-SIMS Study of Sn – Co Alloy Thin Films as Anode for Lithium Ion Battery. *J. Power Sources* **2010**, *195* (24, SI), 8251–8257. https://doi.org/10.1016/j.jpowsour.2010.07.043.

(46) El Ouatani, L.; Dedryvre, R.; Siret, C.; Biensan, P.; Gonbeau, D. Effect of Vinylene Carbonate Additive in Li-Ion Batteries: Comparison of LiCoO2/C, LiFePO4/C, and LiCoO2/Li4Ti5O12 Systems. *J. Electrochem. Soc.* **2009**, *156* (6), A468–A477. https://doi.org/10.1149/1.3111891.

(47) Li, H.; Shi, L. H.; Lu, W.; Huang, X. J.; Chen, L. Q. Studies on Capacity Loss and Capacity Fading of Nanosized SnSb Alloy Anode for Li-Ion Batteries. *J. Electrochem. Soc.* **2001**, *148* (8), A915–A922. https://doi.org/10.1149/1.1383070.

(48) Sherwood, P. M. A. Introduction to Studies of Phosphorus-Oxygen Compounds by XPS. *Surf. Sci. Spectra* **2002**, *9* (1), 62–66. https://doi.org/10.1116/11.20030101.

(49) Shiraishi, S.; Kanamura, K.; Takehara, Z. I. Influence of Initial Surface Condition of Lithium Metal Anodes on Surface Modification with HF. *J. Appl. Electrochem.* **1999**, *29* (7), 869–881.

(50) Park, S.; Heon Ryu, J.; Oh, S. M. Passivating Ability of Surface Film Derived from Vinylene Carbonate on Tin Negative Electrode. *J. Electrochem. Soc.* **2011**, *158* (5), A498–A503. https://doi.org/10.1149/1.3561424.

(51) Marino, C.; Darwiche, A.; Dupre, N.; Wilhelm, H. A.; Lestriez, B.; Martinez, H.; Dedryvere, R.; Zhang, W.; Ghamouss, F.; Lemordant, D.; Monconduit, L. Study of the Electrode/Electrolyte Interface on Cycling of a Conversion Type Electrode Material in Li Batteries. *J. Phys. Chem. C* **2013**, *117* (38), 19302–19313. https://doi.org/10.1021/jp402973h.

(52) *Silicon Electrolyte Interface Stabilization (SEISta) Second Quarter Progress Report 2018*; 2018 https://www.nrel.gov/transportation/assets/pdfs/next_generation_anodes_q2_progress_report_fy18.pdf (Accessed 07/09/2020).

(53) Jackson, E. D.; Prieto, A. L. Copper Antimonide Nanowire Array Lithium Ion Anodes Stabilized by Electrolyte Additives. *ACS Appl. Mater. Interfaces* **2016**, *8* (44), 30379–30386. https://doi.org/10.1021/acsami.6b08033.

(54) Seo, D. M.; Nguyen, C. C.; Young, B. T.; Heskett, D. R.; Woicik, J. C.; Lucht, B. L. Characterizing Solid Electrolyte Interphase on Sn Anode in Lithium Ion Battery. *J. Electrochem. Soc.* **2015**, *162* (13), A7091–A7095. https://doi.org/10.1149/2.0121513jes.

(55) Kilibarda, G.; Schlabach, S.; Winkler, V.; Bruns, M.; Hanemann, T.; Szabo, D. V. Electrochemical Performance of Tin-Based Nano-Composite Electrodes Using a Vinylene Carbonate-Containing Electrolyte for Li-Ion Cells. *J. Power Sources* **2014**, *263*, 145–153. https://doi.org/10.1016/j.jpowsour.2014.04.030.

(56) Li, J.-T. T.; Światowska, J.; Maurice, V.; Seyeux, A.; Huang, L.; Sun, S.-G. G.; Marcus, P. XPS and ToF-SIMS Study of Electrode Processes on Sn-Ni Alloy Anodes for Li-Ion Batteries. *J. Phys. Chem. C* **2011**, *115* (14), 7012–7018. https://doi.org/10.1021/jp201232n.

(57) Nie, M.; Lucht, B. L. Role of Lithium Salt on Solid Electrolyte Interface (SEI) Formation and Structure in Lithium Ion Batteries. *J. Electrochem. Soc.* **2014**, *161* (6), A1001–A1006. https://doi.org/10.1149/2.054406jes.

(58) Jurng, S.; Brown, Z. L.; Kim, J.; Lucht, B. L. Effect of Electrolyte on the Nanostructure of the Solid Electrolyte Interphase (SEI) and Performance of Lithium Metal Anodes. *Energy Environ. Sci.* **2018**, *11* (9), 2600–2608. https://doi.org/10.1039/c8ee00364e.

(59) Madec, L.; Ledeuil, J.-B.; Coquil, G.; Gachot, G.; Monconduit, L.; Martinez, H. Cross-Section Auger Imaging: A Suitable Tool to Study Aging Mechanism of Conversion Type Electrodes. *J. Power Sources* **2019**, *441*, 227213. https://doi.org/10.1016/j.jpowsour.2019.227213.

(60) Bian, X.; Dong, Y.; Zhao, D.; Ma, X.; Qiu, M.; Xu, J.; Jiao, L.; Cheng, F.; Zhang, N. Microsized Antimony as a Stable Anode in Fluoroethylene Carbonate Containing Electrolytes for Rechargeable Lithium-/Sodium-Ion Batteries. *ACS Appl. Mater. Interfaces* **2020**, *12* (3), 3554–3562. https://doi.org/10.1021/acsami.9b18006.

(61) Schulze, M. C.; Belson, R. M.; Kraynak, L. A.; Prieto, A. L. Electrodeposition of Sb/CNT Composite Films as Anodes for Li- and Na-Ion Batteries. *Energy Storage Mater.* **2020**, *25*, 572–584. https://doi.org/10.1016/j.ensm.2019.09.025.

(62) Courtney, I. A.; McKinnon, W. R.; Dahn, J. R. On the Aggregation of Tin in SnO Composite Glasses Caused by the Reversible Reaction with Lithium. *J. Electrochem. Soc.* **1999**, *146* (1), 59–68. https://doi.org/10.1149/1.1391565.

APPENDIX A: SUPPORTING INFORMATION DISCUSSED IN CHAPTER 2

SEI Sample Preparation

All half cells were cycled with Cu_2Sb thin films electrodeposited for 600 s (ca. 0.9 mg/cm^2 and ca. 1.2 mg Cu_2Sb per punch half-inch punch based on mass difference) as the working electrode. Assembled half cells were rested for 18 hours prior to cycling, and the half cells were cycled at a C/20 rate (ca. 19 μA/cm^2) over a given potential range for 20 cycles. Details on the potential limits and electrolyte for a given sample are provided in Table A1 below.

Table A1: Potential limits and electrolyte solutions used for the different samples mentioned in the main text.

Sample name	Potential range (V vs. Li/Li$^+$)	Electrolyte
Sample 1a	1.8–3.0	1 M $LiClO_4$ in EC/DMC/DEC (1:1:1 by vol)
Sample 2a	1.8–3.0	1 M $LiClO_4$ in EC/DMC/DEC (1:1:1 by vol)
Sample 1b	1.8–3.0	1 M $LiClO_4$ in EC/DMC/DEC (1:1:1 by vol) with 5% VC (by vol)
Sample 2b	1.8–3.0	1 M $LiClO_4$ in EC/DMC/DEC (1:1:1 by vol) with 5% VC (by vol)
Sample 1c	0.9–1.8	1 M $LiClO_4$ in EC/DMC/DEC (1:1:1 by vol)
Sample 2c**	0.9–1.8	1 M $LiClO_4$ in EC/DMC/DEC (1:1:1 by vol)
Sample 1d	0.05–0.9	1 M $LiClO_4$ in EC/DMC/DEC (1:1:1 by vol)
Sample 1e	0.05–1.6	1 M $LiClO_4$ in EC/DMC/DEC (1:1:1 by vol)
Sample 1f**	0.9–1.8	1 M $LiClO_4$ in EC/DMC/DEC (1:1:1 by vol)
Sample 1g	0.9–1.8	1 M $LiClO_4$ in EC/DMC/DEC (1:1:1 by vol) with 5% VC (by vol)
Sputtered sample	0.05–3.0	1 M $LiClO_4$ in EC/DMC/DEC (1:1:1 by vol) with 5% VC (by vol)

**Sample 2c and Sample 1f are the same sample but used in different examples and therefore given separate sample names to remain consistent with the naming conventions described in Chapter 2.

Swagelok cell part cleaning procedure

The following cleaning procedure was used to clean the Swagelok cell parts used in the experiments described in the text with the exception of Sample 1b. Any black residue inside of the used PTFE Swagelok cell body parts was scraped away using either a metal rasp or the ends of sharp needle-nosed tweezers and rinsed well with distilled water. Used PTFE Swagelok cell parts (cell body, end caps, and ferrules) were soaked in several changes of distilled water (ca. 2 L each time) for at least 3 hours each time. The cell parts were agitated at the beginning when fresh water was added to reduce the number of

air bubbles trapped in the cell body parts and to help wet the hydrophobic PTFE surface. Afterwards, the PTFE parts were allowed to dry thoroughly in air. We have found that soaking the PTFE cell parts in several changes of water for long periods of time is sufficient for removing residual Li salt and electrolyte degradation products, although others have also had success using a combination of organic solvents and water to clean cell parts.[1]

The metal cell parts (copper and stainless-steel current collectors, stainless-steel mesh, and stainless-steel springs) were rinsed briefly with distilled water and then immediately dried to prevent oxidation. The Cu current collectors were cleaned with Wenol metal polish to remove the oxidized surface layer and then cleaned 3 times by wiping with isopropanol-soaked Kim wipes to remove the organic residue left by the metal polish. The stainless-steel current collectors were cleaned 3 times using isopropanol-soaked Kim wipes, and the stainless-steel springs and mesh punches were sonicated in isopropanol for 5 minutes. Once all of the cell parts were dry, they were pumped down overnight into an Ar-filled glove box to minimize additional oxidation after cleaning.

Table A2: Sample 1a HRES fitting data

Sample description	Transition	Peak position (eV)	FWHM (eV)	Corrected area (A/(RSF*T*MFP))◊	% Atomic composition
Sample 1a Region 1	C 1s	284.97	1.02	577.84	53.3
		286.01	1.97	116.47	10.8
		289.11	1.49	40.86	3.8
	Cl 2p	208.52	1.16	15.18	1.4
		210.18	1.27	7.58	0.7
	O 1s/Sb 3d	527.84	1.21	1.62	0.2
		537.14	1.26	1.08	0.1
		529.99	1.20	1.86	0.2
		539.77	1.37	1.24	0.1
		532.23	2.25	174.60	16.1
		533.56	1.46	53.92	5.0
	Li 1s	55.62	1.45	91.67	8.5
Sample 1a Region 2	C 1s	284.84	1.13	1346.72	56.3
		285.94	2.00	233.06	9.7
		289.05	1.56	92.4144	3.9
	Cl 2p	208.56	1.21	30.6452	1.3
		210.17	1.27	15.316	0.6
	O 1s/Sb 3d	528.36	2.30	4.11582	0.2
		530.18	1.01	2.11491	0.1
		539.79	1.12	1.40634	0.1
		532.18	2.30	374.559	15.6
		533.60	1.50	97.497	4.1
	Li 1s	55.70	2.15	196.277	8.2
Sample 1a Region 3	C 1s	284.62	1.14	1111.61	52.0
		285.61	1.97	197.21	9.2
		288.94	1.39	79.2019	3.7
	Cl 2p	208.59	1.17	50.6045	2.4
		210.21	1.23	25.2914	1.2
	O 1s/Sb 3d	527.92	1.42	1.94068	0.1
		537.13	1.53	1.29064	0.1
		530.00	1.25	2.81002	0.1
		539.73	1.50	1.8685	0.1
		533.47	1.48	202.265	9.5
		532.10	2.04	273.473	12.8
	Li 1s	55.74	1.70	188.431	8.8
Sample 1a Region 4	C 1s	284.70	1.19	20200.3	52.5
		285.91	2.00	3538.47	9.2
		288.93	1.92	1892.41	4.9
	Cl 2p	208.50	1.23	446.158	1.2
		210.16	1.28	223.079	0.6
	O 1s/Sb 3d	527.83	1.45	56.6138	0.2

		537.04	1.45	37.7614	0.1
		529.92	1.30	77.2034	0.2
		539.53	1.58	51.4947	0.1
		532.12	2.30	8178.26	21.2
		533.49	1.38	1256.79	3.3
	Li 1s	55.40	1.84	2555.03	6.6

◊Area (A), relative sensitivity factor (RSF), transmission (T), and mean free path (MFP).

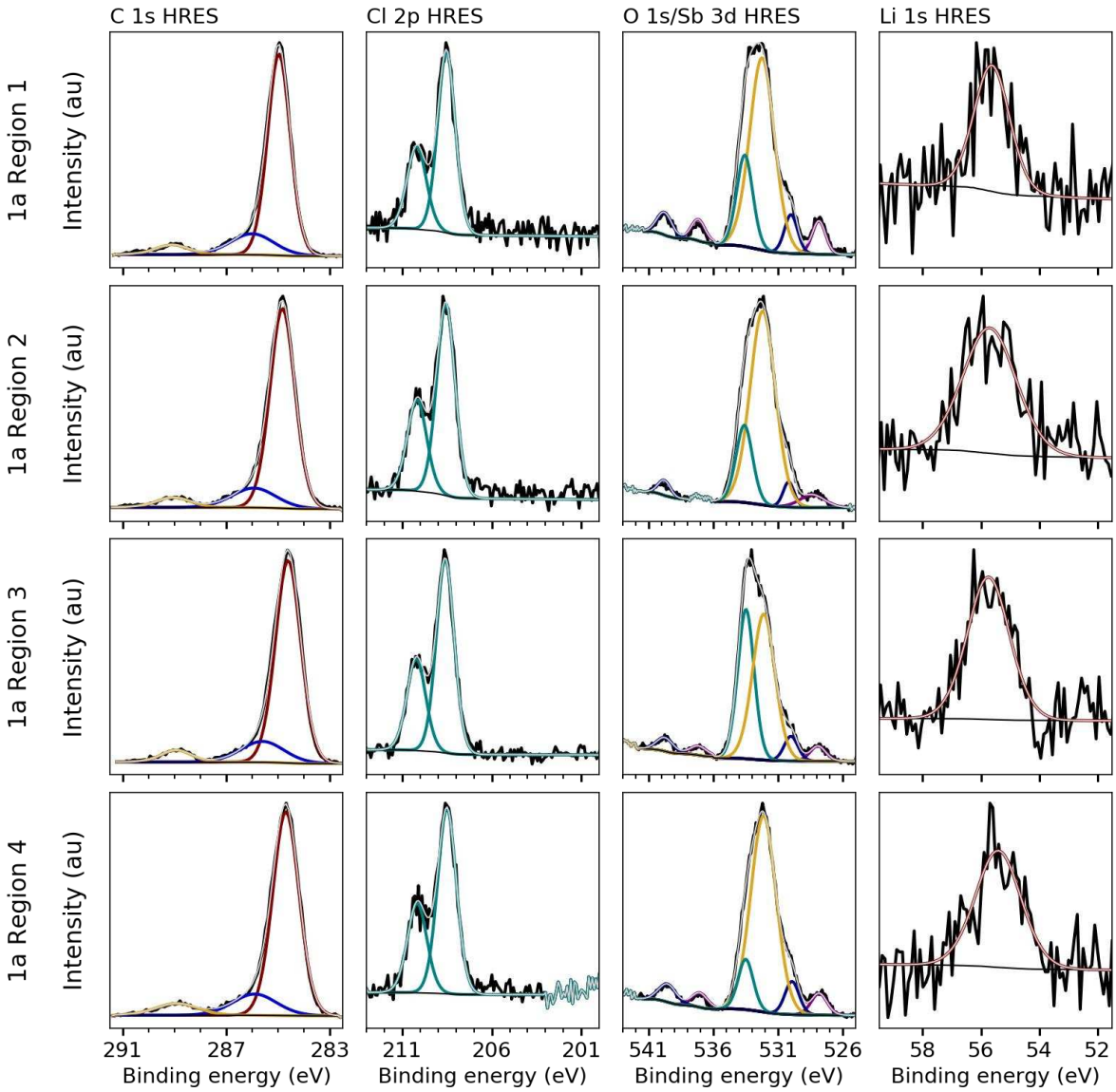

Figure A1: Sample 1a HRES fitting results.

Table A3: Sample 2a HRES fitting results

Sample description	Transition	Peak position (eV)	FWHM (eV)	Corrected area (A/(RSF*T*MFP))◊	% Atomic composition
Sample 2a Region 1	C 1s	284.88	1.27	233.512	37.4
		286.46	1.41	37.6087	6.0
		288.90	1.65	36.9293	5.9
	Cl 2p	208.62	1.28	22.7797	3.7
		210.25	1.17	11.3849	1.8
	O 1s/Sb 3d	530.58	1.23	1.99608	0.3
		539.95	1.36	1.32741	0.2
		531.35	2.30	44.0259	7.1
		533.22	1.54	114.87	18.4
		532.03	1.17	22.8498	3.7
	Li 1s	55.94	1.75	79.6734	12.8
	Cu 2p	932.84	1.31	12.0689	1.9
		952.65	1.68	5.47621	0.9
Sample 2a Region 2	C 1s	284.63	1.20	228.142	37.2
		286.06	1.75	52.2849	8.5
		288.70	1.66	38.1004	6.2
	Cl 2p	208.52	1.18	34.0946	5.6
		210.16	1.08	17.04	2.8
	O 1s/Sb 3d	530.42	1.06	1.59833	0.3
		539.87	1.18	1.0629	0.2
		533.11	1.58	148.437	24.2
		531.71	2.15	77.4502	12.6
	Cu 2p	932.66	1.28	9.59588	1.6
		952.54	1.89	4.89426	0.8
Sample 2a Region 3	C 1s	284.73	1.18	225.363	37.8
		285.92	2.00	69.7505	11.7
		288.83	1.56	38.2244	6.4
	Cl 2p	208.47	1.19	22.5792	3.8
		210.08	1.11	11.2848	1.9
	O 1s/Sb 3d	530.33	1.04	2.78214	0.5
		539.86	1.15	1.85007	0.3
		533.13	1.57	111.177	18.6
		531.72	2.30	92.481	15.5
	Cu 2p	932.70	1.31	14.3746	2.4
		952.70	1.86	6.86124	1.2

◊Area (A), relative sensitivity factor (RSF), transmission (T), and mean free path (MFP).

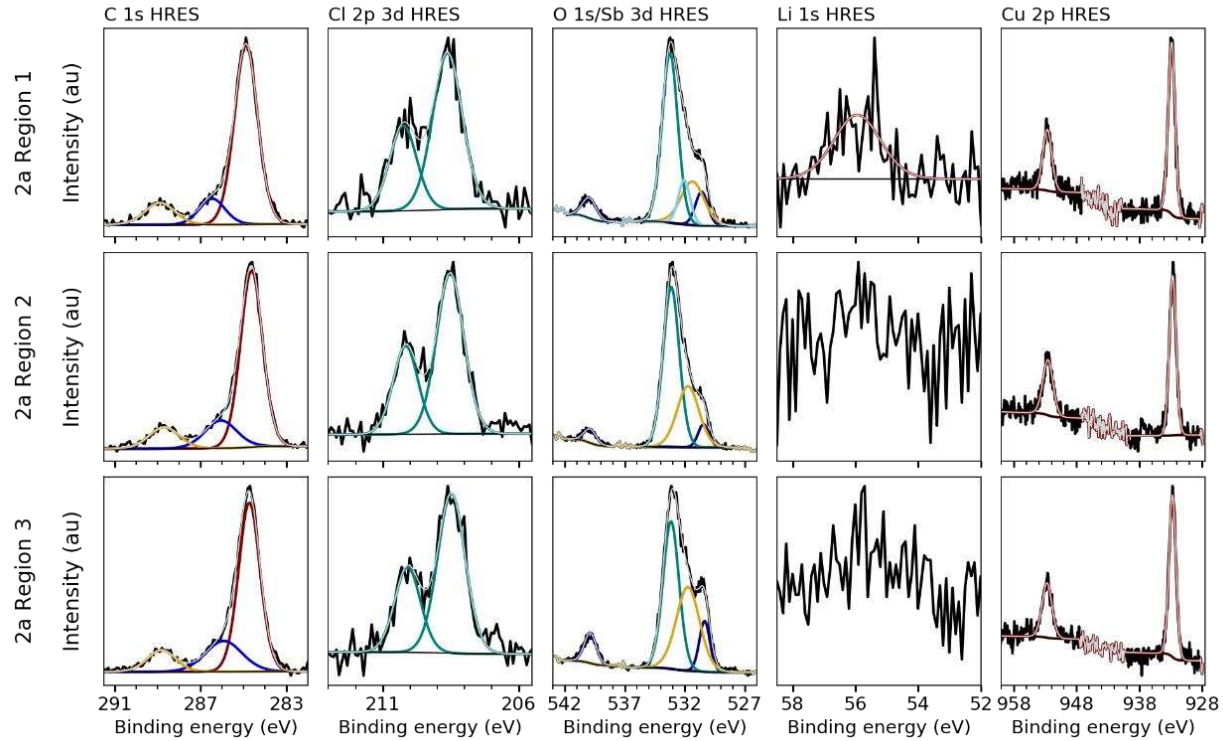

Figure A2: Sample 2a HRES fitting results.

Table A4: Sample 1b HRES fitting results

Sample description	Transition	Peak position (eV)	FWHM (eV)	Corrected area (A/(RSF*T*MFP))◊	% Atomic composition
Sample 1b Region 1	C 1s	285.02	1.13	766.153	31.7
		286.59	2.00	236.619	9.8
		289.11	2.00	143.668	6.0
	Cl 2p	208.58	1.20	22.2365	0.9
		210.31	1.22	11.1128	0.5
		198.11	1.21	8.37924	0.4
		199.73	1.09	4.18784	0.2
	O 1s/Sb 3d	527.81	0.94	14.1181	0.6
		537.22	0.92	9.38862	0.4
		530.72	1.34	35.5699	1.5
		540.12	1.50	23.6542	1.0
		533.18	2.00	315.214	13.0
		531.78	1.42	223.909	9.3
		528.98	2.30	77.4001	3.2
	Li 1s	55.91	1.84	256.791	10.6
	Cu 2p	932.98	1.25	13.8887	0.6
		952.69	2.02	6.30106	0.3
	F 1s	687.18	1.76	208.031	8.6
		685.18	1.46	38.4345	1.6
Sample 1b Region 2	C 1s	284.79	1.12	17936.7	41.0
		285.97	2.00	4235.86	9.7
		288.86	2.00	1771.84	4.0
	Cl 2p	208.44	1.09	413.845	1.0
		210.04	1.26	206.922	0.5
	O 1s/Sb 3d	527.82	0.96	103.343	0.2
		537.16	0.99	68.9301	0.2
		530.58	1.28	229.724	0.5
		539.92	1.41	153.226	0.4
		529.40	1.91	571.057	1.3
		532.00	2.09	5693.98	13.0
		533.09	1.17	1348.52	3.1
		533.84	1.47	1567	3.6
	Li 1s	55.70	2.09	5484.22	12.5
	Cu 2p	932.94	1.21	94.5682	0.2
		953.04	1.70	51.9211	0.1
	F 1s	687.09	1.84	3292.67	7.5
		685.06	1.22	546.761	1.3
Sample 1b Region 3	C 1s	284.95	1.14	13079.4	30.9
		286.61	1.92	3821.34	9.0
		288.67	1.22	961.344	2.3

		289.45	2.00	1652.56	3.9
	Cl 2p	208.47	1.33	375.14	0.9
		210.18	1.43	187.57	0.4
		198.20	1.70	187.566	0.4
		199.91	1.48	93.7828	0.2
	O 1s/Sb 3d	527.77	0.96	328.936	0.8
		537.11	0.98	219.4	0.5
		530.66	1.31	821.64	1.9
		540.00	1.46	548.034	1.3
		529.68	2.11	1680.29	4.0
		531.79	1.32	4613.82	10.9
		532.89	1.38	3083.37	7.3
		533.82	1.45	1549.91	3.7
	Li 1s	55.61	1.75	4969.56	11.7
	F 1s	687.06	1.76	3392.87	8.0
		685.14	1.55	770.735	1.8

◊Area (A), relative sensitivity factor (RSF), transmission (T), and mean free path (MFP).

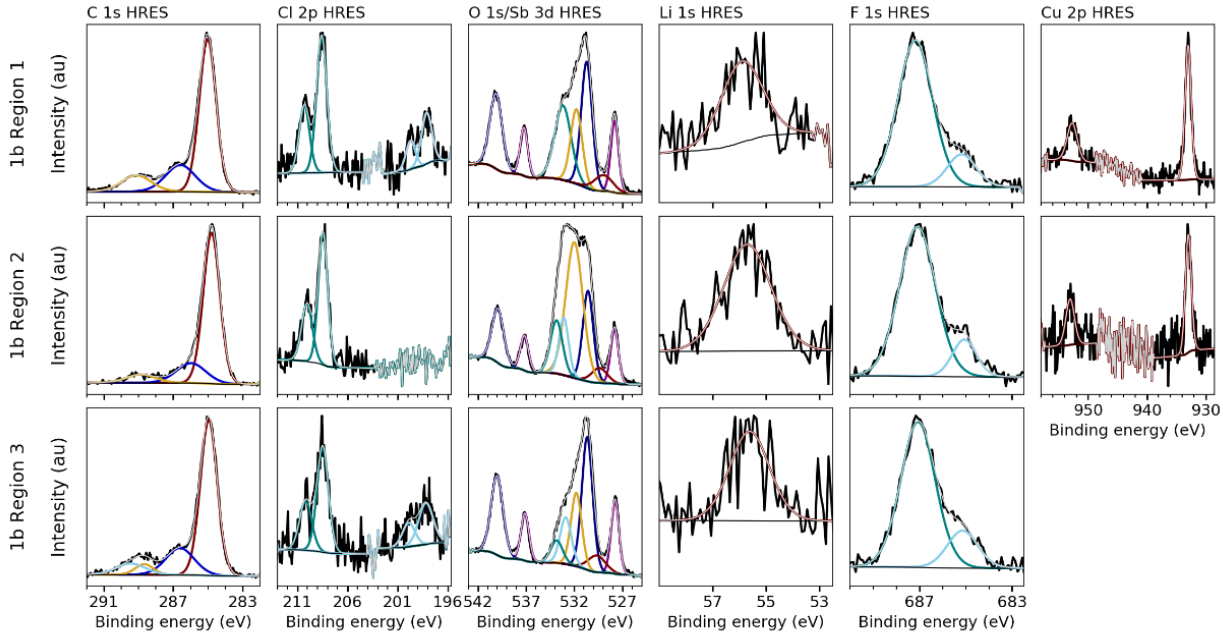

Figure A3: Sample 1b HRES fitting results.

Table A5: Sample 2b HRES fitting results

Sample description	Transition	Peak position (eV)	FWHM (eV)	Corrected area (A/(RSF*T*MFP))[◊]	% Atomic composition
Sample 2b Region 1	C 1s	285.14	1.08	296.095	39.3
		286.08	2.00	65.1837	8.6
		289.06	1.66	69.4528	9.2
	Cl 2p	208.53	1.15	5.0247	0.7
		210.22	0.92	2.51119	0.3
	O 1s/Sb 3d	527.76	1.06	1.03955	0.1
		537.08	1.07	0.691307	0.1
		530.01	1.56	1.82911	0.2
		539.93	1.73	1.21617	0.2
		532.02	1.96	170.315	23.0
		533.89	1.19	9.11307	1.2
	Li 1s	55.50	1.65	131.543	17.5
Sample 2b Region 2	C 1s	285.00	1.04	273.146	34.7
		286.24	2.00	84.9945	10.8
		288.87	1.43	54.0646	6.9
		290.48	2.00	27.6286	3.5
		208.60	1.32	9.83599	1.3
		210.43	1.45	4.91564	0.6
	O 1s/Sb 3d	527.62	0.94	0.636691	0.1
		537.08	0.91	0.423404	0.1
		529.14	1.31	0.871208	0.1
		539.45	1.45	0.579193	0.1
		531.82	1.53	97.5695	12.4
		533.14	2.12	82.9526	10.5
		530.32	1.32	28.3629	3.6
	Li 1s	55.55	1.57	114.472	14.5
	Cu 2p	932.41	1.25	4.93134	0.6
		952.24	2.08	2.69878	0.3
Sample 2b Region 3	C 1s	285.01	1.29	172.52	44.4
		286.40	2.00	29.2523	7.5
		288.93	2.00	32.2146	8.3
	Cl 2p	208.50	1.54	9.40324	2.4
		210.17	1.40	4.6996	1.2
	O 1s/Sb 3d	530.25	1.22	1.93019	0.5
		539.82	1.35	1.28351	0.3
		531.87	2.30	76.3599	19.7
		533.20	2.10	45.6168	11.7
	Cu 2p	932.54	1.40	10.2386	2.6
		952.35	1.77	4.87558	1.3

[◊]Area (A), relative sensitivity factor (RSF), transmission (T), and mean free path (MFP).

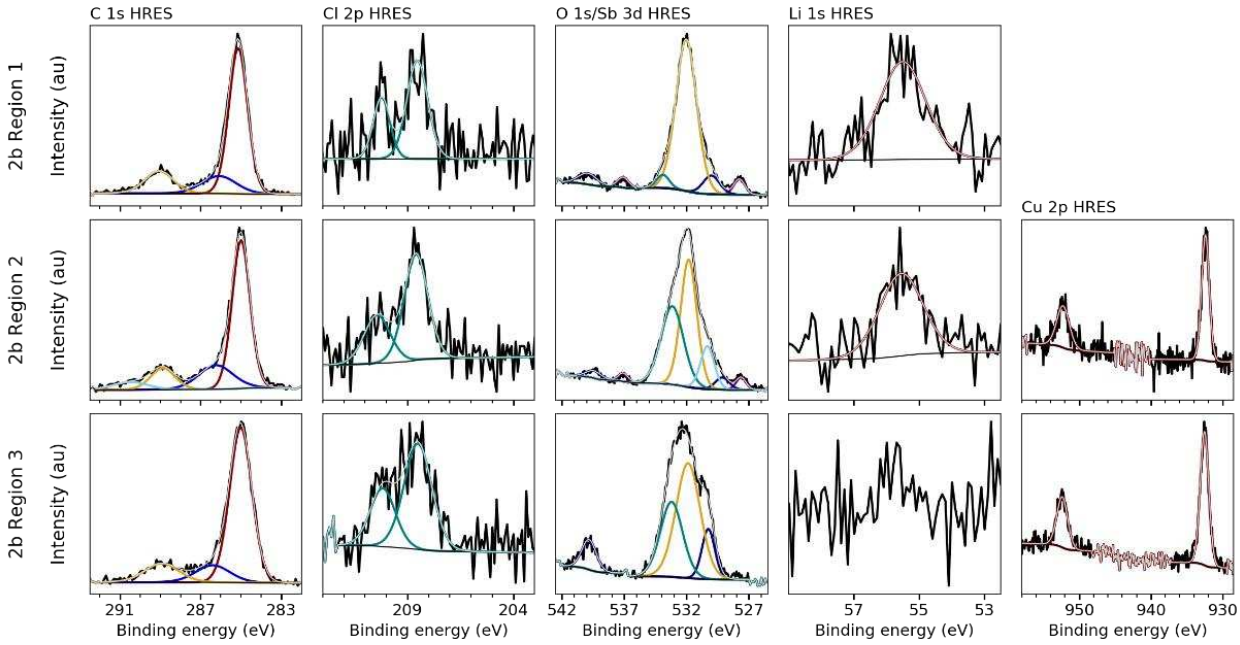

Figure A4: Sample 2b HRES fitting results.

Table A6: Sample 1c HRES fitting results

Sample description	Transition	Peak position (eV)	FWHM (eV)	Corrected area (A/(RSF*T*MFP))◊	% Atomic composition
Sample 1c Region 1	C 1s	284.89	1.21	917.199	32.0
		286.45	1.79	253.075	8.8
		290.22	1.29	134.37	4.7
		288.95	1.25	91.1433	3.2
	Cl 2p	208.55	1.14	49.4134	1.7
		210.16	1.14	24.6961	0.9
	O 1s/Sb 3d	527.88	1.33	4.54563	0.2
		530.16	1.23	8.56287	0.3
		539.67	1.47	5.69419	0.2
		532.14	1.85	656.08	22.9
		533.53	1.61	277.615	9.7
	Li 1s	55.61	1.71	442.389	15.4
Sample 1c Region 2	C 1s	284.98	1.11	838.024	29.3
		286.55	1.78	287.349	10.0
		290.29	1.25	146.951	5.1
		289.03	1.32	113.453	4.0
	Cl 2p	208.51	1.22	33.1305	1.2
		210.12	1.18	16.5581	0.6
	O 1s/Sb 3d	527.76	1.43	6.92095	0.2
		530.11	1.19	9.55181	0.3
		539.65	1.59	6.35161	0.2
		532.22	1.94	762.825	26.6
		533.74	1.57	171.132	6.0
	Li 1s	55.52	1.69	471.329	16.5
Sample 1c Region 3	C 1s	284.96	1.12	867.234	34.4
		286.32	2.00	304.811	12.1
		290.16	1.41	106.686	4.2
		288.91	1.34	90.6212	3.6
	Cl 2p	208.53	1.08	21.0102	0.8
		210.12	1.24	10.5006	0.4
		198.40	1.36	5.55703	0.2
		200.00	1.14	2.77732	0.1
	O 1s/Sb 3d	527.68	1.34	4.26611	0.2
		530.33	1.59	11.1026	0.4
		539.69	1.58	4.60848	0.2
		533.27	1.89	273.208	10.9
		532.11	1.65	513.509	20.4
	Li 1s	55.56	1.40	302.764	12.0

◊Area (A), relative sensitivity factor (RSF), transmission (T), and mean free path (MFP).

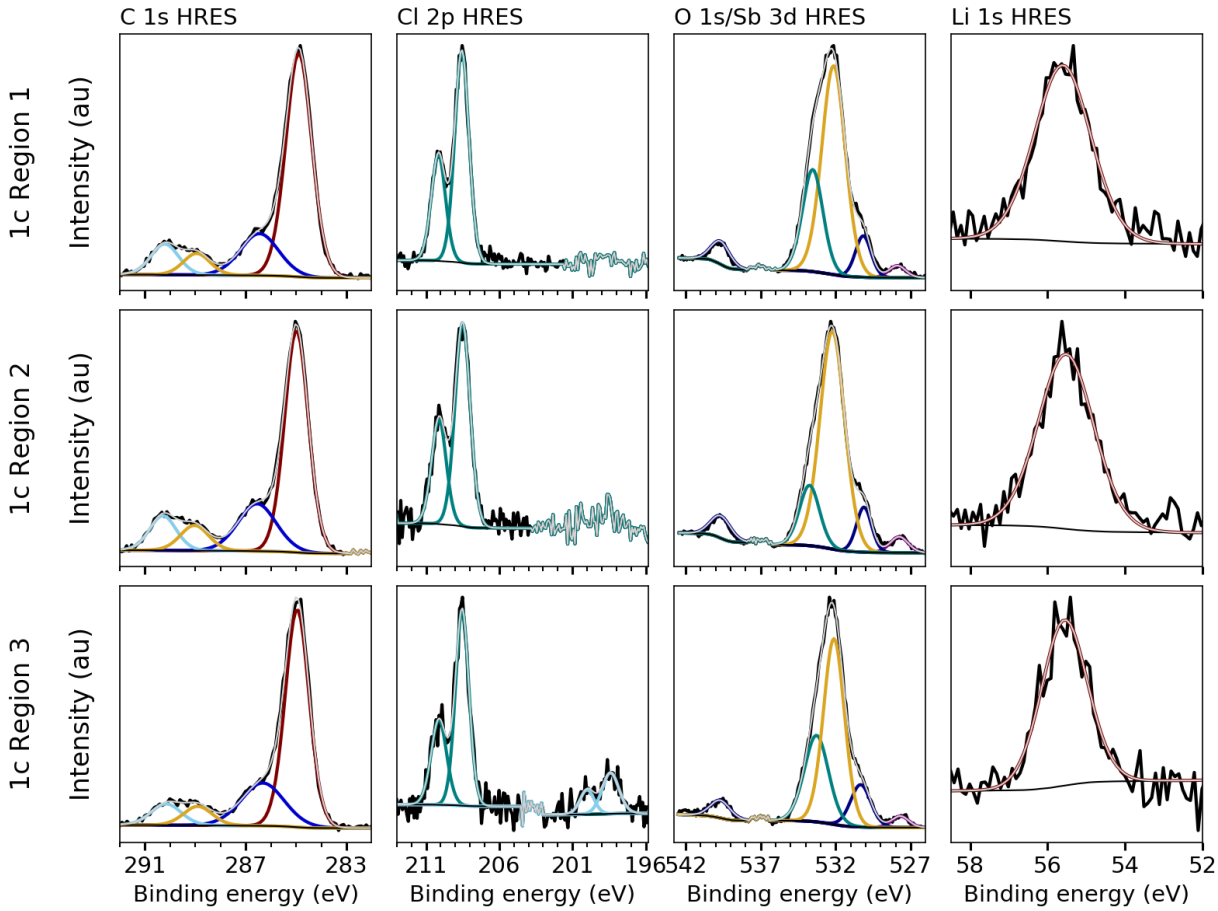

Figure A5: Sample 1c HRES fitting results.

Table A7: Sample 2c/1f HRES fitting results

Sample description	Transition	Peak position (eV)	FWHM (eV)	Corrected area (A/(RSF*T*MFP))◊	% Atomic composition
Sample 2c/1f Region 1	C 1s	284.88	1.16	306.386	40.7
		286.05	2.00	68.9558	9.2
		288.97	1.57	52.7461	7.0
	Cl 2p	208.59	1.19	24.2312	3.2
		210.21	1.02	12.1104	1.6
	O 1s	532.04	1.72	99.8794	13.3
		533.31	1.56	100.248	13.3
	Li 1s	55.91	1.56	88.358	11.7
Sample 2c/1f Region 2	C 1s	284.71	1.34	311.338	41.7
		286.29	1.43	26.2386	3.5
		288.86	1.79	31.6308	4.2
	Cl 2p	208.50	1.34	15.9788	2.1
		210.21	1.34	7.98574	1.1
		198.51	1.74	7.48708	1.0
		200.30	1.78	3.74172	0.5
	O 1s	528.26	1.13	7.70749	1.0
		531.41	2.30	129.445	17.3
		533.17	1.64	54.7739	7.3
	Li 1s	55.20	2.04	150.31	20.1
Sample 2c/1f Region 3	C 1s	284.86	1.21	282.884	40.2
		286.27	1.26	32.348	4.6
		288.96	1.95	58.3801	8.3
	Cl 2p	208.59	1.14	19.1698	2.7
		210.25	1.23	9.58046	1.4
	O 1s	532.06	2.15	134.296	19.1
		533.41	1.40	55.7848	7.98
	Li 1s	55.79	1.93	111.023	15.8

◊Area (A), relative sensitivity factor (RSF), transmission (T), and mean free path (MFP).

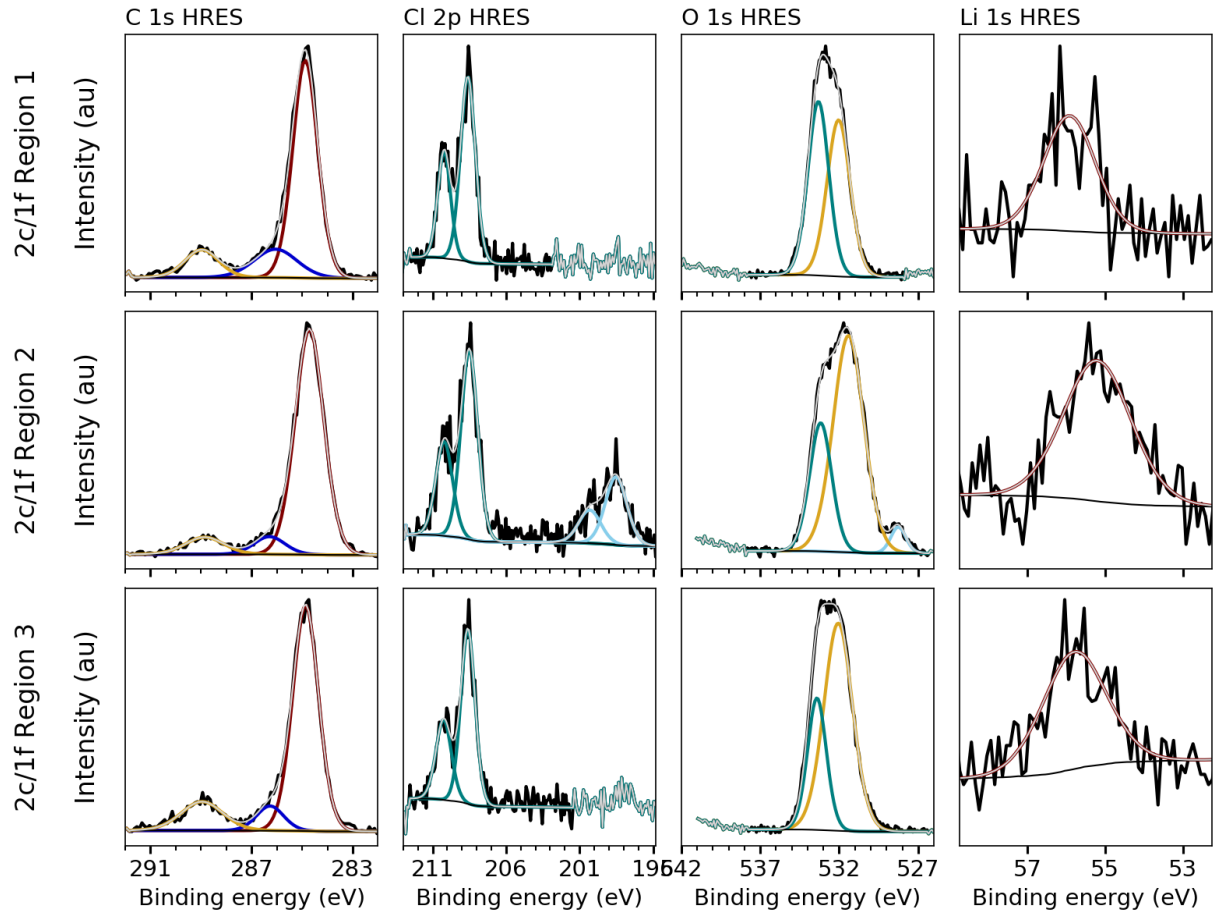

Figure A6: Sample 2c/1f HRES fitting results.

Table A8: Sample 1g HRES fitting results

Sample description	Transition	Peak position (eV)	FWHM (eV)	Corrected area (A/(RSF*T*MFP))◊	% Atomic composition
Sample 1g Region 1	C 1s	284.71	1.22	288.036	33.7
		286.24	2.00	64.4683	7.6
		288.61	1.50	32.9161	3.9
		289.71	2.00	42.3693	5.0
	Cl 2p	208.49	1.17	17.2438	2.0
		210.15	1.23	8.61819	1.0
	O 1s	531.79	2.26	174.081	20.4
		533.35	1.53	65.9385	7.7
	Li 1s	55.37	1.76	160.096	18.8
Sample 1g Region 2	C 1s	284.77	1.22	280.875	32.9
		286.31	2.00	62.7755	7.4
		288.53	1.06	20.3645	2.4
		289.63	1.85	47.038	5.5
	Cl 2p	208.53	1.24	11.8919	1.4
		210.18	1.24	5.94323	0.7
	O 1s	533.49	1.57	42.008	4.9
		531.77	2.20	194.209	22.8
	Li 1s	55.18	2.16	188.08	22.0
Sample 1g Region 3	C 1s	284.78	1.22	259.044	34.8
		286.09	2.00	51.3313	6.9
		288.73	1.44	32.9588	4.4
		290.00	2.00	26.7365	3.6
	Cl 2p	208.61	1.21	15.865	2.1
		210.26	1.11	7.92911	1.1
	O 1s	531.90	2.30	165.904	22.3
		533.46	1.42	41.1318	5.5
	Li 1s	55.27	2.13	142.914	19.2

◊Area (A), relative sensitivity factor (RSF), transmission (T), and mean free path (MFP).

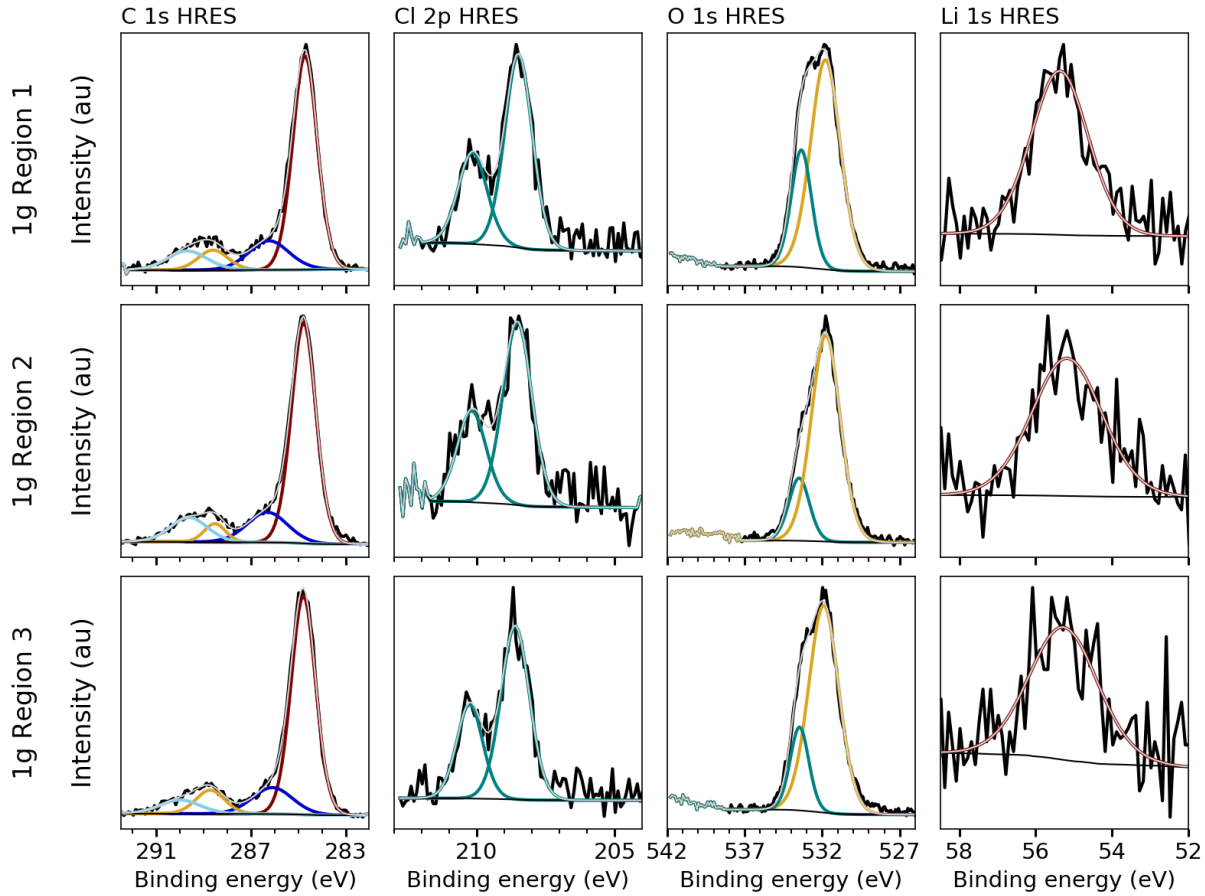

Figure A7: Sample 1g HRES fitting results.

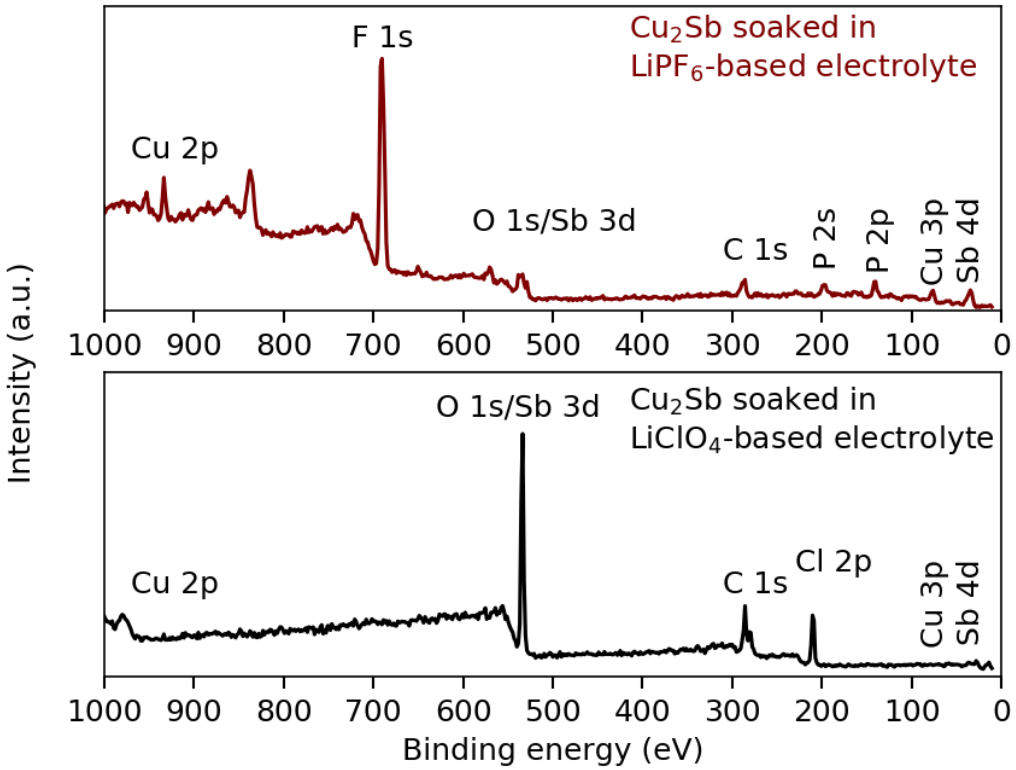

Figure A8: Comparison of XPS survey spectra for Cu_2Sb films soaked in either 1 M $LiPF_6$ in EC/DMC/DEC (1:1:1 by vol.) or 1 M $LiClO_4$ in EC/DMC/DEC (1:1:1 by vol.) electrolyte for 18 hours and then washed prior to XPS characterization. For the sample soaked in $LiPF_6$-based electrolyte, peaks for Cu_2Sb are still detected, but there is also evidence of $LiPF_6$ and $LiPF_6$ decomposition products on the surface based on the F 1s, P 2s, and P 2p peaks detected. For the sample soaked in $LiClO_4$-based electrolyte, there is evidence of $LiClO_4$ on the sample surface but no signal from the Cu_2Sb is observed.

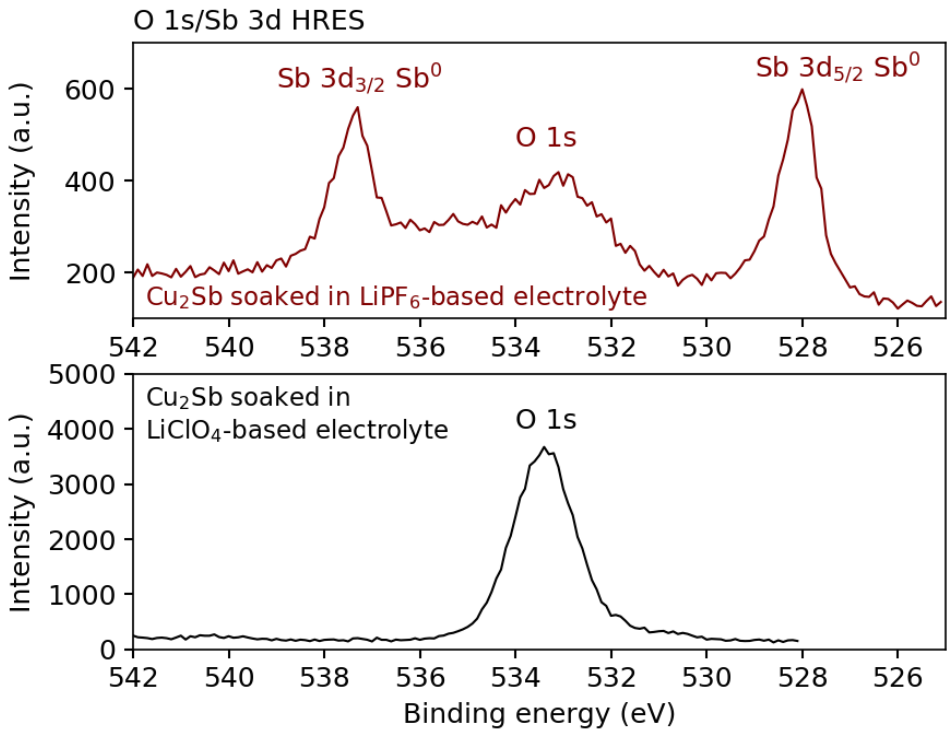

Figure A9: Comparison of XPS O 1s/Sb 3d HRES spectra for Cu_2Sb films soaked in either 1 M $LiPF_6$ in EC/DMC/DEC (1:1:1 by vol.) or 1 M $LiClO_4$ in EC/DMC/DEC (1:1:1 by vol.) electrolyte for 18 hours and then washed prior to XPS characterization. For the sample soaked in $LiPF_6$-based electrolyte, Sb 3d peaks corresponding to metallic Sb are observed but no peaks corresponding to Sb oxide species are observed even though the Cu_2Sb is covered with a surface oxide layer. For the sample soaked in $LiClO_4$-based electrolyte, there are no Sb 3d peaks detected, likely due to the adsorption of $LiClO_4$.

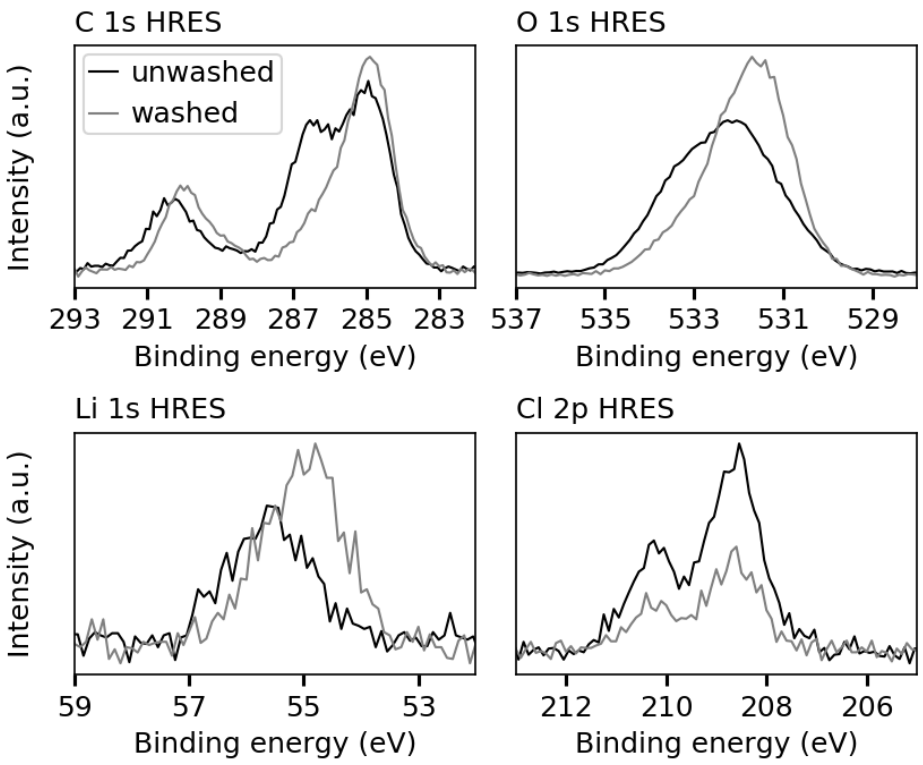

Figure A10: Representative XPS HRES spectra from unwashed and washed SEI samples, demonstrating that washing the sample primarily removes residual supporting electrolyte not incorporated into the SEI from the sample surface, resulting in decreases in O 1s, Li 1s, and Cl 2p signal corresponding to $LiClO_4$.

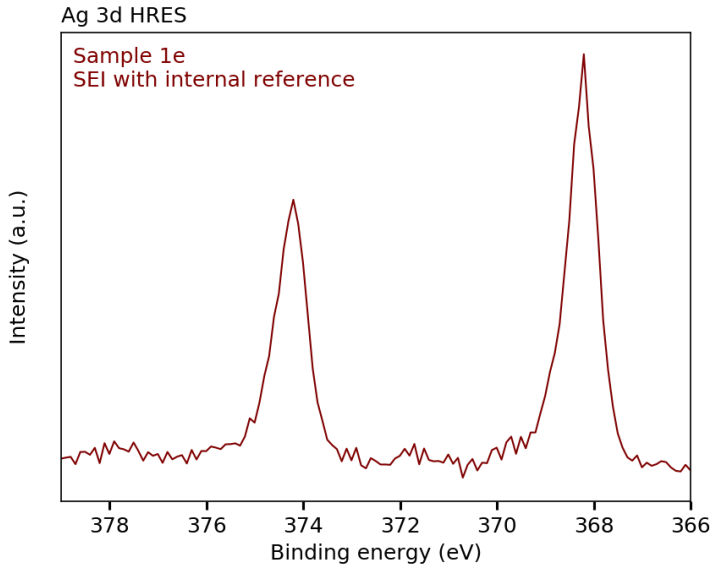

Figure A11: The Ag 3d HRES spectrum from the SEI sample 1e with the Ag internal reference applied to the surface by dropcasting from DMC.

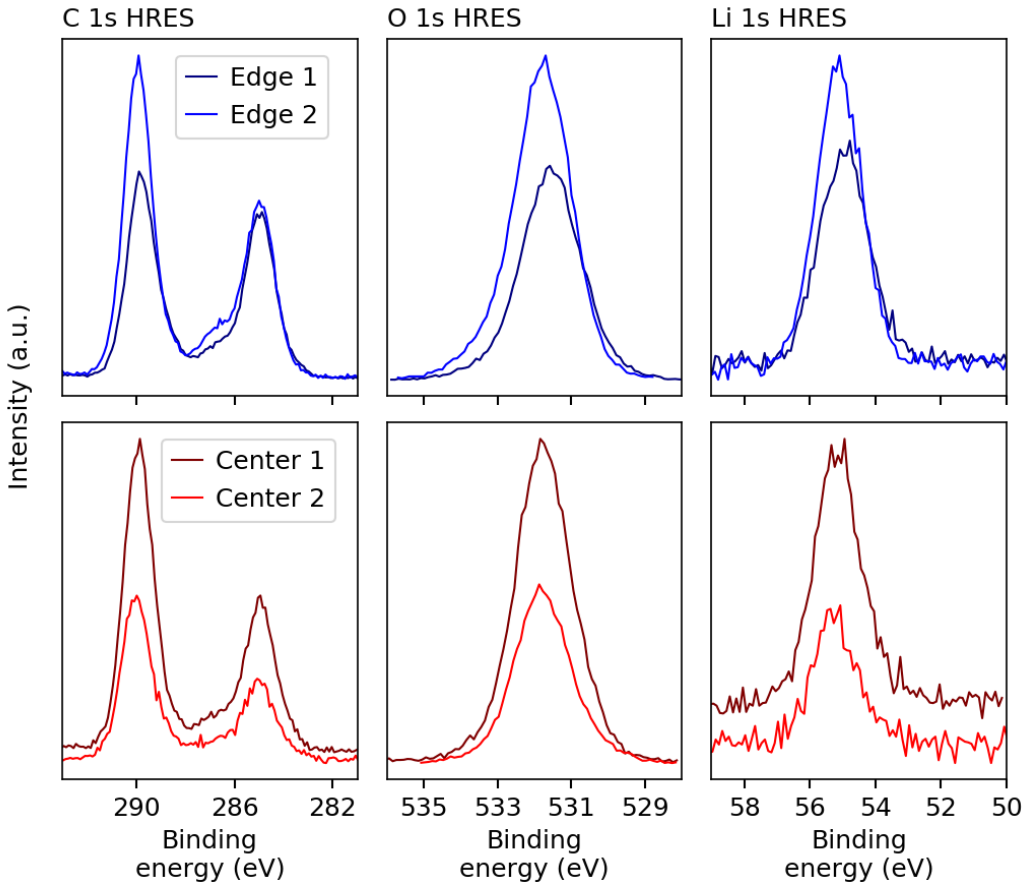

Figure A12: Comparison of XPS HRES spectra from edge and center regions of a SEI sample demonstrating the similarities in features regardless of the location of the analysis region.

Table A9: Comparison of quantitative data based on integrating peak areas from the unfitted spectra rather than from fitted data from XPS HRES spectra from edge and center regions of a SEI sample.

Analysis region	% Atomic Composition			
	C	O	Li	Cl
Edge 1	22.0	41.6	36.1	0.2
Center 1	22.7	43.9	33.4	0.0
Edge 2	21.1	44.7	33.7	0.5
Center 2	23.3	43.7	33.0	0.0

APPENDIX A REFERENCES

(1) *Silicon Electrolyte Interface Stabilization (SEISta) Second Quarter Progress Report 2018*; 2018. https://www.nrel.gov/transportation/assets/pdfs/next_generation_anodes_q2_progress_report_fy18.pdf (Accessed 07/09/2020).

XRD characterization

X-ray diffraction (XRD) was used for structural characterization of the electrodeposited Cu_2Sb films to ensure films were consistent with those reported in previous work from our group.[1] Diffractograms were collected using a Bruker D8 Discover Davinci instrument with Cu Kα radiation (λ = 1.54184 Å).

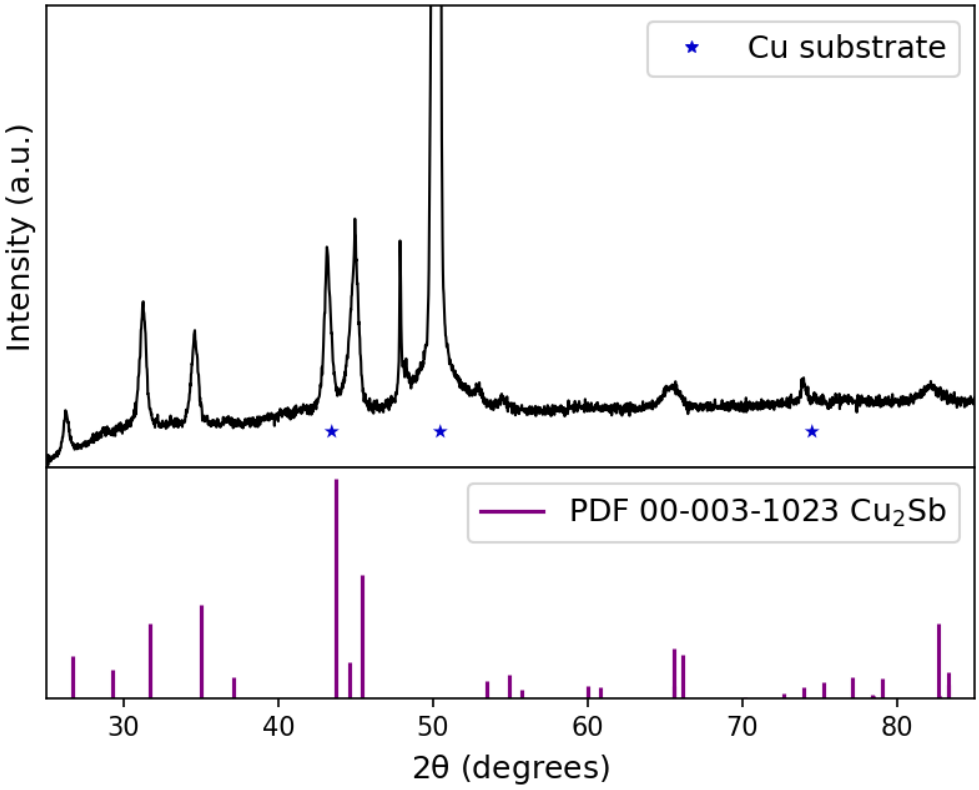

Figure B1: Representative XRD pattern for the Cu_2Sb thin films electrodeposited as described in the main text and in a previously published procedure[1] were indexed to PDF 00-003-1023 for Cu_2Sb. Angles where reflections from the underlying Cu substrate are expected to appear are marked with blue stars.

Description of X-ray photoelectron spectroscopy (XPS) peak fitting procedure

Since not much is known about the solid electrolyte interface (SEI) on Cu_2Sb thin films, the high resolution (HRES) X-ray photoelectron spectra were fit using a simplified approach with minimal fitting constraints in order to obtain rough atomic composition estimates while trying to avoid fits with no

physical basis and drawing unrealistic conclusions from the data. Due to this approach, the fits (summarized in Tables B1–B3 and shown in Figures B4–B9) often differ from the raw data, and in the case of spectra with poor signal to noise such as Li 1s they may result in an overestimation in the percent atomic composition. However, for our purposes of examining trends in the binding environments and compositions for different SEI samples this fitting procedure seems to be sufficient.

Peak fitting was performed on the raw data (no data smoothing algorithms were utilized) with CasaXPS software (version 2.3.17PR1.1) and the following parameters and constraints. The background was defined using the Shirley algorithm, and the Av. width was 1 for all spectra. The lineshape used for peak fitting was 70% Gaussian, 30% Lorentzian.[2] For the C 1s spectra, the upper limit for the FWHM values of the peaks was set to 2, and the PHI RSF value corrected for angular distribution was 0.314089. For the Cl 2p spectra, the ratio of the areas of the $2p_{3/2}$ and $2p_{1/2}$ peaks was set to 2:1, and the FWHM values were constrained such that the FWHM values for the $2p_{3/2}$ and $2p_{1/2}$ peaks varied by no more than 10% of each other. The PHI RSF value corrected for angular distribution for the Cl 2p spectra was 0.696646. A similar approach was used for fitting the Sb 3d spectra; the ratio of the areas of the $3d_{5/2}$ and $3d_{3/2}$ peaks was set to 3:2, and the FWHM values were constrained such that the FWHM values for the $3d_{5/2}$ and $3d_{3/2}$ peaks varied by no more than 10% of each other. The PHI RSF value corrected for angular distribution for the Sb 3d spectra was 7.20613. The peak separations between the Cl $2p_{3/2}$ and Cl $2p_{1/2}$ and Sb $3d_{5/2}$ and Sb $3d_{3/2}$ peaks were not constrained as the peak separations after fitting were similar to the reported peak separation values.[3] The upper limits for the FWHM values of the O 1s peaks were set to 2.3, and the PHI RSF corrected for angular distribution was 0.787404. No constraints were used for the Li 1s spectra, although if the Li 1s peak was not readily distinguishable from the background (as was the case for HPR Region 2) or if the background noise was greater than the peak height (as was the case for HPR VC Region 2), no fitting was performed. The RSF value used for quantifying the Li 1s spectra was 0.0260787 after correction for angular distribution. Finally, for the samples in which Cu was detected, no area constraints

were used for fitting the Cu $2p_{3/2}$ and Cu $2p_{1/2}$ peaks because of possible Super Coster-Kronig effects.[2] The PHI RSF value used for the Cu 2p spectra was 4.28013.

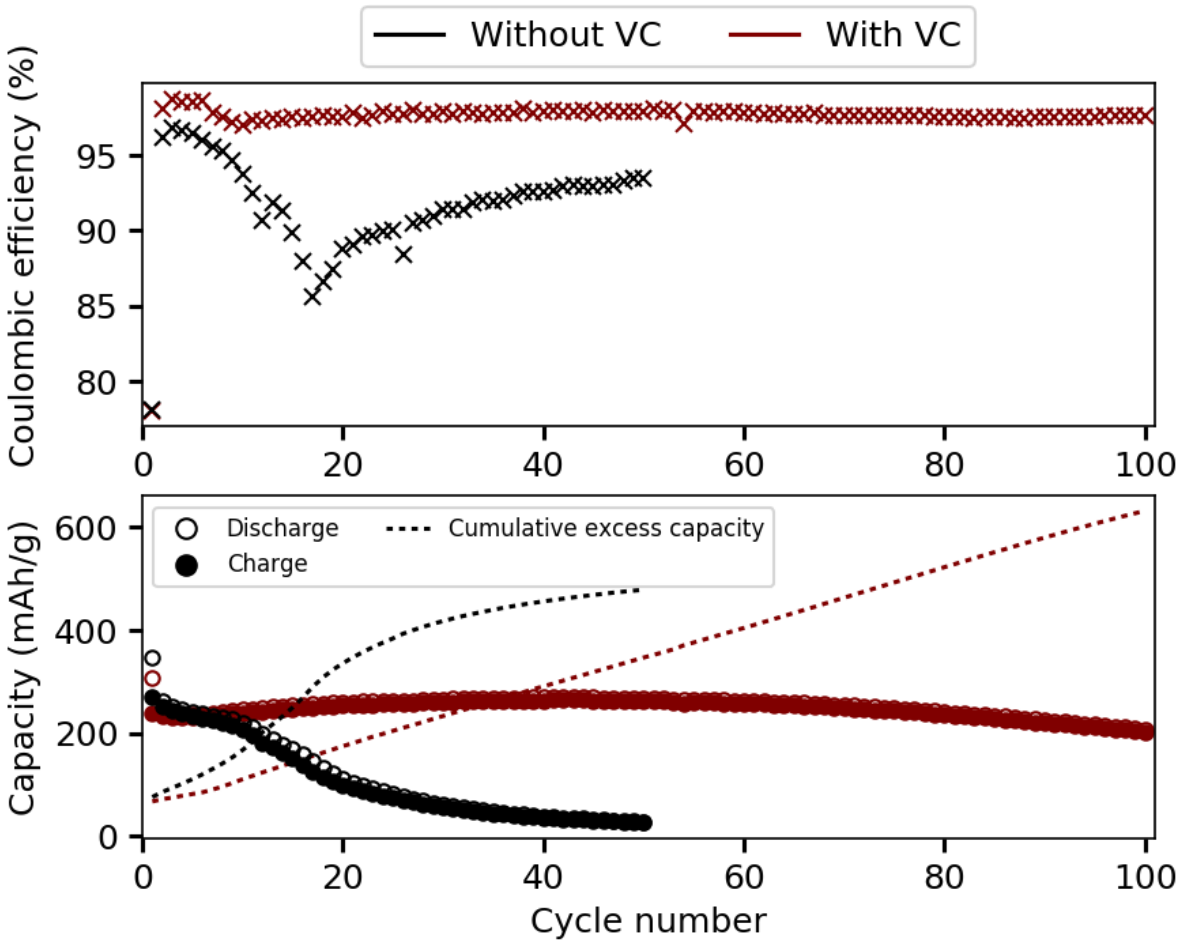

Figure B2: Cycling data showing the capacity retention, cumulative excess capacity, and coulombic efficiency up to 50 cycles for Cu_2Sb cycled in $LiClO_4$-based electrolyte without VC and up to 100 cycles for Cu_2Sb cycled in $LiClO_4$-based electrolyte with VC.

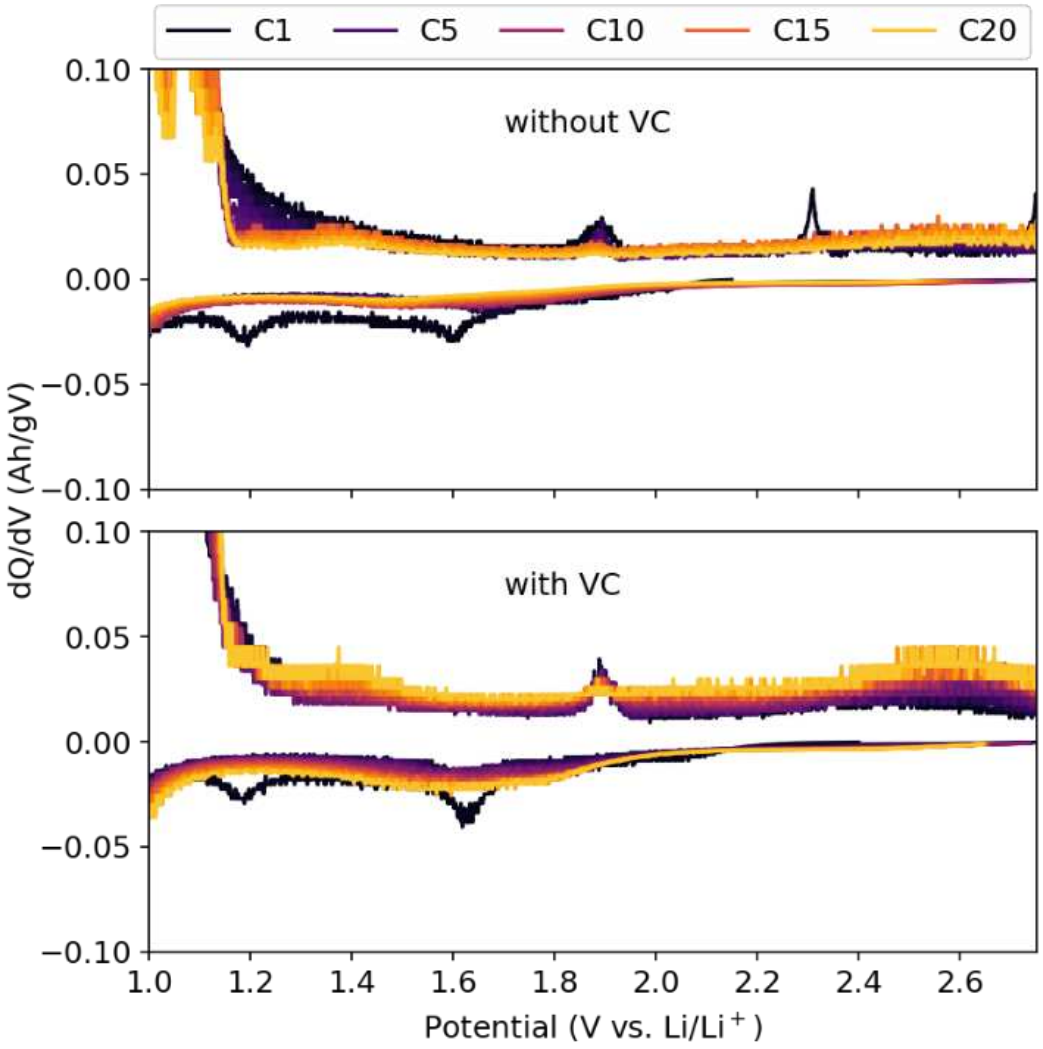

Figure B3: Differential capacity analysis plots (also shown in Figure 3.2 of Chapter 3) for the Cu_2Sb thin films cycled 20 times between 0.05 V and 3.0 V. The y-axis and x-axis ranges have been narrowed to show the low intensity features associated with electrolyte reduction and SEI formation that are not visible in Figure 3.2 when the y-axis range is expanded to show the intense features corresponding to Cu_2Sb lithiation and delithiation.

Table B1: Fitting results for the two representative regions of the HPR and HPR VC SEI samples.

Sample description	Transition	Peak position (eV)	FWHM (eV)	Corrected area (A/(RSF*T*MFP))$^{\Diamond}$	% Atomic Composition	Binding environment
HPR, Region 1	C 1s	284.88	1.27	233.51	37.39	**C**-C/**C**-H
		286.46	1.41	37.61	6.02	**C**-O
		288.90	1.65	36.93	5.91	O=**C**-O
	Cl 2p	208.62	1.28	22.78	3.65	**Cl**O_4^- $2p_{3/2}$
		210.25	1.17	11.38	1.82	**Cl**O_4^- $2p_{1/2}$
	Sb 3d	530.58	1.23	2.00	0.32	**Sb**$_x$O$_y$ $3d_{5/2}$
		539.95	1.36	1.33	0.21	**Sb**$_x$O$_y$ $3d_{3/2}$
	O 1s	531.35	2.30	44.03	7.05	C=**O**
		533.22	1.54	114.87	18.39	Cl**O**$_4^-$
		532.03	1.17	22.85	3.66	C-**O**
	Li 1s	55.94	1.75	79.67	12.76	Li^+
	Cu 2p	932.84	1.31	12.07	1.93	$2p_{3/2}$
		952.65	1.68	5.48	0.88	$2p_{1/2}$
HPR, Region 2	C 1s	284.73	1.18	225.36	37.77	**C**-C/**C**-H
		285.92	2.00	69.75	11.69	**C**-O
		288.83	1.56	38.22	6.41	O=**C**-O
	Cl 2p	208.47	1.19	22.58	3.78	**Cl**O_4^- $2p_{3/2}$
		210.08	1.11	11.28	1.89	**Cl**O_4^- $2p_{1/2}$
	Sb 3d	530.33	1.04	2.78	0.47	**Sb**$_x$O$_y$ $3d_{5/2}$
		539.86	1.15	1.85	0.31	**Sb**$_x$O$_y$ $3d_{3/2}$
	O 1s	533.13	1.57	111.12	18.63	Cl**O**$_4^-$
		531.72	2.30	92.48	15.50	C-**O**, C=**O**
	Cu 2p	932.70	1.31	14.37	2.41	$2p_{3/2}$
		952.70	1.86	6.86	1.15	$2p_{1/2}$
HPR VC, Region 1	C 1s	285.00	1.04	273.15	34.66	**C**-C/**C**-H
		286.24	2.00	84.99	10.78	**C**-O
		288.87	1.43	54.06	6.86	O=**C**-O
		290.48	2.00	27.63	3.51	carbonate
	Cl 2p	208.60	1.32	9.84	1.25	**Cl**O_4^- $2p_{3/2}$
		210.43	1.45	4.92	0.62	**Cl**O_4^- $2p_{1/2}$
	Sb 3d	527.62	0.94	0.64	0.08	**Sb**^{0} $3d_{5/2}$
		537.08	0.91	0.42	0.05	**Sb**^{0} $3d_{3/2}$
		529.14	1.31	0.87	0.11	**Sb**$_x$O$_y$ $3d_{5/2}$
		539.45	1.45	0.58	0.07	**Sb**$_x$O$_y$ $3d_{3/2}$
	O 1s	531.82	1.53	97.57	12.38	C=**O**
		533.14	2.12	82.95	10.53	Cl**O**$_4^-$
		530.32	1.32	28.36	3.60	C-**O**
	Li 1s	55.55	1.57	114.47	14.53	Li^+
	Cu 2p	932.41	1.25	4.93	0.63	$2p_{3/2}$
		952.24	2.08	2.70	0.34	$2p_{1/2}$
HPR VC, Region 2	C 1s	285.01	1.29	172.52	44.42	**C**-C/**C**-H
		286.40	2.00	29.25	7.53	**C**-O

		288.93	2.00	32.21	8.29	O=**C**-O
	Cl 2p	208.50	1.54	9.40	2.42	**Cl**O_4^- $2p_{3/2}$
		210.17	1.40	4.70	1.21	**Cl**O_4^- $2p_{1/2}$
	Sb 3d	530.25	1.22	1.93	0.50	**Sb**$_x$$O_y$ $3d_{5/2}$
		539.82	1.35	1.28	0.33	**Sb**$_x$$O_y$ $3d_{3/2}$
	O 1s	531.87	2.30	76.36	19.66	C-**O**, C=**O**
		533.20	2.10	45.62	11.74	Cl**O**$_4^-$
	Cu 2p	932.54	1.40	10.24	2.64	$2p_{3/2}$
		952.35	1.77	4.88	1.26	$2p_{1/2}$

◊Area (A), relative sensitivity factor (RSF), transmission (T), and mean free path (MFP).

Table B2: Fitting results for the two representative regions of the MPR and MPR VC SEI samples.

Sample description	Transition	Peak position (eV)	FWHM (eV)	Corrected area (A/(RSF*T*MFP))◊	% Atomic Composition	Binding environment
MPR, Region 1	C 1s	284.88	1.16	306.39	40.69	**C**-C/**C**-H
		286.05	2.00	68.96	9.16	**C**-O
		288.97	1.57	52.75	7.01	O=**C**-O
	Cl 2p	208.59	1.19	24.23	3.22	**Cl**O_4^- $2p_{3/2}$
		210.21	1.02	12.11	1.61	**Cl**O_4^- $2p_{1/2}$
	O 1s	532.04	1.72	99.88	13.27	C-**O**, C=**O**
		533.31	1.56	100.25	13.31	Cl**O_4^-**
	Li 1s	55.91	1.56	88.36	11.74	Li^+
MPR, Region 2	C 1s	284.71	1.34	311.34	41.70	**C**-C/**C**-H
		286.29	1.43	26.24	3.51	**C**-O
		288.86	1.79	31.63	4.24	O=**C**-O
	Cl 2p	208.50	1.34	15.98	2.14	**Cl**O_4^- $2p_{3/2}$
		210.21	1.34	7.99	1.07	**Cl**O_4^- $2p_{1/2}$
		198.51	1.74	7.49	1.00	Cl^- $2p_{3/2}$
		200.30	1.78	3.74	0.50	Cl^- $2p_{1/2}$
	O 1s	528.26	1.13	7.71	1.03	Li_2**O**
		531.41	2.30	129.45	17.34	C-**O**, C=**O**
		533.17	1.64	54.77	7.34	Cl**O_4^-**
	Li 1s	55.20	2.04	150.31	20.13	Li^+, **Li**$_2$O
MPR VC, Region 1	C 1s	284.71	1.22	288.04	33.74	**C**-C/**C**-H
		286.24	2.00	64.47	7.55	**C**-O
		288.61	1.50	32.92	3.86	O=**C**-O
		289.71	2.00	42.37	4.96	carbonate
	Cl 2p	208.49	1.17	17.24	2.02	**Cl**O_4^- $2p_{3/2}$
		210.15	1.23	8.62	1.01	**Cl**O_4^- $2p_{1/2}$
	O 1s	531.79	2.26	174.08	20.39	C-**O**, C=**O**
		533.35	1.53	65.94	7.72	Cl**O_4^-**
	Li 1s	55.37	1.76	160.10	18.75	Li^+
MPR VC, Region 2	C 1s	284.77	1.22	280.88	32.92	**C**-C/**C**-H
		286.31	2.00	62.78	7.36	**C**-O
		288.53	1.06	20.36	2.39	O=**C**-O
		289.63	1.85	47.04	5.51	carbonate
	Cl 2p	208.53	1.24	11.89	1.39	**Cl**O_4^- $2p_{3/2}$
		210.18	1.24	5.94	0.70	**Cl**O_4^- $2p_{1/2}$
	O 1s	533.49	1.57	42.01	4.92	Cl**O_4^-**
		531.77	2.20	194.21	22.76	C-**O**, C=**O**
	Li 1s	55.18	2.16	188.08	22.04	Li^+

◊Area (A), relative sensitivity factor (RSF), transmission (T), and mean free path (MFP).

Table B3: Fitting results for the two representative regions of the LPR and LPR VC SEI samples.

Sample description	Transition	Peak position (eV)	FWHM (eV)	Corrected area (A/(RSF*T*MFP))[◊]	% Atomic Composition	Binding environment
LPR, Region 1	C 1s	285.05	1.20	168.61	21.23	**C**-C/**C**-H
		286.51	1.85	99.97	12.59	**C**-O
		288.94	1.17	27.07	3.41	O=**C**-O
		290.38	1.30	38.99	4.91	carbonate
	Cl 2p	208.55	1.18	13.06	1.64	**Cl**O_4^- $2p_{3/2}$
		210.15	1.23	6.53	0.82	**Cl**O_4^- $2p_{1/2}$
	O 1s	532.19	2.30	206.41	25.99	C-**O**, C=**O**
		533.53	1.73	59.41	7.48	Cl**O**$_4^-$
	Li 1s	55.51	1.90	174.15	21.93	Li^+
LPR, Region 2	C 1s	284.76	1.14	234.74	33.28	**C**-C/**C**-H
		286.29	2.00	74.16	10.51	**C**-O
		288.69	1.76	25.18	3.57	O=**C**-O
		290.47	1.71	35.43	5.02	carbonate
	Cl 2p	208.60	1.19	15.97	2.26	**Cl**O_4^- $2p_{3/2}$
		210.22	1.13	7.98	1.13	**Cl**O_4^- $2p_{1/2}$
	O 1s	532.01	2.30	125.16	17.74	C-**O**, C=**O**
		533.40	1.65	68.13	9.66	Cl**O**$_4^-$
	Li 1s	55.73	2.00	118.57	16.81	Li^+
LPR VC, Region 1	C 1s	284.73	1.62	224.74	27.20	**C**-C/**C**-H
		286.68	1.85	29.05	3.52	**C**-O
		289.78	1.45	35.31	4.27	carbonate
	Cl 2p	198.55	1.34	4.51	0.55	Cl^- $2p_{3/2}$
		200.18	1.48	2.26	0.27	Cl^- $2p_{1/2}$
	O 1s	528.29	1.18	25.89	3.13	Li_2**O**
		531.19	2.16	220.37	26.68	C-**O**, C=**O**
	Li 1s	54.72	2.00	283.96	34.37	Li^+, **Li**$_2$O
LPR VC, Region 2	C 1s	284.85	1.46	179.86	18.50	**C**-C/**C**-H
		286.62	1.72	28.16	2.90	**C**-O
		289.85	1.45	24.01	2.47	carbonate
		283.19	1.17	10.44	1.07	sp^2 carbon
	Cl 2p	198.56	1.47	5.53	0.57	Cl^- $2p_{3/2}$
		200.36	1.20	2.76	0.28	Cl^- $2p_{1/2}$
	O 1s	528.60	1.24	72.03	7.41	Li_2**O**
		531.29	1.88	235.00	24.18	C-**O**, C=**O**
	Li 1s	54.54	2.03	414.22	42.61	Li^+, **Li**$_2$O

[◊]Area (A), relative sensitivity factor (RSF), transmission (T), and mean free path (MFP).

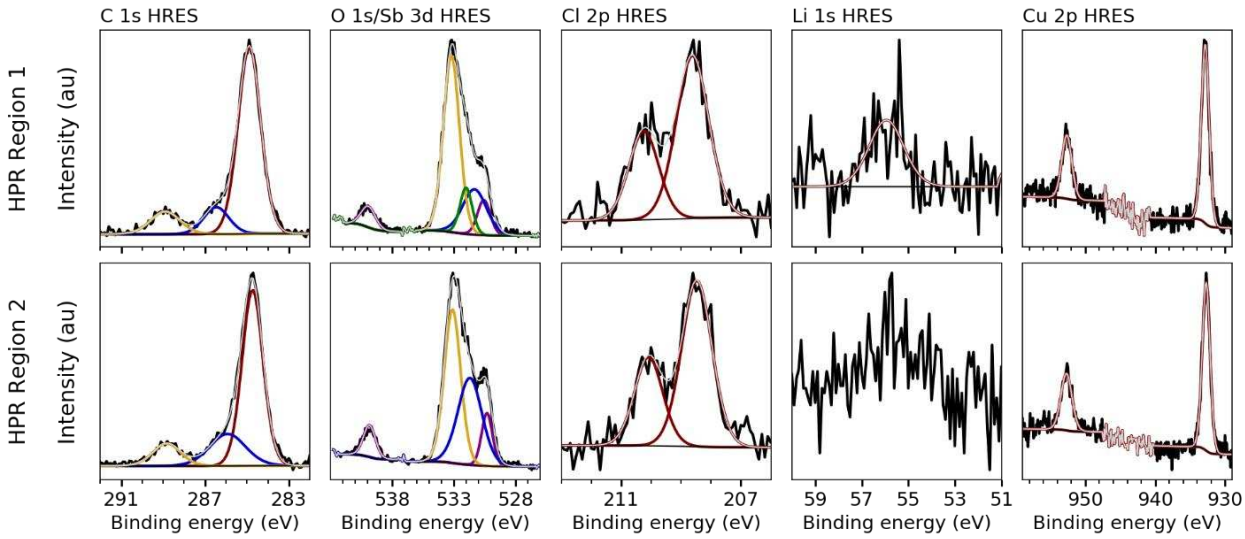

Figure B4: Fitted XPS HRES C 1s, O 1s/Sb 3d, Cl 2p, Li 1s, and Cu 2p spectra for the two representative regions of the HPR SEI sample.

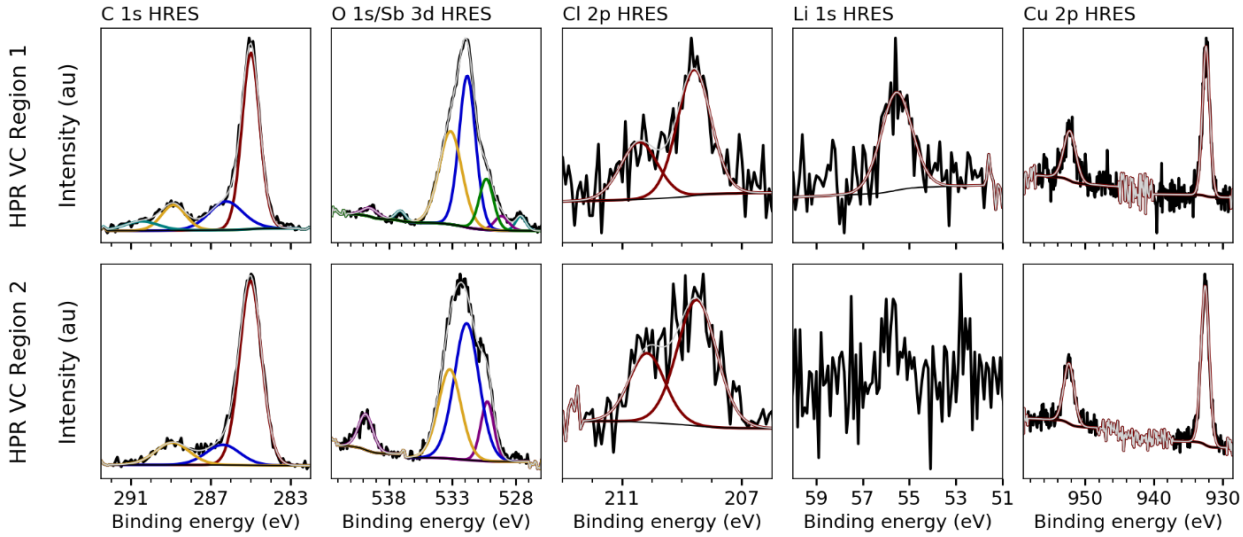

Figure B5: Fitted XPS HRES C 1s, O 1s/Sb 3d, Cl 2p, Li 1s, and Cu 2p spectra for the two representative regions of the HPR VC SEI sample.

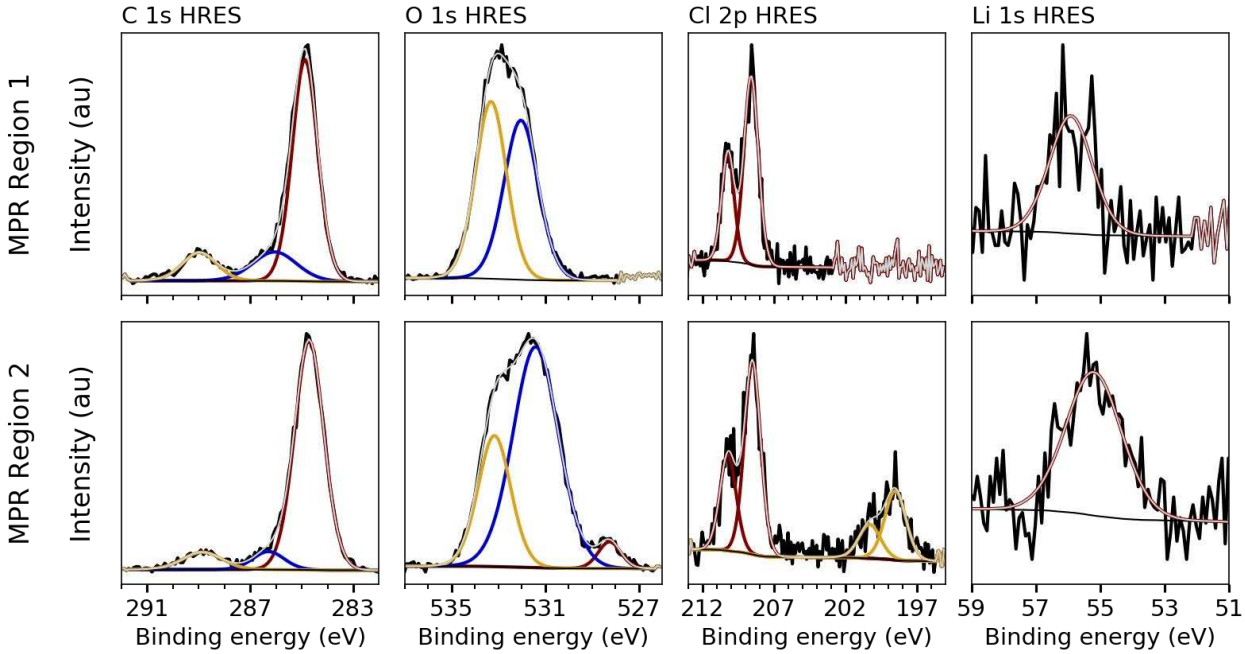

Figure B6: Fitted XPS HRES C 1s, O 1s, Cl 2p, and Li 1s spectra for the two representative regions of the MPR SEI sample.

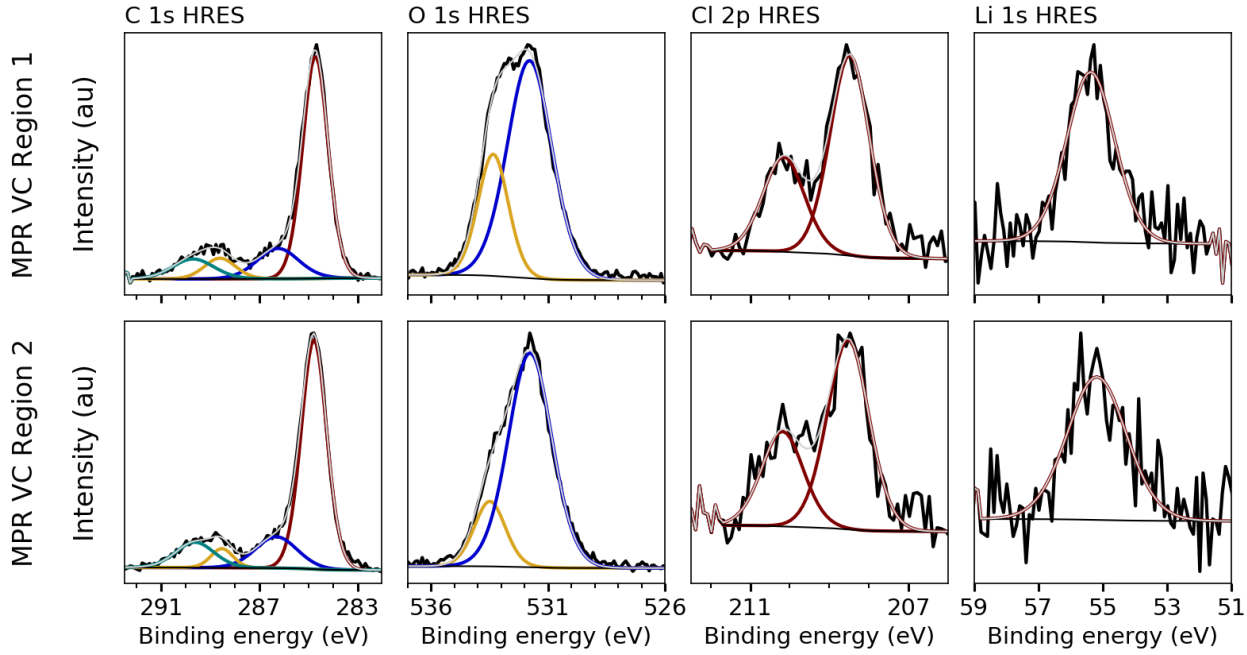

Figure B7: Fitted XPS HRES C 1s, O 1s, Cl 2p, and Li 1s spectra for the two representative regions of the MPR VC SEI sample.

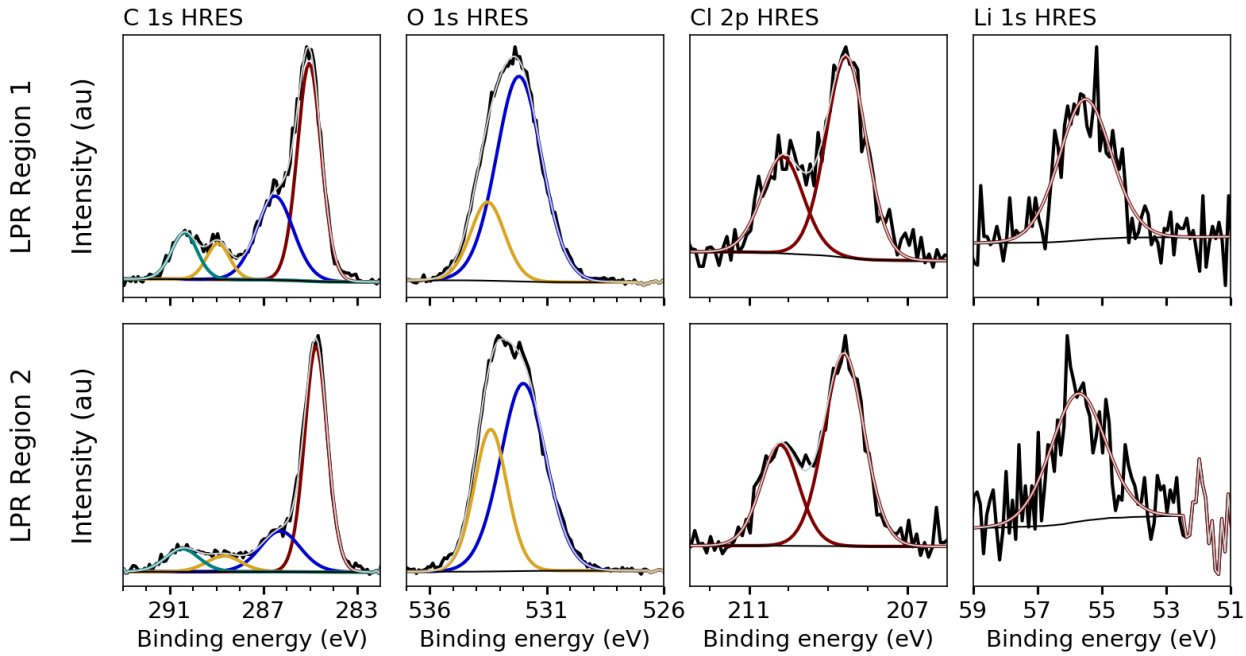

Figure B8: Fitted XPS HRES C 1s, O 1s, Cl 2p, and Li 1s spectra for the two representative regions of the LPR SEI sample.

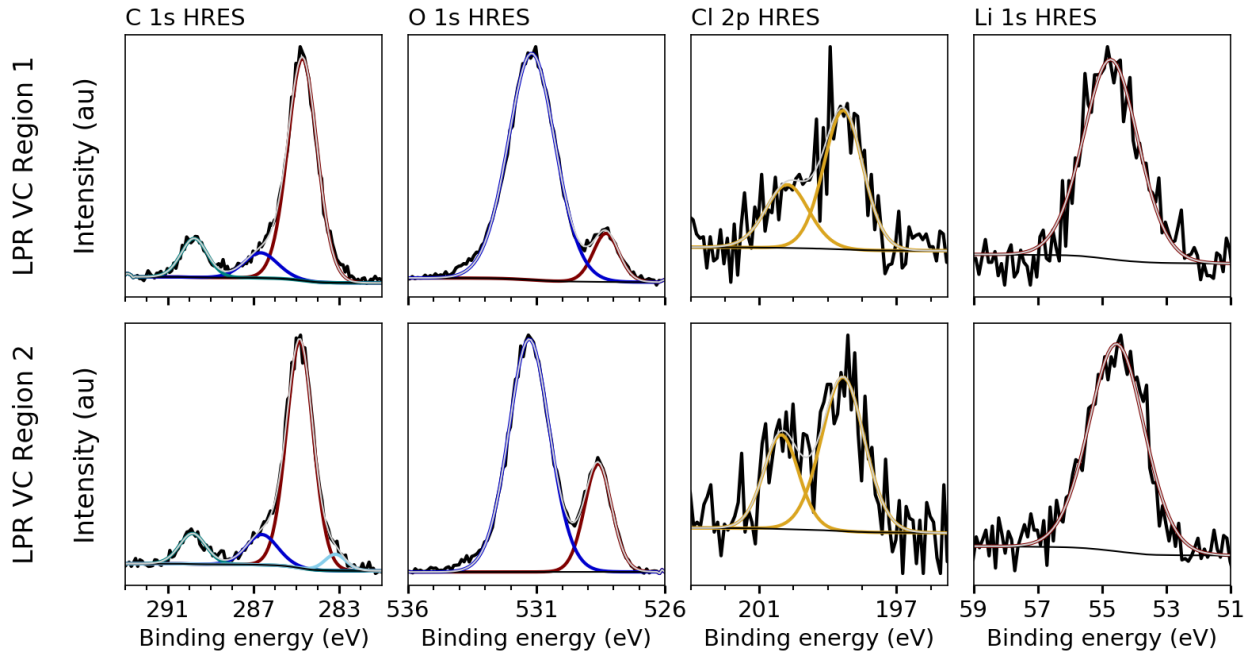

Figure B9: Fitted XPS HRES C 1s, O 1s, Cl 2p, and Li 1s spectra for the two representative regions of the LPR VC SEI sample.

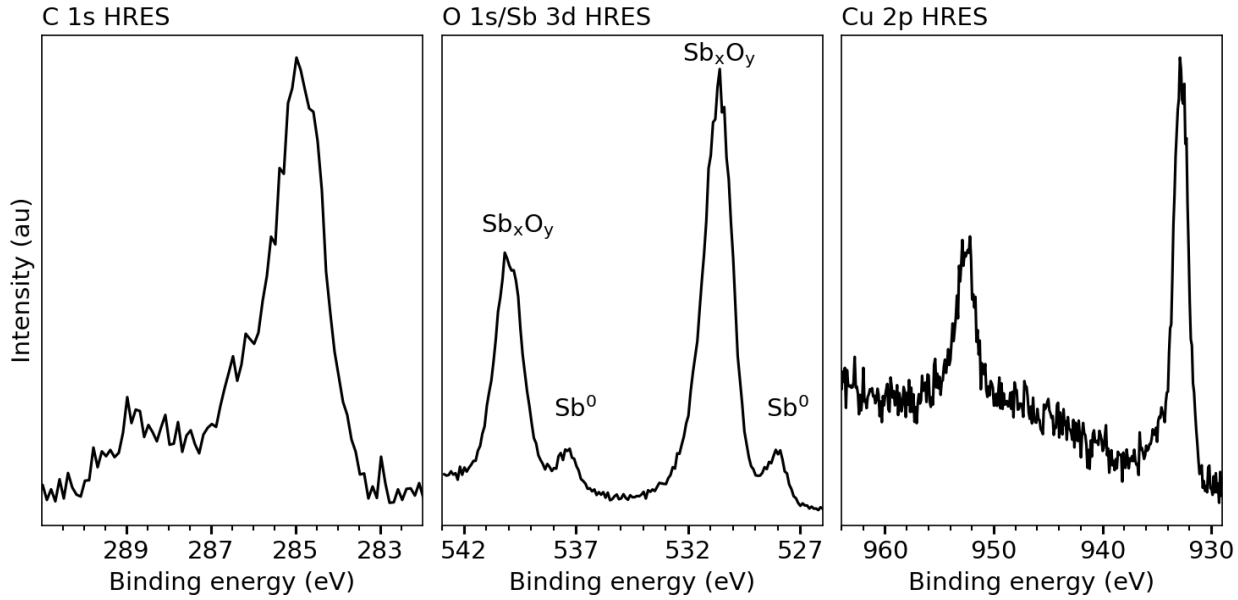

Figure B10: HRES C 1s, O 1s/Sb 3d, and Cu 2p X-ray photoelectron spectra for a pristine (uncycled) Cu_2Sb thin film showing the presence of a surface oxide layer on Cu_2Sb that results in more intense Sb 3d peaks for Sb_xO_y species than for Sb^0 from the Cu_2Sb film. The presence of carbon is due to adventitious carbon, and Cu^0 from the underlying Cu_2Sb underneath the surface oxide layer can also be detected.

Figure B11: Left: representative digital photograph of a discolored polypropylene separator from a disassembled half-cell containing a Cu_2Sb thin film electrode cycled in 1 M $LiClO_4$ in EC/DMC/DEC (1:1:1 vol) electrolyte with an upper voltage cutoff limit of 3.0 V vs Li/Li^+. Right: representative digital photograph of a polypropylene separator recovered from a half cell cycled without VC for comparison.

SEM and EDS characterization

Energy dispersive X-ray spectroscopy (EDS) characterization was performed using an Oxford Instruments 80 X-Max (80 mm) SDD detector with 2048 channels, 20 keV energy range, 10.0 eV/channel, and a SATW type window coupled to a JEOL JSM-6500F scanning electron microscope. EDS mapping and data collection was performed at 25x magnification and a 20.00 kV accelerating voltage.

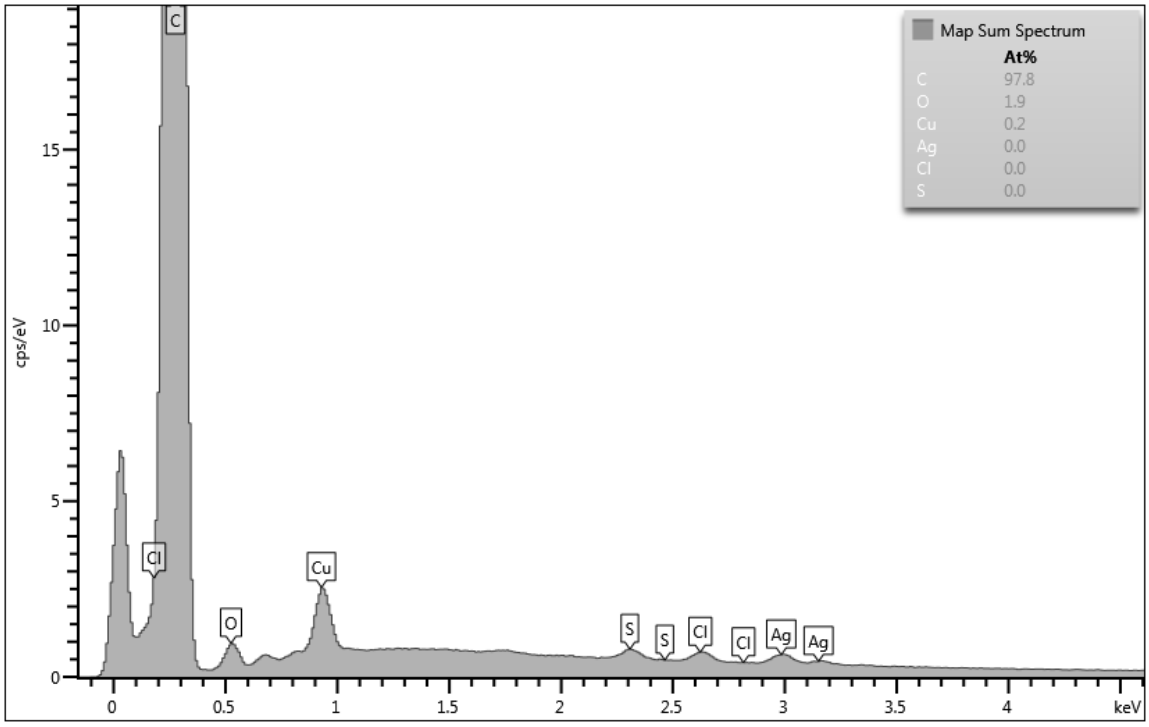

Figure B12: An EDS map-sum spectrum of a discolored separator from a Cu_2Sb half-cell cycled without VC to an upper voltage limit of 3.0 V vs Li/Li^+ demonstrating the presence of Cu in the discolored separator.

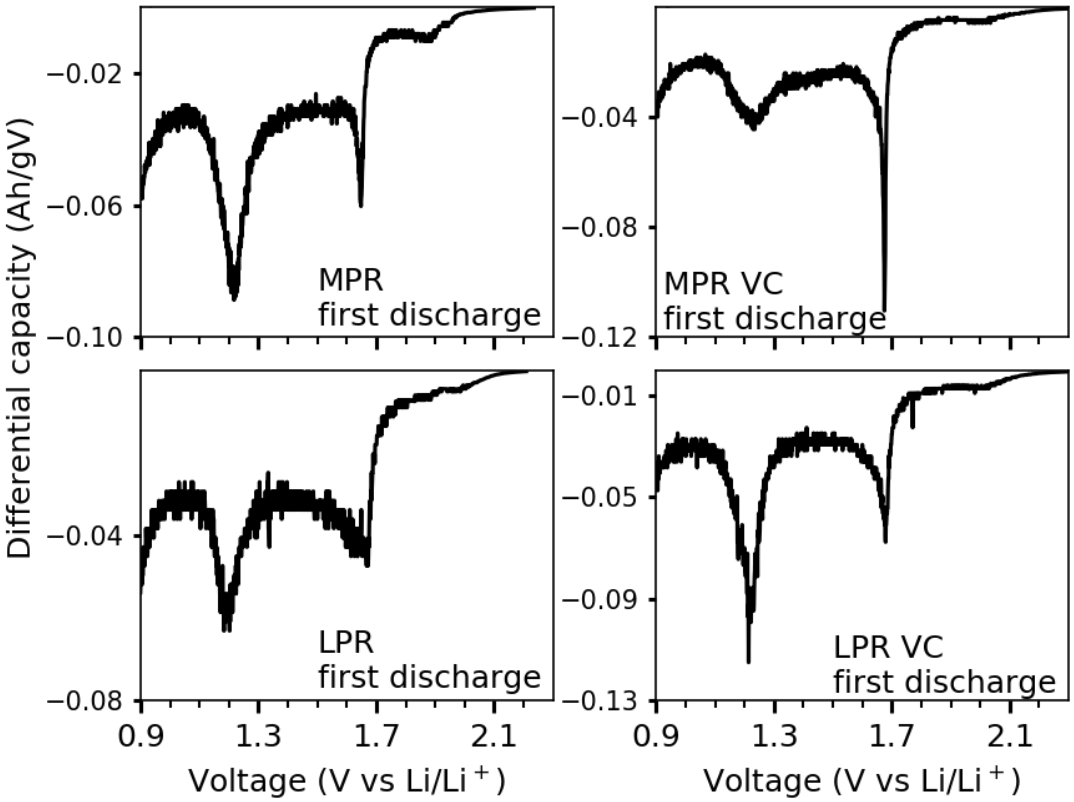

Figure B13: Differential capacity analysis plots for the first cycle discharge of the MPR, MPR VC, LPR, and LPR VC samples showing similar features. The first cycle discharge was the only stage of cycling that showed SEI-related features in the differential capacity analysis, so the rest of the cycling data was excluded from the figure for clarity.

APPENDIX B REFERENCES

(1) Mosby, J. M.; Prieto, A. L. Direct Electrodeposition of Cu_2Sb for Lithium-Ion Battery Anodes. *J. Am. Chem. Soc.* **2008**, *130* (32), 10656–10661. https://doi.org/10.1021/ja801745n.

(2) Sherwood, P. M. A. The Use and Misuse of Curve Fitting in the Analysis of Core X-Ray Photoelectron Spectroscopic Data. *Surf. Interface Anal.* **2019**, *51* (6), 589–610. https://doi.org/10.1002/sia.6629.

(3) Moulder, J. F.; Stickle, W. F.; Sobol, P. E.; Bomben, K. E. *Handbook of X-Ray Photoelectron Spectroscopy*; Chastain, J., King, R. C. J., Eds.; Physical Electronics, Inc., 1995.

APPENDIX C: SUPPORTING INFORMATION FOR CHAPTER 4

Table C1: Tabulated fitting results for the representative pristine SnSb thin film sample sputtered for different total amounts of time

Sample	Name	Position (eV)	FWHM (eV)	Area/(RSF*T*MFP)	% At. Conc.
Pre sputter	C 1s	285.01	1.57	229.93	17.3
		286.68	1.02	30.37	2.3
		288.51	1.85	25.31	1.9
	Sb 3d	527.98	1.05	76.39	5.8
		537.33	1.05	50.80	3.8
		530.53	1.10	38.02	2.9
		539.80	1.39	25.29	1.9
	O 1s	529.99	1.90	299.72	22.6
		531.49	2.30	255.14	19.2
	Sn 3d	486.60	1.60	143.00	10.8
		495.01	1.56	95.13	7.2
		484.93	0.94	36.02	2.7
		493.36	0.90	23.96	1.8
30 s sputter	Sb 3d	528.01	1.09	141.33	16.0
		537.36	1.07	93.99	10.7
	O 1s	530.18	2.19	259.65	29.4
	Sn 3d	485.12	0.90	151.00	17.1
		493.53	0.90	100.46	11.4
		486.39	1.82	81.51	9.2
		494.71	1.94	54.22	6.2
60 s sputter	Sb 3d	528.02	1.08	124.97	15.3
		537.37	1.06	83.11	10.2
	O 1s	529.96	2.30	193.35	23.6
	Sn 3d	485.14	0.90	170.11	20.8
		493.56	0.90	113.17	13.8
		486.14	2.17	80.02	9.8
		494.34	2.30	53.24	6.5
120 s sputter	Sb 3d	528.02	1.09	110.62	14.3
		537.37	1.08	73.56	9.5
	O 1s	529.92	2.26	165.45	21.3
	Sn 3d	485.15	0.90	189.20	24.4
		493.56	0.90	125.87	16.2
		486.14	2.00	66.58	8.6
		494.41	2.21	44.29	5.7

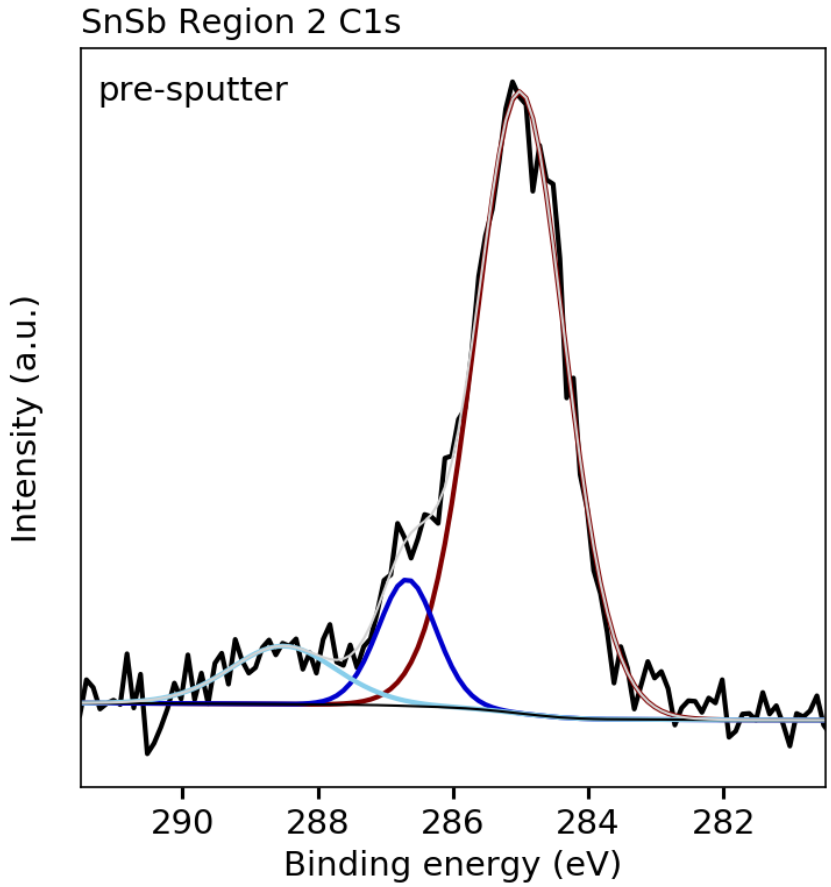

Figure 1C: XPS C 1s HRES spectrum from the representative pristine SnSb thin film sample before sputtering; carbon was detected on the SnSb surface due to the presence of adventitious carbon.

Table 2C: Fitting results for the first discharge SEI Sample 1

Sample region	Name	Position (eV)	FWHM (eV)	Area/(RSF*T*MFP)	% At. Conc.
Region 1	C 1s	284.34	1.53	481.46	20.5
		286.72	2.00	191.92	8.2
		290.75	1.59	47.42	2.0
		288.85	2.00	114.33	4.9
	F 1s	684.93	1.51	172.30	7.3
		686.96	1.96	171.90	7.3
	P 2p	136.55	1.68	20.85	0.9
		137.39	2.00	10.42	0.4
		133.02	2.00	10.96	0.5
		133.86	2.00	5.48	0.2
	O 1s	531.51	2.20	383.27	16.3
		533.95	1.99	129.24	5.5
		527.58	1.19	15.90	0.7

	Sn 3d	481.60	1.36	3.96	0.2
	Sn 3d	490.00	1.18	2.18	0.1
	Li 1s	55.10	1.87	466.68	19.9
		53.06	1.94	121.01	5.2
Region 2	C 1s	284.42	1.47	381.03	18.8
		286.24	2.00	159.79	7.9
		289.61	2.00	110.04	5.4
		287.96	1.89	55.81	2.8
	F 1s	684.88	1.58	87.98	4.4
		687.00	1.76	137.31	6.8
	P 2p	136.53	1.26	17.71	0.9
		137.37	1.16	8.85	0.4
		133.06	2.00	11.25	0.6
		133.90	2.00	5.62	0.3
	O 1s	531.48	2.13	395.46	19.5
		533.90	1.86	87.29	4.3
		527.81	2.30	21.54	1.1
	Sn 3d	481.66	1.40	3.58	0.2
		490.10	1.30	2.42	0.1
	Li 1s	55.00	2.01	433.35	21.4
		52.46	1.66	104.67	5.2
Region 3	C 1s	284.32	1.41	436.68	19.1
		285.87	2.00	140.45	6.2
		289.29	1.85	98.06	4.3
		287.90	2.00	40.66	1.8
		282.52	0.93	13.75	0.6
	F 1s	684.94	1.55	180.97	7.9
		687.22	1.87	175.22	7.7
	P 2p	136.87	1.42	24.57	1.1
		137.71	1.86	12.28	0.5
		132.93	2.00	10.86	0.5
		133.77	2.00	5.43	0.2
	O 1s	531.32	2.12	414.01	18.1
		533.77	1.64	41.94	1.8
		527.80	2.30	28.24	1.2
	Sb 3d	524.83	1.10	0.80	0.0
		534.13	1.21	0.53	0.0
		481.63	1.34	3.31	0.1
		490.05	1.26	2.10	0.1
	Li 1s	55.04	2.03	546.38	23.9
		52.64	2.03	107.43	4.7

Table 3C: Fitting results for the first discharge SEI Sample 2

Region	Name	Position (eV)	FWHM (eV)	Area/(RSF*T*MFP)	% At. Conc.
Region 1	C 1s	284.66	1.64	399.31	18.9
		286.45	1.99	63.12	3.0
		289.96	0.99	17.65	0.8
		289.29	1.57	30.19	1.4
	F 1s	684.99	1.66	56.22	2.7
		687.35	1.76	33.73	1.6
	P 2p	133.07	1.58	7.59	0.4
		133.91	1.74	3.79	0.2
		136.83	1.85	5.81	0.3
		137.67	1.67	2.90	0.1
	O 1s	531.18	1.97	454.27	21.4
		528.31	1.44	163.88	7.7
	Sn 3d	482.08	1.33	1.44	0.1
		490.50	1.09	0.85	0.0
	Li 1s	54.38	2.10	645.38	30.5
		52.93	2.10	232.36	11.0
Region 2	C 1s	284.54	1.57	504.91	28.9
		286.52	1.32	65.22	3.7
		289.74	1.25	68.00	3.9
		288.31	1.09	33.55	1.9
	F 1s	687.29	1.81	73.87	4.2
		684.96	1.58	52.28	3.0
	P 2p	136.85	1.33	9.87	0.6
		137.69	1.55	4.93	0.3
		132.99	1.70	8.22	0.5
		133.83	1.87	4.11	0.2
	O 1s/Sb 3d	531.47	2.17	379.13	21.7
		528.05	1.99	37.37	2.1
		524.94	1.34	1.24	0.1
		534.46	1.49	5.82	0.3
		534.24	1.34	0.82	0.1
	Sn 3d	481.90	1.41	2.90	0.2
		490.29	1.28	1.72	0.1
	Li 1s	55.03	1.77	375.62	21.5
		53.25	1.87	119.48	6.8
Region 3	C 1s	284.52	1.53	597.43	29.1
		286.44	1.74	64.37	3.1
		289.67	1.42	65.55	3.2
		288.48	0.88	15.40	0.8
	F 1s	687.46	1.85	104.05	5.1
		684.99	1.58	75.82	3.7

	P 2p	137.15	1.58	18.16	0.9
		137.99	1.74	9.08	0.4
		132.79	1.99	10.29	0.5
		133.63	1.80	5.14	0.3
	O 1s	531.24	2.20	417.15	20.4
		528.09	1.57	46.53	2.3
		534.74	1.73	9.76	0.5
	Sn 3d	481.90	1.53	2.71	0.1
		490.25	1.37	1.66	0.1
	Li 1s	54.71	2.01	569.97	27.8
		52.50	0.93	37.16	1.8

Table 4C: Fitting results for the first charge SEI Sample 1

Region	Name	Position (eV)	FWHM (eV)	Area/(RSF*T*MFP)	% At. Conc.
Region 1	C 1s	284.47	1.49	321.48	17.0
		287.00	2.00	225.00	11.9
		290.93	1.07	40.14	2.1
		289.32	1.98	100.99	5.3
	F 1s	684.89	1.60	110.04	5.8
		686.85	1.87	151.52	8.1
	P 2p	136.35	1.63	22.67	1.2
		137.19	1.92	11.33	0.6
		133.28	0.76	4.85	0.3
		134.12	0.50	2.43	0.1
	O 1s	531.55	2.30	353.12	18.7
		534.07	2.14	178.71	9.5
		526.61	2.30	20.93	1.1
	Sn1	483.47	1.07	4.19	0.22
		491.87	1.01	2.69	0.14
	Li 1s	55.00	1.93	341.86	18.1
Region 2	C 1s	284.48	1.60	5416.63	17.2
		287.10	2.00	4017.47	12.8
		290.73	1.35	1063.33	3.4
		289.22	1.36	1088.35	3.5
	F 1s	684.85	1.55	1660.15	5.3
		686.79	1.91	2909.38	9.2
	P 2p	136.26	1.64	300.41	1.0
		137.10	1.35	150.21	0.5
	O 1s	531.53	2.30	6070.24	19.3
		534.04	2.17	3284.20	10.4
		526.36	1.50	355.72	1.1
	Sn 3d	483.50	1.31	98.98	0.3
		491.84	1.03	52.80	0.2

	Li 1s	55.07	2.10	5049.94	16.0
Region 3	C 1s	284.43	1.61	304.82	16.3
		286.97	2.00	209.25	11.2
		290.79	1.08	33.43	1.8
		289.29	2.00	99.85	5.3
	F 1s	684.89	1.56	151.43	8.1
		686.72	1.97	136.99	7.3
	P 2p	136.10	1.52	15.88	0.9
		136.94	1.24	7.94	0.4
	O 1s	531.40	2.28	334.86	17.9
		533.90	2.23	170.12	9.1
		526.49	2.17	18.69	1.0
	Sn 3d	483.32	1.13	3.49	0.2
		491.71	0.96	2.14	0.1
	Li 1s	54.98	2.05	381.29	20.4

Table 5C: Fitting results for the first charge SEI Sample 2

Region	Name	Position (eV)	FWHM (eV)	Area/(RSF*T*MFP)	% At. Conc.
Region 1	C 1s	284.33	1.51	357.84	19.3
		286.65	2.00	172.35	9.3
		289.04	2.00	110.24	6.0
		290.81	1.21	31.14	1.7
	F 1s	684.80	1.55	97.53	5.3
		686.87	1.88	197.88	10.7
	P 2p	136.50	1.60	26.29	1.4
		137.34	1.76	13.14	0.7
		133.25	2.00	8.17	0.4
		134.09	1.88	4.08	0.2
	O 1s	531.37	2.14	339.55	18.3
		533.82	2.27	140.42	7.6
		526.49	2.30	21.14	1.1
	Sn 3d	483.22	1.14	3.89	0.2
		491.60	1.03	2.35	0.1
	Li 1s	55.06	1.73	325.30	17.6
Region 2	C 1s	284.37	1.46	432.38	19.9
		286.57	2.00	198.11	9.1
		290.16	2.00	76.24	3.5
		288.56	2.00	102.94	4.7
	F 1s	684.86	1.60	103.86	4.8
		687.01	2.00	224.80	10.3
	P 2p	136.63	1.86	33.90	1.6
		137.47	1.95	16.95	0.8
		133.00	2.35	10.49	0.5

		133.84	1.73	5.24	0.2
	O 1s	531.41	2.10	379.88	17.5
		533.80	2.23	152.64	7.0
		526.72	2.30	21.26	1.0
	Sn 3d	483.33	1.24	4.41	0.2
		491.62	1.11	2.29	0.1
	Li 1s	54.98	2.01	410.01	18.9
Region 3	C 1s	284.38	1.38	432.49	20.4
		286.30	2.00	174.29	8.2
		289.79	2.00	91.44	4.3
		288.13	2.00	82.77	3.9
	F 1s	684.89	1.57	118.26	5.6
		687.07	1.90	214.29	10.1
	P 2p	136.69	1.67	30.92	1.5
		137.53	1.59	15.46	0.7
		133.22	2.47	11.08	0.5
		134.06	2.72	5.54	0.3
	O 1s	531.46	2.09	372.01	17.6
		533.81	2.26	126.53	6.0
		526.74	2.30	20.93	1.0
	Sn 3d	483.39	1.31	4.17	0.2
		491.76	1.20	2.42	0.1
	Li 1s	55.09	1.99	415.65	19.6

LIST OF ABBREVIATIONS

A: area
AFM: atomic force microsopy
CV: cyclic voltammetry
DEC: diethyl carbonate
DEDOHC: diethyl 2,5-dioahexane dicarboxylate
DMC: dimethyl carbonate
DOD: depth of discharge
EC: ethylene carbonate
EDS: energy dispersive X-ray spectroscopy
EIS: electrochemical impedance spectroscopy
EMC: ethyl methyl carbonate
EQCM/EQCM-D: electrochemical quartz crystal microbalance/electrochemical quartz crystal microbalance with dissipation
FEC: fluoroethylene carbonate
FSI: bis(fluorosulfonyl)imide
FTIR: fourier transform infrared spectroscopy
FWHM: full width at half maximum
MALDI: matrix-assisted laser desorption ionization
MFP: mean free path
MPE: mass per moles of electrons
MS: mass spectrometry
OCP: open circuit potential
PC: propylene carbonate
PES: photoelectron spectroscopy
PTFE: polytetrafluoroethylene
PVdF: polyvinylidene fluoride
Pyr_{14}: N-butyl-N-methylpyrrolidinium
RSF: relative sensitivity factor
SEI: solid electrolyte interphase/interface
SEM: scanning electron microscopy
SIMS: secondary ion mass spectrometry
ssNMR: solid state nuclear magnetic resonance spectroscopy
T: transmission
TEM: transmission electron microscopy
THF: tetrahydrofuran
TFSI: bis(trifluorosulfonyl)imide
TMP: trimethyl phosphite
ToF: time-of-flight
VC: vinylene carbonate
XAS: X-ray absorption spectroscopy
XPS: X-ray photoelectron spectroscopy
XRD: X-ray diffraction